Numerical Investigations on Atmosphere -Biosphere Interactions

—

Impact of Radiation Fog and Leaf Surface Water

Tanja Winterrath
geboren in Osnabrück

Mainz 2002

Zusammenfassung

Der Austausch von Spurengasen und Aerosolpartikeln zwischen Atmosphäre und Biosphäre trägt maßgeblich zu deren atmosphärischem Budget bei. Wälder repräsentieren sowohl eine signifikante Senke als auch Quelle für Spurengase und Partikel. Während Laubbäume eine wichtige Quelle organischer Spurenstoffe, insbesondere Isopren, darstellen, wird Stickstoffmonoxid (NO) von Böden emittiert. Isopren und NO beeinflussen die Oxidationskapazität der Atmospäre und die Ozonproduktion. Strahlungsnebel beeinflußt durch Aufnahme, Entfernen und Prozessieren von Aerosolpartikeln und löslichen Spurengasen deren Konzentrationen in der Gasphase.

In dieser Arbeit wird zum ersten Mal ein Modell präsentiert, welches die Simulation des Austausches zwischen Atmosphäre und Biosphäre unter Berücksichtigung der dynamischen Wechselwirkung zwischen Strahlungsnebel, Blattflächenwasser und Mehrphasenchemie ermöglicht. Numerische Fallstudien zur größenabhängigen Flüssigphasenchemie, der Trockendeposition von Ammonia (NH_3) und der Modifikation von primären Emissionen von Isopren und NO durch einen Wald werden präsentiert.

Flüssigphasenkonzentrationen in Nebeltropfen sind größenabhängig. Insbesondere die Einflüsse des Waldes und des Blattflächenwassers werden untersucht. Die Ergebnisse zeigen, daß die Größenabhängigkeit zeitlichen und räumlichen Schwankungen unterliegt.

Trockendepositionsflüsse von NH_3 im Wald hängen vom Blattflächenwasser ab. Simulationen mit unterschiedlichen Behandlungen der Trockendeposition zeigen, daß das neue dynamische Depositionsmodell höhere Depositionsraten von NH_3 liefert, wenn chemische Reaktionen in der Gasphase berücksichtigt werden und das Reservoir an Blattflächenwasser groß genug ist.

Primäre Emissionen von Isopren und NO unterliegen vielfältigen Reduzierungsmechanismen, die zu einer Verminderung der Emissionen auf der Größenskala des Waldbestandes führen. Turbulenter Transport ist entscheidend für den Austausch der Luftmassen innerhalb und oberhalb des Waldes, insbesondere für die NO-Bodenemissionen. Die Berücksichtigung der chemischen Reaktionen von Isopren reduziert sowohl die Isopren- als auch die NO-Emissionen, während die Emissionen von NO_y, dem kompletten reaktiven Stickstoff, erhöht sind. Blattflächenwasser führt aufgrund von Reemissionen aus der Flüssigphase zu einer Erhöhung der NO_y-Konzentration.

iv

Abstract

The exchange of trace gases and aerosol particles between the atmosphere and the biosphere contributes significantly to their atmospheric budgets. Forests represent both an important source and sink for trace gases and particles. While deciduous trees are a significant source of organic compounds, especially isoprene, nitrogen oxide (NO) is emitted from forest soils. Isoprene and NO change the atmosphere's oxidative capacity and modify ozone formation. The presence of radiation fog influences both the trace gas concentrations and the aerosol particle spectrum by uptake, removal, and processing of aerosol particles and soluble trace gases.

In this thesis, for the first time, a model is presented that allows the simulation of atmosphere-biosphere exchange taking the dynamical interactions between radiation fog, leaf surface water, and multi-phase chemistry into account. Numerical case studies are presented focussing on size-dependent aqueous phase chemistry, dry deposition of ammonia (NH_3), and the modification of primary isoprene and NO emissions by a vegetation canopy.

Aqueous phase concentrations in fog droplets are size-dependent. Especially the influence of a vegetation canopy and the presence of leaf surface water are investigated. The simulations reveal that the size-dependence is subject to temporal and spatial variations.

Dry deposition fluxes of NH_3 to a vegetation canopy depend on leaf wetness. Simulations performed with different approaches on dry deposition show that the new dynamic deposition model leads to higher deposition rates of NH_3, if chemical reactions in the aqueous phase are accounted for and the leaf surface water pool remains large enough.

Primary emissions of isoprene and NO are subject to various reduction mechanisms reducing the emissions on the canopy scale. Turbulent transport is decisive for the exchange between air masses within and above the canopy, especially for the NO soil emissions. Inclusion of chemical reactions of isoprene reduce both the isoprene and NO emissions, while the emissions of NO_y, total reactive nitrogen, are enhanced. The presence of leaf surface water leads to an enhanced NO_y concentration due to reemissions from the liquid phase.

Contents

List of Figures

List of Tables

Chapter 1

Introduction

1.1 The Importance of Atmosphere-Biosphere Exchange

Forests, grassland, and crops cover more than 55 % of the Earth's land surface (Graedel and Crutzen, 1993). They act as significant sources and sinks for gases and aerosol particles and, therefore, modify the atmospheric composition. A detailed understanding of the exchange of trace substances between the biosphere and the atmosphere is therefore essential to the determination of atmospheric lifetimes, concentrations, and transport ranges of chemical trace species and aerosol particles.

While in the last decades focus of the atmosphere-biosphere exchange was given to acid deposition and the removal of radioactive gases and particles from the atmosphere, the range of investigations has expanded as the knowlegde on physico-chemical processes has increased. Examples are the emissions of biogenic organic compounds (Günther et al., 1994), the eutrophication of ecosystems, i.e., the excessive exposure to nutrients such as phosphate and nitrate (Zimmerling and Dammgen, 2002), the role of biological aerosol particles (Matthias-Maser and Jaenicke, 1995), and the potential formation of new particles from forest emissions (O'Dowd et al., 2002, Kavouras et al., 1998). However, large uncertainties prevail in the assessment of the source and sink strength to emission and deposition fluxes of trace substances.

In global scale models the atmosphere-biosphere exchange of trace gases used to be described with constant deposition (e.g., Penner et al., 1991) and emission rates. In the last decade, however, the role of the biosphere has attracted more attention, e.g., as an interactive climate component (Cox et al., 1999, Zeng et al., 1999), in dry deposition approaches (Ganzeveld et al., 2002, von Kuhlmann, 2001),

1

and in emission models (Potter et al., 2001). Deposition and emission fluxes are highly variable and depend on processes that cannot be resolved on the global scale. Appropriate measurement and modeling approaches are needed to increase the understanding of the interaction between the biosphere and the atmosphere and to lay the foundations of parametrizations for large scale models.

Important contributors to the deposition and emission fluxes are forests. Emissions from vegetation on the regional scale depend on the source strength of the primary emissions, but also on the physico-chemical processes within the vegetation canopy. These include the transport of the primary emissions from the emission source, e.g., the soil surface or the crown area, to the boundary layer above the canopy, gas phase chemical reactions, and interaction with the liquid water phase, while the primary source strength itself is influenced by, e.g., the radiative transfer within the canopy, the temperature field, the characteristics of the plant species, and the soil moisture.

Amongst other species, volatile organic compounds (VOCs), important precursors of tropospheric photo-oxidants are emitted from the biosphere. The most prominent VOC emitted from deciduous trees is isoprene (C_5H_8). The oxidation of isoprene by OH changes the atmosphere's oxidative capacity (Fehsenfeld et al., 1992) and initiates the formation of ozone (Chameides et al., 1992). Assessments on the global emissions are in the order of 600 $\mathrm{Tg\,C\,a^{-1}}$ (Wang et al., 1998). In addition to the plant emissions, forest soils are important emitters of nitrogen oxide (NO). Nitrogen oxides (NO, NO_2) are important compounds in atmospheric chemistry, because their concentration determines the photochemical ozone production in the troposphere (Crutzen et al., 1999).

Forests also provide significant surfaces for dry deposition. Similar to the impacts on the primary emission fluxes within the canopy, dry deposition fluxes depend on turbulent mixing, chemical reactions, and the uptake into the liquid phase. One important species in dry deposition assessments is ammonia (NH_3). Reduced nitrogen, NH_x, i.e., ammonia (NH_3) and ammonium (NH_4^+), contributes more than half of the total nitrogen input to European ecosystems (Asman, 2001, RGAR, 1997). The input of NH_x to both land and sea surfaces is of great importance for the ecosystems. Excessive deposition of NH_x to the land surface might result in a nitrification of the soil and a change in abundant plant species (Asman, 2001). Nitrogen input to sea water enhances the growth of algae with subsequent effects on the marine flora and fauna. Moreover, NH_3 is the most abundant base in the atmosphere having the potential to neutralize acids in precipitation and fog.

1.2 The Role of Fog in the Troposphere

Fog is an important meteorological phenomenon in various branches of science.

Fog reduces the visibility and, therefore, effects transportation. Thus, the forecast of fog events based on meteorological data and environmental conditions is a task of high economic benefit. Several modeling approaches exist on the forecast of radiation fog, e.g., Bott and Trautmann (2002), Clark and Hopwood (2001), Teixeira and Miranda (2001), Bergot and Guedalia (1994).

The deposition of fog droplets is important for both the input of water and nutrients, but also pollutants into the ecosystem and the removal of trace gases and aerosol particles from the atmosphere.

The water input by fog deposition is important for humans as well as flora and fauna. Cloud forests are provided with water and nutrients by interception of fog droplets, while animals in arid regions benefit from dew formation and fog interception for their water supply. In many arid parts of the world fog collection starts to become an important way in drinking-water production for the population (Schemenauer and Cereceda, 1994).

Along with water also aerosol particles and chemical compounds are removed from the atmosphere by depositing fog droplets. Wet and moist deposition by precipitation and interception of fog droplets with vegetation, respectively, provide an effective sink for aerosol particles and soluble trace gases. Several measurements (Zimmermann and Zimmermann, 2002, Wrzesinsky and Klemm, 2000, Fuzzi, 1998, Millet et al., 1997) and modeling studies (von Glasow and Bott, 1999, Lillis et al., 1999, Bott et al., 1990, Pandis and Seinfeld, 1989) on fog chemical composition and deposition have been performed. Both the deposition velocity of the droplets and the aqueous phase concentrations of the trace substances are size-dependent (Reilly et al., 2001, Rao and Collett, Jr., 1998, Bator and Collett, Jr., 1997, Collett, Jr. et al., 1994, Pandis et al., 1990). Consequently, trace substances enriched in large particles deposit more effectively than species abundant in small particles.

The processing of trace gases and aerosol particles leading to a change in aerosol mass and chemical composition has potential influence on subsequent cloud forming and therefore on the atmosphere's radiative budget as shown by measurements (Krämer et al., 2000) and modeling studies (Feingold and Kreidenweis, 2000, Wurzler et al., 2000, Bott, 1999, Bergin et al., 1996).

1.2.1   The Classification of Fog

The meteorological criterium for the occurrence of fog is a visibility below one kilometer. The reduction of visibility is due to the enhanced scattering of light on fog droplets or ice crystals. Fog develops when water vapor condenses or sublimates onto atmospheric aerosol particles. Depending on the building process six fog types can be distinguished. The reasons for fog development can be atmospheric mixing processes (frontal fog, sea smoke, fog by turbulence) or the cooling of the air mass below the dew point temperature due to streaming of air masses over cold surfaces (advection fog), adiabatic cooling of rising air masses at topographical obstacles (orographic fog), and radiative cooling of the ground surface and the adjacent air masses (radiation fog).

1.2.2   Radiation Fog

Radiative cooling of the ground is responsible for the development of radiation fog. When the temperature of the adjacent air masses falls below the dewpoint condensation or sublimation sets in. Different types of radiation fog can be distinguished depending on the vertical extent and thickness of the fog.

Above moist soils the air in the ground layer is humid. A slight cooling leads to condensation. Under calm conditions a very flat fog layer with a vertical extend of tens of centimeters develops. Wind driven turbulence lifts the cooled air masses. Depending on the intensity of the turbulence and the water vapor reservoir fog layers of a few meters upto several hundert meters can develop. In cases where the dew point is only reached due to a combination of radiative cooling and vertical transport condensation sets in above the ground leading to a lifted fog layer or a very low stratiform cloud.

Dissipation occurs when the radiative heating of the ground and the adjacent air masses induce turbulent mixing and a temperature rise that lead to the lifting and thinning of the radiation fog.

Because of the low dynamics in radiation fogs, entailing low collision and coagulation rates, radiation fogs usually have low liquid water contents and contain particles of a small mean particle size.

1.3 Motivation

In this thesis a model is developed that, for the first time, combines detailed biosphere-atmosphere interactions with the multiphase chemistry in the presence of radiation fog.

The striking feature is the detailed calculation of both the microphysical processes and size-dependent multiphase chemistry. The prognostic description of radiation fog and leaf surface water and the coupling to the detailed multiphase chemical module, along with the multi-layer description of the radiation field and the turbulent transport within the vegetation canopy, result in a highly sophisticated model on atmosphere-biosphere interactions.

The thesis is divided into four parts. The two main parts are each opened with a short overview of the following chapters. Therefore, here only a short description is given.

In Part I the CHEmical-MIcrophysical FOG model including Vegetation (CHEMI-FOG_V) is presented in detail. CHEMIFOG_V is based on the CHEmical-MIcrophysical FOG model (CHEMIFOG, Bott, 1992) and the MIcrophysical FOG model including Vegetation (MIFOG_V, von Glasow and Bott, 1999). The basic equations of all model parts including modules taken over from CHEMIFOG and MIFOG_V are given. New and extended parts of the model are discussed in more detail.

In Part II results of model simulations are presented. First, the meteorological results, that are the same for each study, are given. Three studies on different aspects of the interaction between the atmosphere, the biosphere and multiphase chemistry are presented. In detail, these are numerical studies on size-dependent aqueous phase chemistry, dry deposition of ammonia (NH_3), and the modification of primary isoprene and NO emissions by a vegetation canopy. Each of the three chapters is composed for a publication in a scientific journal and therefore contains separate introductions, results, and conclusions.

Part III gives a summary of the presented work and an outlook of interesting studies to perform in the future.

Part IV comprises the appendices containing tables of data used in the model simulations.

Part I

Model Description

8

Abstract. In this part the CHEmical MIcrophysical FOG model with Vegetation, CHEMIFOG_V, that is designed to study the interactions between radiation fog, vegetation, and chemistry and has been developed within this work, is introduced.

The state of the atmosphere in the height-resolving one-dimensional model is prognostically determined with a closed equation set. Furthermore, the heat and moisture fluxes of the soil are prognosticated. One special feature of the model is the detailed treatment of aerosol and cloud microphysical processes. Especially the two-dimensional particle size bin structure with the total droplet radius and the dry aerosol particle radius as independent variables allows a realistic description of the microphysical characteristics of radiation fog.

Vegetation is represented by a height-resolved multi-layer vegetation module with a vertical grid spacing of two metres. This highly resolved module allows an accurate representation of the complex features of a vegetation canopy and subsequently its influences on the physico-chemical state of the atmosphere, including heat and moisture transfer, the exertion of a dynamic resistance, as well as the emission of chemical species. Because of the various complex interactions of the vegetation with the other model compounds, the vegetation module is not added in a modal structure but accounted for in the respective equations.

Chemical reactions are considered both in the gas and in the liquid phase. Mass transfer between the phases is calculated explicitly. Besides in the fog droplets, also in the leaf surface water, that is a result of deposition and condensation, aqueous phase reactions are calculated.

In the following chapters a description of the single modules is presented.

In Chapter 2, a general overview of the model CHEMIFOG_V is given and advantages but also limitations of the model are discussed.

In Chapter 3 the representation of the canopy in the model is described and the vegetation parameters are defined.

In Chapter 4 the prognostic equations for the atmospheric wind, temperature, and humidity are presented, whereby the treatment of turbulent transport is discussed in detail. Furthermore the set of prognostic equations for the soil heat and moisture fluxes is introduced.

The microphysical module is presented in Chapter 5. After the description of the physico-chemical processes the prognostic equations for the particle spectrum and the leaf surface water, i.e., the water mass that covers the vegetation surfaces, are presented.

The radiative transfer model, that includes the influence of vegetation on the radiation field, is introduced in Chapter 6. Also, the calculation of the photosyn-

thetically active radiation (PAR), that influences plant emissions, and the module to calculate photolysis frequencies are presented.

Chapter 7 contains a detailed description of the physical and chemical processes that modify the chemical composition of both the gas and the liquid phase. Besides the treatment of turbulent transport, deposition, emission, condensation and evaporation, the chemical reaction mechanism is presented.

Chapter 8 gives an overview of the numerical grids and techniques.

CHEMIFOG_V is based on the CHEmical MIcrophysical FOG model CHEMI-FOG by Bott (1992) and Bott and Carmichael (1993) and the MIcrophysical FOG model with Vegetation MIFOG_V by von Glasow and Bott (1999). For more detailed information on these models the reader is referred to the given references. A brief description of CHEMIFOG_V has been pre-published in Winterrath and Bott (2001).

10

Chapter 2

Overview

In this chapter an overview of the model CHEMIFOG_V is given. General features of CHEMIFOG_V are presented and advantages but also limitations of the model are discussed.

CHEMIFOG_V is a one-dimensional model designed to study interactions between radiation fog, multi-phase chemistry, and high vegetation. Simulations are performed to investigate the physico-chemical processes during the build-up, development, and dissipation of a radiation fog event in a forest environment.

Figure 2.1 shows a schematic of the major physico-chemical processes simulated with CHEMIFOG_V. Vegetation is part of the lower model domain with an equidistant grid spacing of 2 m represented by the grey dashed lines. In the presented model simulations 11 vegetation layers were used resulting in a vegetation height of 22 m. The modules for calculating the dynamics, including turbulence, the moisture and heat fluxes both within the atmosphere and the soil, and fog microphysics have been taken from the models MIFOG_V (von Glasow and Bott, 1999) and CHEMIFOG (Bott and Carmichael, 1993) without or with only minor changes. The radiative transfer module has been modified compared to the original work. The chemistry module including the dry deposition and the emission of trace gases and the sedimentation/deposition module have been newly incorporated into the model within the scope of this work.

Various interactions between vegetation, soil and atmosphere have to be taken into account in the dynamical modeling of a forested boundary layer. While the main physico-chemical interactions can be described accurately, two major limitations occur in the presented modeling approach. First, horizontal inhomogeneities in the vegetation and consequently in the physico-chemical parameters are smoothed out or neglected in a one-dimensional approach. Second, the biological processes
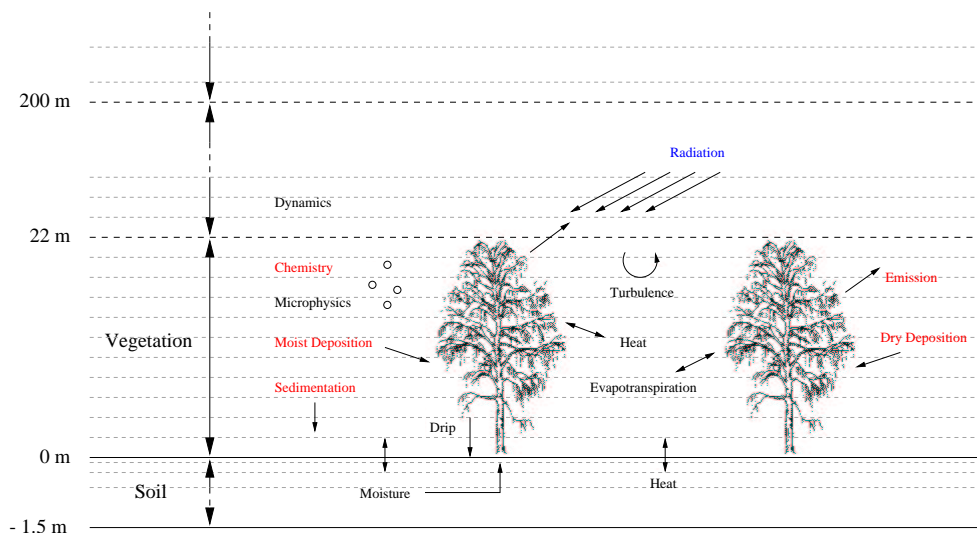
Figure 2.1: Overview of the physico-chemical processes in the lower model domain of CHEMIFOG_V. Modules that have been developed and/or implemented within the scope of this work are red (chemistry, moist deposition, sedimentation, emission, dry deposition), modules that have been modified are blue (radiation), while modules that have been taken over from MIFOG_V or CHEMIFOG are black (dynamics, microphysics heat and moisture fluxes, drip, evapotranspiration).

are not simulated in detail within the scope of this microphysical-chemical model. Thus, coupling of the physico-chemical processes with biological responses has to be adressed in more detailed physiological models. However, the knowledge on both the inhomogeneities of a vegetation canopy and on the plant-atmosphere interactions are still limited and more detailed models rely on a number of assumptions.

In the following, different aspects of the model are highlightened and limitations are discussed.

For the calculation of the radiative transfer in CHEMIFOG_V the optical depth of the vegetation is included in the radiative transfer equation. The optical depth depends on the density of the forest, the optical properties of the plants, and the angular distribution of the leaves. The additional optical depth leads to enhanced attenuation of both the direct and diffuse solar radiation flux. Inhomogeneities of the radiation field, however, are not addressed with the used one-dimensional radiative transfer model PIFM 2 (Loughlin et al., 1997, Zdunkowski et al., 1982). These inhomogeneities are addressed in other models by, e.g., determining the area of sun flecks on the ground that influence the microbiology of the forest floor and therewith the soil emissions (Verstraete, 1987) or by differentiation between sunlit

and shaded leaves modifying plant emissions (Ganzeveld and Lelieveld, 1995). On the canopy scale, nevertheless, radiative transfer simulations are in good agreement with measurements (Flender et al., 2001). Moreover, the module has been extended by the calculation of the photosynthetically active radiation influencing the isoprene emissions of the plants and by the calculation of photolysis frequencies. For the latter purpose, the model of Landgraf and Crutzen (1998) has been applied and adjusted to the vegetation module within this work.

The temperature profile within a vegetation canopy is mainly influenced by the absorption of incoming solar radiation during daytime and longwave emission during nighttime. During daytime, highest temperatures are found within the crown region of the canopy, i.e., the altitude with maximum leaf area density (LAD). As a result, the planetary boundary layer (PBL) is well-mixed above the canopy, while stable conditions prevail within the canopy. During nighttime, the radiative cooling of the canopy leads to a temperature minimum within the crown region. Therefore nocturnal convection prevails within the canopy (Jacobs et al., 1994), while the overlying PBL is stable during nighttime. The reduction of wind shear during the night additionally supports this behaviour. Turbulence in a forest environment, accordingly, separates the canopy from the atmosphere above. Mixing processes mainly occur during sunrise and sunset, when the temperature gradient inverts.

In CHEMIFOG_V turbulent exchange is modeled using the 'K-theory'. As the canopy temperature is prognosticated on a height-resolved atmospheric grid, the thermally induced turbulent exchange processes in a forest environment can be well simulated with CHEMIFOG_V. Turbulence in canopies, however, has additional complex attributes, e.g., counter-gradient transport, that is related to large-scale intermittent turbulent down-sweeps originating in the overlying PBL (Raupach and Thom, 1981, Kruijt et al., 2000). However, counter-gradient processes cannot be resolved in a one-dimensional approach. As canopy concentrations and canopy top fluxes of trace gases are sensitive to turbulent transport (Ganzeveld et al., 2002), this has to be kept in mind, especially when discussing deposition, emission, and canopy reduction.

In CHEMIFOG_V, the sophisticated microphysical module has been taken from CHEMIFOG and MIFOG_V. The main feature is the detailed treatment of the droplet growth due to water vapor condensation. Hereby, no difference is made between non-activated and activated particles that are described by a two-dimensional size distribution with the total and the dry particle radius as independent variables.

Within the scope of this work, a new in-canopy particle sedimentation and moist deposition module has been developed and implemented. In this approach

the canopy is assumed to consist of both vegetation elements and interstitial air. As a consequence, sedimentation of particles within the interstitial air is made possible and an overestimation of the deposition fluxes is prevented. The new calculation of the water deposit on the leaves and the dewfall allow the detailed forecast of the leaf surface water, that is an important parameter in the dry deposition and the new chemical model.

Dry deposition is the diffusion and subsequent sticking of atmospheric trace gases to vegetation surfaces and the soil. Subsequently, the deposition velocity, i.e., the reciprocal of the resistance to dry depostion, depends on both the diffusivity of the trace gas and the properties of the deposition surface. The dry deposition to the vegetation surfaces is commonly calculated with a resistance approach. This implies the assumption, that only mono-directional deposition fluxes occur. In reality, fluxes can be bi-directional depending on the concentration gradient between, first, the leaf interior or, second, the leaf surface water and the ambient air. Bi-directional fluxes to dry surfaces can be approximated by the use of a compensation point assuming a fixed trace gas concentration within the leaf interior (e.g., Nemitz et al., 2001). A more sophisticated approach is the explicit simulation of the chemical processes in both the leaf apoplast and the leaf surface water considering epicuticular fluxes in the case of water covered cuticles (Flechard et al., 1999).

In CHEMIFOG_V dry deposition is splitted into deposition to dry and to wet surfaces. Dry deposition to dry surfaces is mono-directional calculated based on the resistance approach of Ganzeveld and Lelieveld (1995). For the dry deposition to wet surfaces, the dominant dry deposition process during a radiation fog event, a new approach has been developed within the scope of this work. Instead of using resistances, the dry deposition to wet surfaces is simulated via the interfacial mass transfer with subsequent chemical reactions in the leaf surface water allowing the reemission of previously deposited trace gases. As under fog conditions leaf surfaces are mostly covered with water, this combined approach results in a highly sophisticated dry deposition scheme under radiation fog conditions, although biological processes are omitted.

Plant emissions of isoprene and soil emissions of NO have been included within the scope of this work. The implemented parametrizations depend on the meteorological parameters provided in CHEMIFOG_V, however, some plant and soil specific parameters influencing the emission characteristics are not included.

Chemical reactions are calculated in both gas and aqueous phase. For this purpose, a new gas phase mechanism including the condensed Mainz Isoprene Mechanism (MIM) (Pöschl et al., 2000) and a new aqueous phase mechanism including

organic C2-chemistry (Herrmann et al., 2000) have been implemented. These models are well suited for the simulation of the chemical processes in a forest environment. The prognostic determination of the chemical composition of the leaf surface water was implemented for the first time into a dynamical fog model. Here, both the dynamical exchange of species between the gas phase and the leaf surface water and the input of water and chemical species due to deposition of fog droplets allow a sophisticated investigation of leaf surface water chemistry.

CHEMIFOG_V is a chemical-microphysical radiation fog model with detailed description of the microphysics of a radiation fog event. Special emphasis is put on the dry and moist deposition processes to vegetation surfaces, that for the first time, allow the prognostic determination of leaf surface water and the detailed description of chemical reactions within. Overall, CHEMIFOG_V is a powerful tool to investigate the interactions between radiation fog, vegetation and chemistry.

Chapter 3

The Representation of Vegetation

In this chapter the multi-layered representation of vegetation is illustrated and parameters used in the model description are defined[a]. The impact of vegetation on the physical and chemical processes is adressed directly in the respective chapters. Here only the parameters necessary to describe the canopy characteristics are introduced.

The vegetation module implemented in CHEMIFOG_V is a multi-layer module with a vertical resolution of $\Delta z = 2\,\mathrm{m}$. The canopy is defined by the canopy height h, the canopy covering, σ with $\sigma = 1$ corresponding to full covering and $\sigma = 0$ corresponding to no canopy, and the vertical profile of the one-sided leaf area density (LAD), $b(z)$, i.e., the one-sided surface area of the leaves per unit volume.

The one-sided leaf area index (LAI) is the one-sided surface area of the leaves per unit ground area. Consequently, the LAI of one model layer is defined by $b(i)\Delta z$.

Under the assumption of plane leaves for deciduous trees and an isotropic angular distribution of the leaf orientation, the horizontal projection of the LAD, $\tilde{b}(z)$, is given by[b]:

$$\tilde{b}(z) = \frac{b(z)}{2}. \tag{3.1}$$

In CHEMIFOG_V the vegetation canopy is assumed to consist of vegetation elements and the interstitial atmosphere. However, the subgrid feature of vegetation cannot be resolved in the model. Hence, a subgrid homogeneous vertical distribution of the vegetation elements within the model layers has to be assumed. In the following the vertical distribution of vegetation is graphically represented by a diagonal

---

[a]Nomenclature: In the following the single resolved structures are referred to as vegetation or vegetation elements, while the forest as a whole including vegetation elements and interstitial air is named vegetation canopy.

[b]For coniferous trees $\tilde{b}(z) = \frac{b(z)}{\pi}$.
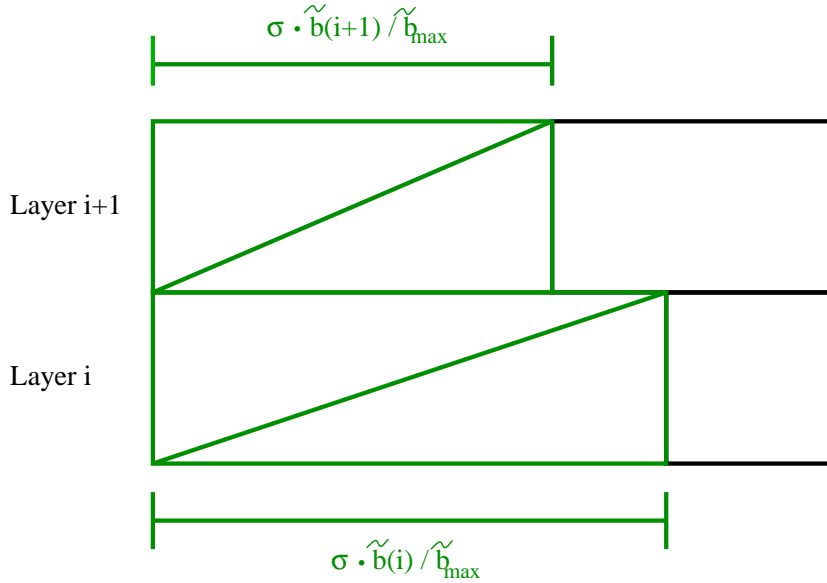
Figure 3.1: Schematic of the representation of the canopy in CHEMIFOG_V.

through the vegetated fraction of one model layer and used for deriving weighing factors in the deposition model.

Figure 3.1 shows a schematic of two layers in a vegatation canopy. Under the assumption that the vegetation covering in each layer is proportional to $\tilde{b}(z)$, the vegetation covering in each layer is $\sigma \frac{\tilde{b}(z)}{\tilde{b}_{max}}$. The vegetation covering in the layer with maximum projected LAD, $\tilde{b}_{max} = \max\left[\tilde{b}(z)\right]$, consequently, equals σ. As a consequence, the area covered by the horizontal projection of the leaves' surface is limited to σ. Hence, in case that the maximum projected LAI, $\tilde{b}_{max}\Delta z$, is larger than σ, an enhancement factor, $\frac{\tilde{b}_{max}\Delta z}{\sigma}$, is introduced, that is used as a proportionality factor in the deposition module representing the density of vegetation elements.

In the following, vegetation elements are in general referred to as leaves. This is justified as 95 % of the vegetation surface is made up by the leaves (Halldin, 1985). If other vegetation elements are considered, it is mentioned explicitly in the text.

Chapter 4

The Thermodynamic Model

The profiles of the three components of the wind vector $\boldsymbol{v}^{\mathrm{a}} = (u, v, w)$, the air temperature T, the air density ρ, and the water content (water vapor, liquid water, and ice) determine the meteorological state of the atmosphere.

In the first section the prognostic equation for the wind vector, the air temperature, and the water vapor content are discussed. In Section 4.2 the treatment of the turbulent transport in the atmosphere is presented in detail. The formulation of an equation for the turbulent kinetic energy closes the set of prognostic equations for the atmospheric budget.

The prognostic equation for the liquid water content of the atmosphere is described in Chapter 5. As the temperature is above freezing point in all simulations the ice phase is omitted.

In the last section the prognostic equations describing the soil fluxes of heat and moisture are given.

In each section special emphasis is put on the influence of vegetation, i.e., the resistance that the vegetation exerts to the wind field, the attenuation of turbulence, and the modification of the moisture and heat fluxes in the atmosphere and in the soil.

4.1 The Prognostic Equations

For the mesoscale modeling of radiation fog several assumptions are justified to simplify the set of equations that defines the meteorological state of the atmosphere. First, as radiative cooling of the ground is responsible for the development of radiation fog and wind velocities are assumed to be small, the assumption of horizontal

---

[a]Vectors are marked by the use of the bold font.

homogeneity, and therefore the use of a one-dimensional model, is justified. Second, incompressibility of the atmosphere, $\boldsymbol{\nabla} \cdot \boldsymbol{v} = 0$, is assumed. As a consequence, $\frac{\partial w}{\partial z} = \frac{\partial w}{\partial t} = 0$ and, therefore, $w = 0$ to guarantee mass conservation. ρ is determined diagnostically according to the ideal gas law for moist air and air pressure is derived diagnostically from hydrostatic equilibrium. Under these assumptions a simplified set of prognostic equations describing the thermodynamic state of the atmosphere can be deduced (Bott, 1992).

The horizontal components of the wind field, u and v, are determined by the equation of motion based on the Navier-Stokes equation:

$$\frac{\partial u}{\partial t} = \frac{\partial}{\partial z}\left(k_m \frac{\partial u}{\partial z}\right) + f'(v - v_g) - \sigma c_d bu|u| \tag{4.1}$$

$$\frac{\partial v}{\partial t} = \frac{\partial}{\partial z}\left(k_m \frac{\partial v}{\partial z}\right) + f'(u - u_g) - \sigma c_d bv|v|, \tag{4.2}$$

where t is the time and z is the altitude. The first terms on the right side of Equations 4.1 and 4.2 describe the vertical turbulent transport with k_m, the turbulent exchange coefficient for momentum, that is described in detail in Section 4.2. The second term accounts for the Coriolis effect, where f' is the Coriolis parameter and u_g and v_g are the horizontal components of the geostrophic wind vector, that have constant values in the model calculations due to the assumption of horizontal homogeneity. The last terms represent the resistance, the vegetation exerts to the wind field, the so-called form drag (Wilson and Shaw, 1977, Yamada, 1982). Here $c_d = 0.2$ (Yamada, 1982) is the dynamic resistance of the canopy.

The prognostic equation for the atmospheric water vapor is expressed in terms of the specific humidity q:

$$\frac{\partial q}{\partial t} = \frac{\partial}{\partial z}\left(k_h \frac{\partial q}{\partial z}\right) + \frac{C'}{\rho} + \frac{\sigma b}{\rho} E \tag{4.3}$$

The first term on the right side of Equation 4.3 describes the vertical turbulent transport with k_h, the turbulent exchange coefficient for heat, that is described in detail in Section 4.2. The second term describes the moisture changes due to evaporation from and condensation to atmospheric particles at the rate C', that is derived from the droplet growth equation presented in Chapter 5. The last term describes the source term for moisture caused by the canopy due to the evapotranspiration flux E, that comprises both evaporation of leaf surface water respective condensation to the leaf surface E^e and the plant's transpiration E^t:

$$E^e = \rho \frac{q_s(T_f) - q}{R_a}\left[1 - \delta_c\left(1 - \epsilon\right)\right] \tag{4.4}$$

$$
\begin{aligned}
E^t &= \rho \frac{q_s(T_f) - q}{R_a + R_{stom}} \delta_c \, (1 - \epsilon) & (4.5) \\
E &= E^e + E^t \\
&= \rho \, (q_s(T_f) - q) \, \frac{1}{R_a} \left[1 - \delta_c \, (1 - \epsilon) \, \frac{R_{stom}}{R_a + R_{stom}} \right] & (4.6)
\end{aligned}
$$

with

$$
\delta_c = \begin{cases} 1 & : \quad q \le q_s(T_f) \\ 0 & : \quad q > q_s(T_f). \end{cases} \tag{4.7}
$$

The moisture fluxes between the plant and the atmosphere are proportional to the moisture gradient, where q_s is the saturation humidity at the leaf surface depending on the leaf temperature T_f. Transpiration is limited to the fraction free of water, where the stomata are uncovered. The stomata are the minute openings of a leaf through which gaseous interchange takes place. They regulate the moisture as well as the chemical species fluxes between the plant and the atmosphere. While condensation can occur to the whole leaf surface, evaporation is limited to the wetted fraction of the leaf ϵ:

$$
\epsilon = \left(\frac{W}{W_{max}} \right)^{\left(\frac{2}{3} \right)}, \tag{4.8}
$$

where W is the actual water mass on the leaves and W_{max} is the maximum storage capacity of the leaves defined in Chapter 5. The exponent is due to the surface tension that leads to droplet forming on the waxy surfaces (Deardorff, 1978). A prognostic equation for W is derived in Chapter 5. Water vapor diffusion from the leaf surface to the atmosphere is limited by the atmospheric resistance R_a:

$$
\begin{aligned}
R_a &= \frac{1}{c_f u} \qquad \text{with} \\
c_f &= 0.01 \left(1 + \frac{0.3}{u} \right),
\end{aligned} \tag{4.9}
$$

where c_f is the heat transfer coefficient between the foliage and the ambient air. Transpiration, that in physical terms is the diffusion of water vapor from the leaf interior to the canopy air, is additionally performed against the stomatal resistance R_{stom}. The stomatal resistance is low, when the leaf stomata are open. R_{stom} is given based on Pielke (1984):

$$
R_{stom} = R_{min} \left[\frac{S_{max}}{0.03 S_{max} + E_\downarrow^{sw}} + P + \left(\frac{\eta_{wilt}}{\eta_{root}} \right)^2 \right]. \tag{4.10}
$$

The stomatal resistance is determined by the downward shortwave irradiance $E_\downarrow^{sw}$ defined in Chapter 6 and the volumetric moisture content of the root zone (see

Section 4.3) η_{root} that is available for transpiration. η_{wilt} is the volumetric moisture content beneath which wilting sets in, $S_{max} = 330\,\mathrm{W\,m^{-2}}$ is the maximum incoming solar irradiance, $R_{min} = 250\,\mathrm{s\,m^{-1}}$ (Larcher, 1994, von Glasow and Bott, 1999) is the minimum stomatal resistance, and P is an empirical constant that accounts for the seasonal change. In the presented model calculations P is set to a value of 2 according to Deardorff (1978) and von Glasow and Bott (1999).

The potential temperature is defined as $\theta := T(p_0/p)^{R/c_p}$, where p is the ambient air pressure and $p_0 = 1013\,\mathrm{hPa}$ is the standard pressure. R is the specific gas constant of dry air, and c_p is the specific heat at constant pressure. With this definition the prognostic equation for θ is given within the canopy of height h and above:

$$\frac{\partial \theta}{\partial t} = \begin{cases} \frac{\partial}{\partial z}\left(k_h \frac{\partial \theta}{\partial z}\right) - \left(\frac{p_0}{p}\right)^{\frac{R}{c_p}}\left[\frac{1}{c_p \rho}\left(LC' + \frac{\partial E_n}{\partial z}\right)\right] & : \quad z > h \\[2ex] \frac{\partial}{\partial z}\left(k_h \frac{\partial \theta}{\partial z}\right) - \left(\frac{p_0}{p}\right)^{\frac{R}{c_p}}\left[\frac{1}{c_p \rho}\,LC' + \alpha_c \sigma b H\right] & : \quad z \le h. \end{cases} \tag{4.11}$$

The first term on the right side of each Equation 4.11 describes the vertical turbulent transport with k_h. The second terms describe the temperature change due to evaporation / condensation, where L is the latent heat of condensation. The third term in the upper equation accounts for the radiative heating respective cooling above the vegetation layers, where E_n is the total net irradiance defined in Chapter 6. Inside the vegetation layer, this formulation would lead to unrealistic results due to the absorption by vegetation elements. Instead the third term in the lower equation describes the source term for heat introduced by the canopy. H is the heat flux between the leaf and the ambient atmosphere. The factor $\alpha_c = 1.1$ (Deardorff, 1978) accounts for twigs that transfer sensible but no latent heat and is therefore only applied in Equation 4.11 but not in Equation 4.3. Equivalent to the moisture flux, the heat flux is formulated as follows (Deardorff, 1978):

$$H = \rho c_p \frac{T_f - T}{R_a}. \tag{4.12}$$

T_f is determined iteratively from the energy flux balance between the leaves and the ambient atmosphere.

4.2   Turbulence

The presented set of prognostic equations for the thermodynamical variables is not closed in terms of the turbulent transport. Mellor and Yamada (1982) proposed a

hierarchy of closure schemes, among which the so-called 2.5-level method has been shown to be a good compromise between accuracy and computing time and is therefore well suited for the use in mesoscale models. In this 1.5th order closure of the turbulent atmospheric system a prognostic equation is used to calculate the turbulent kinetic energy e, from which the turbulent exchange coefficients are determined diagnostically.

The prognostic equation for e writes:

$$
\begin{aligned}
\frac{\partial e}{\partial t} &= \frac{e^{*3}}{\ell}\left(S_m G_m + S_h G_h - \frac{1}{16.6}\right) + \frac{\partial}{\partial z}\left(k_e \frac{\partial e}{\partial z}\right) \\
&\quad + \sigma c_d b(|u|^3 + |v|^3),
\end{aligned} \tag{4.13}
$$

where $e^* = \sqrt{2e}$ and ℓ is the mixing length. The first two terms on the right side represent the atmospheric stability depending on the vertical shearing of the wind field and the temperature profile, respectively. The third term is a constant value for the dissipation of turbulent energy. Turbulent transport of turbulent kinetic energy is considered by the fourth term, where the exchange coefficient for turbulent kinetic energy is defined by $k_e = \min[0.2\ell e^*, k_m]$. The last term describes the impact of vegetation on the production of turbulence (Yamada, 1982).

The turbulent exchange coefficients for heat k_h and momentum k_m, that are included in Equations 4.1 to 4.3, Equation 4.11, Equation 5.26, and implicitly in Equation 4.13 are determined diagnostically:

$$
k_m = \ell e^* S_m \tag{4.14}
$$

$$
k_h = \ell e^* S_h. \tag{4.15}
$$

S_m and S_h are given by the following empirical formulation:

$$
\begin{aligned}
S_m &= \frac{a_5 + a_6 G_h}{A} \\
S_h &= \frac{a_7 + a_8 G_h + a_9 G_m}{A} \qquad \text{with} \\
A &= 1 + a_1 G_h + a_2 G_h^2 + G_m\left(a_3 + a_4 G_h\right),
\end{aligned} \tag{4.16}
$$

where the empirical numbers are given to $a_1 = -36.719$, $a_2 = 187.441$, $a_3 = 5.078$, $a_4 = -88.839$, $a_5 = 0.699$, $a_6 = -9.339$, $a_7 = 0.74$, $a_8 = -4.534$, and $a_9 = 0.902$.

G_m and G_h are atmospheric stability functions for momentum and heat:

$$
\begin{aligned}
G_m &= \frac{\ell^2}{e^{*2}}\left(\left(\frac{\partial u}{\partial z}\right)^2 + \left(\frac{\partial v}{\partial z}\right)^2\right) \quad \wedge \quad G_m \leq 0.815 - 25 G_h \\
G_h &= -\frac{\ell^2 g}{e^{*2} T}\frac{\partial \theta}{\partial z} \qquad\qquad\quad \wedge \quad G_h \leq 0.0326,
\end{aligned} \tag{4.17}
$$

where g is the gravitational acceleration. G_m depends on the vertical shearing of the wind field, while G_h is proportional to the vertical gradient of θ. The restriction given on the right side of Equation 4.17 is necessary to keep numerical stability.

The mixing length ℓ is a measure of the spatial extent of a turbulent element. The calculation of ℓ is performed according to two different approximations, one for the atmosphere above the canopy (Mellor and Yamada, 1982) and one inside the canopy (Watanabe and Kondo, 1990):

$$
\ell(z) = \begin{cases}
\dfrac{\kappa \left(z + z_0 - d\right)}{1 + \frac{\kappa}{\ell_0}\left(z + z_0 - d\right)} & : \quad z > h \\[2em]
\kappa \int_0^z \left[\tilde{r} \exp\left(-\int_0^{\tilde{r}} \mu(z-t)dt\right)\mu(z-\tilde{r})\right] d\tilde{r} \\
\qquad + \kappa z \exp\left(-\int_0^z \mu(z-t)dt\right) & : \quad z \leq h
\end{cases}
\tag{4.18}
$$

with the restriction that, if $\left|\frac{d\ell}{dz}\right| > \kappa$, then ℓ is chosen to fulfil $\left|\frac{d\ell}{dz}\right| = \kappa$, and $\kappa = 0.4$ is the von-Kármán constant, $z_0 = \frac{1}{12}h$ is the roughness length, $d = 0.75h$ is the displacement height, above which a logarithmic wind profile can be assumed (Thom, 1975), and:

$$
l_0 = 0.1 \frac{\int_0^\infty z e^* \, dz}{\int_0^\infty e^* \, dz}.
\tag{4.19}
$$

Inside the vegetation layer the vertical extent of turbulence is reduced due to attenuation by the vegetation. Hereby, $\mu \, d\tilde{r}$ is the probability that an air parcel is disturbed by the canopy while vertically shifted by $d\tilde{r}$ with:

$$
\mu = \frac{c_d b}{2\kappa^2}.
\tag{4.20}
$$

4.3 The Soil Model

In CHEMIFOG_V a multi-layer soil module is implemented. The vertical grid is logarithmically equidistant with 24 layers reaching down to a depth of $1.5\,\mathrm{m}$. The soil module represents both the boundary condition for the atmospheric module, but is also part of a water cycling process between the atmosphere, the soil, and the vegetation. In the module the Earth's surface is assumed as an infinitesimally thin layer with no storage capacity. Therefore the heat and moisture fluxes between the atmosphere and the soil must be in equilibrium at the surface. To fulfil this requirement, the ground temperature T_g and the volumetric soil moisture η_g are adjusted.

The balance equation for the heat fluxes at the Earth's surface is given by:

$$0 = E_\downarrow - \sigma_B T_g^4 - J_h(\eta_g, T_g) + L'(T_g) J_{ph}(\eta_g, T_g) + J_t(T_g) \tag{4.21}$$

comprising the radiative, sensible, and latent heat fluxes at the soil-atmosphere boundary. $E_\downarrow$ is the incoming radiation defined in Chapter 6. $\sigma_B T_g^4$ is the thermal emission with σ_B, the Stefan-Boltzmann constant. J_h is the heat flux into the soil depending on the soil temperature gradient taken at the Earth's surface as marked by $|_{surf}$:

$$J_h(\eta_g, T_g) = -\lambda_g \frac{\partial T_g}{\partial z}\bigg|_{surf}, \tag{4.22}$$

where λ_g is the thermal conductivity of the soil. J_{ph} is the phase transition flux, $L' = L + W'$, where W' is the energy needed to overcome the adhesion forces between soil water and pores, and J_t is the turbulent heat flux.

The balance equation for the moisture fluxes at the Earth's surface is given by:

$$0 = J_{vap}(\eta_g, T_g) - J_m(\eta_g) - J_m^{vap}(\eta_g) + J_s. \tag{4.23}$$

J_{vap} is the turbulent water vapor flux. J_m is the moisture flux in the soil given by:

$$J_m(\eta_g) = -\rho_w K_\eta|_{surf} - \rho_w D_\eta \frac{\partial \eta}{\partial z}\bigg|_{surf}, \tag{4.24}$$

where ρ_w is the density of water, K_η is the hydraulic conductivity and D_η is the diffusivity of water in the soil. J_m^{vap} is the water vapor flux into the soil:

$$J_m^{vap} = \hat{J}^1 + \frac{\rho^1}{\rho^0} J_a \quad \text{with} \tag{4.25}$$

$$\hat{J}^1 = -\frac{D^{vap}}{R_{vap} T_g} \frac{\partial p^1}{\partial z}. \tag{4.26}$$

Here ρ_0 and ρ_1 are the densities of dry air and water vapor, respectively. D^{vap} is the diffusion coefficient in the soil, R_{vap} is the specific gas constant, and p^1 is the partial pressure, all of water vapor. J_a is the flux of dry air into the soil. J_s is the sedimentation flux of water droplets plus the water that drips off the trees as defined in Chapter 5.

In the soil, continuity equations hold for the dry air and the total water. In an approximative form, they are given as follows:

$$\frac{\partial \rho^0}{\partial t} + \frac{\partial J_a}{\partial z} = 0 \tag{4.27}$$

$$\rho_w + \frac{\partial \eta}{\partial t} + \frac{\partial}{\partial z}(J_m^{vap} + J_m) = -S_\eta \tag{4.28}$$

$$C_h \frac{\partial T}{\partial t} + \frac{\partial}{\partial z}(J_h + L' J_m^{vap}) = 0, \tag{4.29}$$

where C_h is the heat capacity of the soil at constant volume and S_η is the water that is extracted from the root zone Δz_{root} by the vegetation and is balanced by the transpiration by the leaves (see Equation 4.5):

$$S_\eta = \sigma b \frac{E^t}{\Delta z_{root}}. \tag{4.30}$$

The root zone is defined as the soil layer, where the difference between the chemical potentials of the soil water and the root system is largest. As the potential of the roots is assumed to be constant, the root zone is the layer with maximum chemical potential.

The gradient of the soil flux of dry air J_a is determined diagnostically:

$$-\frac{\partial J_a}{\partial z} = \left(\frac{\partial \rho^0}{\partial T}\right)_{\eta,p^0+p^1} \frac{\partial T}{\partial t} + \left(\frac{\partial \rho^0}{\partial \eta}\right)_{T,p^0+p^1} \frac{\partial \eta}{\partial t}. \tag{4.31}$$

Coupling of the preceding equations results in a coupled set of prognostic equations for the moisture and heat fluxes within the soil:

$$
\begin{aligned}
\left(\rho_w - \frac{\rho^1}{\rho^0}\left(\frac{\partial \rho^0}{\partial \eta}\right)_{T_g,p^0+p^1}\right)\frac{\partial \eta}{\partial t} - \frac{\rho^1}{\rho^0}\left(\frac{\partial \rho^0}{\partial T_g}\right)_{\eta,p^0+p^1}\frac{\partial T_g}{\partial t} \\
+ J_a \frac{\partial}{\partial z}\left(\frac{\rho^1}{\rho^0}\right) + \frac{\partial}{\partial z}\left(\hat{J}^1 + J_m\right) &= -S_\eta \\
\left(C_h - L'\frac{\rho^1}{\rho^0}\left(\frac{\partial \rho^0}{\partial T_g}\right)_{\eta,p^0+p^1}\right)\frac{\partial T_g}{\partial t} - \frac{\rho^1}{\rho^0}L'\left(\frac{\partial \rho^0}{\partial \eta}\right)_{T_g,p^0+p^1}\frac{\partial \eta}{\partial t} \\
+ \frac{\partial}{\partial z}\left(J_h + L'\hat{J}^1\right) + J_a\frac{\partial}{\partial z}\left(L'\frac{\rho^1}{\rho^0}\right) &= 0,
\end{aligned}
\tag{4.32}
$$

For a more comprehensive description of the soil module the reader is referred to Siebert et al. (1992) and references therein.

Chapter 5

The Microphysical Model

Microphysical processes determine the temporal development of the aerosol particles and fog droplets. In CHEMIFOG_V all particles are described with a two-dimensional number size distribution $f(a, r)$, where the parameter a is the radius of the dry aerosol particle that served as a condensation nuclei, and r is the total particle radius including the water coating. Therefore no distinction is made between dry or water-coated aerosol particles and activated fog droplets. 40 size bins for a and 50 size bins for r, both logarithmically equidistant, cover the complete size spectrum of all particles. The temporal development of the size distribution is influenced by physico-chemical processes that change the single particles, as well as spatial redistributions of the particle spectrum due to transport processes. Moreover the leaf surface water is prognosticated. The processes can be divided into the change due to turbulent transport ($trans$), condensation and evaporation of droplet water (c/e), chemical processing ($chem$), and sedimentation and deposition ($sedi/depo$):

$$\frac{\partial f}{\partial t} = \left(\frac{\partial f}{\partial t}\right)_{trans} + \left(\frac{\partial f}{\partial t}\right)_{c/e} + \left(\frac{\partial f}{\partial t}\right)_{chem} + \left(\frac{\partial f}{\partial t}\right)_{sedi/depo}. \tag{5.1}$$

Collision and coagulation rates in radiation fogs are small and therefore negligible. As temperatures are above freezing point in the simulations, the ice phase is not considered in the present study. The physico-chemical processes are presented in Sections 5.1 (c/e) and 5.2 ($chem$). Sedimentation and deposition including the dripping of water from vegetation surfaces to lower levels or to the soil are introduced in Section 5.3 ($sedi/depo$). The combination of the mentioned processes leads to the formulation of the prognostic equations for $f(a, r)$ and for the leaf surface water W in Section 5.4. With these two prognostic equations the set of prognostic equations to determine the meteorological state of the system is completed.

5.1   The Droplet Growth Equation

Particle growth is determined by temperature and moisture gradients between the droplets and the ambient air. Condensation can occur, when the air is supersaturated with respect to the droplet temperature. Vice versa, in an subsaturated environment droplets evaporate. The rate of condensation and evaporation depends on the size and chemical composition of the particles. The energy needed to overcome for coating the particles increases with decreasing size and salt content. When the effect of radiative cooling of the droplets is considered, condensation can already take place in an otherwise subsaturated environment leading to enhanced droplet growth in regions, where the radiative effect is important. This is the case, e.g., in the upper part of radiation fog (Roach, 1976, Bott, 1992).

Condensation and evaporation change the water content of the particles. In terms of the total particle radius the droplet growth equation is:

$$r\frac{dr}{dt} = \frac{1}{C_1}\left[C_2\left(\frac{S_\infty}{S_r} - 1\right) - \frac{F_d(a,r) - m_w(a,r)c_w\frac{dT}{dt}}{4\pi r}\right]. \tag{5.2}$$

The first part on the right side of Equation 5.2 represents the classical droplet growth equation by water vapor diffusion (Pruppacher and Klett, 1997), where S_∞ is the ambient saturation ratio, and S_r is given by the Köhler equation:

$$S_\infty = \frac{e_\infty}{e_{\infty,s}} \tag{5.3}$$

$$S_r = \exp\left[\frac{A}{r} - \frac{Ba^3}{r^3 - a^3}\right]. \tag{5.4}$$

e_∞ and $e_{\infty,s}$ are the actual and the saturation water vapor partial pressures of the ambient air mass, respectively.

A and B account for the curvature and the solution effect, respectively:

$$A = \frac{2\sigma_{s/a}}{R_{vap}T\rho_w} \tag{5.5}$$

$$B = \frac{\epsilon'\nu\rho_a M_w}{\rho_w M_s}. \tag{5.6}$$

$\sigma_{s/a}$ is the surface tension of the aqueous solution against air, M_w and M_s are the molecular weights of pure water and the dissociated salt, ν is the number of ions, the solute dissociates into, and ϵ' is the soluble mass fraction of the aerosol particle.

The second term of Equation 5.2 accounts for the impact of radiation on the diffusional particle growth, where F_d is the net radiative flux integrated over the

particle surface, $m_w(a, r)$ is the water mass of the particle, and c_w is the specific heat of water. The calculation of F_d is presented in further detail in Chapter 6.

C_1 and C_2 in Equation 5.2 are defined as follows:

$$C_1 = \rho_w L + \frac{\rho_w C_2}{D_v' S_r \rho_s} \tag{5.7}$$

$$C_2 = k'T \left[\frac{L}{R_{vap}T} - 1\right]^{-1}. \tag{5.8}$$

Here ρ_s is the saturation vapor density, k' is the thermal conductivity of moist air, and D_v' is the diffusivity of water vapor, both corrected for gas kinetic effects.

With the droplet growth derived from Equation 5.2 the condensation rate C' used in Equations 4.3 and 4.11 can be calculated:

$$C' = \int_0^\infty \int_0^\infty \frac{\partial}{\partial r}(\dot{r}f(a, r))m_w(a, r)\, da\, dr, \tag{5.9}$$

where $\dot{r} = \frac{dr}{dt}$.

5.2 Chemical Processing

In CHEMIFOG_V the dry aerosol mass m_a of the droplets, and consequently their dry particle radius, can be increased by the formation of nitrate (NO_3^-), sulphate (SO_4^{2-}), ammonium (NH_4^+), chloride (Cl^-), and the sodium ion (Na^+)[a] due to chemical processes in the aqueous phase. The gain in mass can be expressed by the change in the dry particle radius:

$$\frac{dm_a}{dt} = 4\pi\rho_a a^2 \frac{da}{dt} = Q^{chem}. \tag{5.10}$$

The source term Q^{chem} is composed of the chemical production terms of the five compounds:

$$Q^{chem} = \frac{dm_{NO_3^-}}{dt} + \frac{dm_{SO_4^{2-}}}{dt} + \frac{dm_{NH_4^+}}{dt} + \frac{dm_{Cl^-}}{dt} + \frac{dm_{Na^+}}{dt}. \tag{5.11}$$

The chemical mechanism that determines the production terms is presented in Section 7.5.

---

[a]Na^+ is not included in the presented studies, but with the use of marine aerosol.

5.3   Sedimentation and Deposition

In this section, a new scheme to describe the sedimentation and vertical deposition of particles to vegetation surfaces, that has been developed within the scope of this work, is presented. In order to simulate not only the total deposition rate to the canopy, but a height-resolved deposition to the vegetation surfaces, the canopy has to be regarded as a composition of vegetation elements and interstitial air with a subgrid homogeneous distribution of the vegetation elements (see Chapter 3). In contrast to the simple approach, where all particles within the covered fraction deposit, in this new approach particles can also sediment within the interstitial air of the canopy without deposition to vegetation. Due to the homogeneous horizontal particle distribution assumed in the 1-d approach, the deposition rate would otherwise be overestimated.

Sedimentation leads to a spatial redistribution of atmospheric particles and therewith water mass and liquid phase chemical species to lower model layers. Deposition to vegetation surfaces modifies the sedimentation flux. Thereby, deposition is, first, a sink for the atmospheric constituents, but on the other hand, a source for the leaf surface water and the chemical species within. The rate of deposition of water due to droplet sedimentation, Q_{sedi}^{depo}, is derived in the following subsection. In Subsection 5.3.2, the rate of horizontal impaction of water to vegetation surfaces due to transport of particles along the wind vector, Q_{impact}^{depo}, is presented. The sum of both rates give the total deposition rate Q^{depo}, that is a source term for the leaf surface water:

$$Q^{depo} = Q_{sedi}^{depo} + Q_{impact}^{depo}. \tag{5.12}$$

5.3.1   Sedimentation and Vertical Deposition

The fog droplets sediment with their Cunningham corrected terminal velocity w_t, i.e., the velocity at equilibrium between buoyancy-corrected gravitational force and drag force, corrected for the slip-flow. Without vegetation, the sedimentation flux is:

$$\frac{\partial X}{\partial t} = \frac{w_t X}{\Delta z}, \tag{5.13}$$

where X marks the sedimenting variable of interest and Δz is the vertical extent of the respective model layer. In one time step Δt, particles fall down a distance of $-w_t \Delta t = C \Delta z$. The fraction of one layer, out of which the particles sediment to
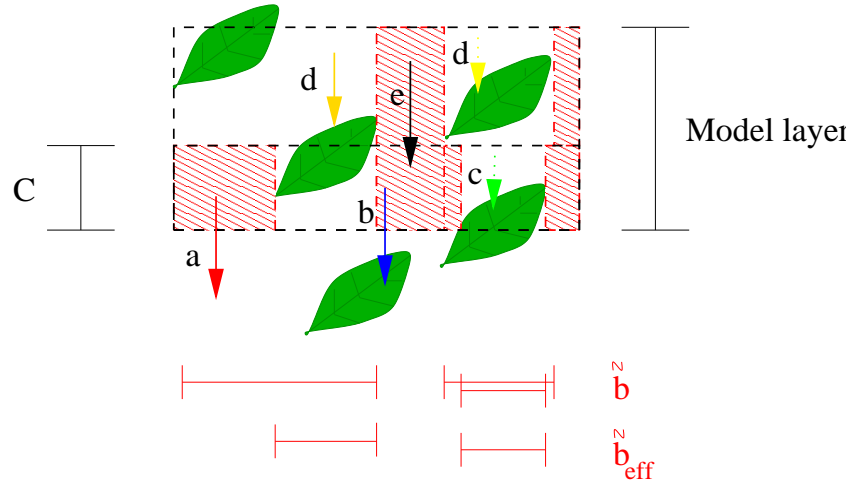
Figure 5.1: Schematic of the sedimentation and deposition processes.

the next lower layer is therefore expressed by the Courant number C[b]:

$$C = -\frac{w_t \Delta t}{\Delta z}. \tag{5.14}$$

With Equation 5.14, Equation 5.13 can be written as:

$$\frac{\partial X}{\partial t} = -C\frac{X}{\Delta t}. \tag{5.15}$$

In the presence of vegetation the sedimentation flux is reduced by deposition to the vegetation.

The sedimentation/deposition process is divided into three parts exemplarily given for layer i[c]:

1. $\Xi(i)$: the sedimentation flux from layer i to layer $i - 1$,

2. $\Upsilon(i)$: the vertical deposition flux within layer i, and

3. $\Omega(i)$: the vertical deposition flux from layer $i + 1$ to the vegetation in layer i.

Figure 5.1 shows a schematic of the different sedimentation and deposition processes, that are distinguished in the present modeling approach. The schematic shows an example of one model layer within the canopy, where the leaves represent the vegetation elements. The arrows represent different types of sedimentation respective

---

[b]$C(i - \frac{1}{2})$ is the Courant number at the boundary betweeen layer i and $i - 1$.

[c]The sedimentation flux describes the gravitational settling within the atmosphere, while the vertical deposition flux describes sedimentation with subsequent deposition onto, e.g., vegetation surfaces.

deposition processes, that take place in a vegetation canopy. As the effective surfaces provided for deposition have to be rectangular to the sedimentation flux, only the horizontal projection of the LAD, $\tilde{b}$, derived in Equation 3.1, has to be taken into account to calculate the impact of vegetation on the vertical sedimentation flux.

$\Xi(i)$ defines the loss of particles from layer i to the next lower layer $i-1$. According to Equation 5.14, particles originating in the lower fraction C of the layer can sediment to the next lower layer within one timestep Δt. The red arrow (a) marks sedimentation to the next lower layer without disturbance by vegetation, while the blue arrow (b) marks sedimentation to the next lower layer with subsequent deposition onto vegetation within the same timestep ($\Omega(i-1)$). For the upper layer, the loss of particles due to the sedimentation represented by the red and the blue arrow (b) is independent on the processes in the next lower layer. However, deposition processes within the same layer modify the sedimentation flux in case of vegetation. The green arrow (c) marks deposition of particles, that would enter the next lower layer during the timestep in case of no vegetation, but already deposit within the upper layer. This process therefore reduces the sedimentation flux to the next lower layer.

The sedimentation flux from one model layer to the next lower one, Ξ, consequently only depends on the processes inside the lower fraction C of the model layer. The fraction free of vegetation, marked by the red striped rectangles, is larger in that relevant fraction of the layer than in the total model layer. Therefore, for this layer fraction an effective projected LAD, $\tilde{b}_{eff}$, has to be determined to not overestimate the deposition flux. In the following, this effective vegetation fraction defines the fraction of the model layer, that is influenced by vegetation represented by e.g., the blue Triangle 1 in Figure 5.2.

The gain of particles within layer i due to the sedimentation flux from layer $i+1$ is given by the difference between $\Xi(i+1)$ and $\Omega(i)$ taking the deposition within layer i into account (blue arrow (b)).

Υ expresses the loss of particles due to deposition within each layer. In addition to the green arrow, the yellow arrows (d) mark sedimentation and subsequent deposition inside the actual layer, but of particles, that would not have reached the next lower layer during the timestep and therefore only have to be considered for the deposition, but not for the sedimentation flux.

If the projected LAI is larger than the vegetation covering in the model layer, the deposition rate is enhanced (dotted arrows), whereby the deposition rate is assumed to be proportional to the enhancement factor derived in Chapter 3. The black arrow (e) represents sedimentation inside the actual layer without deposition
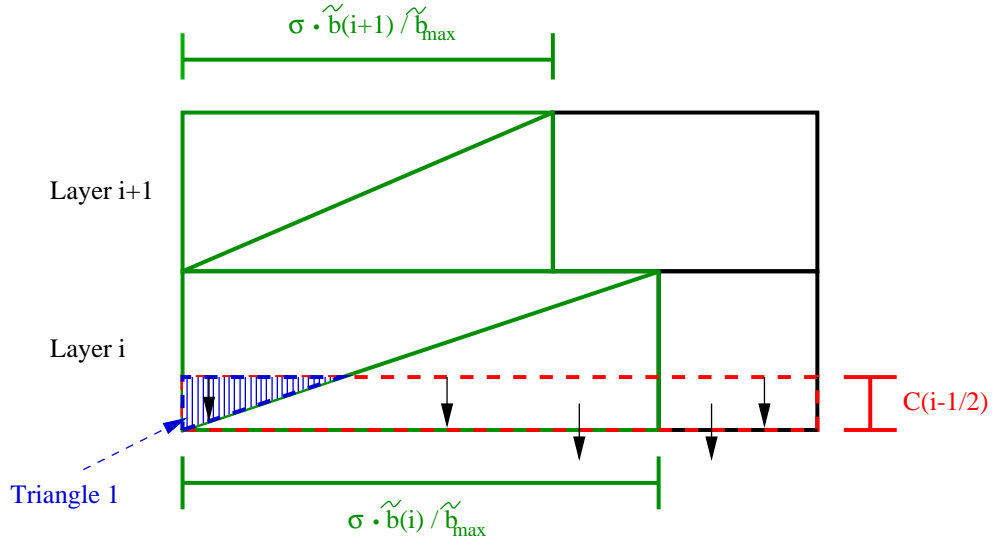
Figure 5.2: Schematic of the sedimentation flux Ξ within the vegetation canopy.

onto vegetation. As particles are assumed to be homogeneously distributed over the whole layer, this process is of no effect.

In the following the three processes are discussed and the derived equations are presented.

Figures 5.2 to 5.4 show schematics of the sedimentation and deposition processes as formulated in the multi-layer vegetation approach. The representation of the vegetation layers has already been shown in Figure 3.1. Vertical extents are given relative to the total layer extent. The black arrows indicate the sedimentation and deposition processes.

1. Figure 5.2 shows a schematic of the sedimentation flux from layer i to layer $i - 1$, $\Xi(i)$. The area of the red dashed rectangle with a vertical extent of $C(i - \frac{1}{2})$ marks the fraction of the particles of layer i, that sediments into layer $i - 1$ during one timestep in case of no vegetation. In the presence of vegetation some particles deposit onto the vegetation before reaching the next lower layer. In the idealized representation of Figure 5.2 this fraction is expressed by the blue Triangle 1. Additionally, the linear increase of deposition with increasing vegetation density is taken into account by multiplication of the area of Triangle 1 with the enhancement factor derived in Chapter 3. Considering only the loss process for layer i the subsequent deposition to the vegetation in layer $i - 1$ is irrelevant. For
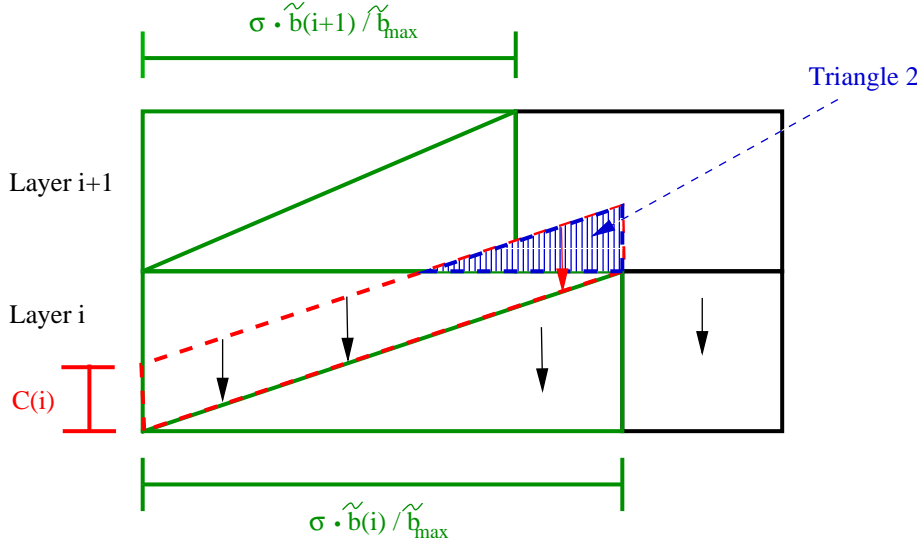
Figure 5.3: Schematic of the deposition flux Υ within the vegetation canopy.

the sedimentation flux $\Xi(i)$ from layer i to layer $i-1$ follows[d]:

$$
\begin{aligned}
\Xi(X, i) &= -\left(1 - \sigma \frac{\tilde{b}(i)}{\tilde{b}_{max}} \frac{\tilde{b}_{max}}{\sigma} \Delta z \frac{C(i - \frac{1}{2})}{2}\right) C(i - \frac{1}{2}) \frac{X(i - \frac{1}{2})}{\Delta t} \\
&= -\left(1 - \tilde{b}(i) \Delta z \frac{C(i - \frac{1}{2})}{2}\right) C(i - \frac{1}{2}) \frac{X(i - \frac{1}{2})}{\Delta t},
\end{aligned} \tag{5.16}
$$

where X stands for the respective sedimented variable.

2.   Figure 5.3 shows a schematic of the deposition flux within one layer, Υ. The fraction of the particles that deposit during one timestep is represented by the area of the red dashed parallelogram with a vertical extent of $C(i)$ over the diagonal. However, this area includes particles that originate from layer $i + 1$ and do not contribute to $\Upsilon(i)$. This process is represented by the red arrow originating in Triangle 2 that quantifies the fraction, that has to be subtracted from the area of the parallelogram. To consider the linear increase of deposition with vegetation density, the retrieved fraction is multiplied with the enhancement factor again. The deposition flux from layer i to the vegetation surfaces in layer i, $\Upsilon(i)$, results to:

$$
\Upsilon(X, i) = -\sigma \frac{\tilde{b}(i)}{\tilde{b}_{max}} \frac{\tilde{b}_{max} \Delta z}{\sigma} \left(1 - \frac{C(i)}{2}\right) C(i) \frac{X(i)}{\Delta t}
$$

---

[d]As the maximum impact of vegetation is limited to the vegetation covering of the respective layer, the complete equation writes: $\Xi(X, i) = -\left[1 - \sigma \frac{\tilde{b}(i)}{\tilde{b}_{max}} \min\left(1, \frac{\tilde{b}_{max}}{\sigma} \Delta z \frac{C(i - \frac{1}{2})}{2}\right)\right] \frac{w_t(i - \frac{1}{2}) X(i - \frac{1}{2})}{\Delta z}$. In the present study, however, both the LAD and the timestep are low enough to use the simplification.
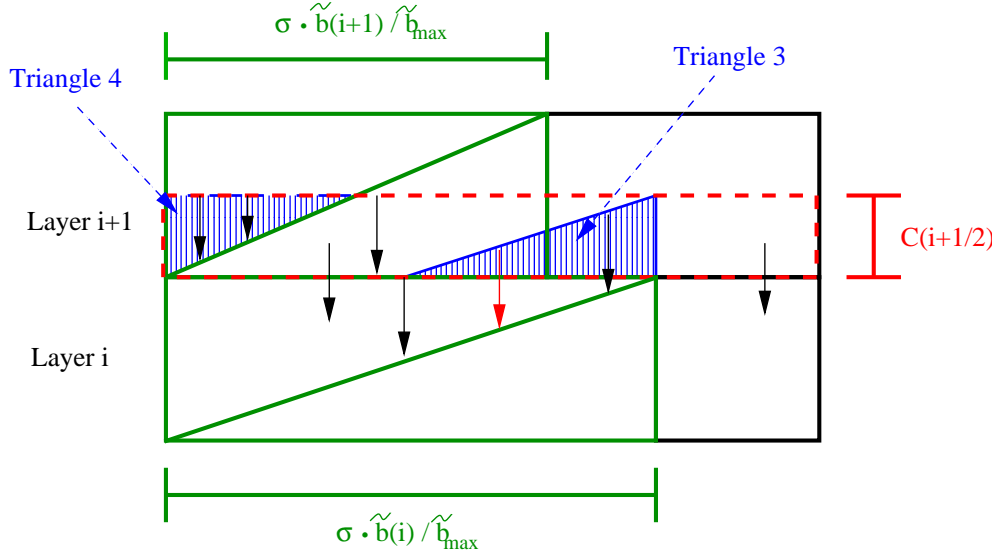
Figure 5.4: Schematic of the sedimentation and deposition flux Ω within the vegetation canopy.

$$= -\tilde{b}(i)\Delta z \left(1 - \frac{C(i)}{2}\right) C(i)\frac{X(i)}{\Delta t}. \tag{5.17}$$

3. In Figure 5.4 the deposition flux from layer $i+1$ to the vegetation surfaces in layer i, $\Omega(i)$, is presented. Analogous to $\Xi(i-1)$, the sedimentation flux from layer i to $i-1$, the fraction of layer $i+1$ that would sediment to layer i in case of no vegetation is represented by the red dashed rectangle. Omitting the impact of the vegetation in layer $i+1$, Triangle 3 represents the fraction of the particles that would deposit onto the vegetation surfaces within layer i. Furthermore, the reduction of the sedimentation flux due to deposition within layer $i+1$, represented by the red arrow, has to be taken into account. Hereby, the percentage of particles that do not enter the next lower layer due to preceding deposition is determined analogously to Ξ, where Triangle 4 in layer $i+1$ marks the area corresponding to Triangle 1 in layer i in Figure 5.2 (see Equation 5.16). The resulting equation is given by[e]:

$$\begin{aligned}
\Omega(X, i) &= -\frac{C(i+\frac{1}{2})}{2}\tilde{b}(i)\Delta z \left(1 - \tilde{b}(i+1)\Delta z\frac{C(i+\frac{1}{2})}{2}\right) C(i+\frac{1}{2})\frac{X(i+\frac{1}{2})}{\Delta t} \\
&= \frac{C(i+1)}{2}\tilde{b}(i)\Delta z \Xi(X, i+1). \tag{5.18}
\end{aligned}$$

---

[e]As the maximum impact of vegetation is limited to the vegetation covering of the respective layer, the complete equation writes: $\Omega(X, i) = -\frac{C(i+\frac{1}{2})}{2}\tilde{b}(i)\Delta z \left[1 - \sigma\frac{\tilde{b}(i+1)}{\tilde{b}_{max}} \min\left(1, \frac{\tilde{b}_{max}}{\sigma}\Delta z\frac{C(i+\frac{1}{2})}{2}\right)\right] C(i+\frac{1}{2})\frac{X(i+\frac{1}{2})}{\Delta t}$. In the present study, however, both the LAD and the timestep are low enough to use the simplification.

In summary, the vertical water deposition flux due to sedimentation Q_{sedi}^{depo} results to:

$$Q_{sedi}^{depo} = \int_0^\infty \int_0^\infty \Upsilon(\overline{m}_w(a,r)) + \Omega(\overline{m}_w(a,r)) \, da \, dr, \qquad (5.19)$$

where $\overline{m}_w$ is the water mass per unit volume.

5.3.2   Impaction

Impaction is the horizontal deposition of particles to vegetation. The formulation used in this work is based on wind tunnel measurements by Shuttleworth (1977) with Q_{impact}^{depo} being the impacted water mass:

$$Q_{impact}^{depo} = \int_0^\infty \int_0^\infty \overline{m}_w(a,r) \, |\mathbf{v}| \, \sigma \sum_{l=1}^{nvtype} b_l' C_l(a,r) \, da \, dr. \qquad (5.20)$$

b_l' is the two-sided area density of the respective vegetation part l, $nvtype$ is the number of different vegetation parts, e. g. twigs, leaves, and C_l is an efficiency function depending on the Stokes number N_{St}:

$$C_l = \frac{1}{\pi} \exp\left(-1.842 + 0.903 \ln N_{St} - 0.11 \left(\ln N_{St}\right)^2 - 0.035 \left(\ln N_{St}\right)^3\right). \qquad (5.21)$$

5.3.3   Dripping

The leaves have a defined storage capacity W_{max}' of water. If more water has condensed or been deposited onto the leaves, the excess water drips from the leaves of one model layer either to the next lower layer or to the ground. The storage capacity of one vegetation layer is given by $W_{max} = \sigma b \Delta z W_{max}'$. In the presented model simulations W_{max}' is set to $0.2 \, \text{kg/m}^2$. The following formulation is based on Flender et al. (2001).

$I_w(i)$ is the excess liquid water that drips off vegetation layer i, if the storage capacity W_{max} is exceeded:

$$I_w(i) = \begin{cases} 0 & \forall \quad 0 \le W(i) \le W_{max} \\ \dfrac{W(i) - W_{max}}{\Delta t} & \forall \quad\quad W(i) > W_{max}. \end{cases} \qquad (5.22)$$

If the LAD of level i is at least as large as the LAD in level $i+1$, then all the dripped-off water is intercepted, otherwise only a fraction is intercepted:

$$I_{leaf}(i) = \begin{cases} I_w(i+1) - I_w(i) & \forall \quad \tilde{b}(i+1) \le \tilde{b}(i) \\ \dfrac{\tilde{b}(i)}{\tilde{b}(i+1)} I_w(i+1) - I_w(i) & \forall \quad \tilde{b}(i+1) > \tilde{b}(i). \end{cases} \qquad (5.23)$$

I_{leaf} is the net liquid water gain or loss due to interception of dripped-off water from the next higher level and drip off the actual layer.

The dripped-off water, that is not intercepted by the canopy, is accumulated at the ground, where it is a source for the moisture balance of the soil. The liquid water flux to the ground, I_{tree}, is given by:

$$I_{tree} = I_w(1) + \sum_{i=1}^{h/\Delta z} \left(1 - \frac{\tilde{b}(i)}{\tilde{b}(i+1)}\right) I_w(i+1) \quad \forall \quad i, \, \tilde{b}(i+1) > \tilde{b}(i). \qquad (5.24)$$

As no interception in non-adjacent layers is implied in the theory, the vertical LAD-profile is limited to a single maximum.

5.3.4 The Soil Sedimentation Flux

The sedimentation flux J_s of both the droplets (see Equation 5.16) and the water dripping to the ground (see Equation 5.24) used in the soil module (see Chapter 4.3) is given by:

$$J_s = \int_0^\infty \int_0^\infty \Xi(\overline{m}_w(a,r), 1) \, da \, dr + I_{tree}. \qquad (5.25)$$

5.4 The Prognostic Equations

Based on the preceding sections the prognostic equations for the particle number size distribution and the leaf surface water are formulated.

5.4.1 The Particle Number Size Distribution

The temporal change of the particle size distribution is described by the following prognostic equation:

$$\begin{aligned}
\frac{\partial f(a,r)}{\partial t} &= \frac{\partial}{\partial z}\left[k_h \rho \frac{\partial}{\partial z}\left(\frac{f(a,r)}{\rho}\right)\right] - \frac{\partial}{\partial r}\left(\dot{r} f(a,r)\right) - \frac{\partial}{\partial a}\left(\dot{a} f(a,r)\right) \\
&\quad - f(a,r)\,|\mathbf{v}|\,\sigma \sum_{l=1}^{nvtype} b_l' C_l(a,r) + \frac{\partial \Xi(f(a,r))}{\partial z} \\
&\quad - \Upsilon(f(a,r)) - \Omega(f(a,r)),
\end{aligned} \qquad (5.26)$$

The first term on the right side describes the vertical turbulent transport. The second and the third terms are the droplet growth due to evaporation/condensation processes and the growth of the dry aerosol radius by chemical processing as derived in Sections 5.1 and 5.2, respectively. The fourth term accounts for the impaction

of droplets to the vegetation surfaces (see Section 5.3.2). Gravitational settling is represented by the last three terms with Ξ, Υ and Ω being defined in Equations 5.16, 5.17, and 5.18.

5.4.2   The Leaf Water

The prognostic equation for the leaf water is given by:

$$\frac{\partial W}{\partial t} = \left(Q^{depo} - \sigma b E^e \right) \Delta z + I_{leaf} \qquad \forall \quad 0 \leq W \leq W_{max}, \qquad (5.27)$$

where Q^{depo} represents the deposition of water due to sedimentation and impaction (see Equation 5.12), the second term accounts for the evaporation of leaf water to the ambient atmosphere and the condensation of water vapor to the leaf surfaces, respectively (see Equation 4.4), and I_{leaf} is the loss respective gain of water due to dripping off the leaves to lower levels or to the ground (see Equation 5.23).

Chapter 6

The Radiation Model

Radiative effects are considered in the droplet growth equation, the calculation of heating rates, the emissions from vegetation, as well as in the chemical processes. In the following section the Practical Improved Flux Method (PIFM 2) (Loughlin et al., 1997, Zdunkowski et al., 1982) to calculate the radiation field is presented. Herein the impact of vegetation based on Flender et al. (2001) and Panhans (1997) is taken into account. In Section 6.2 an approximation to determine the Photosynthetically Active Radiation (PAR) used in the emission module is given. In the last section the parameterization for the determination of photolysis frequencies is presented.

6.1 The Practical Improved Flux Method (PIFM) including Vegetation

In Equation 5.2 the droplet growth equation was presented including the effect of radiative cooling. The relevant radiative quantity is the net radiation flux $F_d(a, r, \tau)$ at the surface of the particle:

$$F_d(a, r, \tau) = \pi r^2 \int_0^\infty Q_{abs}(\lambda, a, r)\Big(F_{act}(\lambda, \tau) - 4\pi B(\lambda)\Big)\, d\lambda, \qquad (6.1)$$

where πB is the Planckian emission of the droplet, Q_{abs} is the efficiency factor for the absorption by a particle of size doublet (a, r), and τ is the optical depth representing the altitude variable.

The actinic flux F_{act} is defined as the diffuse radiance L integrated over the surface of a unit sphere plus the direct radiation S:

$$F_{act}(\lambda, \tau) = \int_0^{2\pi} \int_{-1}^1 L(\lambda, \mu, \phi, \tau)\, d\mu\, d\phi + S(\lambda, \mu_0, \phi_0, \tau). \qquad (6.2)$$

Here ϕ is the azimuth and $\mu = \cos\theta$ with θ the zenith angle of the radiation beam. The index 0 defines the direction of the direct solar beam.

In the δ-two-stream radiative transfer model PIFM2 the wavelength spectrum is divided into 18 wavelength bins i, 6 in the shortwave $(0.2 - 4\,\mu\text{m})$ and 12 in the longwave region $(> 4\,\mu\text{m})$, and $L_i = \int_{(\Delta\lambda)_i} L\,d\lambda$.

Under the two-stream approximation the radiation transfer equation is solved only for the diffuse upward (E_i^+) and downward (E_i^-) irradiance, that are defined by L_i weighted by μ and integrated over the respective hemisphere:

$$E_i^+(\tau) = \int_0^{2\pi} \int_{-1}^0 L_i(\mu,\phi,\tau)\mu\,d\mu\,d\phi \tag{6.3}$$

$$E_i^-(\tau) = \int_0^{2\pi} \int_0^1 L_i(\mu,\phi,\tau)\mu\,d\mu\,d\phi. \tag{6.4}$$

With the actinic flux derived approximately to:

$$F_{act,i}(\tau) = \frac{1}{\overline{\mu}}(E_i^+(\tau) + E_i^-(\tau)) + S_i(\tau), \tag{6.5}$$

where $\overline{\mu}$ is the mean cosine of the diffuse radiation, $F_{d,i}$ is finally determined by:

$$F_{d,i}(a,r,\tau) = \pi r^2 Q_{abs,i}(a,r)\left[\frac{1}{\overline{\mu}}(E_i^+(\tau) + E_i^-(\tau)) + S_i(\tau)\right]$$
$$i = 1,\dots,6 \tag{6.6}$$

$$F_{d,i}(a,r,\tau) = \pi r^2 Q_{abs,i}(a,r)\left[\frac{1}{\overline{\mu}}(E_i^+(\tau) + E_i^-(\tau)) - 4\pi B_i\right]$$
$$i = 7,\dots,18 \tag{6.7}$$

$$F_d(a,r,\tau) = \sum_{i=1}^{18} F_{d,i}(a,r,\tau), \tag{6.8}$$

where Equation 6.6 represents the shortwave and Equation 6.7 the longwave radiation.

With these definitions $E_\downarrow$, used in Equation 4.21 for the soil heat budget, i.e., the net shortwave irradiance plus the downward longwave irradiance, is defined by:

$$E_\downarrow = \sum_{i=1}^{12}(1 - \alpha_i')\left(E_i^-(\tau_0) + \mu_0 S_i(\tau_0)\right) \tag{6.9}$$

with $\tau_0 \equiv \tau(z = 0)$ and the ground albedo $\alpha_i' = 0.2$ in the shortwave and otherwise 0.

Furthermore, the total downward shortwave irradiance $E_\downarrow^{sw}$, used in Equation 4.10 for the determination of the stomatal resistance is given by:

$$E_\downarrow^{sw} = \sum_{i=1}^{6} E_i^- + \mu_0 S_i. \tag{6.10}$$

The total net irradiance used in Equation 4.11 to quantify the radiative heating is determined by:

$$E_n = E^+ - E^- - \mu_0 S. \tag{6.11}$$

In the following the index i is omitted in order to improve the readability. With the δ-approximation the diffuse upward and downward fluxes $E^\pm$ are determined by the following Schuster-Schwarzschild equations:

$$
\begin{aligned}
\frac{dE^+(\tau)}{d\tau} &= \frac{1}{\mu}\left[1 - \omega\left(1 - \beta_0\right)\right] E^+(\tau) - \frac{1}{\mu}\omega\beta_0 E^-(\tau) \\
&\quad -\omega\beta(\mu_0)(1 - f)S(\tau) - \frac{1}{\mu}(1 - \omega)\pi B(\tau)
\end{aligned}
\tag{6.12}
$$

$$
\begin{aligned}
\frac{dE^-(\tau)}{d\tau} &= \frac{1}{\mu}\omega\beta_0 E^+(\tau) - \frac{1}{\mu}\left[1 - \omega\left(1 - \beta_0\right)\right] E^-(\tau) \\
&\quad -\omega\left(1 - \beta(\mu_0)\right)\left(1 - f\right)S(\tau) - \frac{1}{\mu}(1 - \omega)\pi B(\tau).
\end{aligned}
\tag{6.13}
$$

with

$$S(\tau) = S_0 \exp\left(-\int_0^\tau G\frac{1 - \omega f}{\mu_0}\, d\tau'\right). \tag{6.14}$$

Here S_0 is the extraterrestrial solar flux, ω is the single scattering albedo, f is the forward scattering coefficient, β_0 and $\beta(\mu_0)$ are the backscattering coefficients for the diffuse and direct radiation, respectively, and G is a constant factor depending on whether vegetation is present or not. In the following these optical parameters are separately defined for the atmosphere, including Rayleigh scattering by molecules and Mie scattering by aerosol particles and fog droplets (in the following marked by the index atm), as well as for the vegetation (in the following marked by the index v).

The atmospheric backscatter coefficients read:

$$\beta_{0,atm} = \frac{3 - p_1}{8} \tag{6.15}$$

$$\beta_{atm}(\mu_0) = \frac{1}{2} - \frac{\mu_0}{4}\frac{p_1 - 3f_{atm}}{1 - f_{atm}}, \tag{6.16}$$

where the first Legendre-coefficient $p_1 = 3g$ and $f_{atm} = g^2$ with g the asymmetry parameter that depends on the particle size and chemical composition. The scattering and absorption efficiency factors as well as the asymmetry parameters of the particles, $Q_{sca}(a, r)$, $Q_{abs}(a, r)$, and $g(a, r)$, are precalculated using Mie simulations and tabulated for defined (a, r)-doublets, chemical composition, and the respective wavelength interval (Bott, 1992). For each calculation of the radiation field the integral

values are calculated depending on the actual particle number size distribution:

$$\beta_{sca} = \int_0^\infty \int_0^\infty f(a,r) Q_{sca}(a,r) \pi r^2 \, da \, dr \tag{6.17}$$

$$\beta_{abs} = \int_0^\infty \int_0^\infty f(a,r) Q_{abs}(a,r) \pi r^2 \, da \, dr \tag{6.18}$$

$$g = \int_0^\infty \int_0^\infty f(a,r) g(a,r) \pi r^2 \, da \, dr. \tag{6.19}$$

The single scattering albedo ω_{atm} and the optical thickness $\Delta\tau^{atm}$ of the atmospheric layer with the vertical extent Δz are given as follows:

$$\beta_{ext} = \beta_{abs} + \beta_{sca} \tag{6.20}$$

$$\omega_{atm} = \frac{\beta_{sca}}{\beta_{ext}} \tag{6.21}$$

$$\Delta\tau^{atm,ext} = \beta_{ext}\Delta z \tag{6.22}$$

$$\Delta\tau^{atm,sca} = \omega_{atm}\Delta\tau^{atm,ext}. \tag{6.23}$$

The mean cosine of the diffuse radiation in a vegetation free atmosphere $\overline{\mu}_{atm}$ is set to $\frac{1}{2}$ representing an isotropic radiation field. The factor $G_{atm} = 1$ as no vegetation is present. The Planckian radiation B is determined with the air temperature.

Under the assumption of an isotropic leaf angle distribution, $\overline{\mu}_v = 1$, the vegetation coefficients in the shortwave are defined by:

$$\omega_v = r_v + t_v$$

$$\beta_{0,v} = \frac{2r_v + t_v}{3\omega_v}$$

$$\beta_v(\mu_0) = \frac{1+K}{\omega_v K} a_s(\mu_0) \qquad \text{with} \tag{6.24}$$

$$K = \frac{1}{2}\frac{1}{\mu_0}$$

$$a_s(\mu_0) = \frac{\omega_v}{2}\left(1 - \mu_0 \ln \frac{1+\mu_0}{\mu_0}\right),$$

where the reflection and transmittance coefficients for the vegetation, r_v and t_v, respectively, are given in Table 6.1. In the longwave spectrum only absorption but no scattering is regarded, so that $\omega_v, \beta_{0,v}, \beta_v(\mu_0) = 0$.

The optical thickness of vegetation in a layer of the vertical extent Δz is formulated following Kondo and Watanabe (1992):

$$\Delta\tau^{v,ext} = f_c \frac{b_{max}}{\sigma}\Delta z$$
$$\tag{6.25}$$
$$\Delta\tau^{v,sca} = \omega_v \Delta\tau^{v,ext},$$

$\Delta\lambda(\mu m)$	$0.2 - 0.69$	$0.69 - 1.3$	$1.3 - 1.9$	$1.9 - 2.5$	$2.5 - 3.5$	$3.5 - 4.0$
r_v	0.105	0.35	0.18	0.1	0.05	0.05
t_v	0.07	0.42	0.4	0.22	0.11	0.11

Table 6.1: Reflectance and transmittance coefficients of vegetation in the short wavelength bins (Panhans, 1997).

where f_c is an efficiency factor that is 1 in the shortwave and $\frac{1}{2}$ in the longwave region, and $\frac{b_{max}}{\sigma}$ is the LAD of the vegetated fraction in each layer of the canopy. The δ-approximation is not applied in the case of vegetation, so $f_{veg} = 0$. $G_{veg} = \frac{1}{2}$. The Planckian radiation B is determined for the leaf surface temperature.

Having defined the necessary parameters for the atmosphere as well as for the vegetation, the complete set of combined coefficients can be derived. The combined values for the canopy are composed of the parameters for the vegetation elements and the interstitial air, weighted by their respective optical thickness:

$$\Delta\tau^{ext} = \Delta\tau^{atm,ext} + \Delta\tau^{v,ext} \tag{6.26}$$

$$\omega = \frac{\Delta\tau^{atm,sca} + \Delta\tau^{v,sca}}{\Delta\tau^{ext}} \tag{6.27}$$

$$X = \frac{\Delta\tau^{atm,sca} X_{atm} + \Delta\tau^{v,sca} X_v}{\Delta\tau^{atm,sca} + \Delta\tau^{v,sca}} \tag{6.28}$$

with $X = \beta_0, \beta(\mu_0), f, \overline{\mu}, G$.

The radiation fluxes above the canopy are determined with the atmospheric coefficients. Inside the canopy, the shortwave radiation fluxes are given by the atmospheric fluxes weighted by the fraction that is free of vegetation and the combined fluxes, weighted by the vegetation covering inside the respective model layer. The longwave radiation fluxes inside the canopy are calculated using the vegetation coefficients. The total fluxes as well as the boundary fluxes between the canopy and the atmosphere above are determined according to continuity equations, that are described in detail by Panhans (1997).

6.2 Photosynthetically Active Radiation (PAR)

For the calculation of gaseous emissions from plants (see Section 7.4), the photosynthetically active radiation (PAR) has to be determined. PAR is the total downward

irradiance integrated over a wavelength range between 400 and 700 nm. The wavelength bins of PIFM are too wide to extract the PAR region. Therefore PAR is approximated by integrating over the whole solar spectrum weighted by a factor $C_1 = 0.45$ (Baker, 2001) to perform the reduction to the limited wavelength intervall:

$$\text{PAR} = C_1 C_2 E_\downarrow^{sw}. \tag{6.29}$$

As the unit of $E_\downarrow^{sw}$ is W m^{-2} but that of PAR is μmol m^{-2} s^{-1}, unit conversion is wavelength dependent. As no spectral calculation is available, the conversion factor C_2 is approximated to 4.24 μmol s^{-1} W^{-1} for clear and 4.57 μmol s^{-1} W^{-1} for cloudy conditions, respectively (Ganzeveld, 2002, priv. comm.). Conditions are defined cloudy in all layers beneath the top of the fog.

6.3 Photolysis Frequencies

Photodissociation of atmospheric molecules is an important process in atmospheric chemistry leading to the formation of radicals. Considering the photodissociation of a molecule AB into A and B:

$$\text{AB} + \text{h}\nu \overset{J_{AB \to A+B}}{\longrightarrow} \text{A} + \text{B}, \tag{R 6.1}$$

where h is the Planck constant and ν the frequency of the incoming radiation, $J_{AB \to A+B}$ is the photolysis frequency of Reaction R 6.1. The change in the concentration of the species is proportional to the photolysis frequency and the concentration of the photodissociating molecule [AB]:

$$\frac{d\,[A]}{dt} = \frac{d\,[B]}{dt} = -\frac{d\,[AB]}{dt} = J_{AB \to A+B} \cdot [AB]. \tag{6.30}$$

The photolysis frequency $J_{AB \to A+B}$ is determined by:

$$J_{AB \to A+B} = \int_0^\infty \sigma_{AB}(T,\lambda)\phi_{A+B}(T,\lambda)F_{act}(\lambda,\tau)\,d\lambda. \tag{6.31}$$

σ_{AB} is the absorption coefficient of the molecule AB, ϕ_{A+B} is the quantum yield of the photodissociation of AB into the path A + B, and F_{act} is the actinic flux as defined in Equation 6.2. If Reaction R 6.1 takes place in the aqueous phase, the actinic flux inside the water sphere has to be taken into account. For a typical droplet spectrum of a stratus cloud Früh (2000) derived an enhancement factor of 2.33 for the actinic flux inside the aqueous phase droplet compared to the actinic flux in the gas phase. This value is used for the calculation of photolysis frequencies in the fog droplets as well as in the leaf surface water.

The method of Landgraf and Crutzen (1998) is applied for the calculation of the photolysis frequencies. This parameterization allows the calculation of the integral in Equation 6.31 from seven wavelengths, that are representative for the solar spectrum. While the actinic flux is calculated online, mean parameterized values of σ and ϕ are provided in look-up tables. Temperature dependence is considered by a scaling factor. This method highly reduces the needed computer time and has been proved to be of good accuracy.

Chapter 7

The Chemical Composition

The concentrations of the gaseous and aqueous phase species are influenced by physical as well as chemical processes. These include turbulent transport ($trans$), sedimentation and deposition ($sedi/depo$), emission of gaseous species from the soil and the vegetation ($emis$), transfer between different size classes due to both condensation and evaporation processes (c/e), and chemical processes that include gas-droplet transfer and homogeneous chemical reactions ($chem$). In order to reduce the required computer capacity, the aqueous phase chemical reactions in the droplets are calculated in three different size ranges, only, comprising the 2000 particle size classes. Droplets in one size class of the chemistry module have identical chemical compositions. The change in concentration $c_{j,k}$ of species j in particle class k is described by:

$$
\frac{\partial c_{j,k}}{\partial t} = \left(\frac{\partial c_{j,k}}{\partial t}\right)_{trans} + \left(\frac{\partial c_{j,k}}{\partial t}\right)_{sedi/depo} + \left(\frac{\partial c_{j,k}}{\partial t}\right)_{emis}
$$
$$
+ \left(\frac{\partial c_{j,k}}{\partial t}\right)_{c/e} + \left(\frac{\partial c_{j,k}}{\partial t}\right)_{chem},
\tag{7.1}
$$

where $k = 0$ denotes the gas phase, $k = 1, \ldots, 3$ the aqueous phase in the three size classes, and $k = 4$ the leaf surface water. The single processes are described in the following sections.

7.1 Turbulent Transport

Turbulent transport of the volume mixing ratios is performed for both gaseous and the aqueous phase species that are incorporated in the fog droplets:

$$
\left(\frac{\partial c_{j,k}}{\partial t}\right)_{trans} = \frac{\partial}{\partial z}\left[k_h \rho \frac{\partial}{\partial z}\left(\frac{c_{j,k}}{\rho}\right)\right] \qquad \forall \quad k = 0, \ldots, 3.
\tag{7.2}
$$
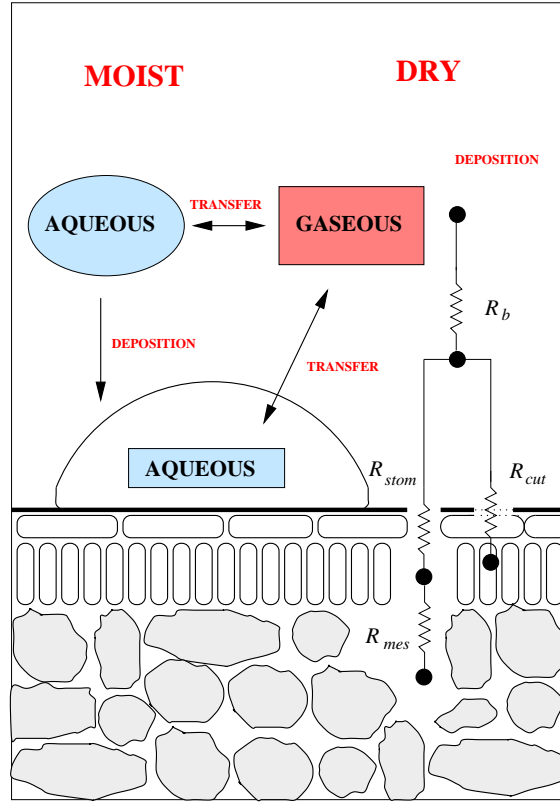
Figure 7.1: Schematic of the dry and moist deposition to a leaf surface.

7.2 Sedimentation and Deposition

Sedimentation and deposition processes comprise the dry deposition (dd) of gaseous species, the sedimentation and moist deposition (md) of aqueous phase species incorporated in depositing fog droplets, and the dripping ($drip$) of leaf surface water, and therefore aqueous phase species, from upper to lower levels:

$$\left(\frac{\partial c_{j,0,\dots,4}}{\partial t}\right)_{sedi/depo} = \left(\frac{\partial c_{j,0}}{\partial t}\right)_{dd} + \left(\frac{\partial c_{j,1,\dots,4}}{\partial t}\right)_{md} + \left(\frac{\partial c_{j,4}}{\partial t}\right)_{drip}. \tag{7.3}$$

Figure 7.1 gives an overview of the dry and moist deposition processes to a leaf surface. The single processes are discussed in detail in the following sections.

7.2.1 The Dry Deposition Model

The dry deposition module is based on the multi-layer scheme of Ganzeveld and Lelieveld (1995). Dry deposition of gaseous species is described by the deposition flux J_d that is the product of the deposition velocity v_d and the concentration of the

respective species per model layer:

$$\left(\frac{\partial c_{j,0}}{\partial t}\right)_{dd} = \frac{J_d}{\Delta z} = -\frac{v_d c_{j,0}}{\Delta z}. \tag{7.4}$$

The deposition velocity is defined as the reciprocal of the total resistance R excerted to the depositing species:

$$v_d = \frac{1}{R} = \frac{1}{R_b + R_{surf}}. \tag{7.5}$$

The total resistance comprises the quasi-laminar leaf boundary layer resistance R_b and the surface resistance R_{surf}. The transport through the turbulent layers is simulated explicitly according to Equation 7.2 and is therefore not considered here. R_b considers the effect of diffusion through the thin laminar layer adjacent to vegetation surfaces (Meyers, 1987):

$$R_b = \alpha \, \delta R_b \sqrt{\frac{l}{|\boldsymbol{v}|}}. \tag{7.6}$$

Here $\alpha = 180$ is an empirical value, $l = 0.07$ corresponds to the mean length of the leaf in the mean wind direction, and δR_b is a correction term for the diffusivity of the respective species compared to water vapor. Values are applied according to Ganzeveld (1999, priv. comm.). The surface resistance inside the canopy is given by the canopy resistance R_c, and in the lowest atmospheric layer, additionally by the parallel ground resistance R_g:

$$R_{surf} = \begin{cases} R_c & \forall \quad z > z(1) \\ \left(\frac{1}{R_c} + \frac{1}{R_g}\right)^{-1} & \forall \quad z = z(1). \end{cases} \tag{7.7}$$

The canopy resistance R_c comprises the resistances the leaves exert against the depositing gas phase species. Dry deposition to a leaf can occur via two pathways. First, the gaseous species deposit to the leaf cuticle, or second, they are taken up through the leaf stomata into the mesophyll, i.e., the intercellular fluid of the apoplast. The canopy resistance is, consequently, composed of the resistance of the cuticle R_{cut}, that is parallel to both the stomatal R_{stom} and mesophyllic R_{mes} resistances, that are in series (see Figure 7.1), both weighted by the leaf area available for dry deposition[a]:

$$R_c = \left(\frac{(1-\epsilon)b'\Delta z}{R_{cut}} + \frac{(1-\epsilon)b\Delta z}{R_{stom}\delta R_{stom} + R_{mes}}\right)^{-1} \tag{7.8}$$

---

[a]If dry deposition to wet surfaces is also simulated with the resistance approach, then $R_c = \left(\frac{(1-\epsilon)b'\Delta z}{R_{cut}} + \frac{(1-\epsilon)b\Delta z}{R_{stom}\delta R_{stom} + R_{mes}} + \frac{\epsilon b\Delta z}{R_{ws}}\right)^{-1}$ with R_{ws} being the resistance of the water film on the leaves.

R_{cut} represents the resistance of the leaf cuticle to deposition of molecules. The dry deposition to the leaf cuticle occurs on both sides of the leaf. Therefore R_{cut} is divided by the dry fraction of the two-sided LAI, $b'\Delta z$. R_{stom} is calculated following Equation 4.10 and corrected for the respective diffusivity compared to water vapor δR_{stom}. R_{mes} represents the resistance caused by the internal leaf concentration of the respective trace gas in the apoplast. For a trace gas, that does not accumulate in the leaf interior, $R_{mes} = 0$. The resistance of this second deposition pathway is divided by the dry fraction of the one-sided LAI, $b\Delta z$, because the leaf stomata of most deciduous trees are located only on the lower leaf side. Dry deposition is only accounted for to dry surfaces. Dry deposition processes to wet surfaces are included in the interfacial mass transfer to the leaf surface water (see Section 7.5.1) and are therefore omitted here. The complete data for the dry deposition resistances are given in Appendix A.

7.2.2   The Sedimentation and Moist Deposition of Aqueous Phase Species

With the sedimentation and both vertical deposition and impaction of aerosol particles and fog droplets aqueous phase species are sedimented to lower height levels or deposited to vegetation surfaces. This leads to a gain or loss in the aqueous phase concentration within the droplets equivalent to Equation 5.26:

$$
\begin{aligned}
\left(\frac{\partial c_{j,k}}{\partial t}\right)_{md} = {} & -\frac{c_{j,k}}{\int_0^{r_k}\int_{r_{k-1}}^{r_k}\overline{m}_w(a,r)\,dr\,da}\int_0^{r_k}\int_{r_{k-1}}^{r_k}\overline{m}_w(a,r)\,|\mathbf{v}|\,\sigma \\
& \cdot \sum_{l=1}^{nvtype} b_l' C_l(a,r)\,dr\,da + \frac{\partial \Xi(c_{j,k})}{\partial z} - \Upsilon(c_{j,k}) - \Omega(c_{j,k}) \\
& \forall k = 1, 2, 3
\end{aligned}
\tag{7.9}
$$

and a gain in the concentration of aqueous phase species in the leaf surface water:

$$
\begin{aligned}
\left(\frac{\partial c_{j,4}}{\partial t}\right)_{md} = {} & \sum_{k=1}^{3} \Upsilon(c_{j,k}) + \Omega(c_{j,k}) + \frac{c_{j,k}}{\int_0^{r_k}\int_{r_{k-1}}^{r_k}\overline{m}_w(a,r)\,dr\,da} \\
& \cdot \int_0^{r_k}\int_{r_{k-1}}^{r_k}\overline{m}_w(a,r)\,|\mathbf{v}|\,\sigma \sum_{l=1}^{nvtype} b_l' C_l(a,r)\,dr\,da.
\end{aligned}
\tag{7.10}
$$

CONDENSATIONAL GROWTH
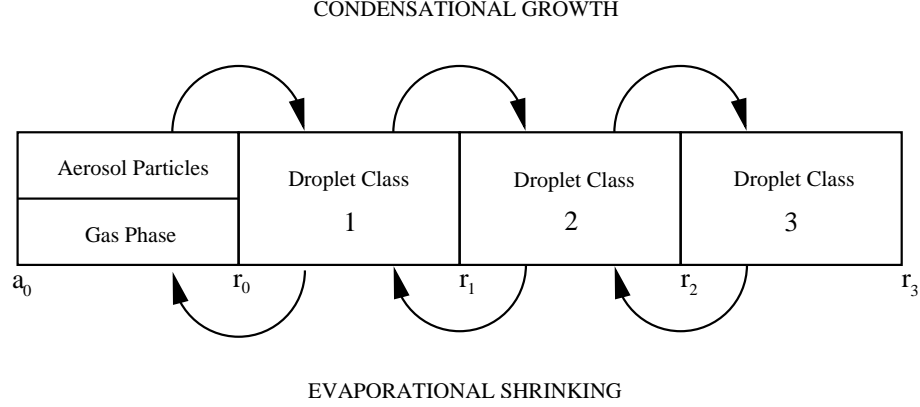
Figure 7.2: Schematic of the particle exchange between the three droplet size classes, gas phase, and dry particle class due to condensational growth and evaporational shrinking.

where Ξ, Υ, and Ω are the respective values from Equations 5.16, 5.17, and 5.18[b].

7.2.3 The Vertical Exchange of Aqueous Phase Species due to Dripping

Drip-off to lower vegetation levels leads to a vertical redistribution of the leaf water species in the vegetation layers. The change in aqueous phase concentration of species in the water films is comprised in the following term:

$$\left(\frac{\partial c_{j,4}}{\partial t}\right)_{drip}(i) = \begin{cases} \dfrac{I_w(i+1)c_{j,4}(i+1)}{W(i+1)} & \forall \quad \tilde{b}(i+1) \leq \tilde{b}(i). \\ \quad -\dfrac{I_w(i)c_{j,4}(i)}{W(i)} \\ \dfrac{\tilde{b}(i)}{\tilde{b}(i+1)}\dfrac{I_w(i+1)c_{j,4}(i+1)}{W(i+1)} & \forall \quad \tilde{b}(i+1) > \tilde{b}(i). \\ \quad -\dfrac{I_w(i)c_{j,4}(i)}{W(i)} \end{cases} \tag{7.11}$$

7.3 Condensation and Evaporation

Due to condensational growth and evaporational shrinking, particles interchange between the three droplet size classes. Therewith, the concentration of aqueous

---

[b]The argument $(c_{j,k})$ is used as abbreviation for $X = \dfrac{f(a,r)}{\int\limits_0^{r_k}\int\limits_{r_{k-1}}^{r_k} f(a,r)\,da\,dr} c_{j,k}$

phase chemical species in the droplet classes are modified. Moreover aqueous phase species are released into the gas phase, when droplets of class 1 evaporate. On the other hand, the initial chemical composition of the dry aerosol particle $c_j(a)$ is taken as input to class 1, when aerosol particles grow to a radius larger than r_0. In CHEMIFOG_V only net transport is regarded. Figure 7.2 shows a schematic of the particle exchange. r_i is the maximum radius of size class i. The change in chemical concentration in the respective size class is given in the following equations, where $\dot{r}$ is given by the droplet growth equation (Equation 5.2):

$$\left(\frac{\partial c_{j,0}}{\partial t}\right)_{c/e} = -\min\left(0, \int_0^{r_0}\int_0^{r_0} \frac{\partial}{\partial r}\left(\dot{r}f(a,r)\right) dr\,da\right) \frac{c_{j,1}}{\int_0^{r_1}\int_{r_0}^{r_1} f(a,r)\,dr\,da} \tag{7.12}$$

$$\left(\frac{\partial c_{j,1}}{\partial t}\right)_{c/e} = -\min\left(0, \int_0^{r_0}\int_0^{r_0} \frac{\partial}{\partial r}\left(\dot{r}f(a,r)\right) c_j(a)\,dr\,da\right) - \left(\frac{\partial c_{j,0}}{\partial t}\right)_{c/e}$$
$$-\max\left(0, \int_0^{r_1}\int_0^{r_1} \frac{\partial}{\partial r}\left(\dot{r}f(a,r)\right) dr\,da\right) \frac{c_{j,1}}{\int_0^{r_1}\int_{r_0}^{r_1} f(a,r)\,dr\,da}$$
$$+\min\left(0, \int_0^{r_1}\int_0^{r_1} \frac{\partial}{\partial r}\left(\dot{r}f(a,r)\right) dr\,da\right) \frac{c_{j,2}}{\int_0^{r_2}\int_{r_1}^{r_2} f(a,r)\,dr\,da} \tag{7.13}$$

$$\left(\frac{\partial c_{j,2}}{\partial t}\right)_{c/e} = +\max\left(0, \int_0^{r_1}\int_0^{r_1} \frac{\partial}{\partial r}\left(\dot{r}f(a,r)\right) dr\,da\right) \frac{c_{j,1}}{\int_0^{r_1}\int_{r_0}^{r_1} f(a,r)\,dr\,da}$$
$$-\min\left(0, \int_0^{r_1}\int_0^{r_1} \frac{\partial}{\partial r}\left(\dot{r}f(a,r)\right) dr\,da\right) \frac{c_{j,2}}{\int_0^{r_2}\int_{r_1}^{r_2} f(a,r)\,dr\,da}$$
$$-\left(\frac{\partial c_{j,3}}{\partial t}\right)_{c/e} \tag{7.14}$$

$$\left(\frac{\partial c_{j,3}}{\partial t}\right)_{c/e} = -\min\left(0, \int_0^{r_3}\int_{r_2}^{r_3} \frac{\partial}{\partial r}\left(\dot{r}f(a,r)\right) dr\,da\right) \frac{c_{j,2}}{\int_0^{r_2}\int_{r_1}^{r_2} f(a,r)\,dr\,da}$$
$$-\max\left(0, \int_0^{r_3}\int_{r_2}^{r_3} \frac{\partial}{\partial r}\left(\dot{r}f(a,r)\right) dr\,da\right) \frac{c_{j,3}}{\int_0^{r_3}\int_{r_2}^{r_3} f(a,r)\,dr\,da}. \tag{7.15}$$

7.4 The Gaseous Emission Model

The change in chemical species concentration according to emissions from the vegetation and the soil is given by:

$$\left(\frac{\partial c_{j,0}}{\partial t}\right)_{emis} = \frac{E_j}{\Delta z} \tag{7.16}$$

with E_j being the emission rate of species j. In the following the parametrization of E_j for plant and soil emissions are presented.

7.4.1 Isoprene Emissions from the Vegetation Canopy

Plants emit a number of volatile organic compounds (VOCs), which play an important role in atmospheric chemistry. One of the dominant emitted VOCs is isoprene, C_5H_8, which is primarily emitted by deciduous trees. The strength of the isoprene source generally depends on the type and density of vegetation. Additionally the influence of temperature and radiation has to be taken into account. For the use in CHEMIFOG_V parameters were selected to represent a typical deciduous forest. To determine the foliar density of a deciduous forest the one-sided LAI = 5 and the specific leaf weight $S_{LW} = 80 \, \frac{\text{g-leaf-biomass}}{\text{m}^2}$ of a summergreen forest are taken from Box (1981). With these values the foliar density is derived to $\rho_v = \text{LAI} \cdot S_{LW} = 400 \, \frac{\text{g-leaf-biomass}}{\text{m}^2}$.

For the determination of the isoprene emissions, the relative contribution of isoprene emitting plant species to the total foliar density are taken from Lamb et al. (1993) for the mixed forest type 'Other Deciduous'. Non-isoprene emitting deciduous and coniferous tree species are also part of this forest type, but do not contribute to the isoprene emission flux. Table 7.1 gives the resulting mean foliar densities for high- and low-isoprene emitting species as well as the respective isoprene emission factors (Lamb et al., 1987).

Standard emission rates $E_{C_5H_8,i,s}$ of isoprene in layer i are calculated as the product of the standard forest emission factors $\alpha_{l,s}$ given for the respective species l and the foliar densities $\rho_{l,v}$ weighted by the respective LAI:

$$E_{C_5H_8,i,s} = \sum_{l=1}^{2} \alpha_{l,s} \rho_{l,v} \frac{b(i)}{\sum_i b(i)}. \tag{7.17}$$

The emission rate of isoprene $E_{C_5H_8}$ depends on the incoming photosynthetically active radiation (PAR) (see Equation 6.29) and on the leaf temperature. Empirical

		Total	High Isoprene		Low Isoprene	
LAI	S_{LW}	ρ_v	$\rho_{1,v}$	$\alpha_{1,s}$	$\rho_{2,v}$	$\alpha_{2,s}$
5	80	400	51	13.6	158	5.95

Table 7.1: Foliar densities $\rho_{l,v}$ [g-foliar-dry-mass m^{-2}] (after Lamb et al. (1993) and Box (1981)) and forest emission factors for isoprene $\alpha_{l,s}$ [μg-C(g-foliar-dry-mass)$^{-1}$ h^{-1}] for standard conditions (PAR = 800 μmol m^{-2} s^{-1}; T_s=303 K) for the different emission types (Lamb et al., 1987).

formulas are given by Geron et al. (1994) and Günther et al. (1995):

$$E_{C_5H_8} = E_{C_5H_8,s}C_LC_T, \tag{7.18}$$

where C_L and C_T are empirical correction factors for radiation and temperature:

$$C_L = \frac{\alpha C_{L1}\text{PAR}}{\sqrt{\left(1 + \alpha^2\text{PAR}^2\right)}} \tag{7.19}$$

$$C_T = \frac{\exp\left[\frac{C_{T1}(T_f - T_s)}{RT_sT_f}\right]}{1 + \exp\left[\frac{C_{T2}(T_f - T_M)}{RT_sT_f}\right]}. \tag{7.20}$$

Here $\alpha = 0.0027$, $C_{L1} = 1.066$, $T_M = 314$ K, $C_{T1} = 9.5 \cdot 10^4$ J mol^{-1}, and $C_{T2} = 2.3 \cdot 10^5$ J mol^{-1}.

7.4.2 NO Emissions from the Soil

Nitrogen emissions from the soil are mainly controlled by bacterial activity in the soils and dominated by the emission of NO. Yienger and Levy II (1995) propose a scheme for the use in global and regional climate models for different biomes. In CHEMIFOG_V mean values for a deciduous forest are taken. As only temperate forests are regarded, soil moisture condition is always wet and pulsing due to large increases in soil wetness has not to be considered. Fertilization has not to be taken into account for natural forests. As chemical transformation to NO_2 and subsequent deposition are calculated explicitly, no canopy reduction factor has to be considered. Therefore only the temperature dependence is applied:

$$E_{\text{NO},1} = \begin{cases} 0.28A_wT_g & \forall \quad 0°\text{C} \leq T_g \leq 10°\text{C} \\ A_we^{0.103T_g} & \forall \quad 10°\text{C} < T_g \leq 30°\text{C} \\ 21.97A_w & \forall \quad 30°\text{C} < T_g. \end{cases} \tag{7.21}$$

Here A_w is a biome-dependent coefficient for wet soils. According to the mean value given in Yienger and Levy II (1995) $A_w = 0.03 \left[\frac{\text{ng N}}{\text{m}^2 \text{s}} \right]$. As this parametrization yields net emissions, dry deposition of NO to the soil is omitted. Soil emissions of NO are introduced in the lowest model layer.

7.5 The Chemistry Model

The change in the gas and aqueous phase chemical species concentration due to chemical processes can be separated into the interfacial mass transfer of molecules between the gas phase and the aqueous phase (mt) and the reactions taking place in the respective media ($reac$):

$$\left(\frac{\partial c_{j,k}}{\partial t} \right)_{chem} = \left(\frac{\partial c_{j,k}}{\partial t} \right)_{mt} + \left(\frac{\partial c_{j,k}}{\partial t} \right)_{reac}. \tag{7.22}$$

After the description of the mass transfer in the next subsection the chemical mechanism is presented in the following subsections.

7.5.1 Gaseous-Aqueous Exchange

The interfacial mass transfer between the gaseous and aqueous phase is described by the following equation:

$$\sum_{k=1}^{4} \left(\frac{\partial c_{j,k}}{\partial t} \right)_{mt} = -\left(\frac{\partial c_{j,0}}{\partial t} \right)_{mt} = \sum_{k=1}^{4} k_{mt,k} \left(m_{j,k}\, c_{j,0} - \frac{c_{j,k}}{k_H^{cc}} \right), \tag{7.23}$$

where k_H^{cc} is the Henry's law coefficient. Gaseous-aqueous exchange is performed simultaneously between the gas phase and both all three droplet classes and the leaf surface water. The mass transfer coefficient between the gas phase and the aqueous phase of class k , $k_{mt,k}$, is defined as proposed by Schwartz (1986):

$$k_{mt,k} = \left(\frac{\bar{r}_k^2}{3 D_g} + \frac{4 \bar{r}_k}{3 \bar{\nu} \alpha} \right)^{-1} \tag{7.24}$$

$$\bar{\nu} = \sqrt{\frac{8 R T}{M_j \pi}}. \tag{7.25}$$

D_g is the gas-phase diffusivity, $\bar{\nu}$ is the mean molecular velocity, M_j is the molar mass, α is the accomodation coefficient, and $\bar{r}_k$ is the mass weighted mean radius of the respective particle class. Note that k_{mt} includes a unit conversion between the atmospheric and the water volume. The values for D_g and α can be found in Table A.2 in Appendix A.

For the mass transfer between the gas phase and the leaf surface water, the leaf surface water is assumed to be present as droplets on the waxy leaf surfaces. Therefore, the leaf surface water is assumed to consist of half spheres with the radius $r_{1/2}$. The radius is calculated depending on the actual water mass on the leaves (see Equation 5.27) and the fraction of the leaves that is covered (see Equation 4.8):

$$r_{1/2} = \frac{3V}{2A} = \frac{3}{2}\frac{W}{\epsilon b' \Delta z \sigma \rho_w} \tag{7.26}$$

with V being the volume of the half sphere and A the area of the cross-section. In case of maximum covering, i.e., $W = W_{max}$, $r_{1/2} = 150\,\mu$m.

7.5.2   The Gas Phase Mechanism

The gas-phase mechanism describes the chemical composition of the troposphere, including the chemical reactions of isoprene, that is emitted by plants and therefore abundant in a forest environment. Besides the chemistry of nitrogen oxides, NO_x, and sulphuric oxides, SO_x, the oxidation of carbon monoxide, CO, methane, CH_4, ethane, C_2H_6, as well as ammonia, NH_3, are described. Special attention is paid to the oxidation of isoprene, C_5H_8. The reaction mechanism of isoprene is highly complex and rather fairly known. Therefore the condensed Mainz Isoprene Mechanism (MIM, Pöschl et al., 2000) is included. The mechanism has been tested against detailed schemes with good results. The complete set of included species and reactions is listet in Table B.2 in Appendix B.

7.5.3   The Aqueous Phase Mechanism

The aqueous-phase mechanism is based on CAPRAM2.3 (Chemical Aqueous Phase RAdical Mechanism version 2.3, Herrmann et al., 2000) that is designed to model tropospheric multiphase chemistry. The key characteristics of CAPRAM2.3 are "(1) a detailed treatment of the oxidation of organic compounds with one and two carbon atoms, (2) an explicit description of S(IV)-oxidation by radicals and iron(III), as well as by peroxides and ozone, (3) the reactions of OH, NO_3, Cl_2^-, Br_2^-, and CO_3^- radicals, as well as reactions of the transition metal ions (TMI) iron, manganese and copper" (Herrmann et al., 2000). CAPRAM2.3 is therefore well suited for studies on multiphase and acid deposition processes in a forest environment. The mechanism includes 70 aqueous-phase species involved in 199 aqueous-phase reactions, 34 equilibria, and six photolysis reactions. Photolysis frequencies are calculated as explained in Section 6.3. The set of aqueous phase reactions is given in Table C.2 in Appendix C.

7.5.4 The Activity Coefficients

In general, the chemical reaction rates in the aqueous phase depend on both the rate constant and on the activities of the educts. The activity of a species A is defined as the product of the molality of A, M_A, and the respective activity coefficient γ_A:

$$[A] = \gamma_A M_A. \tag{7.27}$$

In ideal solutions $\gamma_A = 1$, so that the activity equals the molality. In weak solutions this assumption is also a reasonable approximation. In strong electrolytes, however, interactions between ions are not negligible and the activities significantly differ from unity. Under the meteorological conditions of radiation fog events small particles have a relatively long lifetime allowing an effective uptake of gases leading to highly concentrated solutions. Furthermore, in the leaf surface water deposited trace species effectively accumulate. Consequently, the activity coefficients are not negligible.

Species	Reference Species	Reference
HSO_3^-	HSO_4^-	Liang and Jacobsen (1999)
SO_3^{2-}	SO_4^{2-}	Liang and Jacobsen (1999)
SO_4^-	HSO_4^-	Liang and Jacobsen (1999)
HCO_3^-	HSO_3^-	Chameides and Stelson (1992)
O_2^-	HSO_3^-	Chameides and Stelson (1992)
NO_2^-	NO_3^-	Liang and Jacobsen (1999)
Cl_2^-	HSO_3^-	Chameides and Stelson (1992)
$HCOO^-$	HSO_3^-	assumed
Br^-	Cl^-	assumed
Br_2^-	HSO_3^-	Chameides and Stelson (1992)

Table 7.2: Ions, for which activity coefficients are calculated. Activity coefficients for the reference species are calculated explicitly; activity coefficients for the species in the first column are equated to the ones of the respective reference species.

For the calculation of the activity coefficients the molality-based module from Luo et al. (1995) based on Pitzer (1991) and Clegg and Brimblecombe (1995) was

used. This method is semi-empirical based on statistical thermodynamics with the
results fitted to measurements.

The logarithm of the activity coefficient is given by the derivation of the excess
Gibbs energy G^{ex} per kg of solvent:

$$\ln \gamma_j = \left[\frac{\partial}{\partial M_j} \left(\frac{G^{ex}}{\overline{m}_w RT} \right) \right]_{n_w} , \tag{7.28}$$

where w_w is the mass of solvent and n_w is the number of moles of solvent. G^{ex} is
determined by "a Debye-Hückel term (in the square root of ionic strength) describing
the long-range interactions that dominate in dilute solutions, together with a virial
expansion in species molality for short range binary (in m^2) and triplet (in m^3)
interactions." (Luo et al., 1995). Under atmospheric conditions a limitation to
interactions between maximum three ions is sufficient, whereby terms involving three
ions of the same sign are omitted.

In CHEMIFOG_V activity coefficients for the ions H^+, NH_4^+, Na^+, HSO_4^-, SO_4^{2-},
NO_3^-, and Cl^- are calculated explicitly. In addition, Table 7.2 gives the species,
the activity coefficients of which are equated to the ones calculated explicitly (von
Glasow, 2001, priv. comm.). For a more comprehensive description the reader is
referred to Pitzer (1991).

Chapter 8

Numerical Aspects

In this chapter numerical and computational aspects of CHEMIFOG_V are presented. Section 8.1 gives an overview over the spatial atmospheric and soil grid as well as the particle size grid. The timesteps applied for the different modules are given in Section 8.2. Section 8.3 gives information on the numerical methods, especially on the pre-processor used in the chemistry module.

8.1 Numerical Grids

CHEMIFOG_V is a one-dimensional model with the vertical atmospheric grid being divided into three regimes as shown in Figure 8.1. Between the Earth's surface and 200 m the vertical grid spacing is 2 m. This part includes the vegetation layers and marks the region, to which the calculation of microphysics is limited. Above 200 m the grid spacing is logarithmically equidistant up to 50 km, that marks the upper boundary of the model. 2200 m marks the upper limit of the dynamics simulations. Radiative transfer is considered over the whole vertical extent. The soil grid consists of 24 logarithmic equidistant layers extending to a depth of 1.5 m.

At the upper boundary of the dynamic model (2200 m), the temperature and moisture gradient as well as the wind velocity are held fixed. At the lower boundary of the soil model all prognostic variables are assumed to be stationary. At the atmosphere-soil boundary wind velocity is zero according to the no-slip criterion. $T|_{surf}$ and $q|_{surf}$ result from the balance equations, where the Earth's surface is assumed as an infinitesimal layer without storage capacity.

The aerosol particles and fog droplets are described on a two-dimensional size

- z = 50000m

                                  Radiation

    logarithmically equidistant   ─────────────────────   z = 2200m

                          + Dynamics

    ───   z = 200m

    equidistant: dz=2m   + Microphysics   · · · · · · · · · · · ·   z = h
                                          Vegetation   z = 0
    ━━━

    logarithmically equidistant (24 layers)   Soil

- z = -1.5m
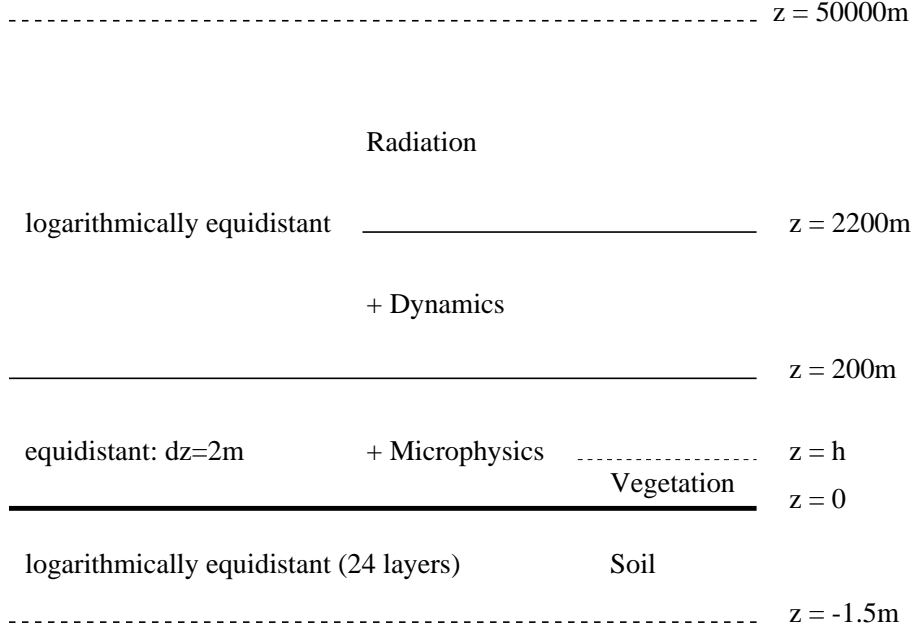
Figure 8.1: Schematic of the vertical atmospheric and soil grid.

grid depending on the dry particle radius a and the total particle radius r with:

$$
\begin{aligned}
0.025\,\mu m \ &\leq a \leq \ 2\,\mu m \\
a \ &\leq r \leq \ 50\,\mu m.
\end{aligned}
\tag{8.1}
$$

The particles are distributed into logarithmically equidistant mass bins, 40 bins for the dry aerosol mass and 50 bins for the total particle mass with $\rho_a = 2\,\mathrm{kg\,dm^{-3}}$.

Chemistry is calculated in three particle size classes:

$$
\begin{aligned}
1: \quad 0.5\,\mu m \ &< \ r \ \leq \ 2\,\mu m \\
2: \quad 2\,\mu m \ &< \ r \ \leq \ 11.5\,\mu m \\
3: \quad 11.5\,\mu m \ &< \ r.
\end{aligned}
\tag{8.2}
$$

8.2 Timesteps

The single processes in CHEMIFOG_V are calculated successively applying the operator-splitting method. The timestep of the complete model is 60 s. The timesteps used for the different modules are given in Table 8.1. The error introduced by the operator-splitting time intervall of 60 s was investigated in sensitivity runs to be small.

Process		No. of Loops		Timestep (s)	
Thermodynamics, Turbulence		1200 – 1		$5 \cdot 10^{-2} - 60$	
Microphysics		6		10	
Radiation		1		60	
Chemistry	Gas Phase	3	1, 1, 1	20	1, 4, 15
	Aqueous Phase		1000, 9, 199		10^{-5}, 10^{-2}, 10^{-1}
Total		1		60	

Table 8.1: Timesteps of the single modules of CHEMIFOG_V. Processes are carried out in the shown order. The right column shows the internal timesteps, the middle column contains the number of internal loops for each process. The operator-splitting timestep is 60 s.

8.3 Numerical Solvers

Diffusion equations are solved with the implicit scheme of Roache (1982). The set of differential equations of the soil module (Equation 4.32) is solved iteratively with the Crank-Nicholson scheme. For the microphysics of the particle spectrum (condensation/evaporation, sedimentation/deposition) the advection scheme of Bott (1989) is used. The computer code of the chemistry module was produced with the Kinetic PreProcessor (KPP) (Damian-Iordache, 1996). KPP allows an easy combination of reaction mechanisms and numerical solvers. The numerical solution of the differential equation system of the chemical module is performed using a 2-stage Rosenbrock method (ROS2) (Verwer et al., 1997, 1999). ROS2 needs low computer time and shows satisfactory results for timesteps of up to a few minutes, so that negligible numerical errors are introduced under the presented conditions (von Kuhlmann, 2001).

Part II

Numerical Studies

64

Abstract. In this part results from numerical case studies performed with CHEMI-FOG_V are presented.

Chapter 9 introduces the parameters used for the model initialization. These parameters are used for the REFERENCE model simulation as well as the sensitivity simulations, as long as no other values are defined. The model parameters used for initialization are chosen to represent a typical autumn day in the mid-latitudes. Initialization of the chemical species represents a remote forest area.

In Chapter 10 general results of the REFERENCE model simulation are presented and discussed. First a general description of the meteorological parameters are given. These include the temporal development of the radiation field, the air temperature, the turbulent exchange coefficient, and the fog and leaf surface liquid water. Additionally, the microphysical characteristics of the fog event are discussed in detail.

Chapters 11 to 13 present the results of sensitivity studies. These chapters are composed of independent studies on different aspects:

In Chapter 11 a study on the aqueous phase chemical composition of the fog droplets is presented. Focus is given to the drop size-dependence of ammonium and sulphate concentrations and the influence of both the vegetation canopy and droplet growth on the results.

In Chapter 12 investigations on the influence of leaf surface water on trace gas deposition rates are presented. Focus is given to the treatment of the uptake of species into the leaf surface water and to the chemical reactions in the leaf surface water. Sensitivity simulations including three different approaches to describe deposition are presented and discussed.

In Chapter 13 model simulations of the influence of physical and chemical processes within a vegetation canopy on the reduction of primary emissions of NO and isoprene are presented. Moreover, sensitivity studies on the influence of isoprene chemical reactions and on the presence of radiation fog and leaf surface water are discussed.

Chapter 9

Model Initialization

In this chapter the initial parameters used in the REFERENCE model simulation are defined. Model simulations are performed for a latitude of 50°N and a sun declination of $-14°$, which represents the mid of October. Sunrise is at 07.00 and sunset at 17.00. Simulations are performed for 36 hours model time starting at 08.00, including a complete fog cycle as well as a full leaf surface water cycle.

9.1 Thermodynamics

The thermodynamic state of the atmosphere is defined by the vertical profiles of pressure, temperature, and relative humidity and the wind field. The pressure at ground level is set to normal pressure and an exponential decrease with height is assumed. The initial vertical temperature profile is isothermal between the ground and 200 m height with a value of 12°C. Between 200 m and 600 m a lapse rate of $-3°C\,km^{-1}$ and between 600 m and 2000 m a lapse rate of $-4°C\,km^{-1}$ are applied. The relative humidity is initialized with 94 % between the ground and 200 m altitude, 72 % between 200 m and 400 m, 65 % between 400 m and 800 m, and 35 % above. The horizontal wind speed is initialized with the geostrophic wind to 3 m s^{-1} and decreases in the three lowermost layers to a value of 0 m s^{-1} at ground level. The geostrophic wind is kept constant during the simulation.

9.2 Aerosol Particles

The particle size distribution as well as the chemical composition of the aerosol particles are representative for a rural environment.

a_1	$1.1791 \cdot 10^4$	b_1	9.8765	c_1	$7.39 \cdot 10^{-3}$
a_2	$1.0529 \cdot 10^2$	b_2	1.6116	c_2	$2.69 \cdot 10^{-2}$
a_3	$2.9846 \cdot 10^3$	b_3	7.0665	c_3	$4.19 \cdot 10^{-2}$

Table 9.1: Parameters of the lognormal particle number size distribution of rural aerosol particles (Equation 9.1,   Jaenicke, 1988).

9.2.1   Particle Size Distribution

The aerosol particle size distribution is taken from Jaenicke (1988) using the analytical expression for the number concentration of the aerosol particles:

$$\frac{dn}{d \log a} = \sum_{i=1}^{3} a_i \exp \left[-b_i \left(\log \frac{a}{c_i} \right)^2 \right]. \tag{9.1}$$

The coefficients are given in Table 9.1.

Depending on the initial relative humidity the particles grow to their equilibrium radius according to Köhler's equation in the first time step.

9.2.2   Chemical Composition

The rural aerosol particles consist of a soluble and an insoluble fraction. The soluble part is pure $(NH_4)_2SO_4$ and makes up 50 % of the total particle mass for radii larger than $1 \, \mu m$. For smaller particles the soluble fraction increases linearly up to 89.9 % for the smallest particle with radius $a = 2.5 \, nm$. This partitioning of the water soluble and unsoluble mass fraction is taken from Winkler (1974). Additionally, the dry aerosol particles with $a < 1 \, \mu m$ contain both 0.02 % Fe^{3+} and Fe^{2+}, while the particles with $a > 1 \, \mu m$ contain both 0.21 % Fe^{3+} and Fe^{2+} of the aerosol mass (Hoffmann et al., 2001, Stevens et al., 1984). Mn^{2+} is initialized with 10 % of Fe^{3+}. The remaining components are assumed to not dissociate in the aqueous phase and are therefore not considered in this study.

9.3   Soil

The soil type is set to 'sandy loam'. Parameters are taken from Pielke (1984). The initial volumetric moisture content is $0.12 \, m^3 m^{-3}$. For the initial soil temperature a value of 12°C is applied uniformly to all depth levels.
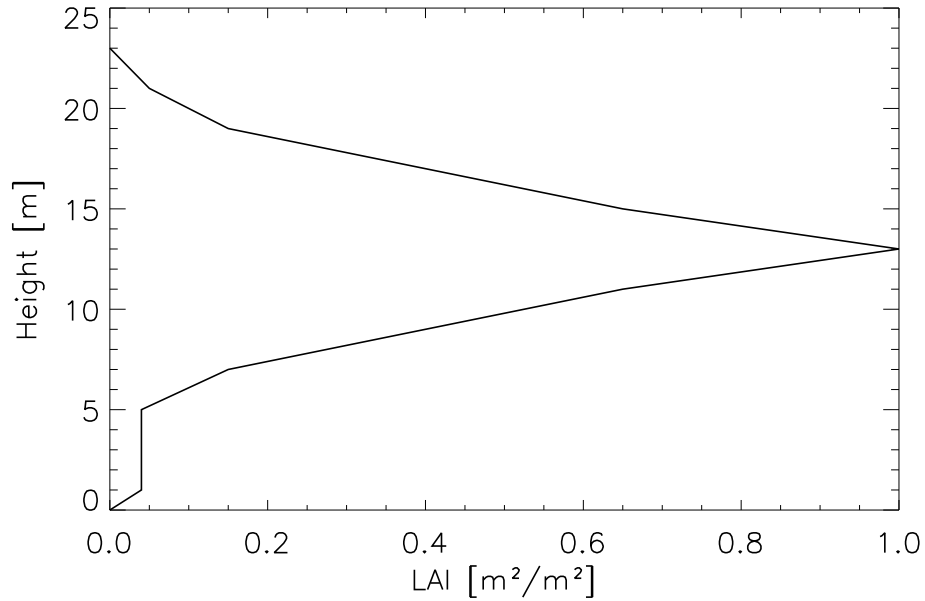
Figure 9.1: Vertical profile of the leaf area index (LAI).

9.4 Vegetation

The vegetation is characterized by

- the type of vegetation,

- the vegetation coverage,

- the height, and

- the vertical profile of the LAI.

The presented numerical studies are performed for a deciduous forest. The vegetation coverage is $\sigma = 0.7$, representing a medium dense forest. Eleven equidistant levels are included in the vegetation module resulting in a vegetation height of 22 m. The vertical profile of the LAI shown in Figure 9.1 is specific to represent a deciduous forest with a defined overstorey maximum. The integrated LAI of the canopy is 5.

9.5 Chemistry

9.5.1 Gas Phase Species

Initial values for the gaseous chemical species are taken from the MATCH model (von Kuhlmann, 2001, Lawrence et al., 1999) for a remote mid-latitude Canadian forest region except for isoprene and methanol (MacDonald and Fall, 1993) as well as HCl (Herrmann et al., 2000). Table 9.2 shows the initial values for the gas phase species.

Gas Phase Species	ppb	ALD	0.1
CO	110	PAN	0.18
O_3	18	PAA	0.005
H_2O_2	0.06	CH_3COOH	0.01
NO	0.02	EtOH	0.24
NO_2	0.25	HCOOH	0.002
HNO_3	0.045	C_5H_8	2.0
CH_4	1843	SO_2	1
MeOOH	0.065	HCl	0.7
HCHO	0.065		
MeOH	8.0	Aqueous Phase Species	$mole\,l^{-1}$
NH_3	1.2	Cl^-	$1 \cdot 10^{-4}$
N_2O	320	Br^-	$3 \cdot 10^{-7}$
C_2H_6	0.975	Cu^+	$2.5 \cdot 10^{-8}$
EtOOH	0.006	pH	7

Table 9.2: Initial values for gas and aqueous phase species given in parts per billion (ppb) and $mole\,l^{-1}$, respectively. Species' abbreviations are given in Table B.1 in Appendix B.

9.5.2   Aqueous Phase Species

In general, aqueous phase concentrations are initialized to zero and determined by the uptake from the gas phase and aqueous phase reactions. However, some aqueous phase species are initialized. The pH is initialized with a value of 7 to avoid numerical instabilities. Chlorine and bromine are not considered thoroughly in the gas phase model and therefore chloride and bromide are initialized in the aqueous phase. Iron, manganese, ammonium (NH_4^+) and sulphate (SO_4^{2-}) are initialized depending on the aerosol mass according to Section 9.2.2. Copper is initialized with a constant value. Values are given in Table 9.2.

Chapter 10

Description of the Radiation Fog Event focussing on the Microphysical Properties

In this chapter the physical characteristics of the radiation fog event resulting from the REFERENCE model simulation are presented. Initialization is performed according to Chapter 9. In Section 10.1 the main meteorological features are presented followed by investigations on the modifications of the aerosol particle spectrum due to the radiation fog event in Section 10.2. Special emphasis is given to the microphysical properties of the droplets in the three droplet size classes used in the chemistry calculations.

10.1 Thermodynamics

Solar radiation determines the temperature and, therefore, also the atmospheric stability in the planetary boundary layer (PBL) during daytime. The attenuation of the solar radiation as well as the heating of the atmosphere due to molecular absorption is small within the PBL compared to the interaction of the radiation with the vegetation canopy that leads to a significant modification of both the radiation and the temperature in the canopy. Figure 10.1 shows the total downward solar irradiance within the lower 30 m of the model domain. Sunrise is at 07.00 and sunset at 17.00 with maximum irradiance at 12.00. Solar radiation in the canopy is attenuated by the extinction of the vegetation elements. A strong vertical gradient of the irradiance in the crown area is evident during daytime. Figure 10.2 shows three vertical profiles of the total downward shortwave irradiance at 10.00, 12.00,
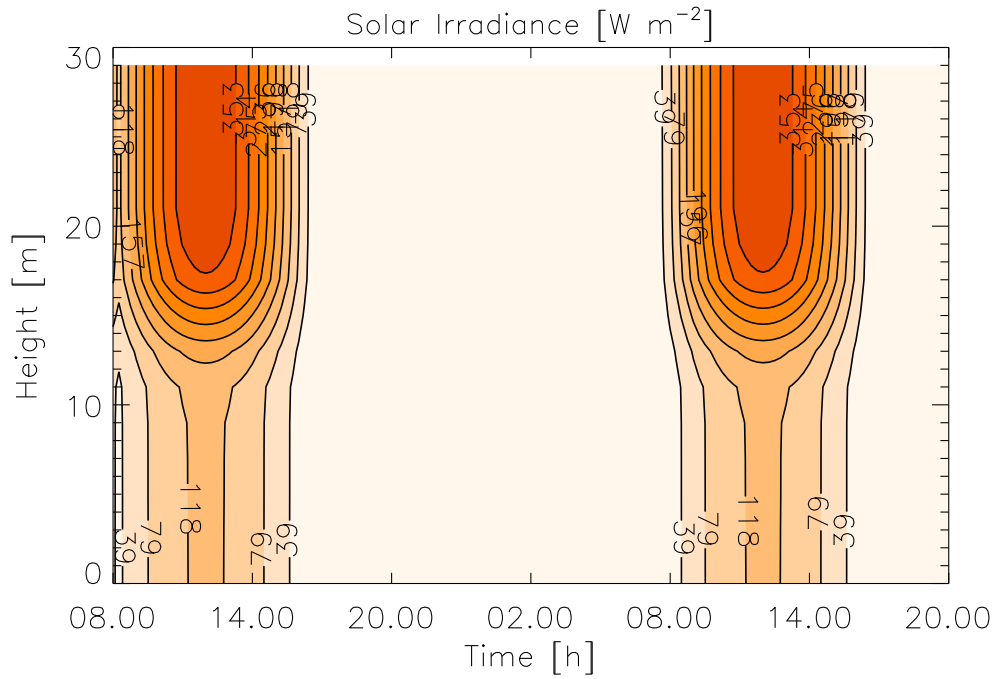
Figure 10.1: Contour plot of the temporal development of the total downward solar irradiance in the lowest 30 m.
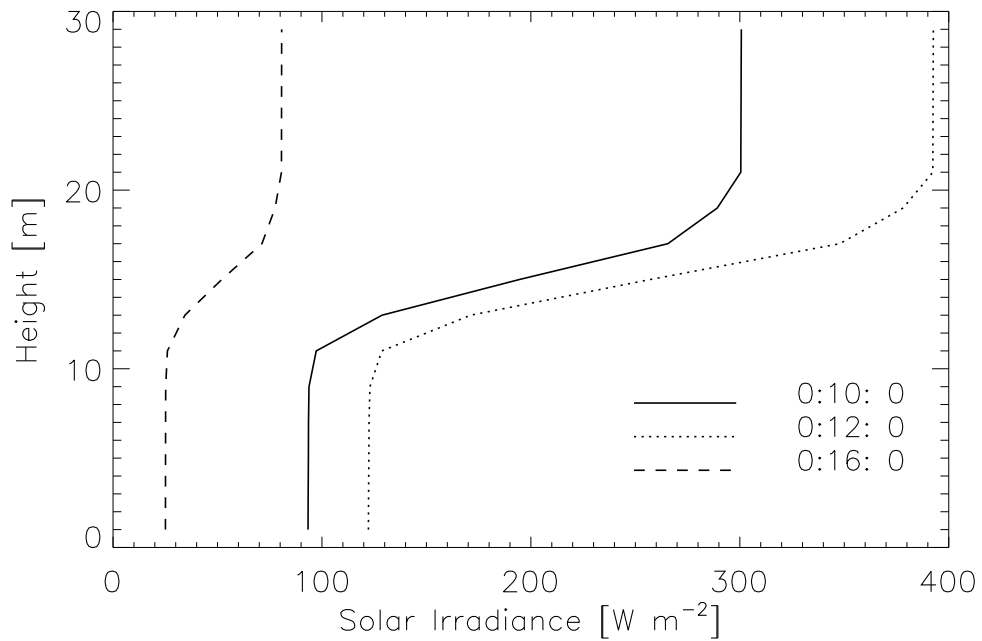
Figure 10.2: Vertical profiles of the downward solar irradiance in the lowest 30 m for three times on the first model day.
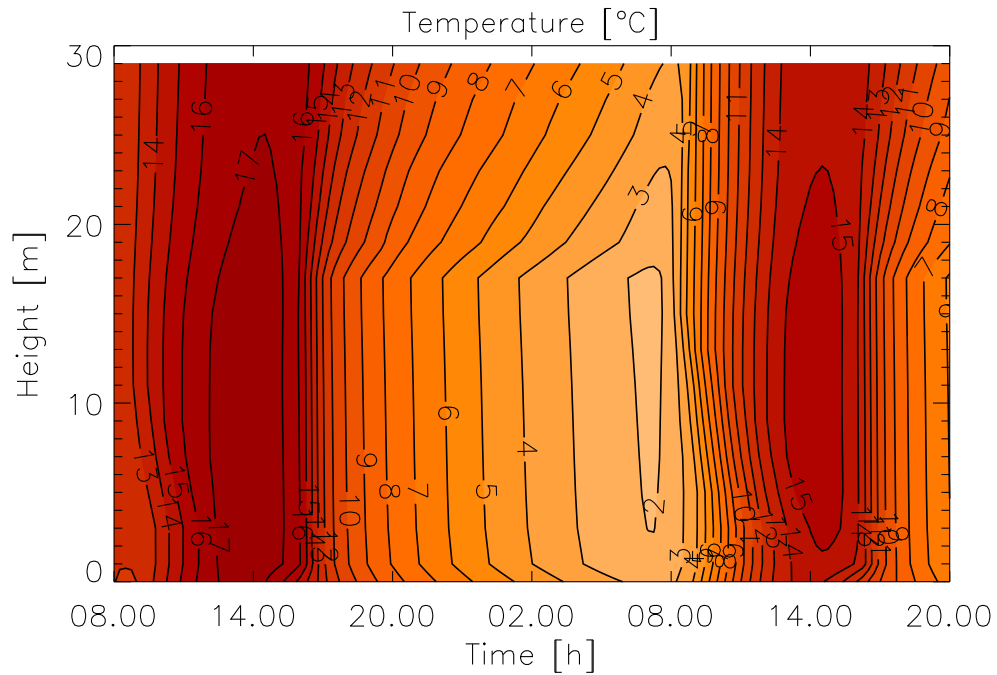
Figure 10.3: Contour plot of the temporal development of the air temperature in the lowest 30 metres.

and 16.00 on the first model day. In the crown area the irradiance is reduced to approximately one third of the value above the canopy in all three cases, while in the lowest 10 m the solar irradiance is constant with altitude.

The effect of the interaction between the radiation field and the vegetation elements is reflected in the temporal development of the air temperature in the lowest 30 m during the model simulation shown in Figure 10.3. During daytime the absorption of solar radiation causes a maximum in the foliar temperature and therewith of the temperature of the interstitial air within the crown area of the vegetation canopy. Below, the temperature slightly decreases with decreasing altitude. During nighttime the temperature profile shows a minimum within the crown region, because radiative cooling is the major physical process determining the canopy temperature. Accordingly, an inversion layer develops above 17 m altitude. The temperature profile reverses at 16.00 on the first model day and at 8.00 on the second model day. In the soil adjacent layer the temperature is always slightly enhanced compared to above.

The temperature field determines the turbulent transport expressed by the turbulent exchange coefficients shown exemplarily for k_h in Figure 10.4. During daytime the boundary layer above the canopy is well mixed, while within the canopy k_h is
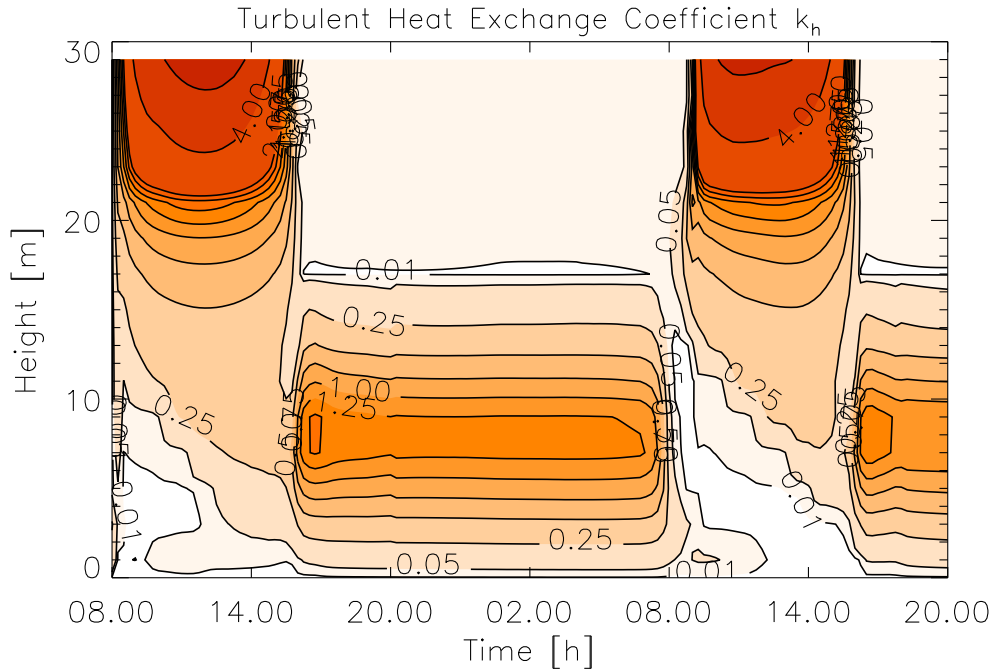
Figure 10.4: Contour plot of the temporal development of k_h in the lowest 60 metres.

steadily decreasing with decreasing altitude. Below the crown area the values of k_h are small and in the lowest model layers turbulence is reduced to zero in the morning hours of the first model day. During the day turbulence steadily penetrates deeper into the canopy. Around 16.00 conditions rapidly change and the turbulent exchange coefficients increase within the vegetation canopy, while above the canopy the turbulence breaks down. This situation is due to the inversion of the temperature profile as shown in Figure 10.3 and stays constant during the night. Around 08.00 on the second model day the turbulent conditions reverse again. Between approximately 12.00 and 16.00 k_h is zero within the lowest model layers. Overall, during daytime, the atmosphere within the vegetation canopy is stable, while the boundary layer above is well-mixed. During nighttime conditions reverse. The nocturnal PBL above the canopy is stable, while convection prevails within the canopy. The two regions above and below the canopy crown area are dynamically separated during most of the time. While the altitude range of the crown area is both part of the diurnal and nocturnal mixing layer, the ground adjacent model layer is excluded from the diurnal turbulent exchange.

The radiation field and the resulting turbulence determine the temporal and spatial development of the radiation fog. Figure 10.5 shows the fog liquid water content (LWC). A radiation fog event can be divided into three stages: the initial,
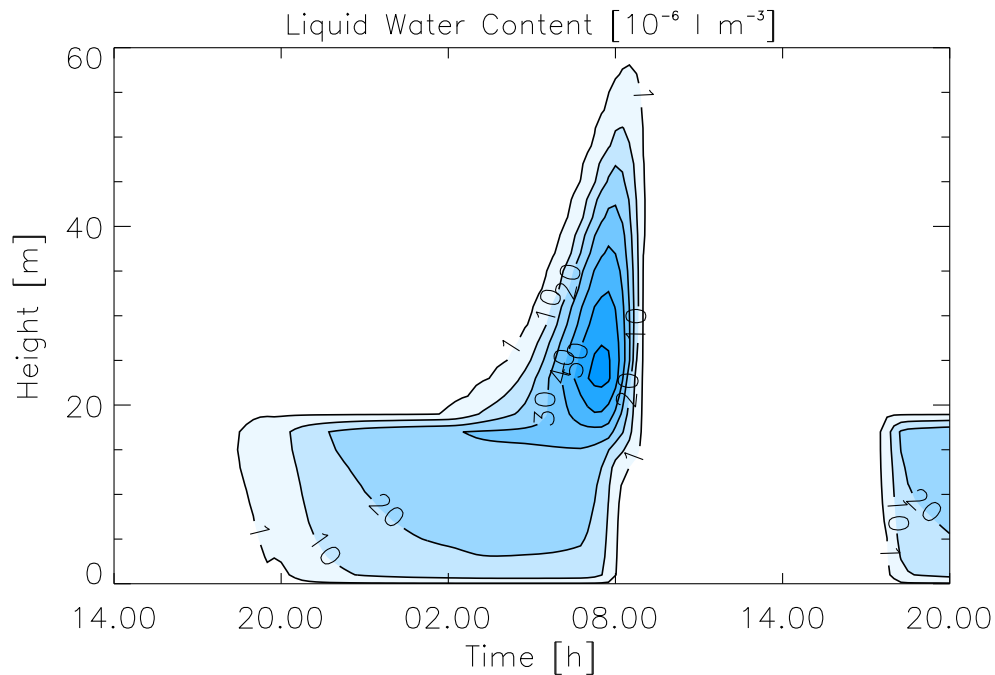
Figure 10.5: Contour plot of the temporal development of the fog liquid water content in the lowest 60 metres.

the mature, and the dissipation stage. The initial stage of the presented radiation fog event extends from the beginning of the fog at around 18.30 on the first model day until approximately 02.00 on the second model day. After sunset the atmospheric temperature decreases and the relative humidity increases up to supersaturation. Consequently, water vapor condenses onto the aerosol particles forming fog droplets. During the initial stage the fog droplets are distributed rather uniformly throughout the well-mixed vegetation canopy. The liquid water content slowly increases with time, but shows only slight variability with altitude with maximum values located at an altitude of 17 m within the crown area of the canopy.

During the mature stage starting around 02.00 and ending around 08.00 on the second model day, the radiative cooling leads to the formation of fog droplets in higher altitudes. The liquid water content above the canopy steadily increases, while within the canopy only a slight increase is observed. However, the fog is still stable as no turbulent exchange takes place above the vegetation.

The dissipation stage of the radiation fog event is limited to the time interval between approximately 08.00 and 08.30 on the second model day. After sunrise the temperature increases leading to the evaporation of the fog droplets. Additionally turbulence sets in causing the immediate rise and dissipation of the fog droplets.
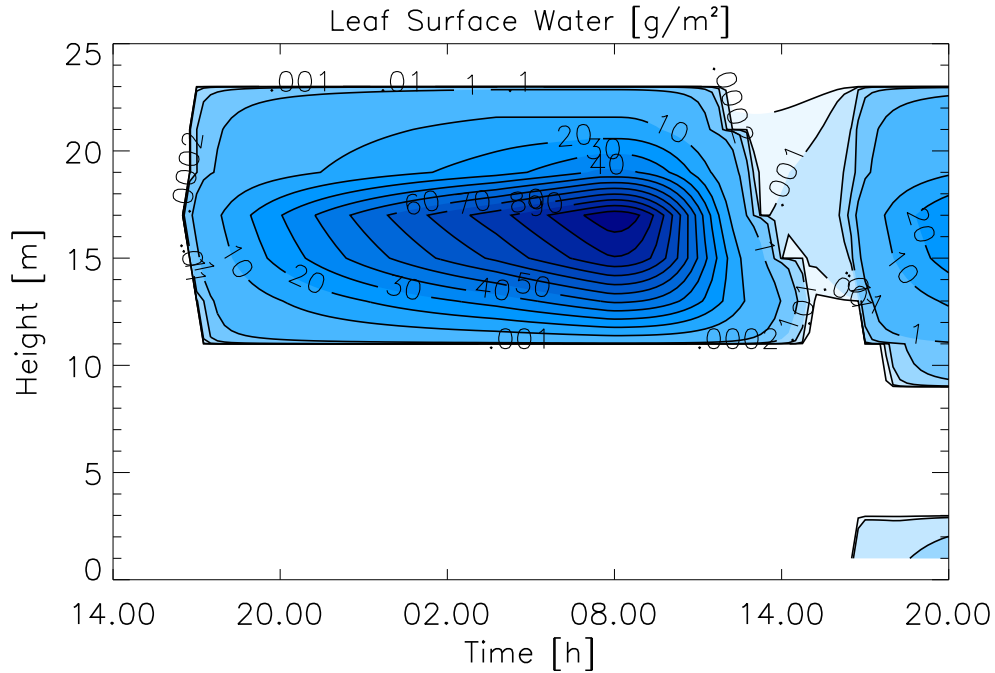
Figure 10.6: Contour plot of the temporal development of the leaf surface liquid water content.

Besides the condensation of water vapor to aerosol particles condensation to the leaf surfaces takes place. Figure 10.6 shows a contour plot of the temporal development of the leaf surface water within the vegetation canopy. Around 16.00 on the first model day in the crown region between $12\,m$ and $22\,m$ leaf surface water develops. Besides the condensation of water vapor to the leaf surfaces, additionally, deposition of fog droplets causes the build-up of leaf surface water. The maximum value of more than $100\,g\,m^{-2}$ is reached at 08.00 on the second model day in $17\,m$ altitude, the same altitude, where the maximum in the LWC of the fog is located. After sunrise the leaf surface water partly evaporates. Around 14.00 on the second model day the concentration of the leaf surface water is strongly reduced in all model layers. However, within the altitude range of $14\,m$ to $20\,m$ the leaf surface water concentration remains larger than the limit of $0.2\,mg\,m^{-2}$, above which chemical reactions are calculated. Around 16.00 on the second model day a second leaf surface water cycle starts equivalent to the first one. Differences between the two days are due to the slightly more humid atmosphere on the second model day.
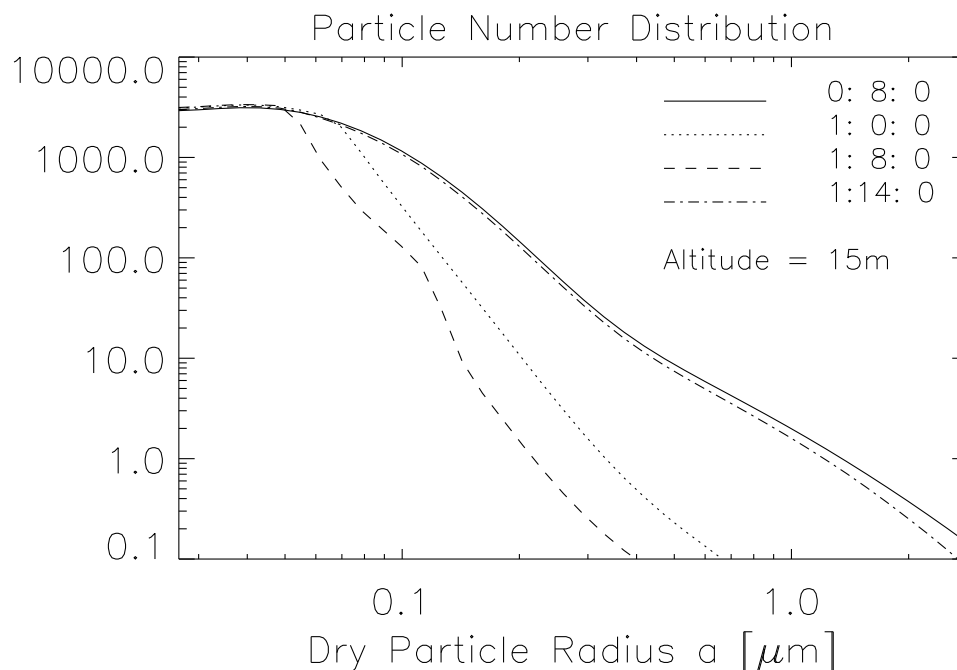
Figure 10.7: Aerosol particle number size distribution, $f_a = \int_r f(a, r)\, dr$, for different times at $15\,\mathrm{m}$ altitude (0: 8: 0 = first model day, 08.00).

10.2 Microphysics

The two-dimensional droplet size distribution is modified by condensation and evaporation, sedimentation, turbulent transport, deposition to vegetation surfaces and the soil, and chemical processing according to Equation 5.26. In this section the temporal and spatial variations of the particle spectrum are presented and discussed in terms of the different processes. First, the temporal development of the aerosol particle size spectrum is discussed and the influences of a radiation fog event and a vegetation canopy are investigated. Moreover, the temporal and spatial development of the droplet size spectrum is presented and discussed. The importance of the detailed description of the particles by the two-dimensional particle grid to distinguish between the physical processes that modify the spectrum is underlined. Additionally, the microphysical processes in the three size classes of the chemical module are investigated.

10.2.1 Aerosol Particle Size Distribution

Aerosol particles are removed from the atmosphere by dry and wet deposition. Vegetation provides an effective sink for aerosol particles because of the large surface

area. During the radiation fog event aersol particles are included into the droplets, that deposit onto the vegetation surfaces and to the ground. This process reduces the number of particles in the atmosphere. Figure 10.7 shows the particle number distribution versus the dry particle radius at an altitude of 15 m. The solid line is the initial spectrum at 08.00 on the first model day. The dotted and the dashed curves show the spectrum at 00.00 during the initial stage and at 08.00 at the end of the mature stage of the fog event. Obviously, the large particles are effectively removed from the atmosphere indicating that the large aerosol particles serve as condensation nuclei for the large fog droplets that effectively deposit. Particles with a radius smaller than $0.04\,\mu$m are not affected as they are not activated. The dashed-dotted line shows the particle spectrum at 14.00 on the second model day representing the resulting particle spectrum after the fog event, when turbulent transport has mixed the boundary layer. The number of large aerosol particles is strongly reduced compared to the initial spectrum. Figure 10.8 shows the ratio of the aerosol particle spectrum after the fog event to the initial particle spectrum in 39 m altitude in the well mixed boundary layer. The reduction in number density is 10% to 20% between $0.1\,\mu$m and $1.1\,\mu$m and increases up to nearly 40% for the largest particles with a radius of $3\,\mu$m. The deposition of droplets to the vegetation during the fog event therefore leads to a significant reduction of the particle number concentration in the boundary layer, especially of particles with a radius $a > 1.1\,\mu$m. This modification of the particle spectrum has a potential influence on the future cloud droplet forming and, therefore, on the radiative properties of the cloud.

10.2.2   Droplet Size Distribution

Besides the dry particle spectrum the total droplet size spectrum during the radiation fog event varies in time and space. In the following the temporal and spatial variations of the droplet size spectrum are investigated. Figure 10.9 shows the water mass as function of the particle size for five different times at an altitude of 15 m, i.e., in the crown area of the canopy. At the beginning of the fog event at 20.00 a broad droplet spectrum with the maximum water mass located at a radius of around $4\,\mu$m to $5\,\mu$m develops. During the initial stage the spectrum is shifted to larger radii, while the liquid water mass increases as seen in the spectrum at 00.00. The mature stage of the fog is represented by the two spectra taken at 04.00 and 07.00 on the second model day. The maximum of the water mass is reached at 04.00 with the highest mass concentration at a radius of $r = 7.5\,\mu$m. At 07.00 a second mode develops with the maximum at a radius of more than $15\,\mu$m. At 08.00 during the
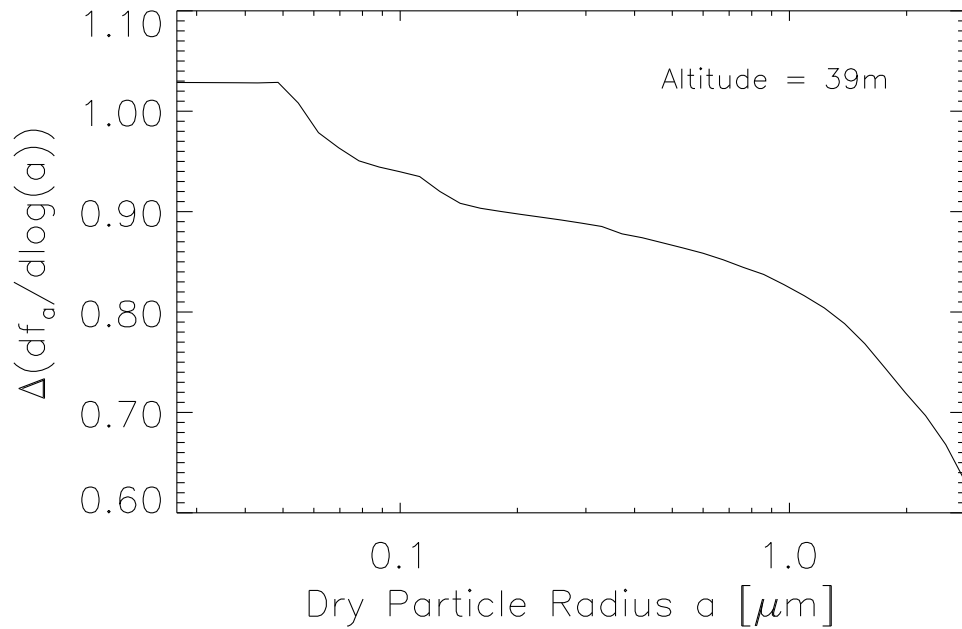
Figure 10.8: Ratio of the aerosol particle number size distribution at 39 m altitude at 14.00 and at 08.00 on the second model day.
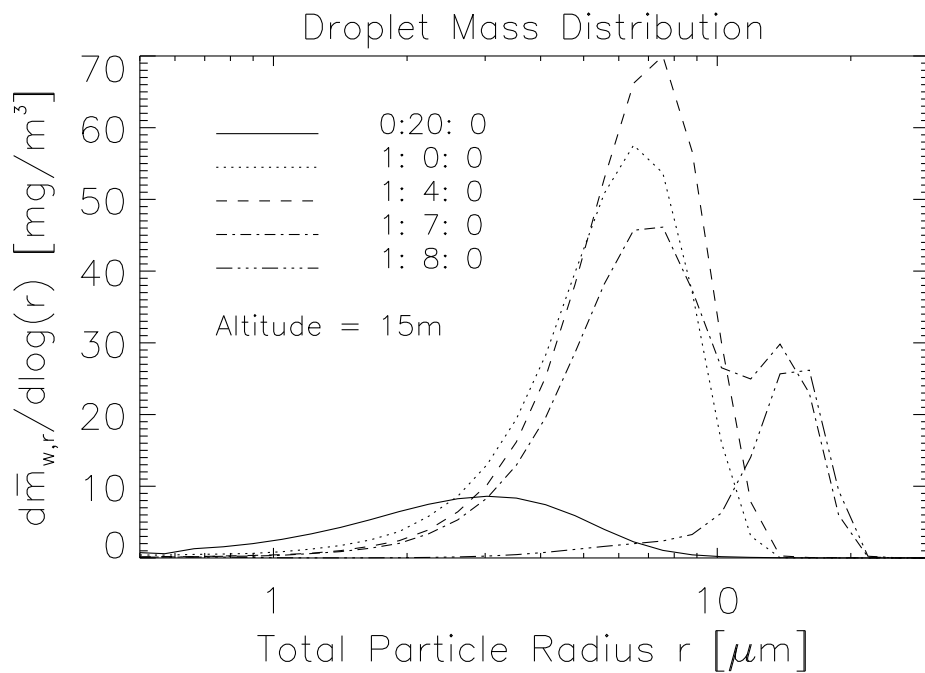
Figure 10.9: Size distribution of the droplet water mass, $\overline{m}_{w,r} = \int_a \overline{m}_w \, da$, at different times in 15 m altitude.
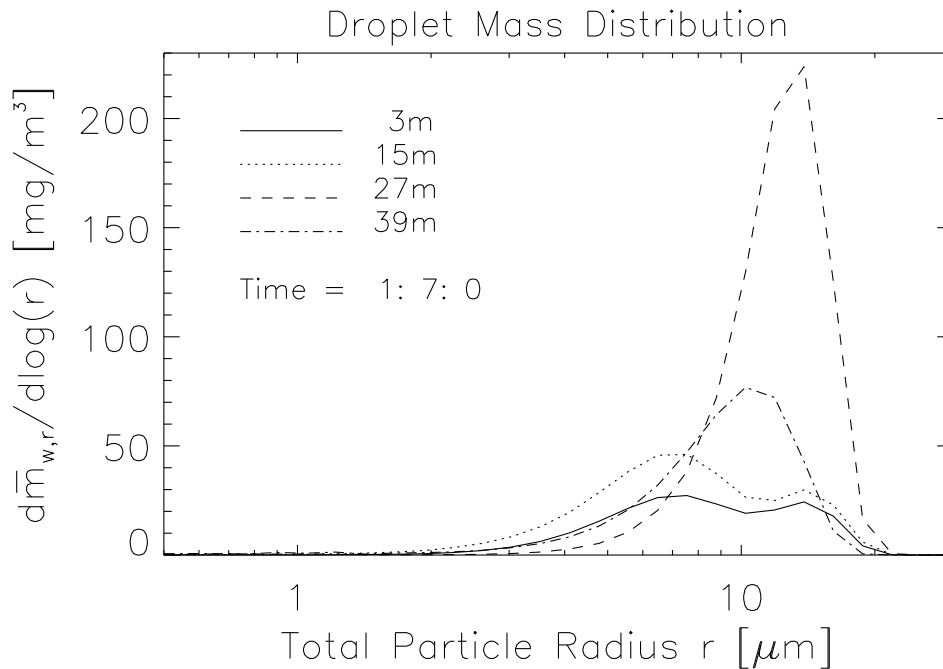
Figure 10.10: Size distribution of the droplet water mass at different altitudes at 07.00 on the second model day.

dissipation stage the smaller mode has disappeared.

Figure 10.10 also shows the mass distribution, but for four different altitudes at 07.00 on the second model day. In the two lower layers at 3 m and 15 m within the canopy, two modes are present at this stage of the fog event, while in 27 m and 39 m altitude the distribution is monomodal. The mode in 27 m coincides with the larger modes within the canopy indicating that large droplets sediment from layers above the canopy to the lower levels.

10.2.3   Two-dimensional Droplet Size Distribution

The two-dimensional droplet size spectrum contains the information on the dry aerosol radius as well as the total droplet radius allowing the separation of cloud microphysical and dynamical processes. Figures 10.11 to 10.13 show contour plots of the water mass as a function of the two-dimensional particle spectrum at 15 m height at 04.00, 07.00, and 08.00 on the second model day. The colour code and the isolines represent the water mass. The black line represents the critical radius of the aerosol particles derived from Köhler's equation. Consequently, the upper left triangles in the figures represent the region, where the droplets are activated. In Figure 10.11 the simulated particle spectrum is shown for 04.00 on the second

Figure 10.11: Two-dimensional size spectrum of the droplet water mass at 15 m altitude and 04.00 on the second model day.

model day. The aerosol particles with a dry radius between $0.04\,\mu$m and $0.6\,\mu$m have grown beyond the critical radius. While larger particles remain inactivated, the smaller particles retain their equilibrium size. The highest water mass is found for droplets containing aerosol particles with a dry radius of between $0.05\,\mu$m and $0.12\,\mu$m. In Figure 10.12, that shows the water mass at the same altitude as Figure 10.11 but at 07.00, two major differences are visible. First, an increase in droplet size is found for aerosol particles with a $> 0.2\mu$m, and second, a second maximum of the total droplet water mass develops centered at dry particle radii of $0.15\,\mu$m. At 08.00, Figure 10.13, during the dissipation stage, the small droplets have evaporated causing the maximum at the small particle size to disappear.

At 15 m altitude at 04.00 the fog has reached its maximum liquid water content. Sedimenting droplets intruding the canopy have already been discussed as a possible source for the second mode developing at larger radii in the previous section. In order to investigate the origin of the particles of this second maximum, Figure 10.14 shows the two-dimensional distribution of the liquid water mass at 07.00 at 27 m altitude. The maximum water mass coincides with the second mode in Figure 10.12 considering both the droplet radius and the dry aerosol radius, indicating that the second maximum in the liquid water mass that occurs in 15 m height is caused by
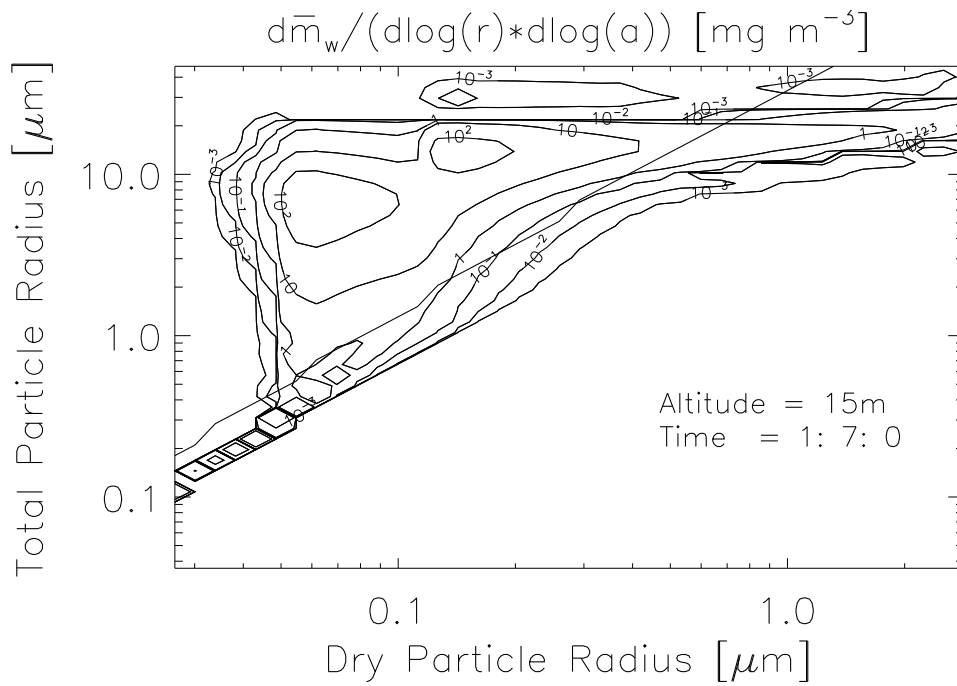
Figure 10.12: Two-dimensional size spectrum of the droplet water mass at 15 m altitude and 07.00 on the second model day.

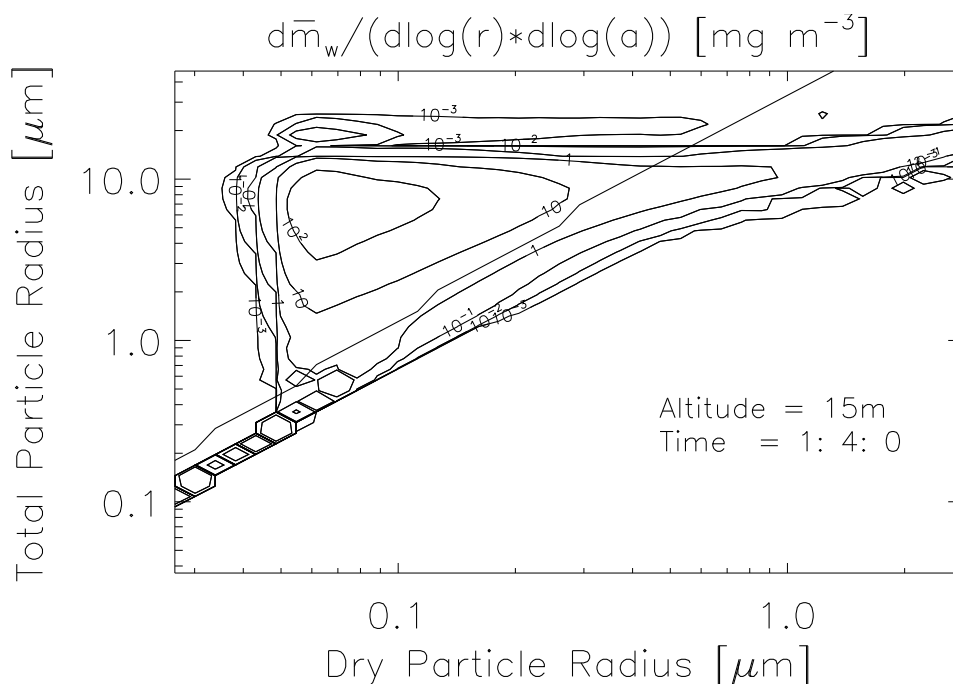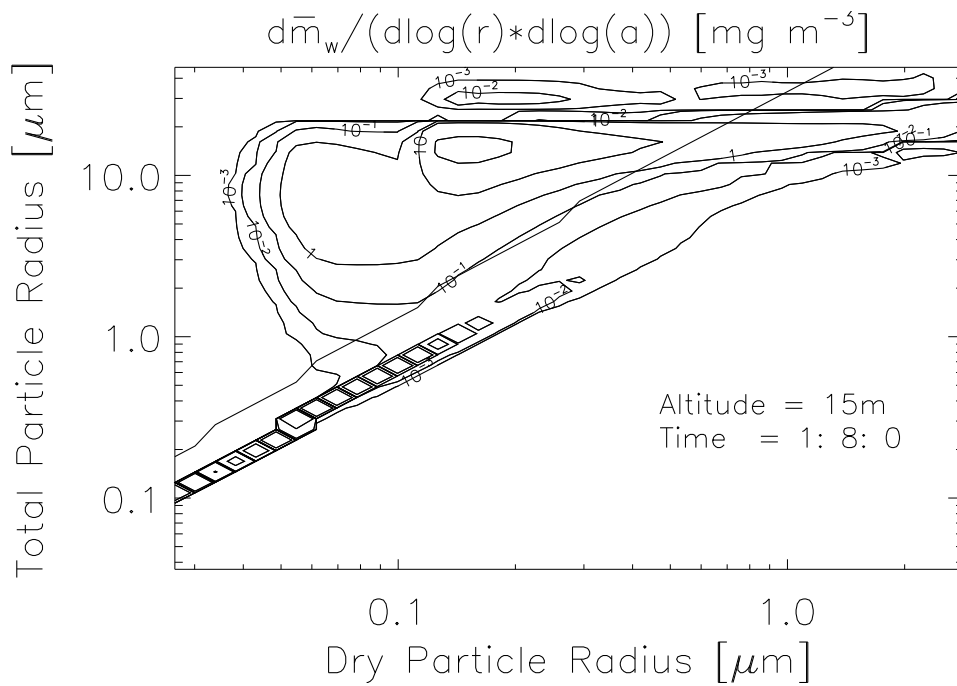Figure 10.13: Two-dimensional size spectrum of the droplet water mass at 15 m altitude and 08.00 on the second model day.
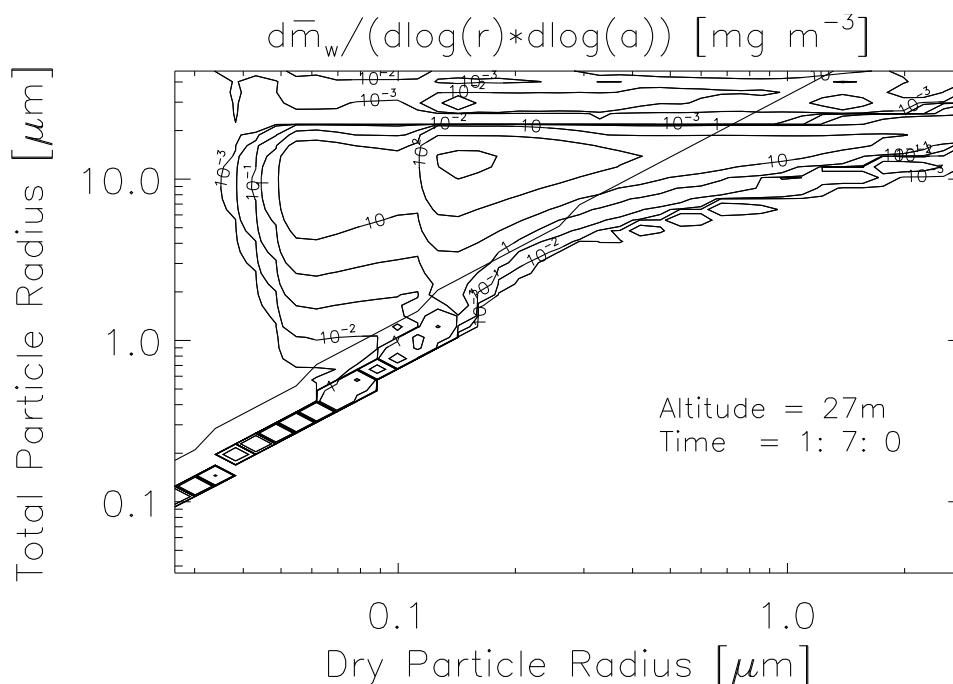
Figure 10.14: Two-dimensional size spectrum of the droplet water mass at 27 m altitude and 07.00 on the second model day.

sedimenting droplets from higher altitudes. The dry particle radius, consequently, can serve as a tracer for the particle movement.

10.2.4   Microphysical Properties of the Chemistry Size Classes

Figures 10.15 to 10.20 show contour plots of the temporal and spatial development of the liquid water content and the mean droplet radius in the three droplet size classes, where chemical processes are considered (see Equation 8.2)[a]. The fog characteristics in the two small droplet size classes differ significantly within and above the canopy. The largest droplet size class does not show this vertical structure but mainly follows the temporal development of the fog discussed in Section 10.1.

During the initial stage the fog is restricted to the canopy. In size class 1 the mean radius slightly rises, while the LWC decreases. This indicates, that the small fog droplets grow to larger sizes and enter the second size class. In size class 2 both the mean radius and the LWC increase. This implies that the major part of the droplets of the second size class grow steadily during the initial stage. However, due to the high deposition rates the lifetime of large particles within the canopy is

---

[a]Note the different scales in the colour coding.
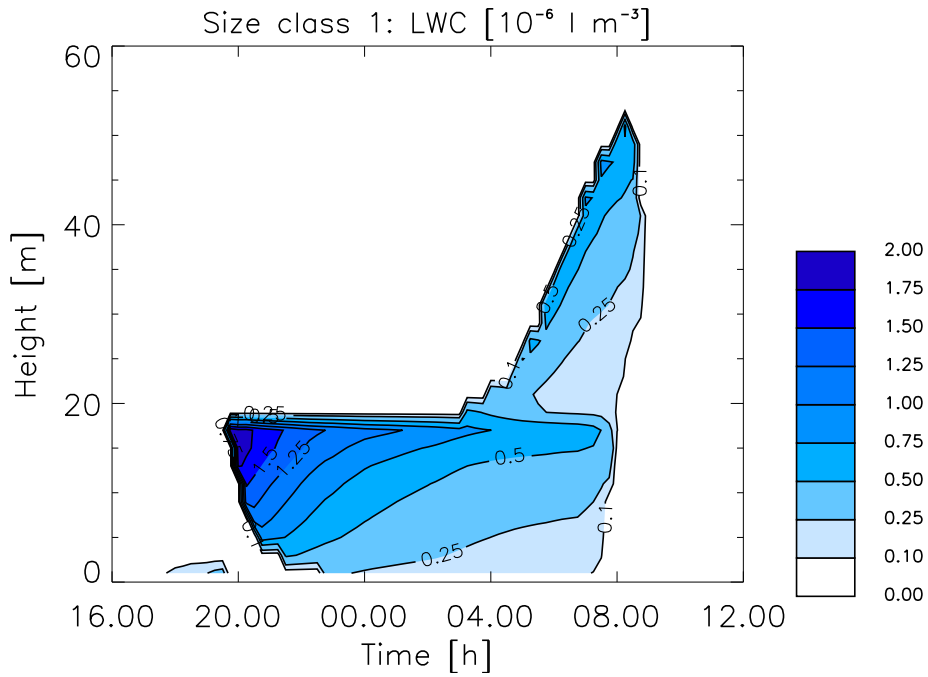
Figure 10.15: Temporal and spatial development of the fog liquid water content (LWC) in size class 1 ($0.5\,\mu$m $< r < 2\,\mu$m).
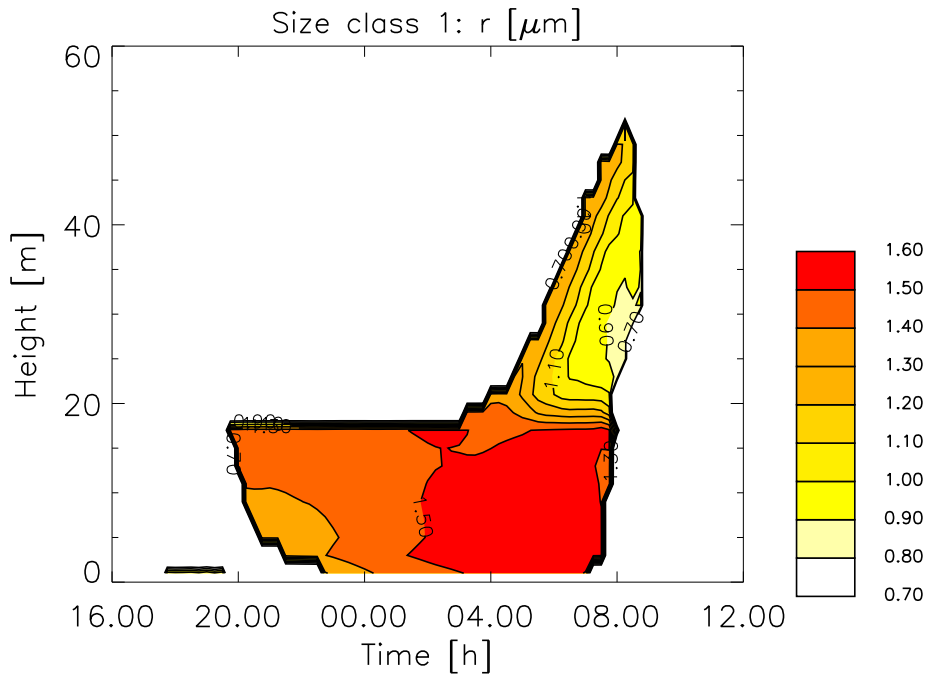
Figure 10.16: Mean radius of the fog droplets in size class 1.
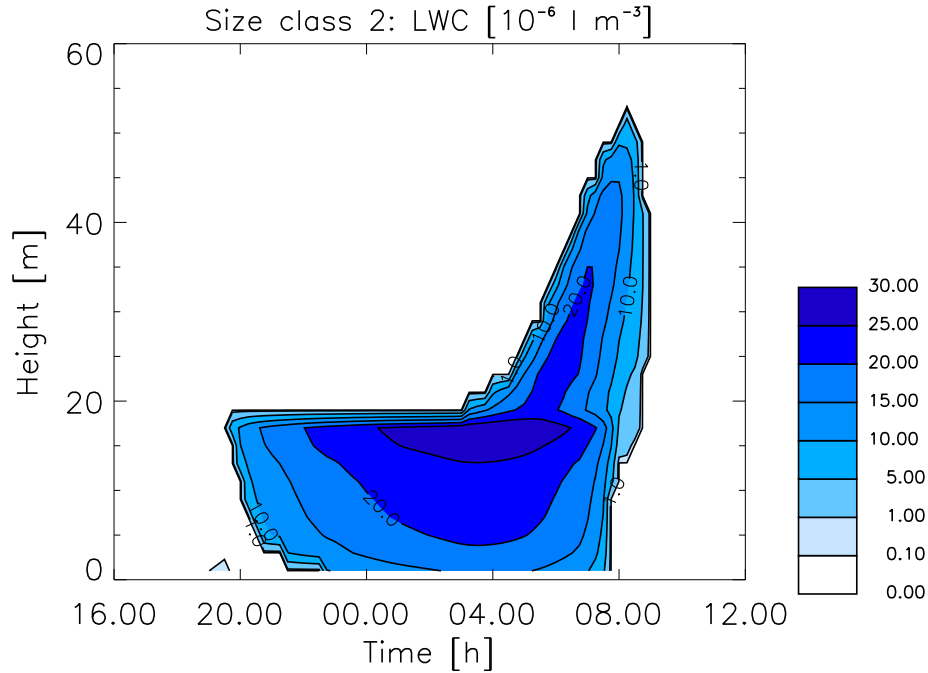
Figure 10.17: Temporal and spatial development of the LWC in size class 2 ($2\,\mu\mathrm{m} <$ $r < 11.5\,\mu\mathrm{m}$).

too short for a significant number of particles to grow into size class 3. The highest LWC, consequently, is found in the second size class, while in the large size class the LWC is negligible.

During the mature stage the development of the LWC and the mean radius in size classes 1 and 2 remains mainly unchanged within the canopy until the highest LWC is reached in the second size class with a value of more than $2.5 \cdot 10^{-5}\,\mathrm{l\,m^{-3}}$ at the top of the canopy around 04.00 on the second model day. Afterwards, the LWC in the second size class decreases, while the mean radius reaches its maximum in the beginning of the mature stage and afterwards slightly decreases. Evaporation of the smaller particles of size class 1 and 2 leads to the reduction of the LWC in both size classes. The LWC and the mean radius in the largest size class rise during the mature stage. As already shown, large particles that belong to size class 3 intrude into the canopy due to sedimentation and lead to an increase of the LWC and mean radius within the canopy.

During the mature stage the fog also forms above the canopy, where both the LWC and the mean radius of the smallest size class decrease. In contrast, the mean radius of size class 2 increases with decreasing LWC, while in size class 3 both the LWC and the mean radius increase. The droplets in the first size class evaporate, as
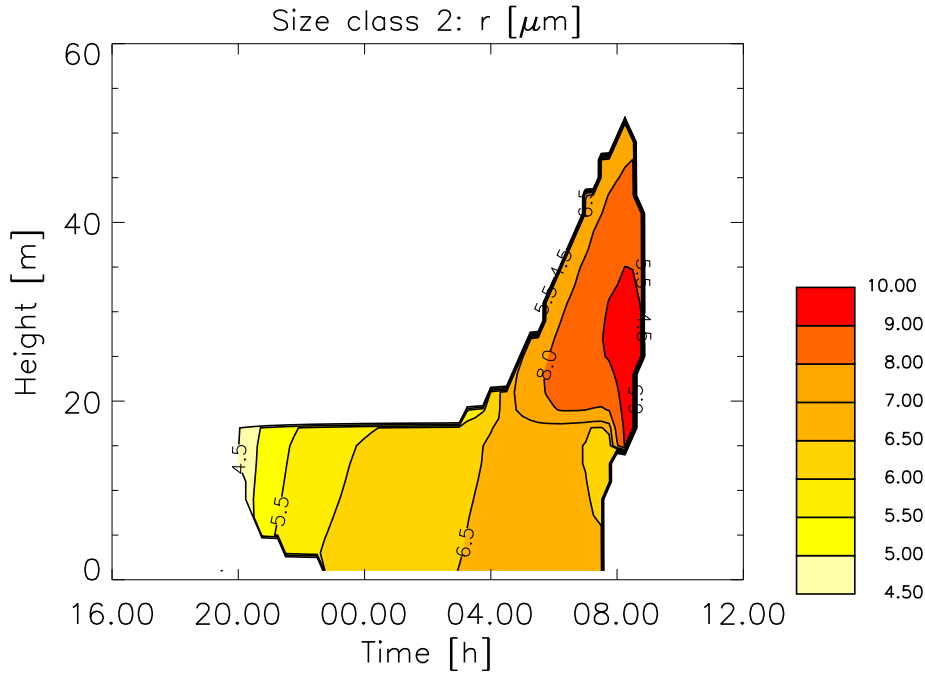
Figure 10.18: Mean radius of the fog droplets in size class 2.

the larger droplets grow to the expense of the smaller ones. However, in contrast to the situation within the canopy, above the canopy a significant number of droplets of size class 2 effectively grow in size and enter the largest size class causing the observed changes in the LWC's. However, small particles of the second size class also evaporate.

As mentioned previously, the characteristics of the third size class are less separated between the in-canopy and the above-canopy region. In Figure 10.20 the isolines of the mean radius of size class 3 show a similar pattern within and above the canopy. The large droplet sizes in class 3 have large terminal velocities causing effective sedimentation. As a consequence, particles of size class 3 intrude into the canopy. The LWC, however, is reduced within the canopy due to deposition. During the dissipation stage of the fog the smaller droplets evaporate earlier than the larger ones. Due to the rapid dissipation of the fog in the morning of the second model day, the shrinking of the particles due to evaporation is not resolved in these figures.
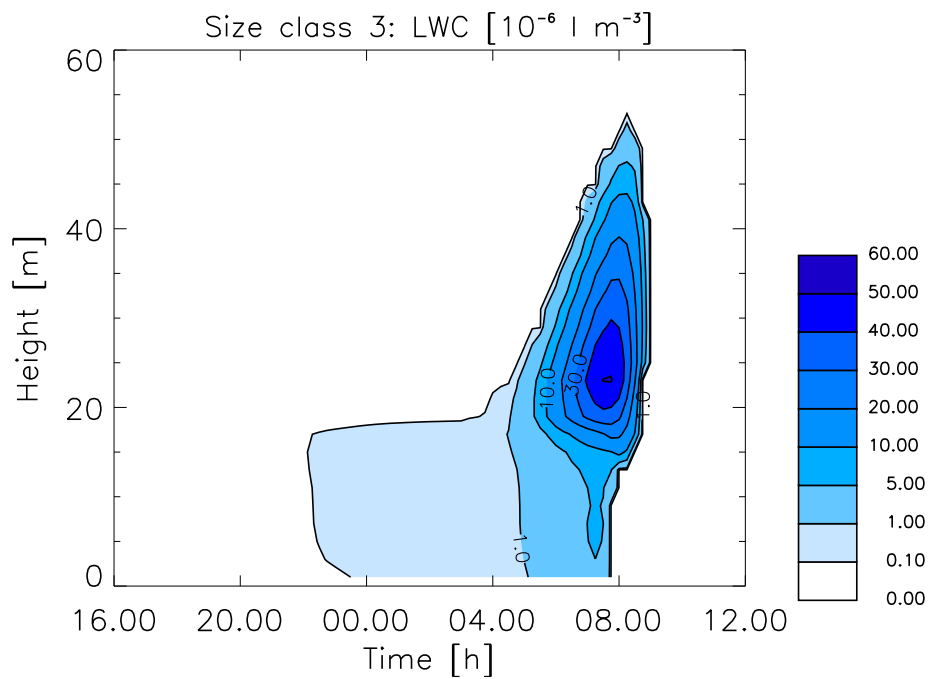
Figure 10.19: Temporal and spatial development of the LWC in size class 3 ($r >$ 11.5 μm).
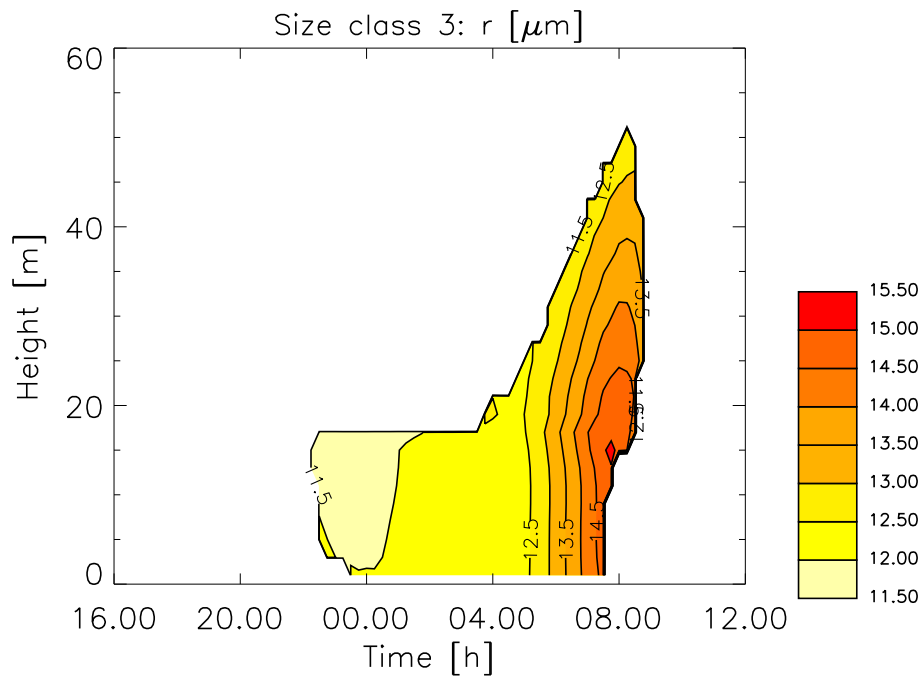
Figure 10.20: Mean radius of the fog droplets in size class 3.

Chapter 11

The Influence of a Vegetation Canopy on the Chemical Properties of Radiation Fog: Implications for Size-Dependent Sulphate Production

Abstract. In this chapter the size-dependent chemical composition of radiation fog droplets is discussed. Model simulations are performed with the one-dimensional chemical-microphysical fog model CHEMIFOG_V. Aqueous phase chemistry is calculated in three size classes. The range of the size classes is $0.5\,\mu$m $< r < 2\,\mu$m for size class 1, $2\,\mu$m $< r < 11.5\,\mu$m for size class 2, and $r > 11.5\,\mu$m for size class 3. Focus is given to both the impact of a vegetation canopy on and the size-dependence of the chemical composition of fog droplets.

pH values are found to be lowest for particles with a radius $r < 2\,\mu$m and largest for particles with a radius $r > 11.5\,\mu$m. For particles with a radius $r > 2\,\mu$m pH values are larger above the canopy compared to within the canopy due to the uptake of ammonia.

The aqueous phase concentrations of ammonium and sulphate are used to investigate the origin of S(VI), i.e., sulphur with valence of six, and the efficiency of sulphur oxidation. In the smallest size class comprising droplets with $r < 2\,\mu$m the sulphate concentration is determined by the dissociation of the aerosol particle. Within the canopy this also holds for particles with a radius $r < 11.5\,\mu$m. Above the canopy, the uptake of geseous NH_3 and SO_2 leads to significant changes in the

aqueous phase concentrations of particles with radii $r > 2\,\mu$m. Highest uptake of SO_2 takes place at the beginning of the mature stage of the radiation fog above the canopy into droplets of radii $2\,\mu$m $< r < 11.5\,\mu$m.

Hydroxy methane sulphonate (HMS^-) is used to trace the exchange of sulphur compounds between the size classes due to condensation and evaporation of droplets. The exchange of particles between the size classes leads to a temporal and spatial variation of the size-dependence of the sulphate concentration.

Leaf surface water provides an additional water pool within the vegetation canopy. Both the interfacial exchange of trace species and the aqueous phase chemistry model are applied for the leaf surface water. As a result, the leaf surface water effectively takes up atmospheric trace gases within the canopy leading to a reduction of the atmospheric gas phase concentrations. Moreover, due to uptake and deposition of fog droplets the concentrations in the leaf surface water exceed the concentrations in the fog droplets by two orders of magnitude.

11.1   Introduction

Ammonia (NH_3) and sulphur dioxide (SO_2) are important trace gases determining the alkalinizing and acidifying potential of the atmosphere, respectively. The uptake of SO_2 into fog droplets and subsequent oxidation into sulphate is an important process in the troposphere mainly for two reasons. First, it increases the acidity of the droplet, and second, the produced sulphate modifies the aerosol particle spectrum, when droplets evaporate after a fog event. As a consequence, the enhancement of the aerosol particle mass and the change in the chemical composition influences the conditions for cloud droplet formation (Wurzler et al., 2000, Chuang and Penner, 1995) and the radiative effect of the aerosol.

Aqueous phase chemical composition is generally measured by the mean concentration of the respective trace species and the concentration of the bulk water. Fog chemistry, however, is droplet size-dependent leading to differences in chemical composition and concentration (Bator and Collett, Jr., 1997, Noone et al., 1988). The impacts of the droplet size-dependence of the chemical composition on the sulphate production has been investigated in measurements (e.g., Rattigan et al., 2001, Rao and Collett, Jr., 1998, Collett, Jr. et al., 1994) and modeling studies (e.g., Bott, 1992).

11.1.1 Background

Ammonia and sulphur dioxide are the main gaseous precursors of ammonium (NH_4^+) and $S(IV) = SO_2 + HSO_3^- + SO_3^{2-}$ (sulphur of valence four), respectively. For pH values between 3 and 6, S(IV) is present as HSO_3^-, while SO_3^{2-} and SO_2 are dominant for pH > 7 and pH < 2, respectively (Seinfeld and Pandis, 1998). An important process in atmospheric chemistry is the oxidation of S(IV) to $S(VI) = H_2SO_4 + HSO_4^- + SO_4^{2-}$ (sulphur of valence six). The oxidation process is not only important for the acidification but also contributes to the production of aerosol particle mass (see Equation 5.11).

The main sources of ammonium and sulphate in a fog droplet are the dissociation of the aerosol particle, that served as condensation nucleus:

$$(NH_4)_2SO_4 \longleftrightarrow 2\,NH_4^+ + SO_4^{2-} \tag{R 11.1}$$

and the uptake of NH_3 and SO_2 from the gas phase:

$$NH_3 + H_2O \quad \longleftrightarrow \quad NH_4^+ + OH^- \tag{R 11.2}$$
$$SO_2 + H_2O \quad \longleftrightarrow \quad HSO_3^- + H^+ \tag{R 11.3}$$
$$HSO_3^- \quad \longleftrightarrow \quad SO_3^{2-} + H^+. \tag{R 11.4}$$
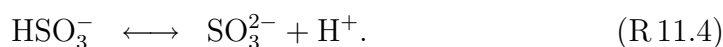
The major pathways of the S(IV) oxidation in the fog droplets are the aqueous phase reactions with hydrogen peroxide (H_2O_2) and ozone:

$$HSO_3^- + H_2O_2 + H^+ \quad \longrightarrow \quad HSO_4^- + H_2O + H^+ \tag{R 11.5}$$
$$HSO_3^- + O_3 \quad \longrightarrow \quad HSO_4^- + O_2 \tag{R 11.6}$$
$$HSO_4^- \quad \longleftrightarrow \quad SO_4^{2-} + H^+ \tag{R 11.7}$$
$$SO_3^{2-} + O_3 \quad \longrightarrow \quad SO_4^{2-} + O_2. \tag{R 11.8}$$
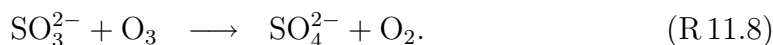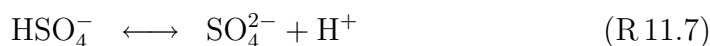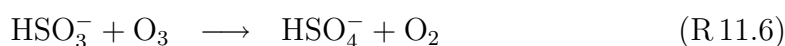
as well as the oxidation by iron(III).

As Reaction R 11.5 looses importance with rising pH, Reactions R 11.6 and R 11.8 become more important within neutral and alkaline solutions.

Additionally, the following reactions in which S(IV) builds a complex with a hydroxy alkyl compound take place within the liquid phase:

$$HSO_3^- + CH_2(OH)_2 \quad \longleftrightarrow \quad HMS^- + H_2O \tag{R 11.9}$$
$$SO_3^{2-} + CH_2(OH)_2 \quad \longleftrightarrow \quad HMS^- + OH^-. \tag{R 11.10}$$

Because of its low reactivity hydroxy methane sulphonate, HMS^-, is regarded as a reservoir species for S(IV) and therefore limits the S(VI) production.

11.1.2 Model Simulations

In this chapter, results of model simulations performed with the chemical-microphysical radiation fog model CHEMIFOG_V are presented. Environmental conditions have been chosen typical for a temperate deciduous forest of 22 m altitude in October. The initialization of the model parameters for the REFERENCE simulation has been described in Chapter 9. Radiation fog is present during nighttime, while leaf surface water on the vegetation surfaces is present from 16.00 on the first model day until the end of the simulation time. In Chapter 10 the main meteorological and microphysical features of the radiation fog event have been presented. The temporal development of the liquid water content and the mean radius of the three droplet size classes have already been discussed in Section 10.2.

While in CHEMIFOG_V the highly resolved two-dimensional particle size spectrum is used for the sophisticated description of the microphysical processes in a radiation fog, chemical reactions within the fog droplets are calculated within three size classes (see Equation 8.2).

In this section the dependence of the aqueous phase concentrations in the three size classes on the physico-chemical processes, especially the influence of the vegetation canopy, is investigated. The chemical composition of fog droplets is determined by the dissociating aerosol particle that serves as condensation nucleus, the species taken up from the gas phase, and aqueous phase chemical reactions within the droplets. While the initial aerosol composition of one size class is identical throughout the boundary layer, the atmospheric composition differs between the interstitial canopy air and the atmosphere above. It is significantly altered due to the presence of leaf surface water within the canopy that serves as an effective sink for soluble trace gases. Moreover, physical processes like condensation and evaporation as well as deposition and sedimentation modify the chemical composition within one size class. Additionally, turbulent mixing causes the vertical transport of droplets and therewith aqueous phase species. In CHEMIFOG_V these processes modify the chemical composition simultaneously. In the following the results of the REFERENCE model simulation are presented and the responsible processes are discussed.

11.2 Results

In this chapter the results of the REFERENCE model simulation for SO_4^{2-}, the dominant species of S(VI), and NH_4^+ are presented. Differences between the three droplets size classes and the two altitude regions within and above the vegetation
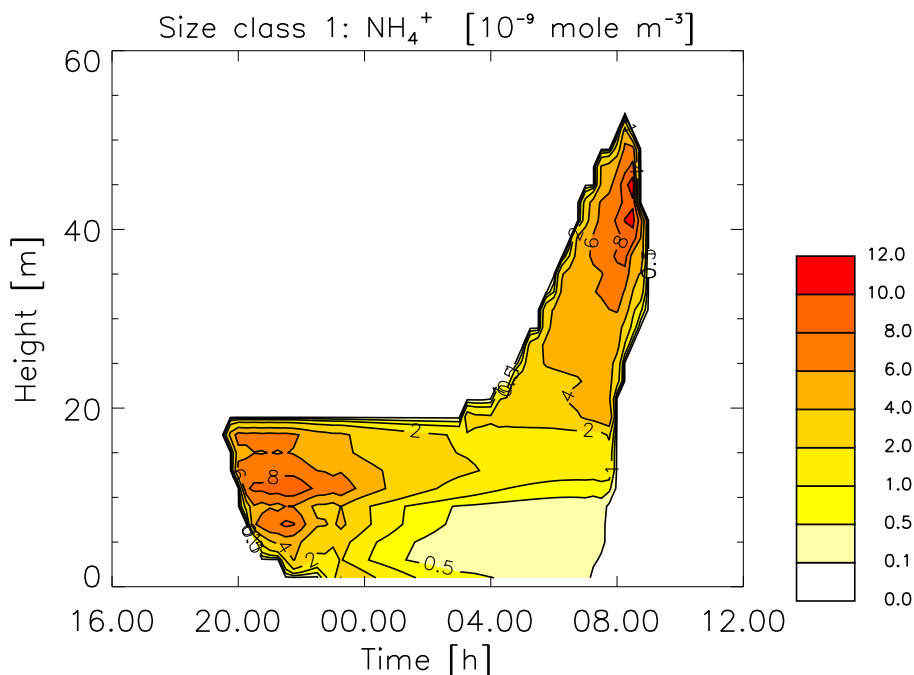
Figure 11.1: Aqueous phase concentration of ammonium in size class 1.

canopy are discussed. While S(IV) undergoes fast decomposition, HMS$^-$ is more stable. Therefore, S(IV) is used for the localization of the SO$_2$ uptake into the droplets, while HMS$^-$ traces the particle exchange between size classes due to condensation and evaporation. Moreover the pH values within the three droplet classes and the leaf surface water are presented.

11.2.1 Size-Dependent Aqueous Phase Chemical Composition of the Radiation Fog

Sulphate and Ammonium

In the following the differences in the NH$_4^+$, SO$_4^{2-}$, S(IV), and HMS$^-$ concentrations within the three size classes are presented and discussed. Special attention is given to the dependence of S(IV) oxidation on the vegetation canopy and the droplet size.

The concentration of ammonium and sulphate within the smallest size class is shown in Figures 11.1 and 11.2. Largest values are found within the canopy at the beginning of the fog event and at the top of the fog during the last hours of the fog event with maximum NH$_4^+$ values in the order of 10^{-8} mole m^{-3}. The signature of the temporal and spatial development is similar for both ions, while the concentration of NH$_4^+$ is approximately twice that of SO$_4^{2-}$. This indicates that

Figure 11.2: Aqueous phase concentration of sulphate in size class 1.

Figure 11.3: Aqueous phase concentration of S(IV) in size class 1.

Figure 11.4: Aqueous phase concentration of HMS^- in size class 1.

the main source of ammonium and sulphate in size class 1 is the dissociation of the particulate ammonium sulphate described in Reaction R 11.1 that yields two moles of ammonium and one mole of sulphate per mole dissociating ammonium sulphate. Within the canopy the ion concentration decreases with decreasing LWC, because particles grow into size class 2 as shown in Section 10.2. Above the canopy the maximum ion concentration is found at the top of the fog. The temporal decrease that is found in the LWC, however, is not reflected. This points to the conclusion, that particles of size class 2 reenter size class 1 due to evaporation. Uptake of gas phase ammonia and sulphur dioxide has no significant impact on the sulphate and ammonium concentration in the smallest size class.

Figure 11.3 shows the S(IV) concentration in size class 1. Within the canopy the uptake of S(IV) is largest when fog sets in. Above the canopy largest concentrations are found at the top of the fog during the mature stage. The S(IV) concentration shows a similar temporal and spatial decrease as the LWC. Figure 11.4 shows the concentration of HMS^- in the smallest size class. The concentration of HMS^- is two orders of magnitude larger than that of S(IV). Significant values are reached during the mature and dissipation stage. Two maxima develop above the vegetation canopy. Possible reasons for the maximum located at the top of the fog are the uptake of SO_2 to the first size class and subsequent reaction as well as the gain of chemical
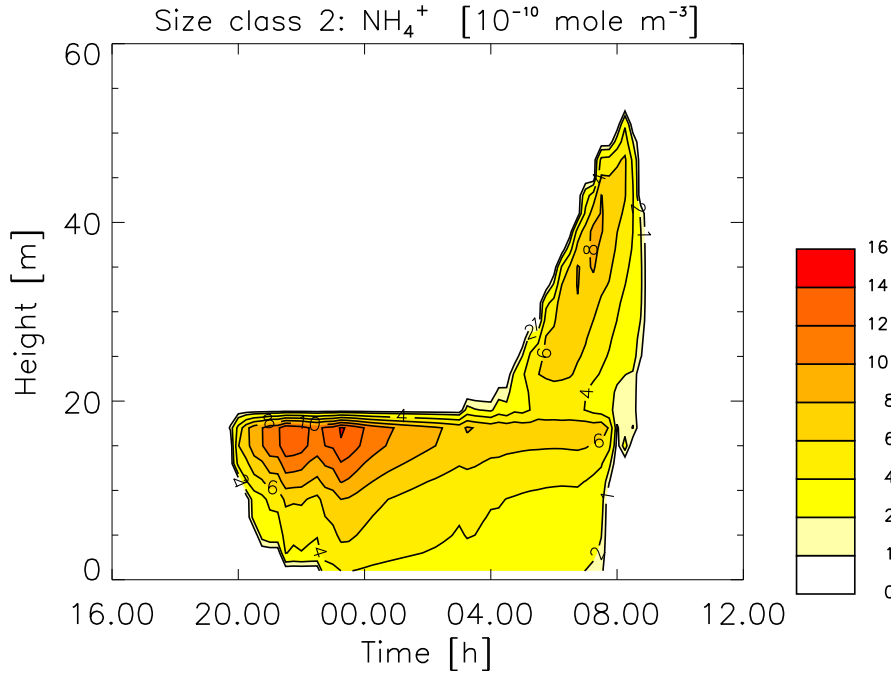
Figure 11.5: Aqueous phase concentration of ammonium in size class 2.

species from evaporating droplets that enter from the second size class. The second maximum is located right above the canopy at the end of the mature stage. This maximum is due to the evaporation of droplets of size class 2 that enter size class 1.

In size class 2 the signatures of the ammonium and sulphate concentration are similar within the canopy but differ significantly above the vegetation canopy as can be seen in Figures 11.5 and 11.6. Within the canopy, similar to size class 1, the concentration of ammonium is approximately doubled compared to sulphate, which points to the particulate origin, however, absolute values are one order of magnitude lower compared to size class 1. The concentration of SO_4^{2-} is slightly enhanced compared to NH_4^+, although the solubility of NH_3 is higher than that of SO_2. However, ambient gas phase concentrations within the canopy are influenced by the leaf surface water that has already effectively taken up gas phase ammonia. The temporal decrease in both concentrations is due to the increase in size and the subsequent loss of particles to the larger size class and due to deposition. Above the canopy, on the other hand, the concentration of ammonium is much larger than the concentration of sulphate. Consequently, uptake of gas phase ammonia significantly enhances the aqueous phase ammonium concentration. Overall, within the canopy the sulphate and ammonium concentrations are larger than above, where particles effectively grow into size class 3 and therefore no longer contribute to
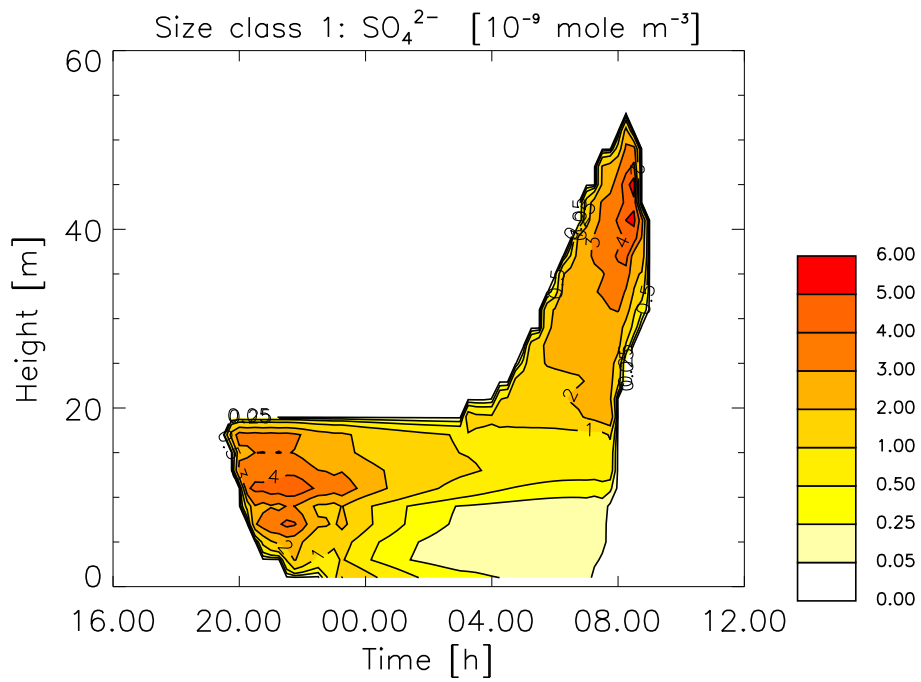
Figure 11.6: Aqueous phase concentration of sulphate in size class 2.
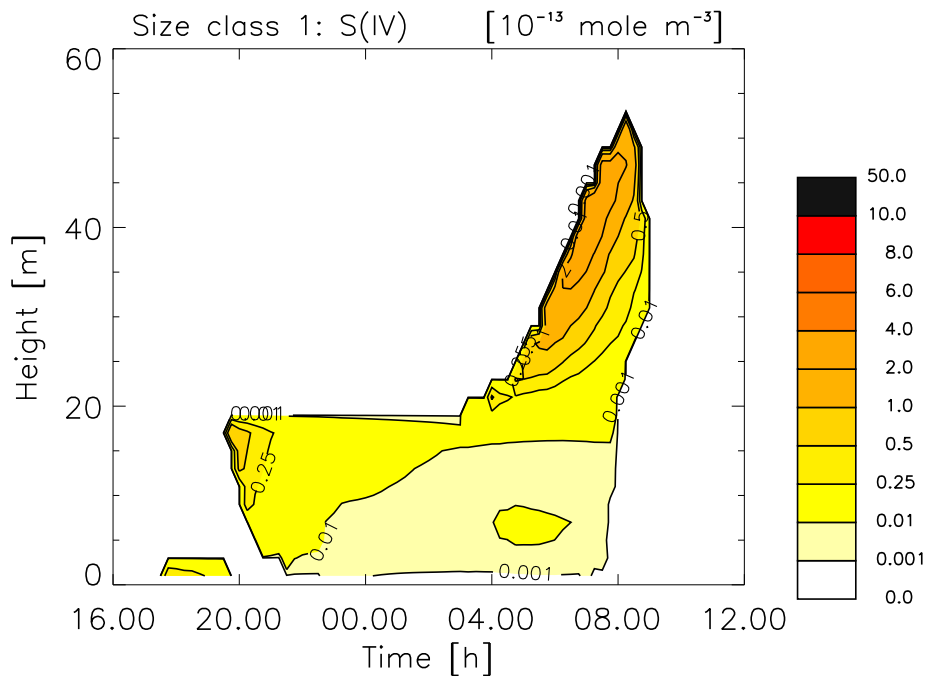

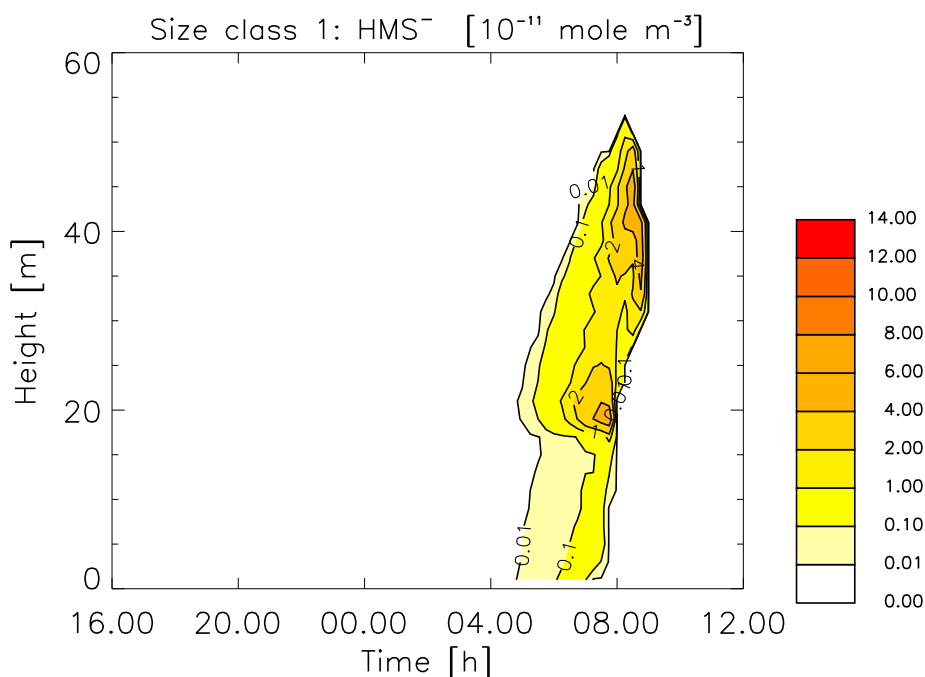Figure 11.7: Aqueous phase concentration of S(IV) in size class 2.
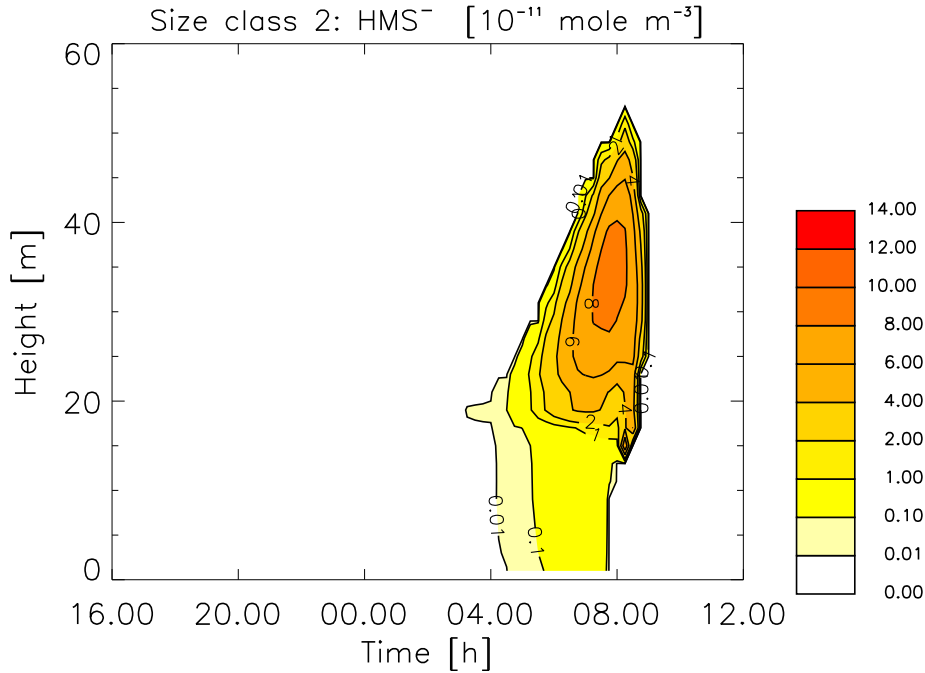
Figure 11.8: Aqueous phase concentration of HMS$^-$ in size class 2.

the sulphate and ammonium concentrations in size class 2. Figure 11.7 shows the S(IV) concentration in the second size class. Within the canopy concentrations are largest in the beginning of the fog event and decrease with time due to chemical decomposition and deposition. Above the canopy the uptake of S(IV) is largest above the canopy top in the beginning of the mature stage, when the maximum LWC is found in size class 2. The altitude of the maximum in S(IV) coincides with the maximum in HMS$^-$ found in size class 1 that is due to evaporating droplets of size class 2. The HMS$^-$ concentration of size class 2 is shown in Figure 11.8. While within the canopy HMS$^-$ concentrations are negligible, above the canopy the HMS$^-$ concentration is of the same order of magnitude as the S(VI) concentration indicating a significant uptake of S(IV) from the gas phase and potential of a significant S(IV) oxidation.

In size class 3 (see Figures 11.9 and 11.10) concentrations of ammonium and sulphate are small within the vegetation canopy, while above maximum values of more than $7 \cdot 10^{-10}$ mole m^{-3} NH$_4^+$ are reached. Hereby, ammonium concentrations are up to ten times larger than sulphate concentrations. The signature of the ion concentration reflects the temporal development of the LWC, indicating the continuous gain of particle mass from size class 2. The S(IV) concentration shown in Figure 11.11 is similarly linked to the LWC of the largest size class. Moreover, the
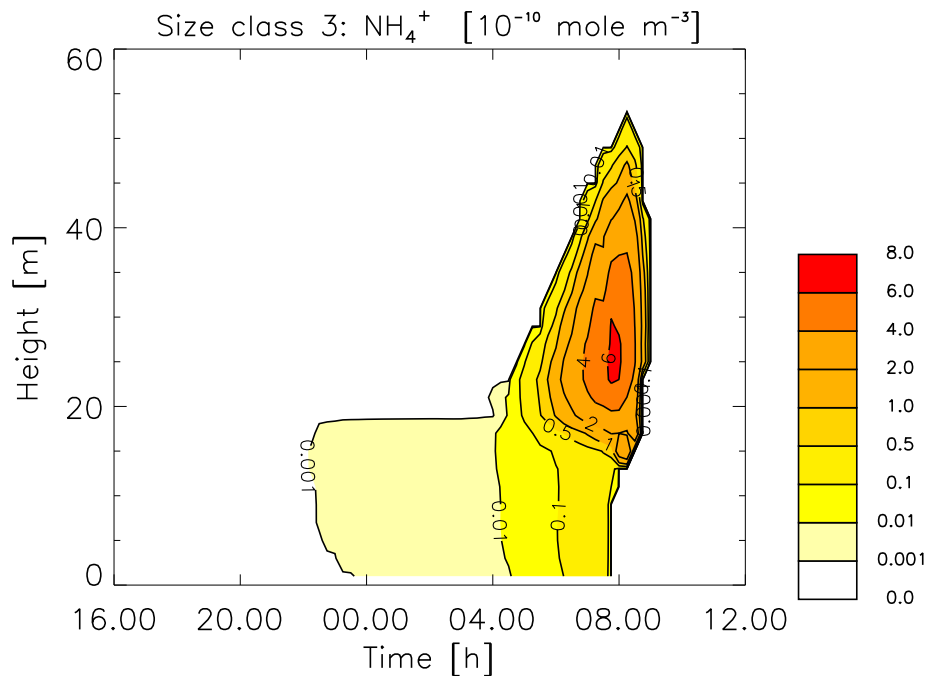
Figure 11.9: Aqueous phase concentration of ammonium in size class 3.
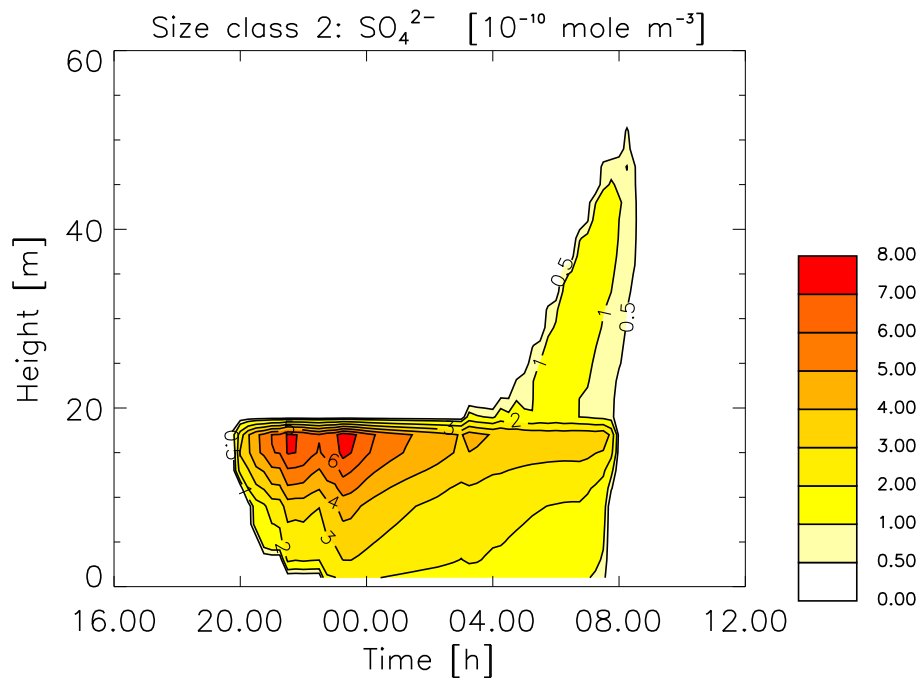

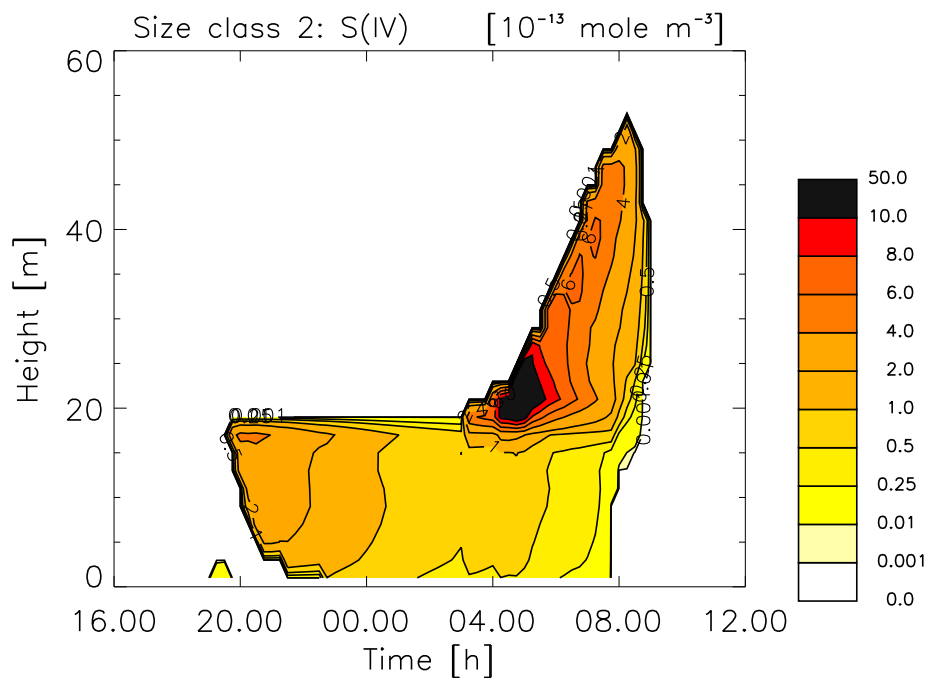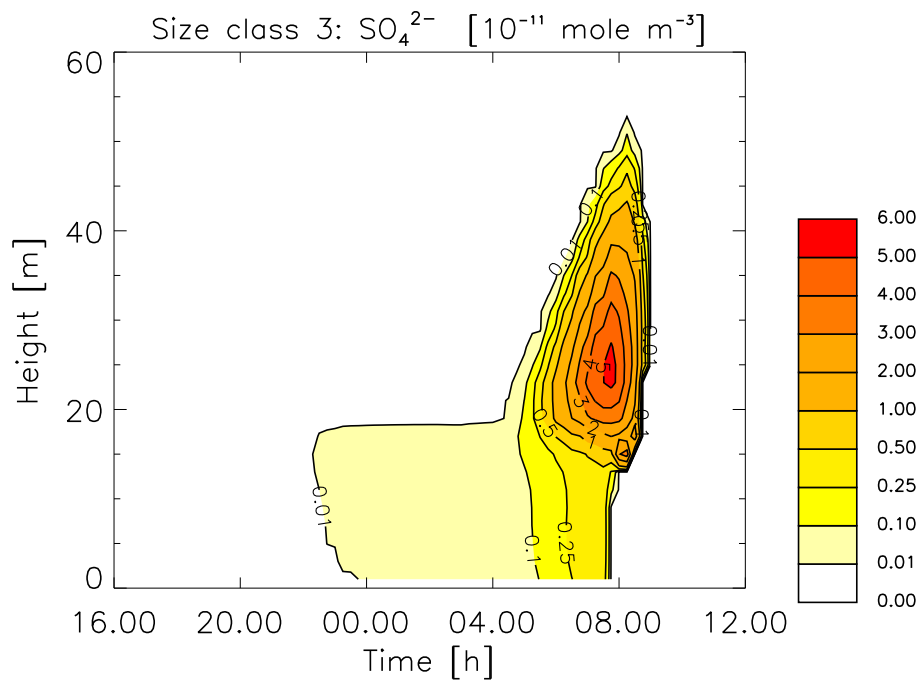Figure 11.10: Aqueous phase concentration of sulphate in size class 3.
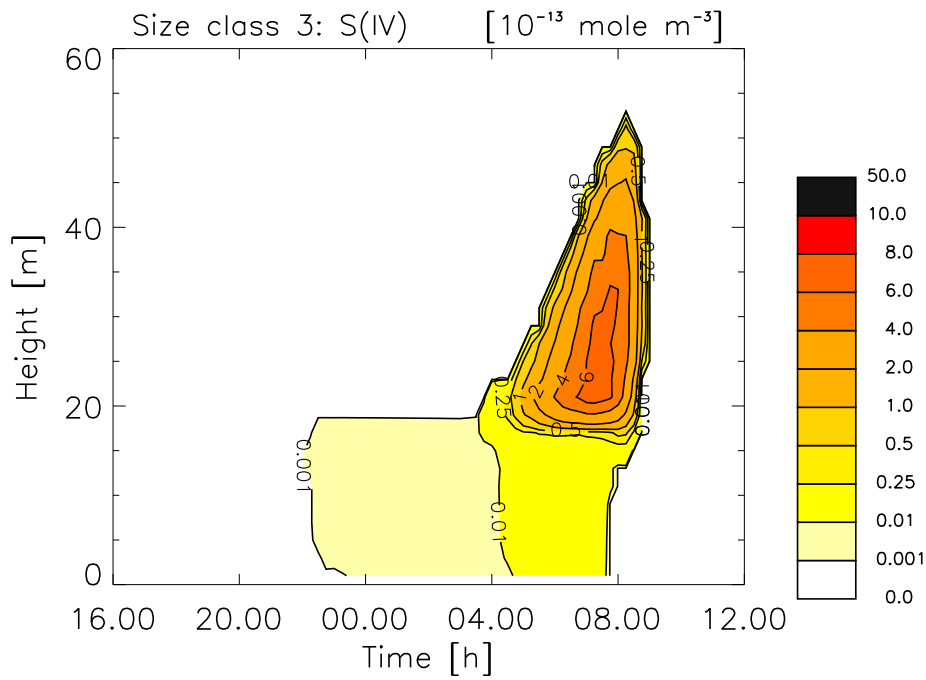
Figure 11.11: Aqueous phase concentration of S(IV) in size class 3.
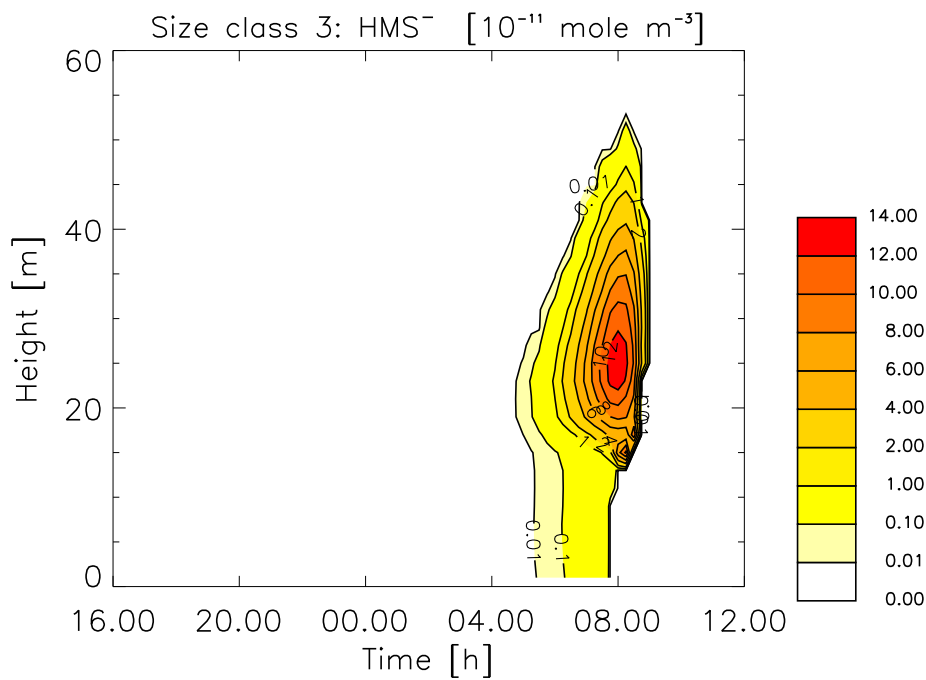
Figure 11.12: Aqueous phase concentration of HMS⁻ in size class 3.
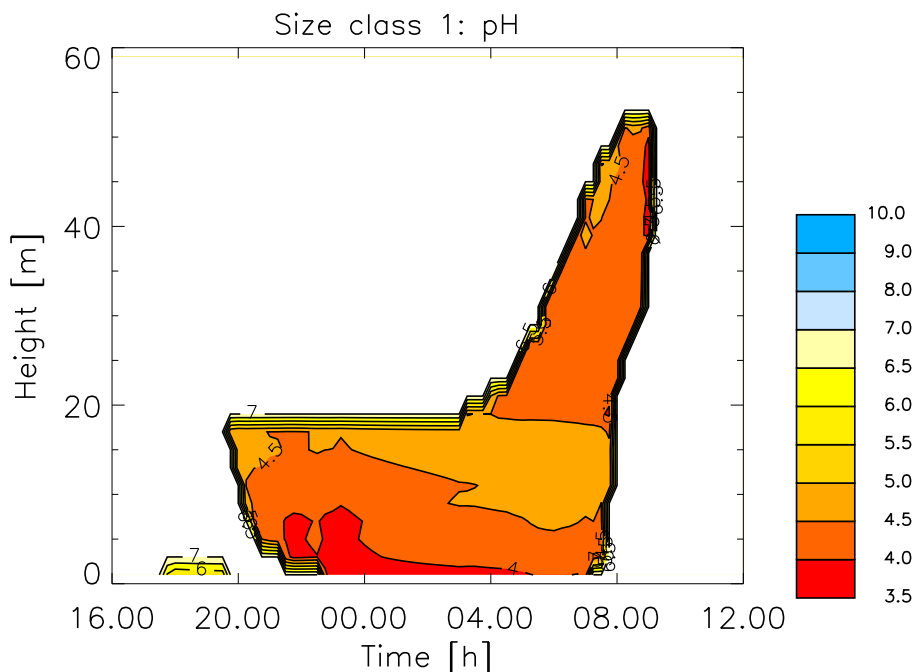
Figure 11.13: pH of the fog droplets in size class 1.

uptake of SO_2 from the gas phase is mostly limited to the altitude region above the canopy. Figure 11.12 shows the HMS^- concentration of the largest droplet size class. Highest values are found above the canopy. The maximum is found in 25 m altitude at 08.00 on the second model day. Besides the chemical production of HMS^- in size class 3, the growth of particles of size class 2 that have taken up SO_2 in the beginning of the mature stage is responsible for this maximum.

pH

Figures 11.13 to 11.15 show the pH[a] of the fog water in the three size classes. In size class 1 the pH varies between 3.5 and 5. Within the canopy pH increases with altitude and time, while above the canopy during the mature stage the pH stays rather constant between 4 and 4.5. In the second size class, pH lies between 5 and 6 within the canopy with increasing values with time. Above the canopy pH values are between 6 and 7 with slightly higher values at the top of the fog at the end of the mature stage. In size class 3 pH lies between 5 and 6.5 within the canopy during the whole simulation time, while above the canopy, pH reaches values between 7 and 8 and up to 10 at the top of the fog at the end of the mature stage. During the mature

---

[a]The strong gradients at the boundaries of the aqueous phase region are caused by the background value that is set to 7 and are, consequently, artificial.
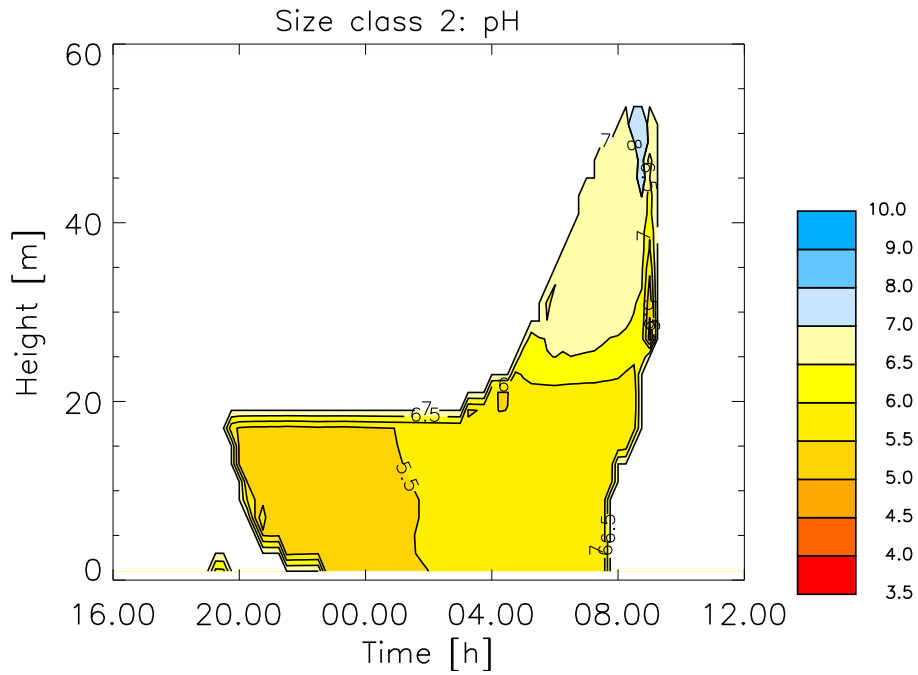
Figure 11.14: pH of the fog droplets in size class 2.
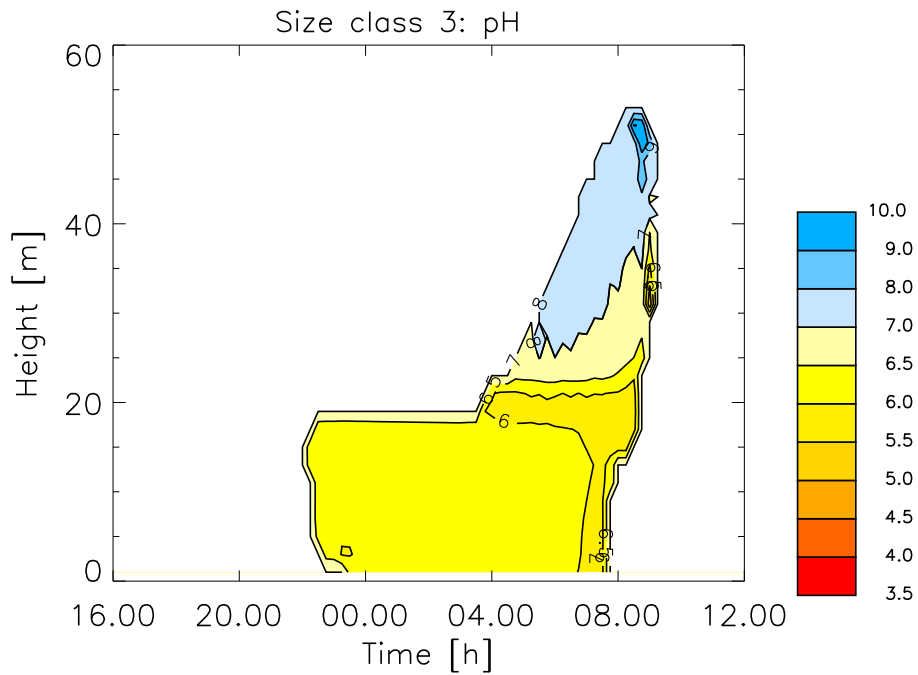
Figure 11.15: pH of the fog droplets in size class 3.
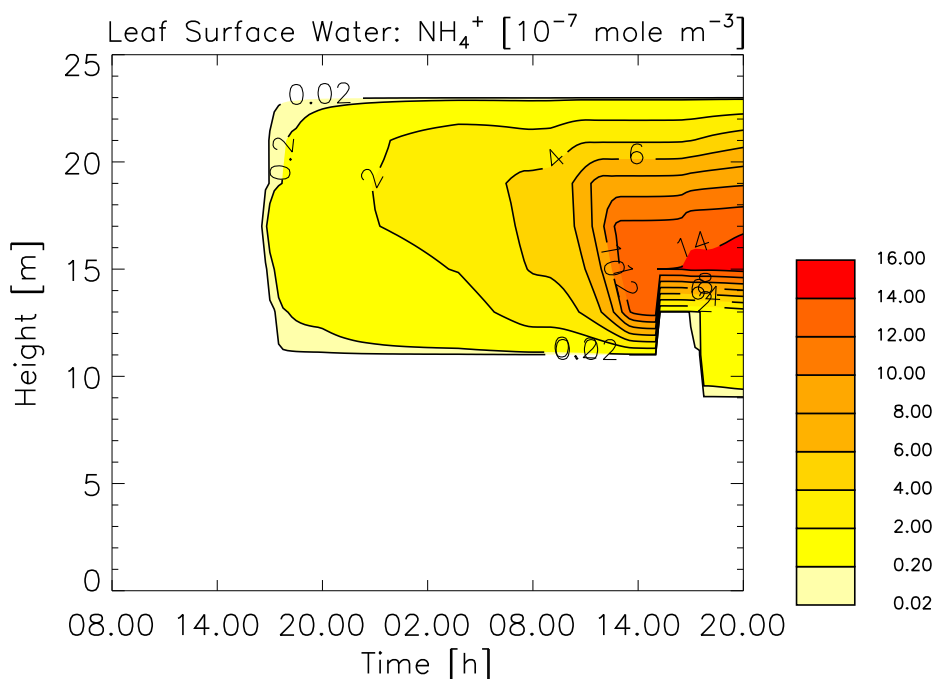
Figure 11.16: Aqueous phase concentration of ammonium in the leaf surface water.

stage the pH in size class 1 shows its maximum value within the upper part of the vegetation canopy, whereas in the two larger size classes the pH above the canopy is larger than within the canopy caused by the effective uptake of ammonia. Overall, the fog water in size class 3 is more alkaline than in size class 2, whereas the fog water in size class 1 is most acidic consistent with the findings of Collett, Jr. et al. (1994). Differences in pH between droplet size classes lead to a significant enhancement of the sulphur oxidation compared to bulk estimates (Collett, Jr. et al., 1994).

11.2.2 Aqueous Phase Chemical Composition within the Leaf Surface Water

Sulphate and Ammonium

While within the canopy the ammonium and sulphate concentrations in the fog droplets are determined by the aerosol particles, the leaf surface water takes up ammonia and sulphur dioxide from the atmosphere causing a significant decrease in their gas phase concentrations. Figures 11.16 and 11.17 show the concentrations of NH_4^+ and SO_4^{2-} in the leaf surface water. The ammonium concentration steadily rises due to the uptake of ammonia from the gas phase and the deposition of fog droplets contributing to the ion concentrations in the leaf surface water. The concentration
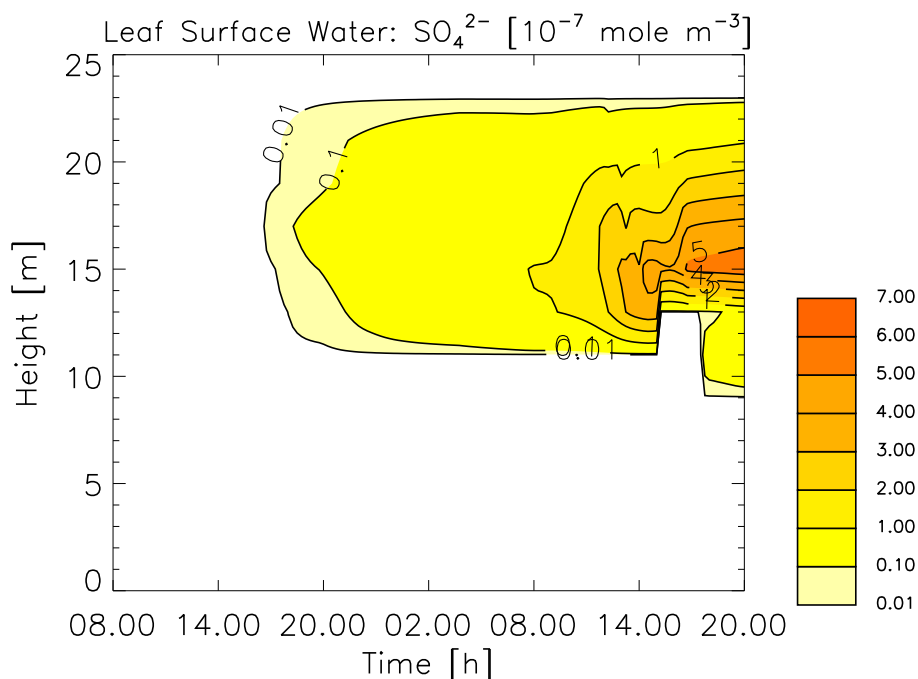
Figure 11.17: Aqueous phase concentration of sulphate in the leaf surface water.

of ammonium and sulphate in the leaf surface water are two orders of magnitude larger than within the fog droplets caused by both the longer lifetime of the leaf surface water and the subsequent accumulation of depositing species.

pH

The pH of the leaf surface water is presented in Figure 11.18[b]. From the beginning until approximately 12.00 on the second model day the pH mainly varies between 5 and 6. During the first hours slightly higher values are reached in the top layers of the leaf surface water. After 12.00 the pH value rapidly drops with a minimum value of 1.2 around 14.00. After approximately 17.00 the pH rises again to values between 4.5 and 5. The significant drop in pH is due to the fast evaporation of the leaf surface water as shown in Figure 10.6 leading to higher H^+ concentrations in the remaining water.

---

[b]Note the difference in the colour coding compared to Figures 11.13 to 11.15.
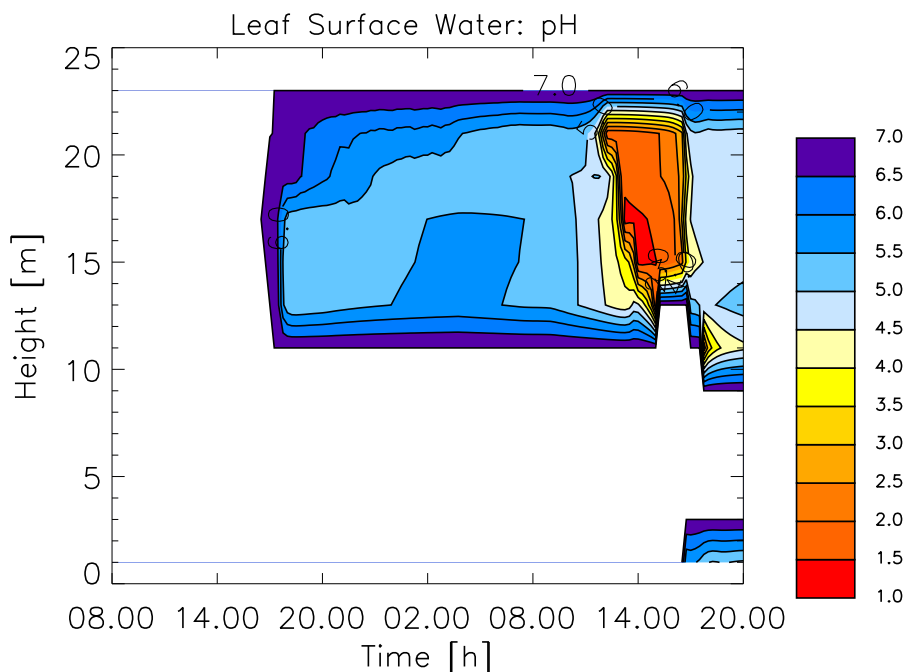
Figure 11.18: pH of the leaf surface water; maximum: 7.0, minimum: 1.2.

11.3 Summary and Discussion

Modeling studies on the drop size-dependence of sulphate and ammonium concentrations within the fog droplets of a radiation fog event have been presented. Focus has been given to the differences induced by the vegetation canopy. Simulations have been performed with the one-dimensional chemical-microphysical radiation fog model CHEMIFOG_V. Environmental conditions have been chosen typical for a temperate deciduous forest of 22 m altitude in October. Radiation fog is present during nighttime, while leaf surface water on the vegetation surfaces is present from 16.00 on the first model day until the end of the simulation time.

While the S(VI) concentrations in the size classes 1 and 2, i.e., for droplets with $r < 11.5\,\mu\text{m}$, are mainly governed by the dissociating aerosol particles in this model simulation, in size class 3 the uptake and subsequent oxidation of S(IV) contributes significantly to the concentration of S(VI).

The uptake of NH_3 and SO_2 into the fog droplets is low within the canopy, because the leaf surface water effectively reduces their atmospheric concentrations before fog sets in. Only in the second size class, significant S(IV) concentration are found indicating uptake of SO_2. Above the canopy, SO_2 uptake and S(IV) concentrations are also largest in the second size class.

The concentration of HMS^- has been used for tracing microphysical droplet

exchanges between the three size classes. The results show that the concentrations of sulphur compounds within fog droplets depends on the microphysical history of the droplet. Therefore, while determining S(VI) oxidation rates from size-dependent measurements, one has to consider the temporal stage of the fog event and the microphysical history of the sampled droplets.

pH values are found to rise with droplet size in agreement with the findings of Collett, Jr. et al. (1994). Moreover, large differences in pH are found between the altitude regions within and above the canopy. Above the canopy pH values are much higher in the two larger size classes due to the effective uptake of ammonia. As the drop size-dependence of the pH within one fog event modifies sulphate production compared to bulk estimates (Collett, Jr. et al., 1994), also spatial variations influence the overall sulphate production.

In the leaf surface water concentrations of ammonium and sulphate are determined by both the uptake from the gas phase and subsequent chemical reactions and the deposition of fog droplets to the vegetation surfaces. Concentrations are two orders of magnitude higher than within the fog droplets due to the longer lifetime of leaf surface water and the accumulation of the deposits. Leaf surface water, consequently, provides a water pool for multi-phase chemical processes which is potentially important for chemical processes within a vegetation canopy.

pH values of the leaf surface water lie mainly between 4.5 and 6.5. When the evaporation of most of the leaf surface water leads to low concentrations of water, i.e., between 12.00 and 17.00 on the second model day, however, pH drops to 1.2 in minimum and increases again when the leaf surface water content increases.

Overall, this study has shown, that size-dependent differences in sulphate concentrations in radiation fog droplets are not necessarily due to the differences in the uptake of S(IV) and subsequent oxidation within the fog droplets. In addition, evaporation and condensation cause the exchange of sulphur species between the size classes. Therefore the temporal development of the size-dependence of sulphur contents is an important parameter that has to be considered in future studies. Moreover, the influence of leaf surface water on the gas phase concentrations of ammonia and sulphur dioxide and the connected influence on the aqueous phase concentrations of ammonium and sulphate in the fog droplets is not negligible.

Chapter 12

The Impact of Leaf Surface Chemistry on the Dry Deposition Flux of NH_3 to a Vegetation Canopy

Abstract. The impact of chemical reactions in leaf surface water on the dry deposition flux of NH_3 to vegetation surfaces is investigated in sensitivity studies. Simulations are performed with the one-dimensional chemical-microphysical model CHEMIFOG_V designed to study radiation fog events in a forest environment. The vegetation is represented by a detailed module with a height-resolved grid spacing of $2\,m$. Chemical reactions are simulated in the fog droplets as well as in the leaf surface water. NH_3 dry deposition onto wet leaf surfaces is incorporated into the multiphase chemical model and calculated according to interfacial mass transfer. In two sensitivity studies, first, the chemical reactions within the leaf surface water were omitted and second, the dry deposition to wet surfaces was calculated according to the resistance approach. Due to chemical reactions within the leaf surface water, NH_3 deposition in the REFERENCE model simulation was most effective. Only few NH_3 was released within the modeling time interval, as the leaf surface water did not evaporate sufficiently. Omitting the chemical reactions within the leaf surface water leads to unrealistic low deposition rates, because the solution is about in equilibrium over the whole period allowing both deposition and emission fluxes. The different treatment of dry deposition leads to significant differences in the boundary layer ammonia concentration after turbulent mixing on the second model day in the order of 15 to $50\,\%$.

12.1   Introduction

Reduced nitrogen, NH$_x$, i.e., ammonia (NH$_3$) and ammonium (NH$_4^+$), contributes more than half of the total nitrogen input to European ecosystems (Asman, 2001, RGAR, 1997). The input of NH$_x$ to both land and sea surfaces is of great importance for the ecosystems. Excessive deposition of NH$_x$ to land surfaces might result in a change in abundant plant species, whereby nitrogen input to sea water enhances the growth of algae with subsequent effects on the marine flora and fauna. NH$_x$ deposition to the soil might lead to a nitrification with effects on the vegetation (Asman, 2001). Additionally, NH$_3$ is the most abundant base in the atmosphere having the potential to neutralize acids in precipitation and fog. To quantify the input of reduced nitrogen the dependence of ammonia dry deposition on the surface properties has to be considered (see e.g., Spindler et al., 2001). The deposition velocity of ammonia to the canopy is highly dependent on the leaf wetness. Leaf surface water reduces the deposition resistance to soluble gases. Moreover chemical reactions inside the leaf surface water buffer the alkalinizing effect of NH$_3$. As long as the leaf surface water pool is large enough, deposition of NH$_3$ is retained. During evaporation of the water, NH$_3$ is reemitted to the atmosphere from supersaturated solutions. Moreover, NH$_4^+$ and SO$_4^{2-}$ form ammonium sulphate that remains on the dry leaf surfaces after complete evaporation.

Several approaches have been used to simulate the dry deposition fluxes of NH$_3$. The most general approach to dry deposition are the canopy resistance models (e.g., Ganzeveld and Lelieveld, 1995, Erisman et al., 1994), which assume zero concentration of the trace species at the surface and can therefore only simulate monodirectional deposition fluxes. The compensation point models (e.g., Nemitz et al., 2001, Sutton et al., 1995) allow for bi-directional fluxes assuming a non-zero surface concentration. This approach leads to the emission of NH$_3$, when the NH$_3$ concentration in the ambient air falls below a certain concentration, the so-called compensation point. However, no dependence on the surface properties can be expressed with a constant compensation point. Flechard et al. (1999) presented a dynamic canopy compensation point model. Besides the use of both a stomatal compensation point and cuticular absorption/desorption, a dynamic leaf surface water chemistry module to simulate epicuticular fluxes is implemented. Leaf surface chemistry is performed for a few trace gases only, using the Henry equilibrium. Activity coefficients are taken into account for highly concentrated solutions. In long-term estimates of the dry deposition of ammonia over a moorland Flechard et al. (1999) found a 30% overestimate by the resistance model, whereas the static and dynamic

compensation models represented measurements within 10% accuracy.

In this chapter a sophisticated approach of the leaf surface chemistry embedded in a complex dynamic model is presented. While the dry deposition to dry surfaces is calculated with a resistance model the dry deposition to wet surfaces is simulated according to the formulation of the mass transfer between the gaseous and aqueous phase of Schwartz (1986). Additionally, within the leaf surface water the complete aqueous phase chemistry mechanism CAPRAM2.3 (Ervens, 2001, Herrmann et al., 2000) is applied. Therefore co-deposition of alkaline and acidic species can be considered in detail. Moreover, the model produces both time and height resolved deposition fluxes under given environmental conditions. Not included in the model are both the epicuticular fluxes between the leaf surface water and the leaf's interior, and chemical reactions in the leaf apoplast. As the relative humidity is always above the deliquescence point in the simulations of the radiation fog event the build-up of salts can be omitted in this study.

12.1.1 Model Simulations

To investigate the dependence of NH_3 dry deposition fluxes on the leaf wetness and the chemical processes in the leaf surface water, three different model simulations were performed. The development of the radiation fog and the leaf surface water is identical in all simulations and has been shown in Figures 10.5 and 10.6. The thermodynamic and radiative parameters are given in Chapter 10. Model initialization is presented in Chapter 9.2. The only difference between the three studies is the treatment of the dry deposition to the moist vegetation surfaces.

The REFERENCE model simulation has been described in detail in Chapter 10. Within this model simulation the newly developed, sophisticated dry deposition module presented in Section 7.5.1 is used. While the dry deposition to dry surfaces is calculated with a modified version of the treatment by Ganzeveld and Lelieveld (1995) (see Section 7.2.1), the dry deposition to wet surfaces is simulated according to the interfacial mass transfer according to Schwartz (1986). Additionally, within the leaf surface water the chemical reaction scheme presented in Section 7.5 is applied. This allows the consideration of the buffering effect on the depostion fluxes due to the consumption of species by chemical reactions retaining the concentration gradient between the atmosphere and the leaf surface water.

In the UPTAKE model simulation the dry deposition to wet surfaces is simulated according to the mass transfer theory, but without subsequent chemical reactions in the aqueous phase. The dry deposition on dry surfaces is calculated with a modified
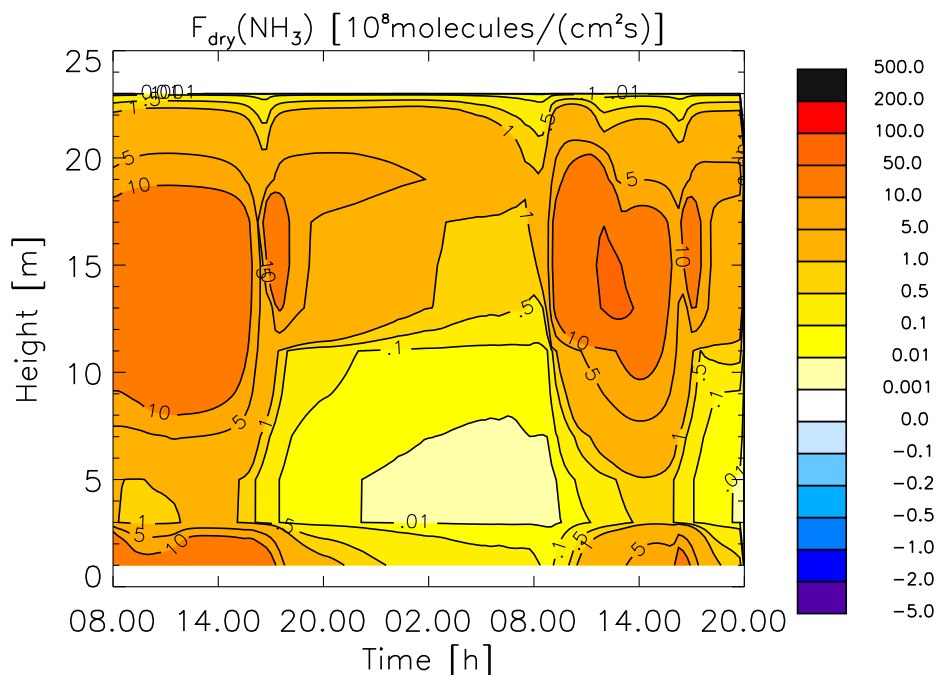
Figure 12.1: Dry deposition flux of NH$_3$ (RESISTANCE).

version of Ganzeveld and Lelieveld (1995). Also in this approach bi-directional fluxes between the leaf surface water and the atmosphere can be considered.

The RESISTANCE model simulation includes a dry depostion scheme based on Ganzeveld and Lelieveld (1995), where both the dry deposition to dry and to wet surfaces are calculated via a resistance approach. The resistance of the wet plant surface to NH$_3$ is $188 \, \mathrm{s \, m^{-1}}$, while the dry deposition of NH$_3$ to dry vegetation surfaces is mainly governed by the stomatal uptake. With this approach only mono-directional fluxes can be simulated.

12.2   Results

Figure 12.1 shows the dry deposition flux of NH$_3$ for the RESISTANCE model simulation. During the daytime dry deposition of NH$_3$ is mainly determined by the stomatal conductance. Maximum deposition fluxes occur in the crown area of the canopy, where the largest surface area is provided, and to the ground. During nighttime the deposition flux is reduced below $12 \, \mathrm{m}$ altitude, because the stomata are closed and the atmospheric concentration of NH$_3$ is small as NH$_3$ has been taken up by the fog droplets or deposited. The larger deposition within the crown area compared to below is due to the coverage with leaf surface water, that reduces
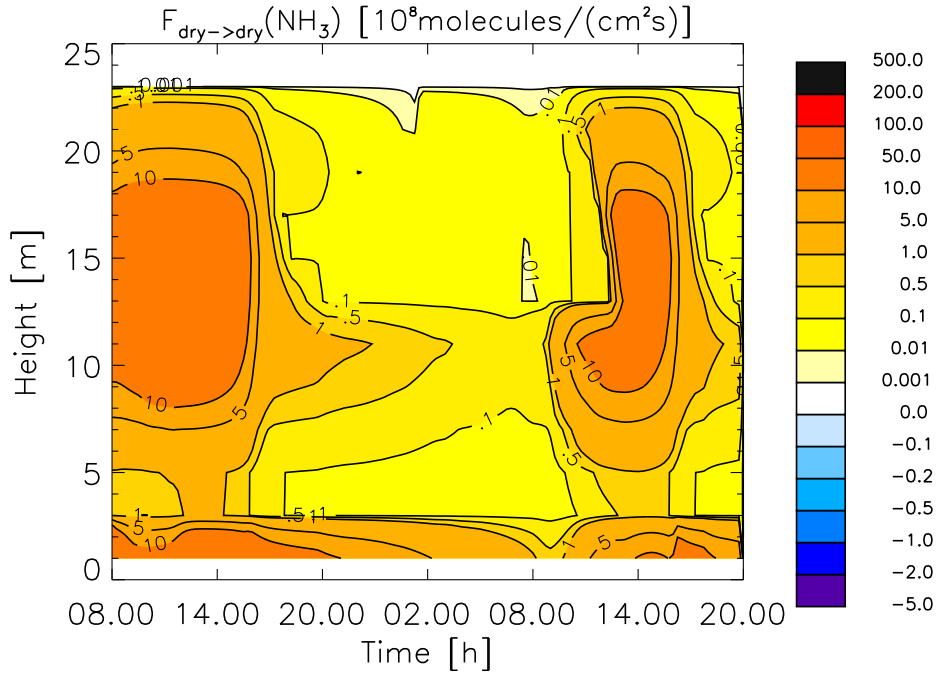
Figure 12.2: Dry deposition flux of NH_3 to dry surfaces (UPTAKE).

the canopy resistance to the soluble trace gases in the atmosphere. After sunrise the fog droplets evaporate and release NH_3 again providing a source for deposition. Additionally, NH_3 is transported into the canopy by turbulence. Subsequently, at 08.00 on the second model day the dry deposition flux increases. The pattern of the contours is due to both the stomatal deposition pathway similar to the first model day and the layers, where the leaves are covered by dew and fog water. Maximum deposition rates are in the order of 10^9 to 10^{10} molecules $cm^{-2} s^{-1}$.

Figures 12.2 and 12.3 show the results for the dry deposition flux of NH_3 in the UPTAKE model run. Here the deposition flux is divided into the flux to dry surfaces, $F_{dry \rightarrow dry}$ as determined with the resistance approach, and the flux to moist surfaces $F_{dry \rightarrow moist}$, that is calculated according to the mass transfer theory. The results for $F_{dry \rightarrow dry}$ are similar to the RESISTANCE model run. However, as only dry surfaces are regarded in this approach, $F_{dry \rightarrow dry}$ is reduced in the layers, where the leaf surface water is located. The deposition to wet surfaces is bi-directional in the UPTAKE model simulation as shown in Figure 12.3. In the beginning NH_3 is taken up by the leaf surface water until it is saturated. Due to the decrease of the NH_3 concentration in the ambient air NH_3 is reemitted from the leaf surface water between approximately 02.00 and 08.00 on the second model day. Around 08.00 the air concentration of NH_3 rapidly increases due to both the release of
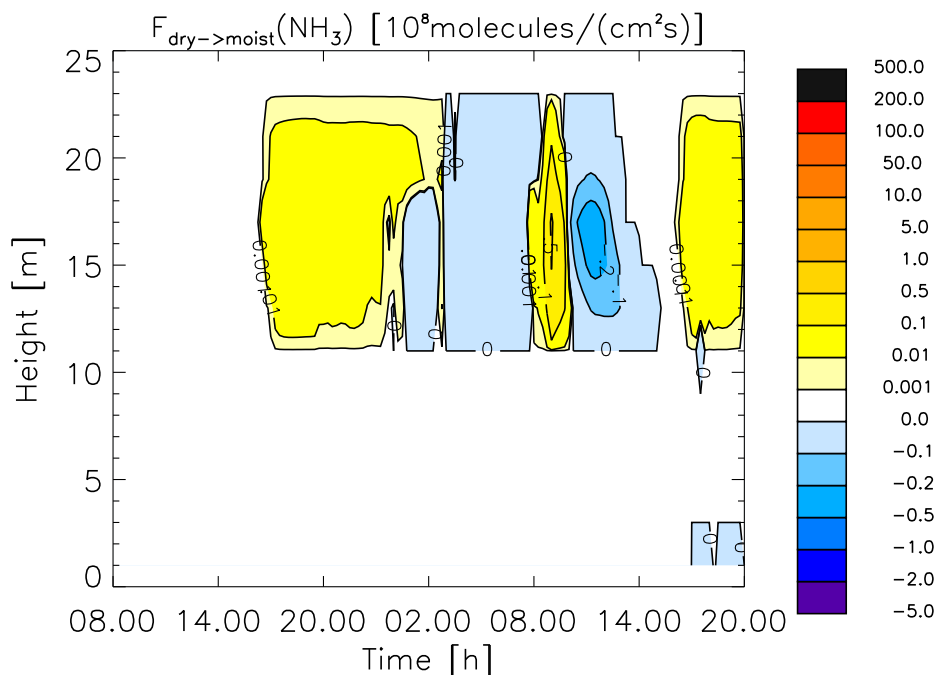
Figure 12.3: Dry deposition flux of NH$_3$ to moist surfaces (UPTAKE).

NH$_3$ from evaporating fog droplets and turbulent intrusion of NH$_3$ from above the canopy leading to an uptake of NH$_3$ to the leaf surface water again. When the leaf surface water evaporates, NH$_3$ is again released from the leaf surface water. The absolute values of $F_{dry \to moist}$ are, however, small compared to $F_{dry \to dry}$. In total, consequently, the UPTAKE approach leads to significantly lower deposition fluxes than the resistance approach of the RESISTANCE model simulations.

In Figures 12.4 and 12.5 the results for the REFERENCE model simulation are presented. The results for $F_{dry \to dry}$ have the same pattern as in the UPTAKE model simulation. The values are, however, slightly lower, because the air concentration of NH$_3$ is reduced in the REFERENCE simulation. This reduction is caused by the efficient uptake of NH$_3$ by the leaf surface water as shown in Figure 12.5. From the beginning until 08.00 on the second model day $F_{dry \to moist}$ is in the same order of magnitude as F_{dry} of the RESISTANCE simulation presented in Figure 12.1. When the NH$_3$ concentrations increase due to both the release of NH$_3$ from the evaporating fog droplets and the turbulent transport of boundary layer air masses into the canopy after sunrise, the deposition flux increases to values of more than 10^{10} molecules cm^{-2} s^{-1}. As in the presented model simulation the leaf surface water does not evaporate completely and the solution is rather acidic, only partly small reemission fluxes are observed. After sunset at 17.00 on the second model day the
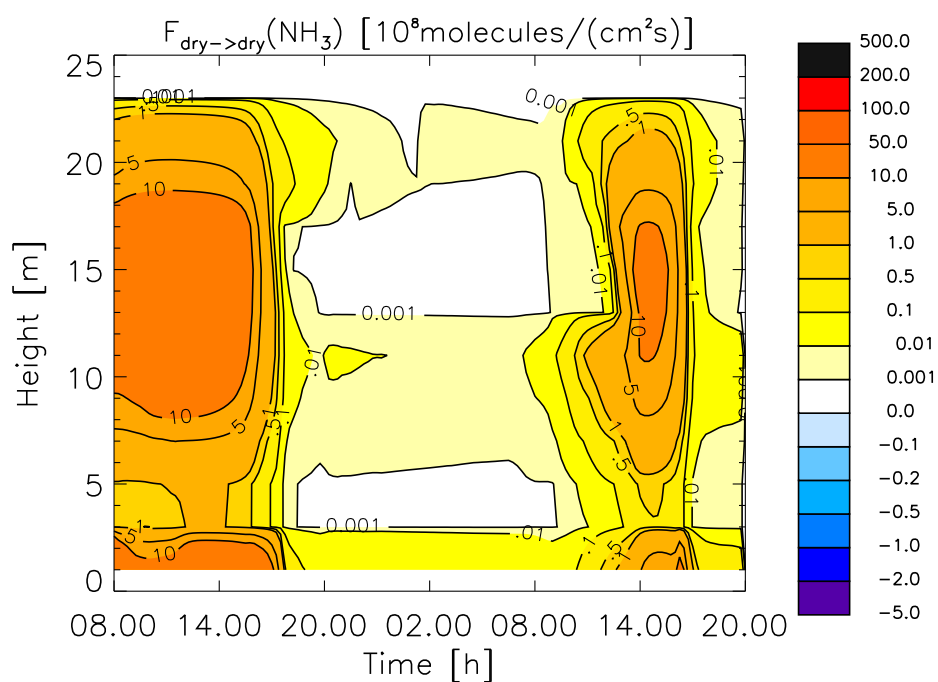
Figure 12.4: Dry deposition flux of NH₃ to dry surfaces (REFERENCE).
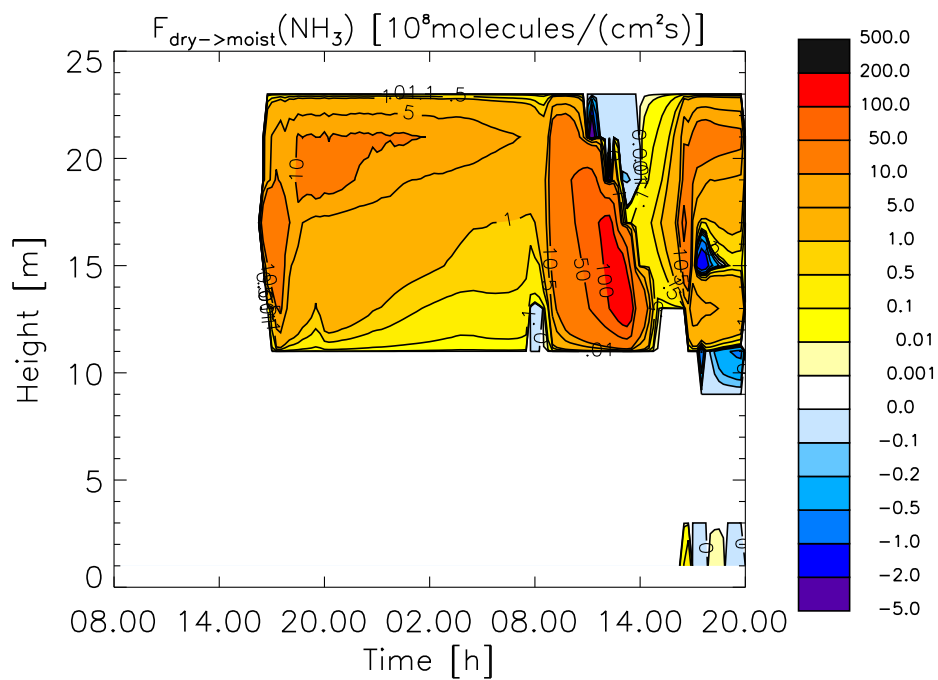
Figure 12.5: Dry deposition flux of NH₃ to moist surfaces (REFERENCE).
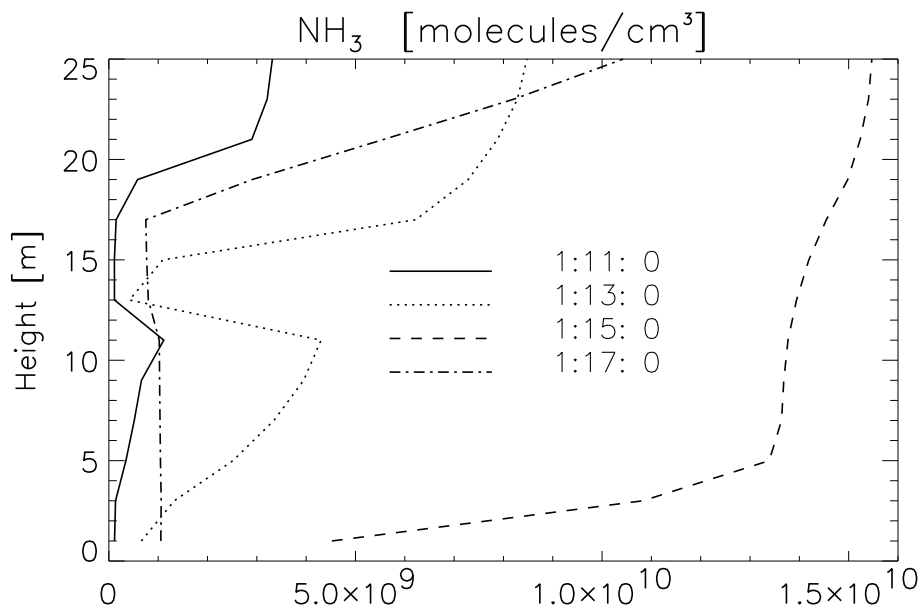
Figure 12.6: Vertical profiles of the NH$_3$ concentration for four different times (REF-ERENCE).

leaf surface water mass increases and radiation fog develops again. As a consequence, in the upper layers of the leaf surface water the deposition flux is slightly enhanced like on the first model day. However, between 14 m and 16 m, where the highest deposition flux occured, reemission of NH$_3$ with values more than one order of magnitude smaller than the deposition fluxes is observed. The increase in the uptake by wet leaf surfaces in the REFERENCE simulation compared to the UP-TAKE simulation is caused by taking chemical reactions into account buffering of the alkalinizing effect of NH$_3$ by the acidic solution:

$$\mathrm{NH}_3^{gas} \quad \longleftrightarrow \quad \mathrm{NH}_3^{aqua} \tag{R 12.1}$$

$$\mathrm{NH}_3^{aqua} + \mathrm{H}_2\mathrm{O} \quad \longleftrightarrow \quad \mathrm{NH}_4^+ + \mathrm{OH}^-. \tag{R 12.2}$$
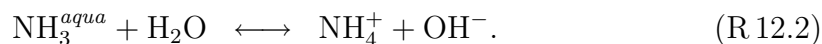
Consequently, the Equilibrium R 12.2 is shifted to the protonated form and further uptake of NH$_3^{gas}$ (Reaction R 12.1) is possible. When the leaf surface water evaporates, NH$_3^{aqua}$ is released again, if the saturation of the solution is exceeded.

Figure 12.6 shows four vertical profiles of gaseous NH$_3$ at different times of the second model day during the model simulation. At 11.00 and 13.00 leaf surface water is present within the crown area, while the fog droplets have evaporated and turbulent mixing propagates through the forest. The minima within the crown area
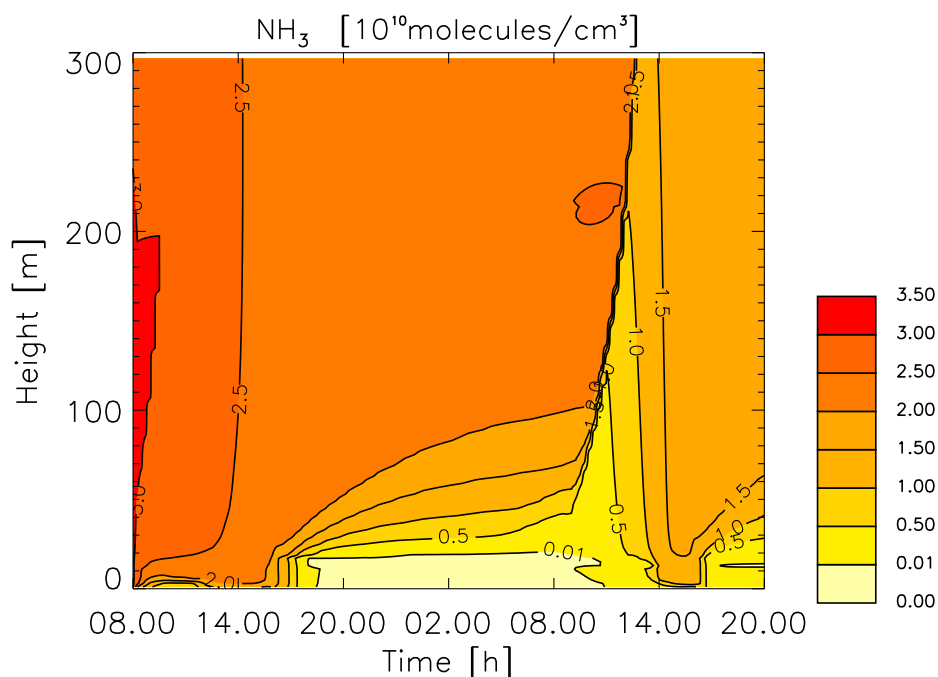
Figure 12.7: NH$_3$ concentration in the lowest 300 m (REFERENCE).

are due to the effective uptake of ammonia by the leaf surface water. Evaporation of the fog droplets has released some NH$_3$ in the lower vegetation layers and intrusion from the boundary layer has transported NH$_3$ into the canopy, but concentration is still low, because the leaf surface water takes up NH$_3$ efficiently. At 15.00 most of the leaf surface water has evaporated. Due to the reduced uptake capacity the concentration of ammonia within the canopy has increased. At 17.00 the second radiation fog event has started and the leaf surface water has recovered leading to the large reduction of NH$_3$ within the canopy. Figure 12.6 shows, that the vertical profile of the NH$_3$ concentration is highly variable with time and altitude in the presented study. Therefore not only the treatment of the uptake of ammonia into the aqueous phase is a crucial parameter for ammonia deposition, but also the ammonia concentration at the surface is highly variable due to dynamical and chemical processes. As depostion rates depend on the surface concentration, this study highlightens the need for an accurate height-resolved dynamical model to calculate deposition rates in detail.

The temporal development of the atmospheric NH$_3$ concentration in the lowest 300 m simulated with the REFERENCE model configuration is presented in Figure 12.7. NH$_3$ is slightly reduced during daytime due to dry deposition onto dry surfaces. After sunset radiation fog as well as leaf surface water build which efficiently take up
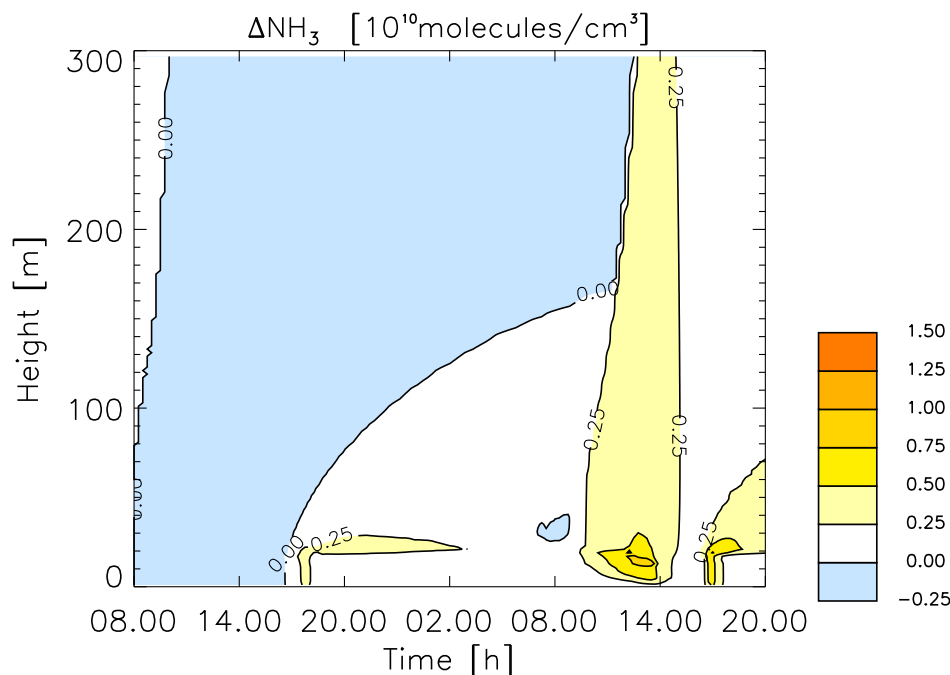
Figure 12.8: Differences in NH$_3$ in RESISTANCE compared to REFERENCE.

the atmospheric NH$_3$. Within the canopy the NH$_3$ concentration is reduced to nearly zero. The rising concentration of NH$_3$ within the canopy after sunrise in the morning of the second model day is due to the release of NH$_3$ from evaporating fog droplets and turbulent transport from higher altitudes. The local minimum induced by the leaf surface water that has already been explained in Figure 12.6 is again visible here. Turbulent transport leads to the outflow of air masses from the vegetation canopy that are reduced in ammonia. This results in a reduction of NH$_3$ in the boundary layer from about $3 \cdot 10^{10}$ molecules cm^{-3} to below $1.5 \cdot 10^{10}$ molecules cm^{-3}.

Figures 12.9 and 12.8 show the absolute differences between the two model runs UPTAKE respective RESISTANCE to the results of the REFERENCE model run presented in Figure 12.7. In the first hours differences only occur in the RESIS-TANCE simulation. Here, slightly smaller concentrations of ammonia are calculated than in the REFERENCE model simulation. This difference is due to the dry deposition of NH$_3$ to wet surfaces, that is regarded in RESISTANCE during the whole simulation time, whereas in the REFERENCE and UPTAKE model simulations, for numerical reasons, dry deposition to wet surfaces is not taken into account as long as the leaf surface water has not increased above the critical value of 10^{-7} l m^{-3}. Major differences occur above and within the canopy, especially during the setting-in of turbulence after 08.00 on the second model day. The NH$_3$ concentration in
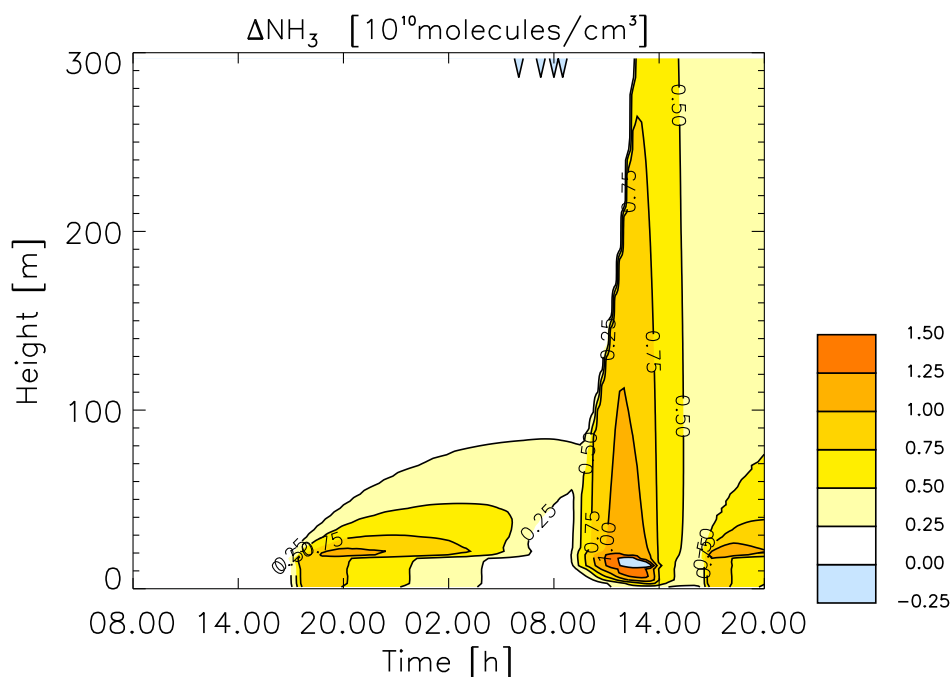
Figure 12.9: Differences in NH_3 in UPTAKE compared to REFERENCE.

both the UPTAKE and the RESISTANCE model simulation is larger than in the REFERENCE model simulation due to the differences in the dry deposition rate as shown before. After the radiation fog event the NH_3 concentration in the well-mixed boundary layer is enhanced by 0.5 to $0.75 \cdot 10^{10}$ molecules cm^{-3} in the UPTAKE run compared to the REFERENCE simulation. In the RESISTANCE run only a slight enhancement of 0.25 to $0.5 \cdot 10^{10}$ molecules cm^{-3} is observed after turbulent mixing of the boundary layer. This points to the importance of detailed simulations of deposition processes to vegetation in PBL studies.

12.3   Summary and Discussion

A model study on the dependence of dry deposition of NH_3 to vegetation surfaces on leaf wetness and chemical processes in the leaf surface water was presented. The studies were performed with a one-dimensional chemical-microphysical radiation fog model that includes a height-resolved vegetation module. Three sensitivity studies were presented in order to investigate different approaches to describe dry deposition to wet surfaces, a resistance model (RESISTANCE), uptake according to the mass transfer theory (UPTAKE), and a model including dynamic leaf surface chemistry (REFERENCE). The dry deposition flux of ammonia was smallest in the UPTAKE

simulation, because the leaf surface water changed between super- and subsaturation with respect to NH$_3$ during the whole period. The REFERENCE model simulation yielded the highest deposition fluxes, because the dissociation of ammonia favoured the further uptake of NH$_3$ from the gas phase. The RESISTANCE approach yielded similar results as the REFERENCE simulation, although only one-directional fluxes can be simulated. In contrast to the RESISTANCE approach, however, the temporal behaviour of the deposition flux as influenced by the multi-phase chemistry is only simulated in the REFERENCE approach, especially between 08.00 and 14.00 on the second model day. The possibility of bi-directional fluxes in the dynamic approach leads to a reduction in the calculated deposition flux in long-term studies (Flechard et al., 1999). However, this is not appropriate for simulations on a daily time scale. This study revealed, that under typical meteorological fog conditions the leaf surface water does not evaporate sufficiently for ammonia to be reemitted into the atmosphere. In this case the NH$_3$ deposition rate is increased compared to the resistance approach.

The vertical profile of the NH$_3$ concentration within the canopy strongly varies with time and altitude in the presented study. As depostion rates depend on the concentration gradient, this study highlights the need for an accurate height-resolved dynamical model like CHEMIFOG_V to calculate realistic deposition rates.

Chapter 13

The Influence of Physical and Multiphase Chemical Processes within a Vegetation Canopy on the Emissions of NO and Isoprene

Abstract. The concentrations of gas phase chemical species in a vegetation canopy are modified by chemical reactions, photolysis, dry deposition to the dry vegetation respective soil surface, as well as mass transfer between the gas and the liquid phase. Nitric oxide (NO) and isoprene are, moreover, emitted from the soil and the plants, respectively. In this chapter results of model simulations of the gas phase concentrations of selected compounds in a temperate deciduous forest are presented. Focus is given to the impact of a vegetation canopy on the soil and plant emissions of NO and isoprene, respectively, leading to the reduction of the canopy emissions compared to the primary source strength. The meteorological conditions are chosen for radiation fog to develop during nighttime. The physico-chemical processes within a vegetation canopy and its influences on the boundary layer concentration of NO and isoprene are investigated in sensitivity studies. An important parameter determining the fate of the emissions within the canopy is the turbulent transport, that modifies the vertical distribution of the trace gases within the canopy and governs the mixing of canopy air into the boundary layer. Turbulent exchange and chemical reactions are the major processes determining the canopy emission of NO. In the presented model simulation NO is effectively oxidized by ozone during nighttime. During daytime turbulent exchange of the air within the canopy with the boundary layer above the canopy does not reach to the

ground preventing the NO soil emissions from effective transport into the boundary layer. Consequently, the NO soil emissions are effectively reduced by the vegetation canopy leading to much smaller NO emissions from the canopy compared to the primary emissions. On the other hand, due to the nighttime oxidation of NO NO_y accumulates within the well-mixed canopy and is transported into the boundary layer in the morning. The outflow of NO_y, however, is more than compensated by the deposition flux. Isoprene emissions are largest during daytime within the crown area of the canopy and are, therefore, transported out of the canopy during daytime. While the reaction with OH is an important process reducing the isoprene emission on the canopy scale during daytime, dry deposition is most effective during nighttime, when turbulent mixing transports the emissions to the ground surface.

Omitting the chemical reactions of isoprene results in two different tendencies in the nitrogen oxide concentrations. While the NO concentration is enhanced, the NO_y concentration is reduced. Instead of ONIT, more HNO_3 is produced and, subsequently, more effectively deposited or taken up into the liquid phase.

In the presence of leaf surface water, depositing NO_y species are taken up into the liquid phase. The leaf surface water represents a reservoir for these species that are reemitted when the liquid water evaporates. Overall, this leads to a reduced deposition flux of NO_y due to bi-directional deposition fluxes.

13.1 Introduction

Ozone is an important species in atmospheric chemistry, because it is the main precursor of the OH radical (Crutzen et al., 1999), acts as a greenhouse gas, and is the principal toxic component of smog. Tropospheric ozone production depends on the concentrations of nitrogen oxides and volatile organic compounds and their ratio (Crutzen et al., 1999). Several studies on atmospheric nitrogen have been performed and summarized by Erisman et al. (1998) and Emmons et al. (1997). Sources of nitric oxide (NO) are both anthropogenic and natural (fossil fuel combustion, biomass burning, microbial activity in soils, and lightning). Globally, 30 to 50 teragrams of nitrogen per year ($Tg\,N\,a^{-1}$) are emitted by these sources, of which the microbial decomposition in the soils is estimated to contribute 5 to 10 $Tg\,N\,a^{-1}$ (Lerdau et al., 2000). Several studies have been performed to quantify this emission source (see e.g., Kirkman et al., 2001, Ludwig et al., 2001, Yienger and Levy II, 1995). An important parameter in the investigation of emission sources is the reduction of emissions near the source (see e.g., Munger et al., 1998) leading to reduced emissions

on the regional scale. As soils are often covered by plants (e.g., forests, crops) the interaction of the primary soil emissions with the vegetation canopy influences the effective NO emissions on the regional scale leading to reduced NO canopy emissions compared to the primary emissions from the soil. This vegetation canopy reduction has been investigated in several studies (see e.g., Rummel et al., 2002, Jacob and Bakwin, 1991, Jacob and Wofsy, 1990). Canopy reduction depends on chemical transformation, dry deposition, as well as on transport conditions like the turbulent exchange between the source area and the above-canopy boundary layer. Many estimates of global nitrogen emissions by soils are based on canopy reduction factors between 0.2 and 0.5, i.e., 50–80 % of the primary emissions are released from the top of the canopy, (Lerdau et al., 2000, Wang et al., 1998, Yienger and Levy II, 1995) based on observations in tropical forests (Jacob and Bakwin, 1991). However, this may not be applicable for temperate forests as meteorological conditions significantly differ. Ganzeveld et al. (2002) showed that in pristine regions an explicit representation of the vegetation is required to model NO_x emissions.

The importance of leaf surface water has been given attention to in recent studies on dry deposition of various atmospheric trace gases (Klemm et al., 2002, Spindler et al., 2001, Grantz et al., 1997). To the author's knowledge, however, no modeling studies on the impact of fog water and leaf surface water on the canopy reduction of NO emissions have been performed so far.

Isoprene is an important biogenic volatile organic compound (BVOC) emitted by plants. The oxidation of isoprene by OH changes the atmosphere's oxidative capacity (Fehsenfeld et al., 1992), initiates the formation of ozone (Chameides et al., 1992), and leads to the formation of organic compounds, e.g., organic acids, that influence the liquid phase pH. Wang et al. (1998) quantify the global emissions to be 597 $Tg\,C\,a^{-1}$. Several laboratory and field measurements have been performed to investigate the emission fluxes on the leaf (Günther et al., 1995) as well as on the canopy scale (Wiedinmyer et al., 2001, Schween et al., 1997). Inclán et al. (1999) presented a modeling study on the BVOC emission flux on the canopy scale using a one-dimensional multi-layer prognostic model. They concluded that the upscaling of emission parametrizations on the canopy scale requires additional micrometeorological information to be comparable to measurements. However, they omitted chemical processes within the canopy. Consequently, detailed investigation on the canopy reduction of isoprene simulating micrometerological as well as chemical processes is required in order to improve parametrizations for the use in largescale models.

13.1.1   Background

Nitrogen Oxides

Nitrogen oxides (NO, NO_2) are important compounds for the atmospheric chemistry, because their concentration determines the photochemical ozone production in the troposphere.

During daytime, NO, NO_2, and O_3 are in photochemical equilibrium:

$$NO_2 + h\nu \quad \longrightarrow \quad NO + O(^3P) \tag{R 13.1}$$

$$NO + O_3 \quad \longrightarrow \quad NO_2 + O_2 \tag{R 13.2}$$

$$O_2 + O(^3P) \quad \longrightarrow \quad O_3. \tag{R 13.3}$$
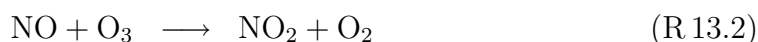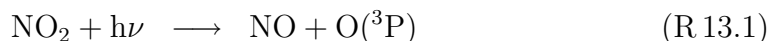
During the night, no photodissociation of NO_2 and therefore no NO production via Reaction R 13.1 takes place. NO is effectively decomposed by the reaction with ozone (Reaction R 13.2).

The reaction of NO_2 with the hydroxyl radical leads to the formation of nitric acid, HNO_3, an important reservoir species of the nitrogen oxides:

$$NO_2 + OH + M \longrightarrow HNO_3 \tag{R 13.4}$$
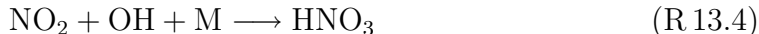
with $M = O_2, N_2$.

HNO_3 is rapidly deposited to both the dry vegetation surfaces and the soil. In the presence of radiation fog or leaf surface water HNO_3 is effectively taken up into the liquid phase.

In the presence of isoprene the following reactions lead to the production of organic C5-nitrates (ONIT) as reservoir species:

$$C_5H_8 + NO_3 \quad \longrightarrow \quad ONIT \tag{R 13.5}$$

$$C_5H_8 + OH \quad \xrightarrow{+O_2} \quad ISO_2 \tag{R 13.6}$$

$$ISO_2 + NO \quad \longrightarrow \quad ONIT, \tag{R 13.7}$$
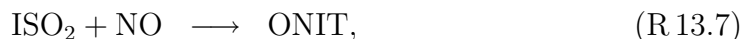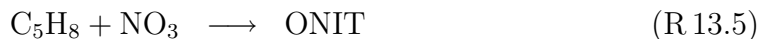
where ISO_2 are isoprene (hydroxy) peroxy radicals.

The chemical canopy reduction of NO, consequently, depends on both the availability of ozone and on the emission flux of isoprene.

As NO reacts rapidly with ozone and ISO_2 canopy emission fluxes of NO are reduced, however without extracting reactive nitrogen from the atmosphere. To investigate the total nitrogen canopy emission fluxes, thus, the concentration of $NO_y = NO + NO_2 + NO_3 + 2 \cdot N_2O_5 + HNO_3 + HNO_4 + PAN + HONO + MeO_2NO_2 +$

MPAN + ONIT + NACA[a] is considered. NO_y is the sum of all reactive nitrogen compounds and therefore the total concentration is constant with respect to chemical reactions and only influenced by emission, deposition, and transport.

Isoprene

Isoprene is the major BVOC emitted by plants, especially deciduous trees. The chemical reduction of the isoprene concentration is initiated by reaction with OH, O_3 and NO_3. During daytime, the chemical reaction with the hydroxyl radical (OH) represents the major sink of isoprene, when 95 % of the oxidized isoprene is destroyed by OH (Zimmerman et al., 1988). During nighttime, besides dry deposition to the soil, Reaction R 13.5 is the major chemical decomposition pathway of isoprene (Fehsenfeld et al., 1992). As there is no atmospheric chemical production of isoprene, the destruction reactions are irreversible and reduce the isoprene concentration.

13.1.2 Model Simulations

In the present study results of simulations performed with the multilayer chemical-microphysical radiation fog model CHEMIFOG_V are presented. CHEMIFOG_V is a one-dimensional fog model with temperature, wind, moisture, and turbulent kinetic energy being prognosticated within the multilayer vegetation canopy of 22 m altitude. Emission fluxes of NO and isoprene are calculated according to Yienger and Levy II (1995) and Günther et al. (1995), respectively (see Section 7.4). Additionally the formation of radiation fog and leaf surface water is simulated explicitly. For a detailed model description the reader is referred to Part I of this thesis.

The presented results are taken from the REFERENCE model simulation. The model initialization of the REFERENCE simulations has been described in Chapter 9, while the results of the meteorological parameters have been presented in Chapter 10. Radiation fog is present between 18.30 on the first model day and 08.30 on the second model day (see Figure 10.5), while the leaf surface water forms at 16.00 on the first model day and is present during the whole simulation time afterwards (see Figure 10.6).

Three sensitivity studies have been performed to investigate the various influences on the canopy reduction. In the model simulation no_NO-EMIS the soil emissions of NO are set to zero to separate the source of NO_y from the sink. In the model simulation no_UPTAKE the uptake of atmospheric gases into the liquid phase is not

---

[a]MeO_2NO_2 = methyl peroxy nitrate; MPAN = peroxymethacryloyl nitrate; NACA = nito-oxy acetaldehyde

considered, and vegetation surfaces are assumed to be dry. Thus, in the no_UPTAKE simulation dry deposition is calculated based on the resistance approach based on Ganzeveld and Lelieveld (1995) (see Section 7.2.1), while within the REFERENCE model simulation the newly developed, sophisticated dry deposition module presented in Section 7.5.1 is used, in which the dry deposition to wet surfaces is simulated according to the interfacial mass transfer according to Schwartz (1986). In the model simulation no_ISO-CHEM the chemical reactions of isoprene are omitted to reduce the canopy reduction to turbulence and dry deposition processes.

13.2 Results

The aim of this section is to identify the physico-chemical processes that influence the canopy reduction of NO and isoprene emissions. These processes comprise chemical reactions, the actinic flux available for photodissociation, deposition, uptake into the aqueous phase of the fog droplets and the leaf surface water, and turbulent transport.

The separation of these processes responsible for the retrieved spatial and temporal pattern of NO and isoprene is very complex. To identify the dynamical impact on the trace gas distribution, ozone is used, as because of its abundance, the ozone concentration is only poorly affected by chemical reactions. On the other hand, the ozone concentration is an important parameter for the chemical lifetime of NO within the vegetation canopy.

13.2.1 Ozone

The temporal development of the ozone volume mixing ratio (VMR) within the canopy is shown in Figure 13.1. During daytime of the first model day the ozone concentration is largely reduced in the soil adjacent layers, while in the upper half of the canopy the ozone mixing ratio remains constant between 15 and 20 ppb (parts per billion). Until 16.00 ozone concentrations steadily rise in the lower model layers. This pattern of the spatial and temporal ozone distribution is linked to the turbulent exchange coefficient shown in Figure 10.4. Air masses with higher ozone concentrations intrude the canopy from above during daytime, whereby the depth of intrusion increases during the day. During the night reduction of the ozone mixing ratio is observed throughout the canopy due to dry deposition. Turbulent mixing within the canopy results in the uniform distribution of ozone within the lowest 17 m. The same pattern as on the first model day develops on the second model day. Around
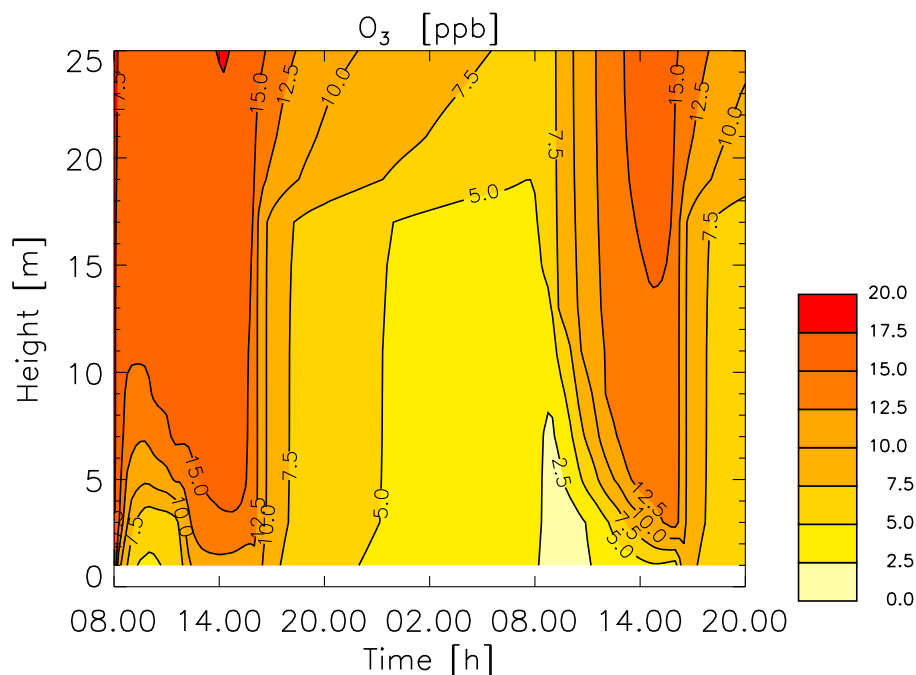
Figure 13.1: Volume mixing ratio (VMR) of O_3 within the vegetation canopy (REFERENCE).

08.00 air masses transport ozone into the canopy, while again the depth of intrusion increases during the day. During the whole simulation time, the ozone concentration exceeds the NO concentration. Therefore, Reaction R 13.2 is not limited by the availability of O_3.

The most important sink of ozone within a vegetation canopy is dry deposition. Dry deposition to vegetation surfaces is divided into two parts: The dry deposition flux to dry surfaces, $F_{dry \to dry}$, is calculated with the resistance approach presented in Section 7.2.1, while the dry deposition to moist surfaces, $F_{dry \to moist}$, is included in the model calculating the exchange of species between gas and aqueous phase (see Section 7.5.1). The dry deposition flux to dry surfaces, i.e., the O_3 concentration multiplied by the dry deposition velocity, is shown in Figure 13.2. While the deposition to the dry vegetation surfaces depends on the stomatal conductance, the deposition velocity to the soil is constant in the model, and therefore, the deposition flux to the soil reflects the ozone concentration in the ground adjacent layers.

The soil provides an effective sink to ozone[b]. Maximum deposition fluxes are

---

[b]Note that the data is given for the middle of the model layer, e.g. 1 m for the soil deposition and emission, respectively, and is interpolated between the 1 m and 3 m layer in the graphical representation.
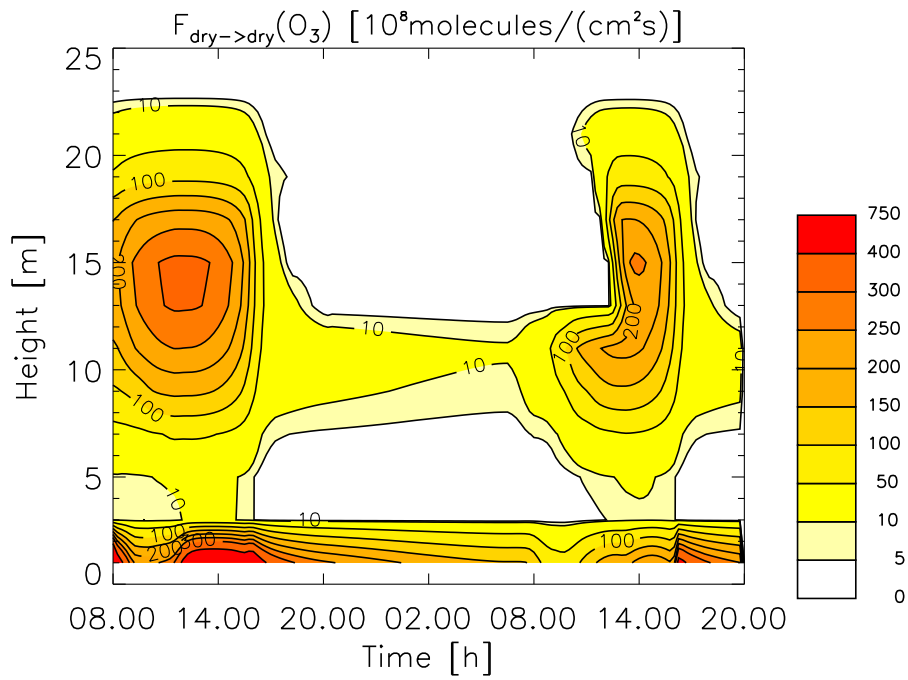
Figure 13.2: Dry deposition flux of O_3 to dry surfaces (REFERENCE).
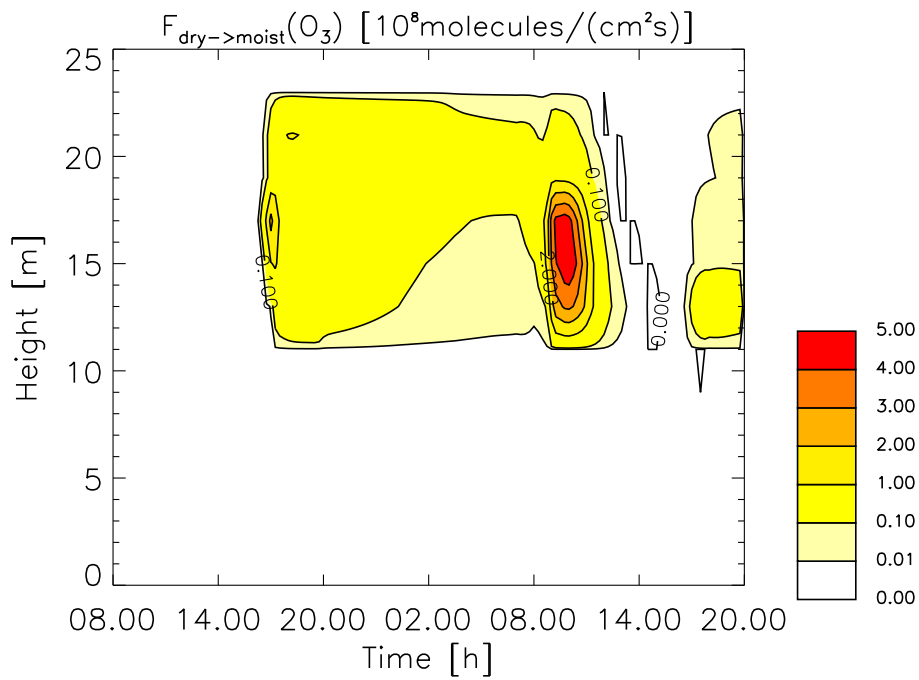
Figure 13.3: Dry deposition flux of O_3 to moist surfaces (REFERENCE).
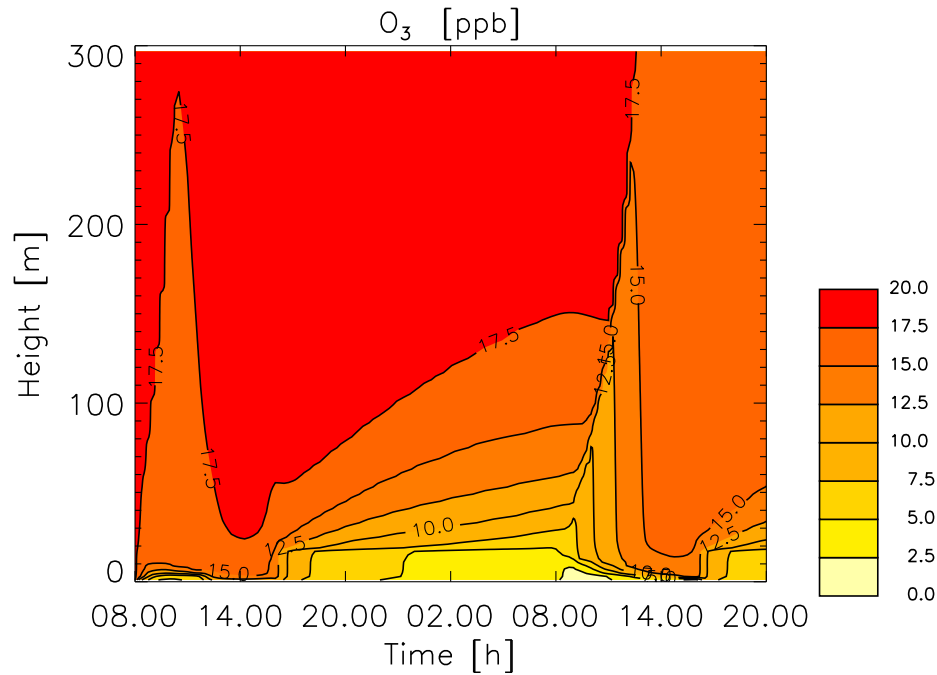
Figure 13.4: VMR of O_3 in the lowest 300 m (REFERENCE).

found around 14.00 on the first model day, when the ozone concentrations in the ground adjacent layers are highest. During nighttime, concentrations in the lowest atmospheric model layers are reduced and, as a consequence, deposition to the soil is reduced, however, provides still the major sink.

The dry deposition to the dry vegetation surfaces is most effective during daytime via stomatal uptake with the maximum deposition flux of $3.1 \cdot 10^{10}$ molecules $cm^{-2} s^{-1}$.

During nighttime the main part of the vegetation surfaces is covered with water as shown in Figure 10.6. Therefore less dry surfaces are provided for dry deposition. Within the crown area ozone deposits to the moist surfaces as shown in Figure 13.3. Between 08.00 and 12.00 on the second model day the deposition flux increases when ambient ozone concentrations increase due to turbulent intrusion of boundary layer air masses. Because of the low solubility the dry deposition flux of ozone to moist surfaces, however, is much less important than the dry deposition to the soil and to the dry vegetation surfaces.

Figure 13.4 shows the ozone VMR in the lowest 300 m during the simulation time. During the first model day ozone concentrations are reduced within the boundary layer. The reason for this is the dry deposition of ozone to the dry vegetation surfaces within the crown area of the canopy and subsequent turbulent mixing of the canopy air into the boundary layer. During the night ozone concentrations are effectively
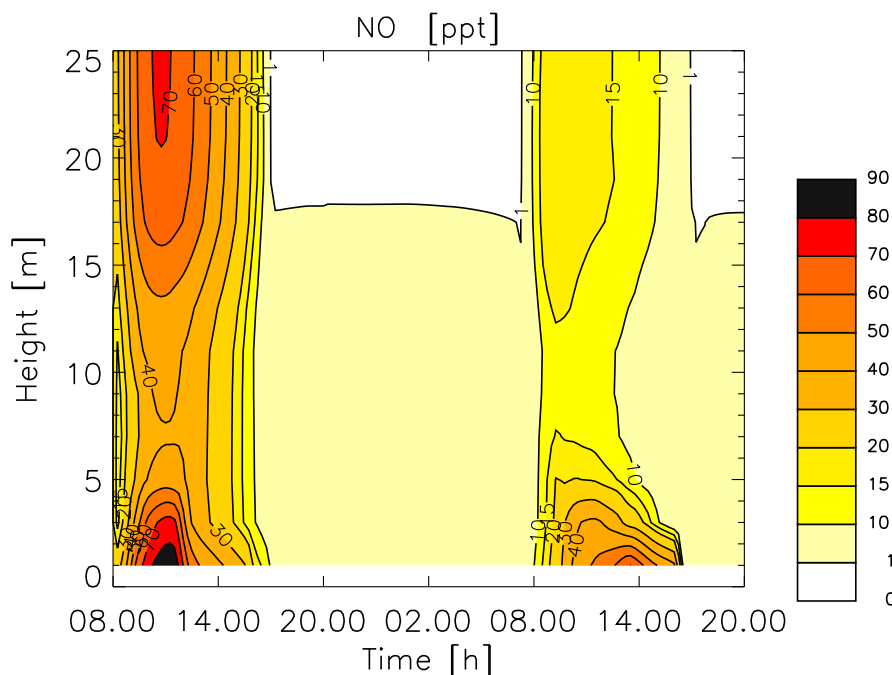
Figure 13.5: VMR of NO within the vegetation canopy (REFERENCE).

reduced within the canopy, mainly by deposition to the soil, while the exchange with the air masses above is low. In the morning of the second model day, ozone-poor air masses are transported out of the canopy leading to an ozone reduction within the boundary layer.

13.2.2 Nitric Oxide

REFERENCE

Figure 13.5 shows the VMR of NO in parts per trillion (ppt) within the canopy. NO concentrations are largest during daytime and reduce to nearly zero during the night. During daytime two regions in the vertical NO profile related to different production mechanisms can be divided. Above the canopy NO is exclusively produced by photochemical reactions with the photolysis of NO_2 being the major source of NO (Reaction R 13.1). The photolysis frequency $J(NO_2)$ is shown in Figure 13.6. The actinic flux and therewith $J(NO_2)$ is effectively attenuated within the crown region of the vegetation canopy. Consequently, below the crown area the concentration of NO is reduced due to the lower photochemical activity. The maximum of the NO concentration, however, occurs earlier than the maximum of $J(NO_2)$ due to the chemical loss of NO_x into reservoir species. On the other hand, in the lowest
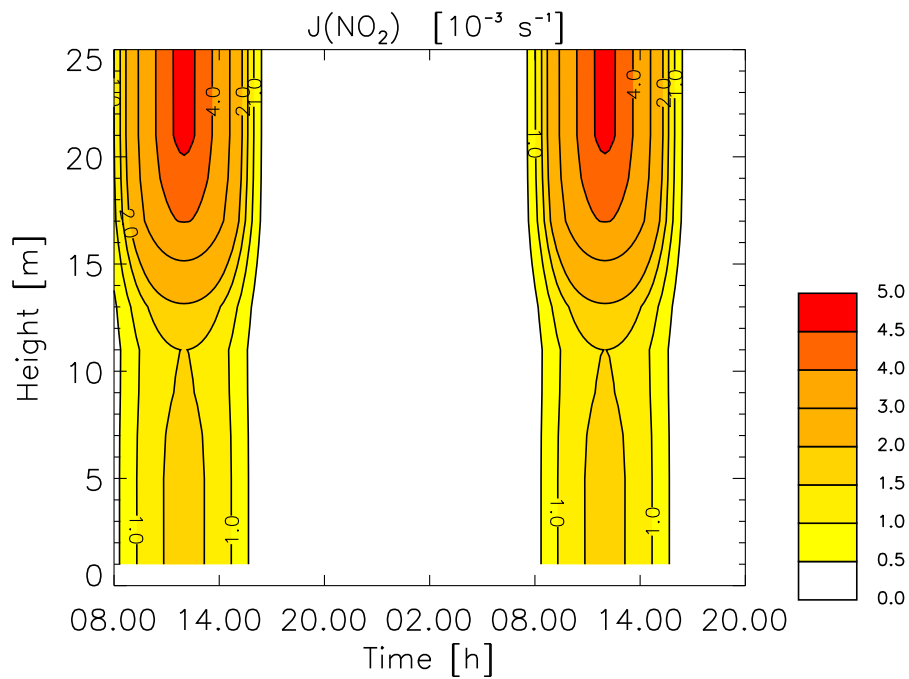
Figure 13.6: Photolysis frequency of NO_2, $J(NO_2)$, within the vegetation canopy (REFERENCE).
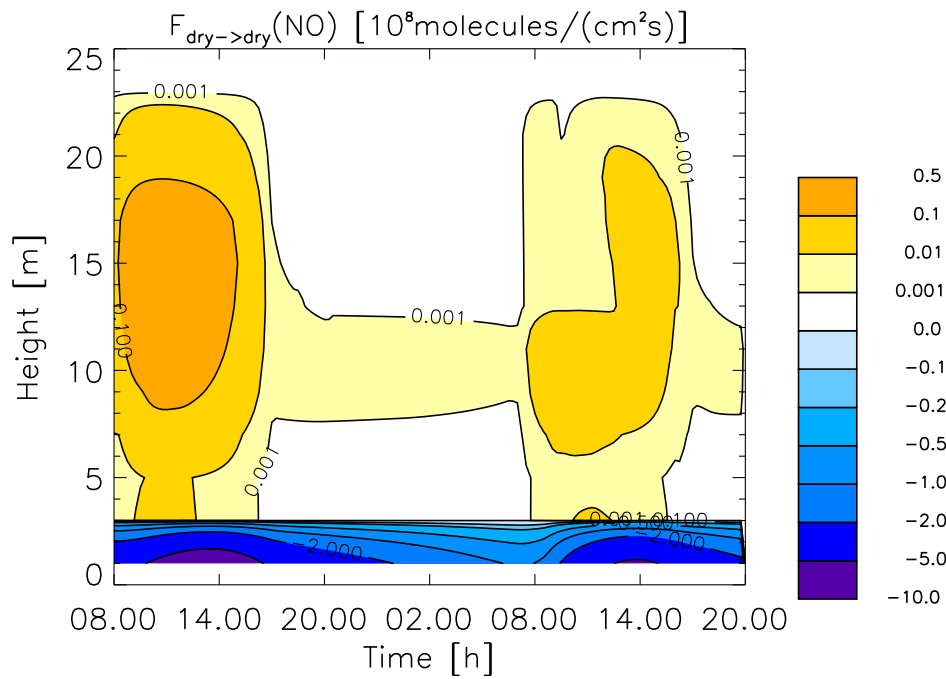
Figure 13.7: Dry deposition flux of NO to dry surfaces (REFERENCE).
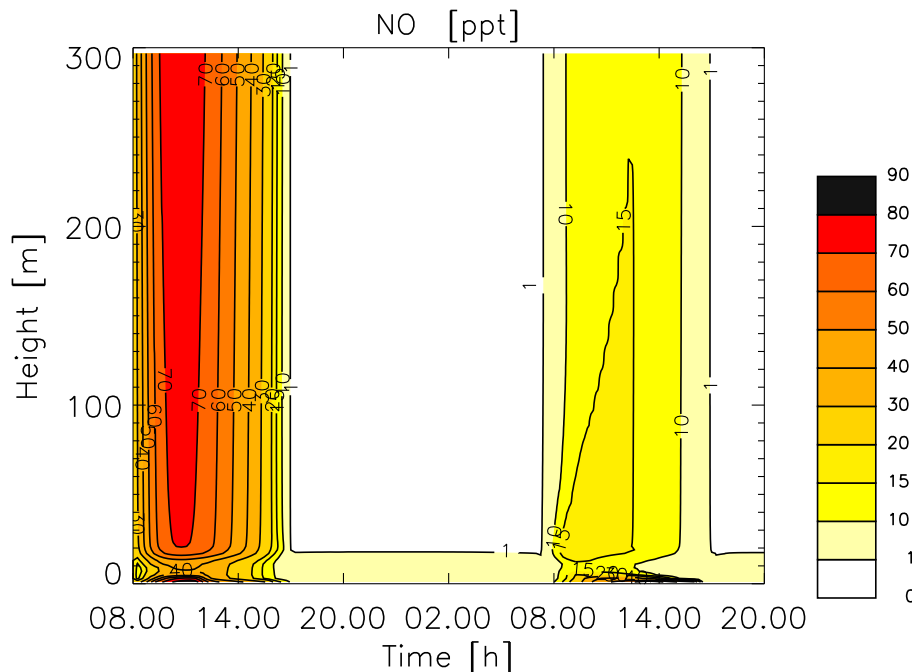
Figure 13.8: VMR of NO in the lowest 300 m (REFERENCE).

model layers the concentration of NO is enhanced due to the soil emission flux. The emission respective dry deposition flux of NO is shown in Figure 13.7^c. Maximum emission fluxes of $7.6 \cdot 10^8$ molecules $cm^{-2} s^{-1}$ and $5.5 \cdot 10^8$ molecules $cm^{-2} s^{-1}$ are reached at 12.00 on the first model day and at 14.00 on the second model day, respectively, depending on the soil temperature (see Equation 7.21). During the night the cooling of the soil reduces the emission flux to about 10 % of the maximum value. Dry deposition, on the other hand, is rather ineffective for NO compared to the soil emissions. As the turbulent exchange between the air within the canopy and above excludes the lowest model layers, as already discussed in Section 13.2.1, NO accumulates in the soil adjacent layers.

During nighttime both the photochemical production of NO stops and the remaining source, the NO soil emission, is low. Thus, the NO is nearly completely destroyed by reaction with ozone (Reaction R 13.2).

Figure 13.8 shows the NO concentration in the lowest 300 m of the model. On the first model day, the diurnal variation of NO above the canopy is mainly driven by radiation. On the second model day, a slight enhancement in the NO concentration above the canopy due to the turbulent canopy outflow is visible. As in the presented model run during the whole simulation time enough ozone is present to oxidize NO

---

^{c}Negative values mark emission fluxes. Dry deposition to moist surfaces is negligible for NO.
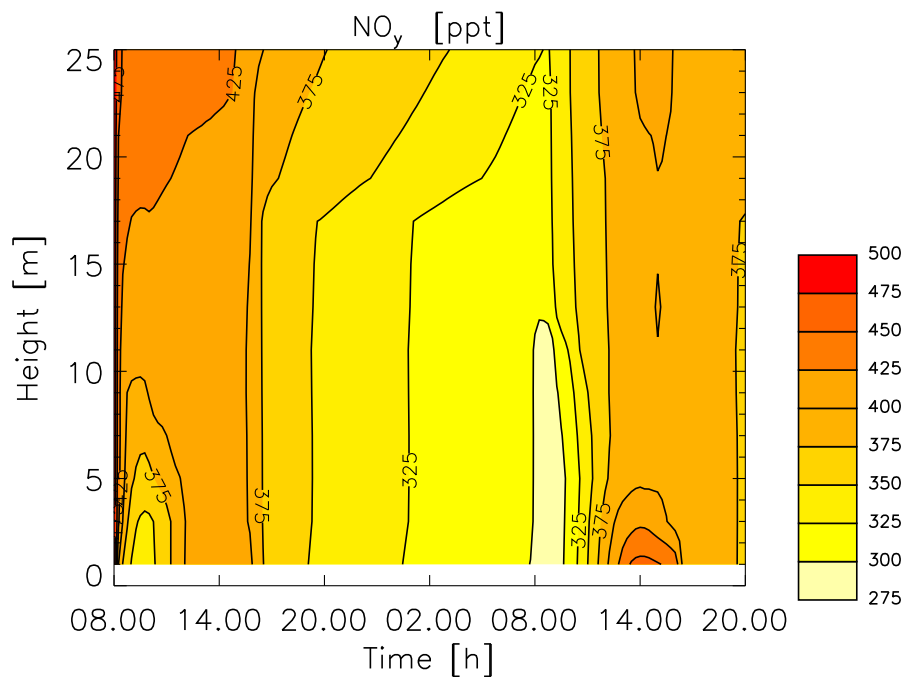
Figure 13.9: VMR of NO$_y$ within the vegetation canopy (REFERENCE).
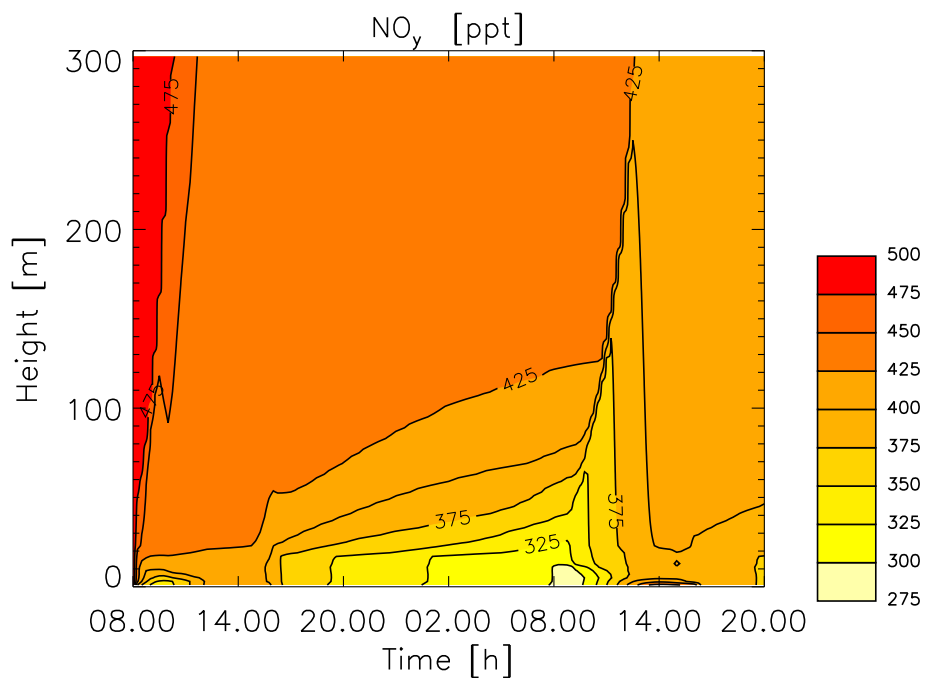
Figure 13.10: VMR of NO$_y$ in the lowest 300 m (REFERENCE).
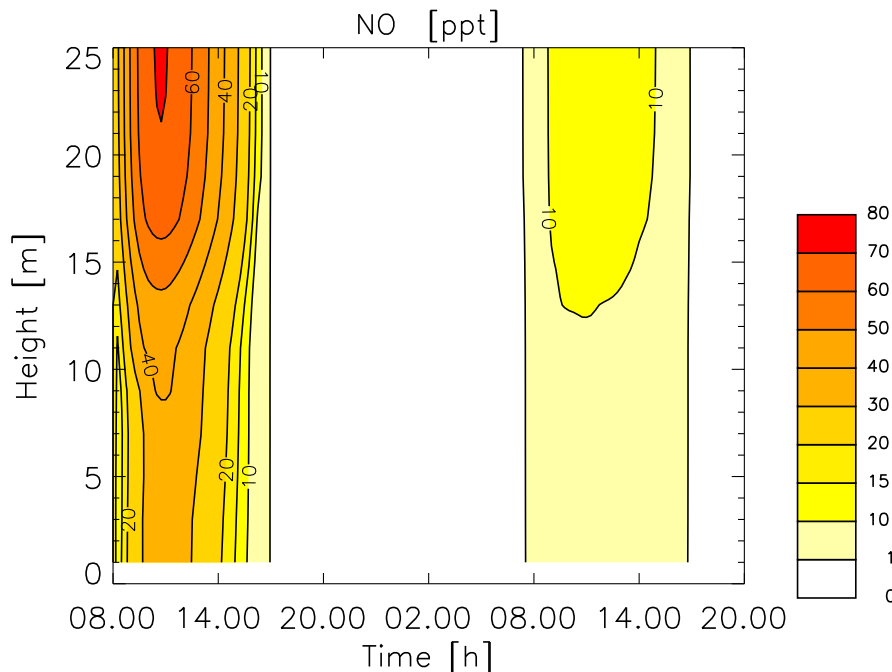
Figure 13.11: VMR of NO within the vegetation canopy (no_NO-EMIS).

only few NO accumulates in the forest during the night. In the morning, when turbulence sets in, the transport of NO out of the canopy is therefore relatively ineffective. The observed enhancement of NO, however, might be both due to soil generated NO and caused by a modification of the local chemical composition like the reduction of the ozone concentration due to the turbulent outflow.

To investigate the total nitrogen canopy emission fluxes, Figure 13.9 shows the concentration of NO_y within the canopy. During the night, when the canopy is dynamically separated from the atmosphere above, NO_y is reduced by deposition. On the second day a maximum of NO_y can be found in the soil adjacent layers. Between approximately 12.00 and 16.00 on the second model day turbulent transport propagates deeper into the canopy having the potential to transport NO_y out of the canopy. However, the lowest model layers are separated from above during most of the day.

Figure 13.10 shows the NO_y VMR within the lowest 300 m. The pattern of the temporal and spatial distribution is comparable to the ozone VMR shown in Figure 13.4. The turbulent mixing on the second model day transports cleaned air masses throughout the boundary layer. Overall, thus, NO_y concentrations in the boundary layer are reduced due to deposition processes within the canopy. The concentration are, nevertheless, higher than the results of a model simulation without NO emissions
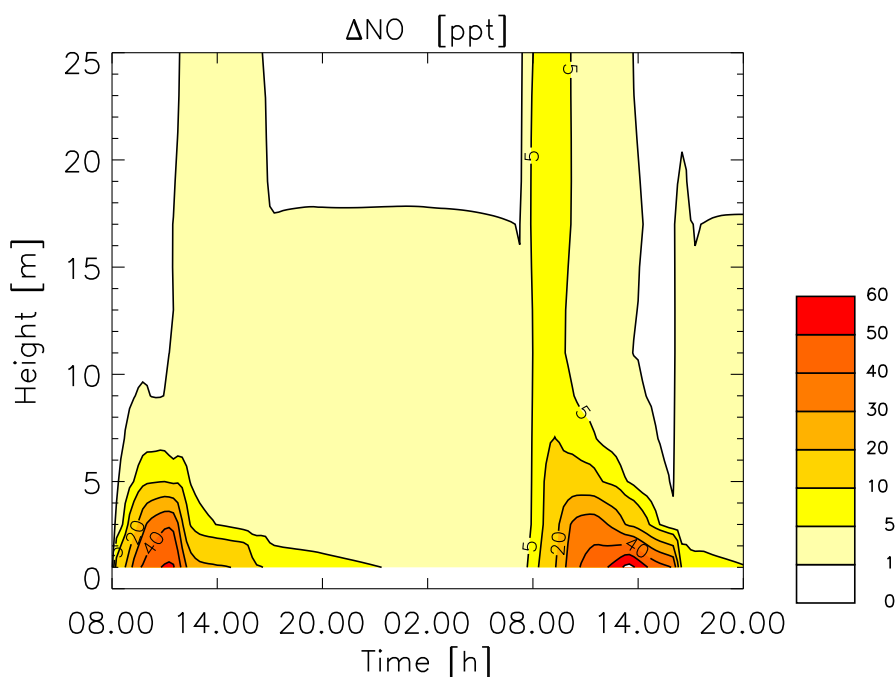
Figure 13.12: Difference between the VMR of NO within the vegetation canopy of the REFERENCE and the no_NO-EMIS simulation.

discussed in the following section.

no_NO-EMIS

To identify the contribution of the NO soil emissions to the total NO_y canopy emissions the sensitivity study no_NO-EMIS has been carried out. In this model simulation the NO emissions are neglected. Figure 13.11 shows the VMR of NO within the canopy. The daytime maxima in the lowest model layers caused by the soil emissions are not present in this model study. Moreover the nighttime concentration is zero due to the lack of the NO source. While on the first model day only small differences occur in the upper part of the canopy, on the second model day the NO concentration is reduced. Figure 13.12 shows the difference between the VMR of NO in the REFERENCE model simulation and the result of the no_NO-EMIS sensitivity simulation. Obviously, the largest differences are found during daytime in the lowest model layers. At 08.00 on the second model day turbulent mixing of the canopy air with the air masses above leads to an outflow of about 5 ppt NO out of the canopy. This NO flux either originates directly from the soil emissions or is photochemically produced from the reservoir species produced during nighttime.

In Figure 13.13 the result for NO_y of the no_NO-EMIS simulation is given. The
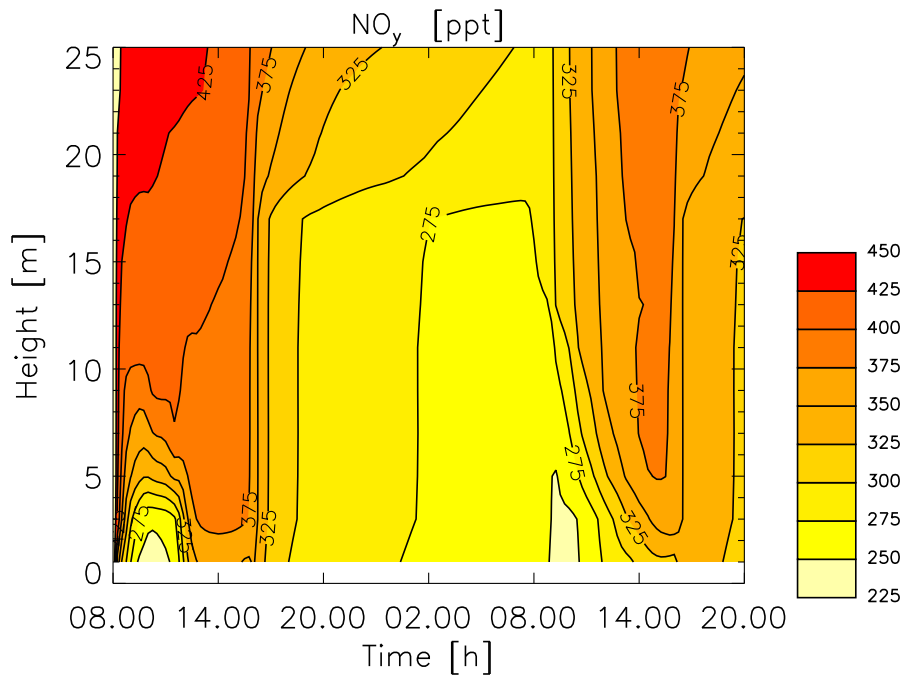
Figure 13.13: VMR of NO_y within the vegetation canopy (no_NO-EMIS).
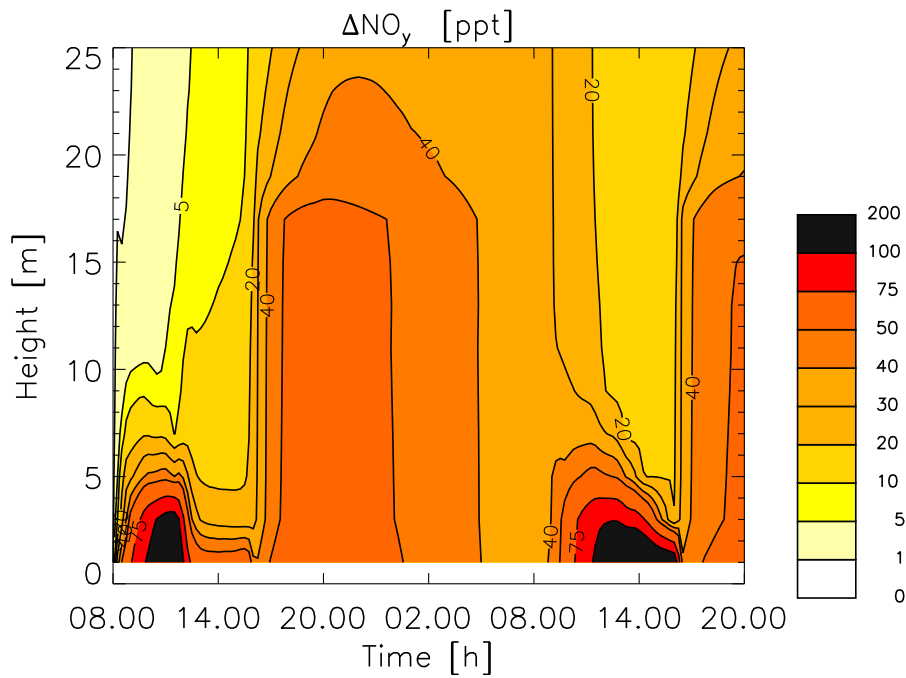
Figure 13.14: Difference between the VMR of NO_y within the vegetation canopy of the REFERENCE and the no_NO-EMIS simulation.
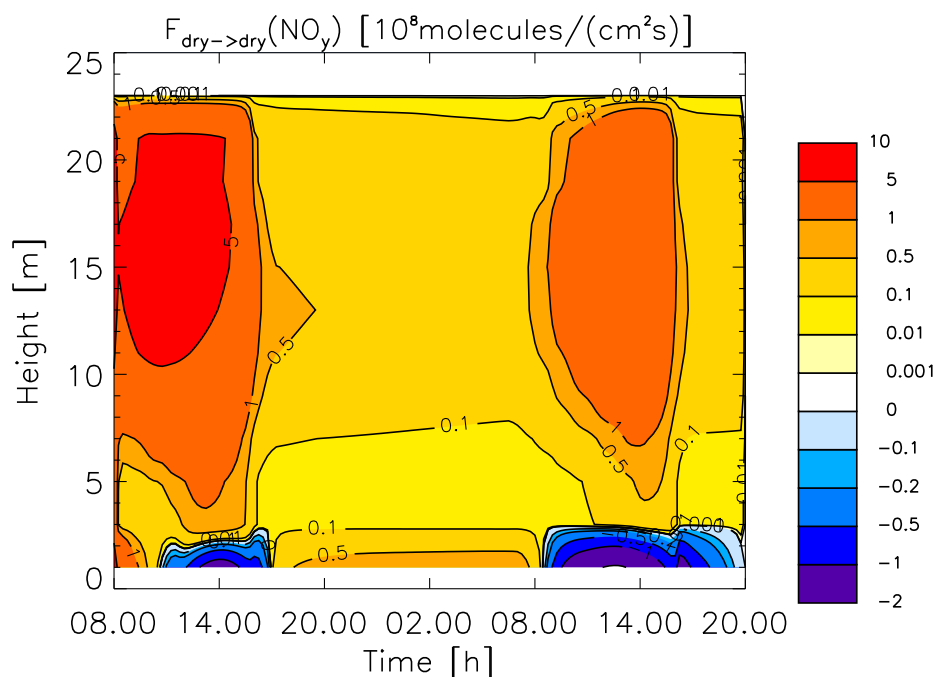
Figure 13.15: Dry deposition flux of NO_y to dry surfaces (no_UPTAKE).

maximum within the ground adjacent layers is not present in this simulation. Figure 13.14 shows the VMR of NO_y of the REFERENCE simulation minus the results of the no_NO-EMIS study. In the no_NO-EMIS simulation the concentration of NO_y is reduced in all altitudes. Largest differences are found during daytime in the lowest model layers. Moreover, large differences are found during nighttime within the well-mixed canopy. Nighttime NO emissions are rapidly oxidized by ozone. Consequently, although only slight differences are visible in the NO concentration, the accumulation of NO_y is significant in the REFERENCE simulation. The turbulent outflow of canopy air on the second model day is therefore enriched in NO_y under consideration of NO soil emissions.

no_UPTAKE

In the sensitivity simulation no_UPTAKE the exchange of trace species between the gas phase and the aqueous phase is omitted. Moreover, the leaves are assumed to be dry providing the whole surface for dry deposition. The following investigation focusses on the effect of the leaf surface water that provides the dominant liquid water pool in the REFERENCE simulation.

Figure 13.15 shows the dry deposition flux of NO_y to the dry vegetation surface and to the soil in the no_UPTAKE simulation. The dry deposition to vegetation
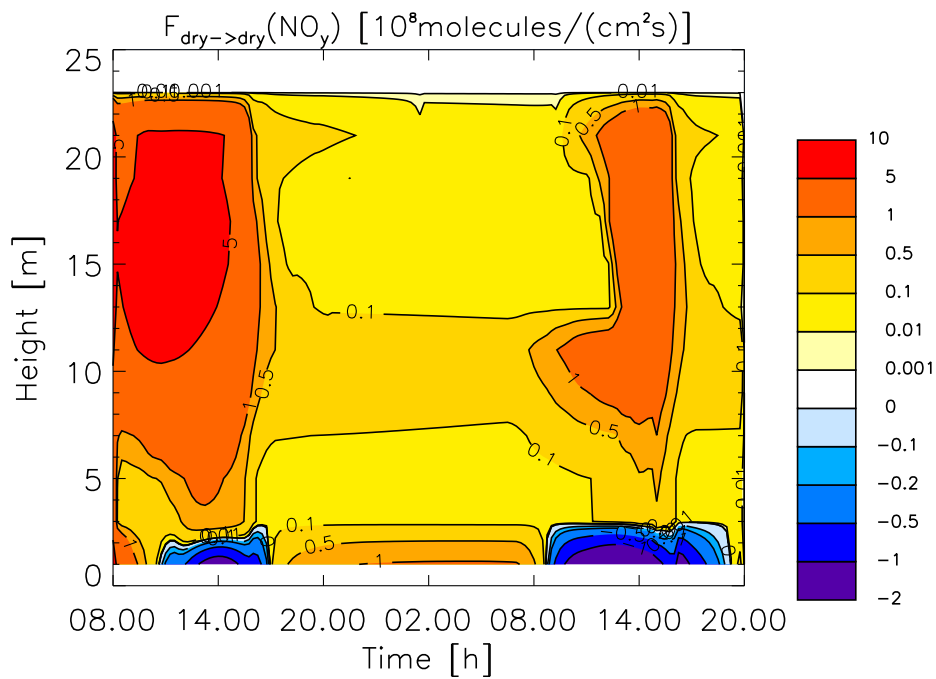
Figure 13.16: Dry deposition flux of NO_y to dry surfaces (REFERENCE).
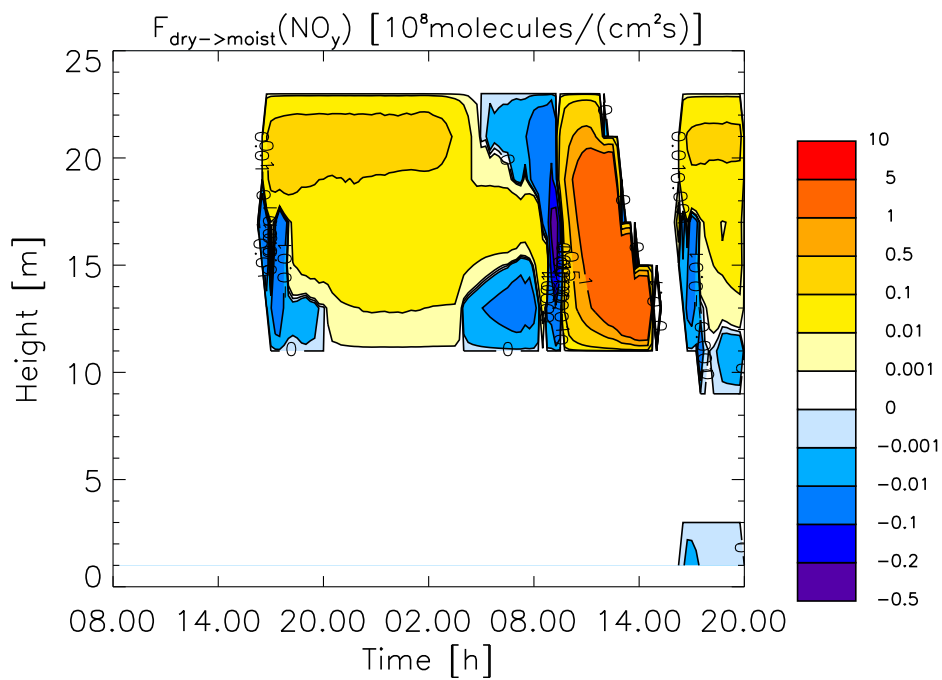
Figure 13.17: Dry deposition flux of NO_y to moist surfaces (REFERENCE).
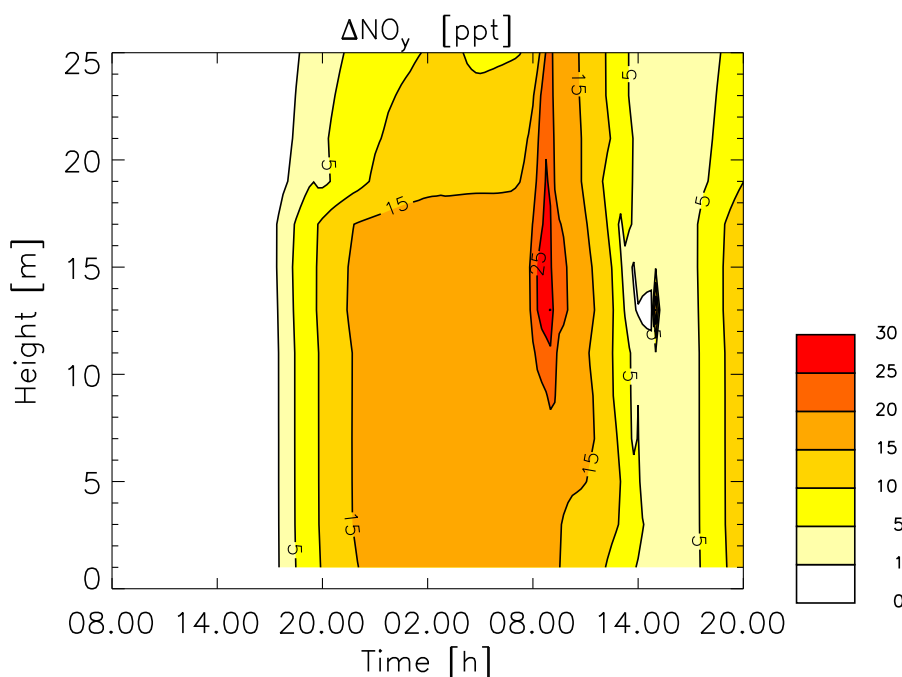
Figure 13.18: Difference between the VMR of NO_y within the vegetation canopy of the REFERENCE and the no_UPTAKE simulation.

surfaces is largest during the daytime when both stomatal conductance and atmospheric NO_y concentrations are largest. During daytime the NO emissions from the soil determine the net emission flux of NO_y, while during nighttime the deposition flux of NO_y predominates.

Figure 13.16 shows the same as Figure 13.15 but for the REFERENCE simulation. The dry deposition flux is reduced, where the vegetation surfaces are covered with leaf surface water (see Figure 10.6). The dry deposition flux to moist surfaces is given in Figure 13.17. During nighttime both deposition and emission fluxes of comparable magnitude take place. Overall, this leads to a reduction of the dry deposition flux in the REFERENCE simulation compared to the no_UPTAKE simulation. At 08.00 significant reemissions of NO_y are observed. Afterwards the deposition flux again predominates, when ambient atmospheric concentrations have risen due to turbulent intrusion of air into the canopy.

The resulting difference in the VMR of NO_y between the REFERENCE and the no_UPTAKE simulation within the canopy is shown in Figure 13.18. During daytime of the first model day no difference exists, because no liquid phase is present. During nighttime, fog droplets and leaf surface water develop. Because of the reemissions of deposited NO_y in the REFERENCE simulation the NO_y concentration in the
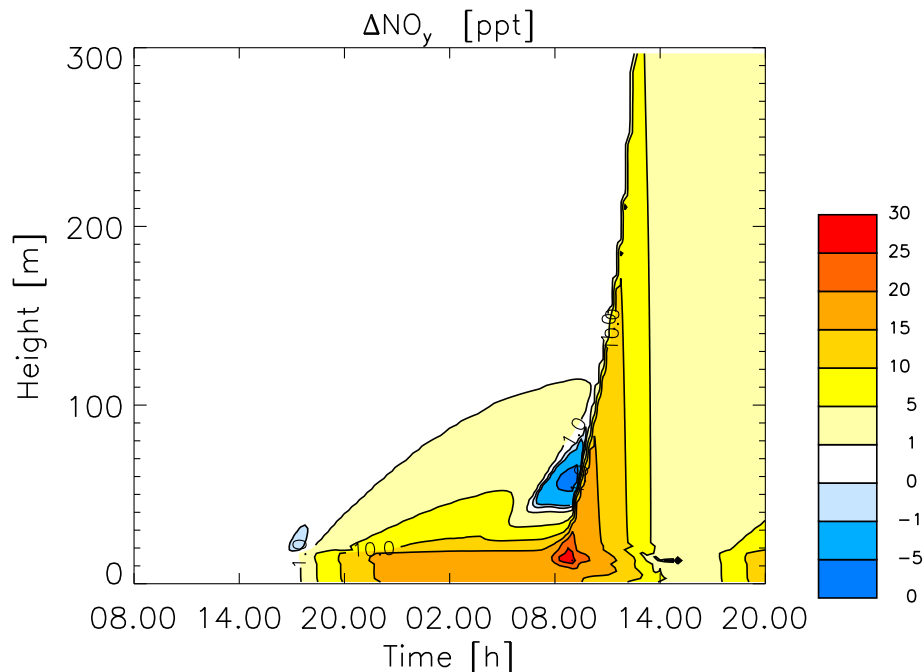
Figure 13.19: Difference between the VMR of NO_y in the lowest 300 m of the REF-ERENCE and the no_UPTAKE simulation.

REFERENCE study exceeds the one in the no_UPTAKE study by more than 15 ppt. Due to the large emission of NO_y from the leaf surface water at 08.00 on the second model day, the difference shortly rises above 25 ppt. Due to the turbulent mixing of air masses the difference reduces again afterwards.

Figure 13.19 shows the difference in the VMR of NO_y between the REFERENCE and the no_UPTAKE simulation in the lowest 300 m. Most of the time the NO_y concentration is larger in the REFERENCE simulation as already discussed before. However, between 07.00 and 10.00 on the second model day in an altitude region between 40 m and 85 m the NO_y concentration in the REFERENCE simulation is reduced. This is caused by the uptake of NO_y into the fog droplets and subsequent sedimentation to lower model layers and deposition to the leaf surfaces. From the leaf surface water the deposited NO_y again emits as shown in Figure 13.17. Turbulent mixing of the air masses within and above the canopy results in an enhancement of the VMR of NO_y due to the bi-directional fluxes between the gas and the aqueous phase.
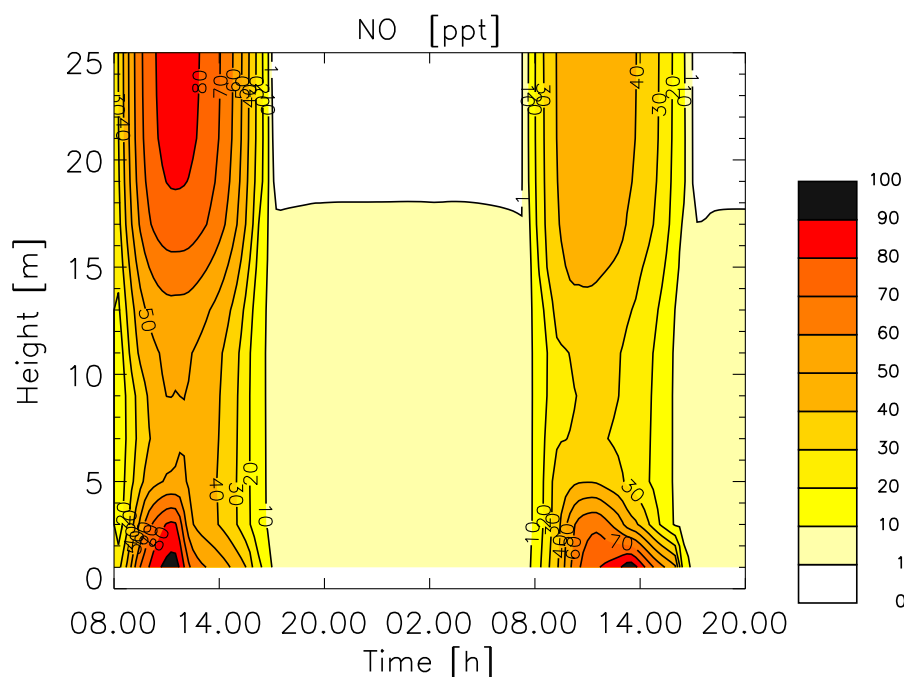
Figure 13.20: VMR of NO within the vegetation canopy (no_ISO-CHEM).

no_ISO-CHEM

In the no_ISO-CHEM simulation the chemical reactions of isoprene are omitted to investigate the importance of isoprene for the canopy reduction of NO. Figure 13.20 shows the VMR of NO within the canopy for the no_ISO-CHEM simulation. The pattern of the spatial and temporal distribution is similar to the NO retrieved from the REFERENCE model simulation (see Figure 13.5). However, two major differences arise: First, the daytime concentration of NO is significantly larger in the no_ISO-CHEM simulation, especially on the second model day; second, the maximum above the canopy occurs delayed compared to the REFERENCE simulation.

The difference between the NO concentration between the model simulation no_ISO-CHEM and REFERENCE is shown in Figure 13.21. On the first model day the enhancement in the NO concentration as well as the shift of the maximum are visible. On the second model day the NO concentration within the crown area is three times the concentration of the REFERENCE simulation.

Figure 13.22 shows the NO_y concentration within the canopy. While the pattern of the temporal and spatial distributions remains unchanged, the VMR in the no_ISO-CHEM simulation is significantly reduced and reaches values of about half the values of the REFERENCE simulation.

In the no_ISO-CHEM simulation the chemical reactions of isoprene are omitted.
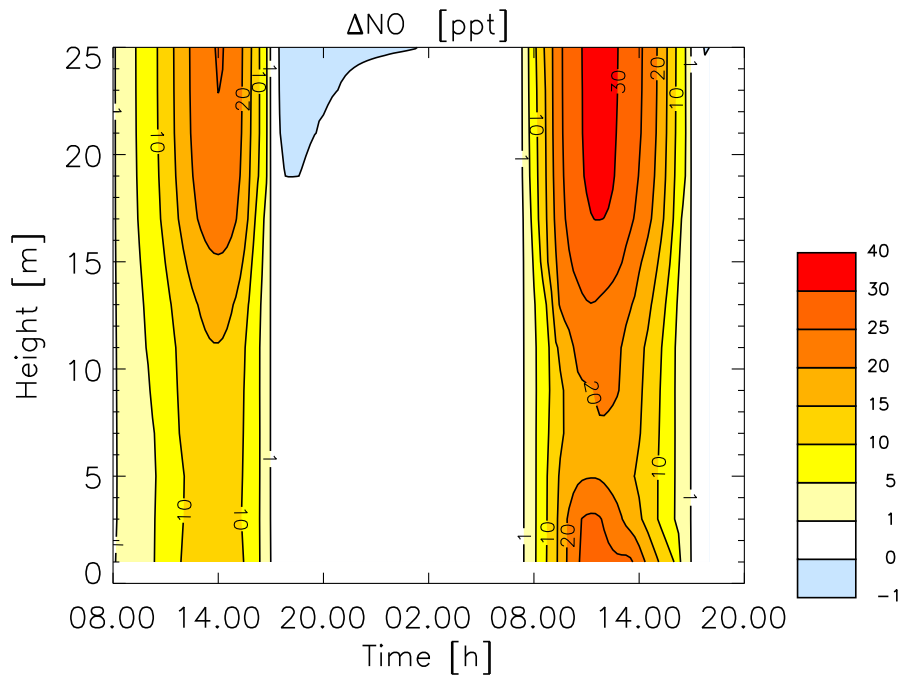
Figure 13.21: Difference between the VMR of NO within the vegetation canopy of the no_ISO-CHEM and the REFERENCE simulation.
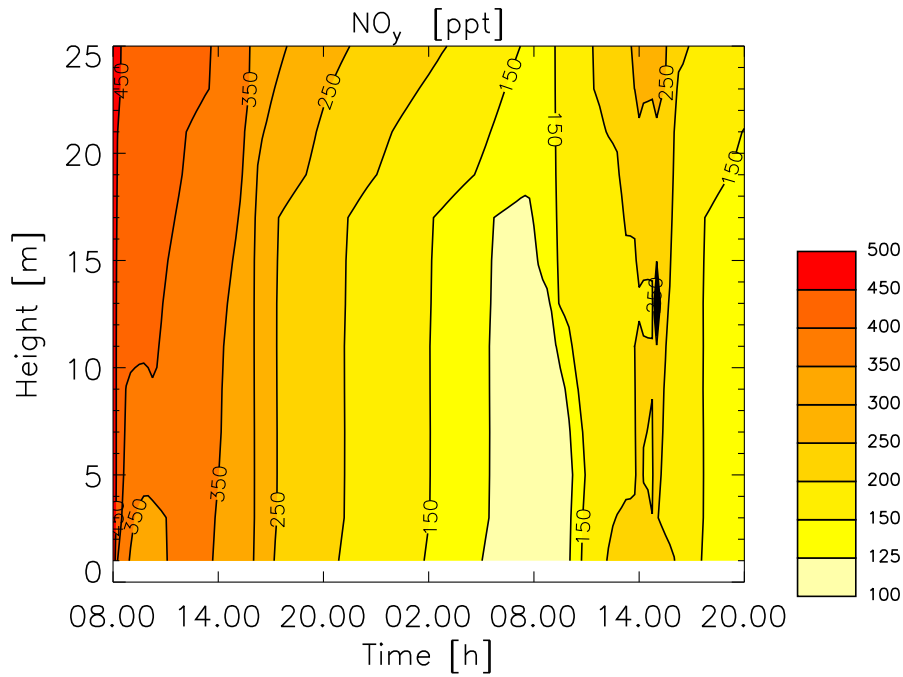
Figure 13.22: VMR of NO_y within the vegetation canopy (no_ISO-CHEM).
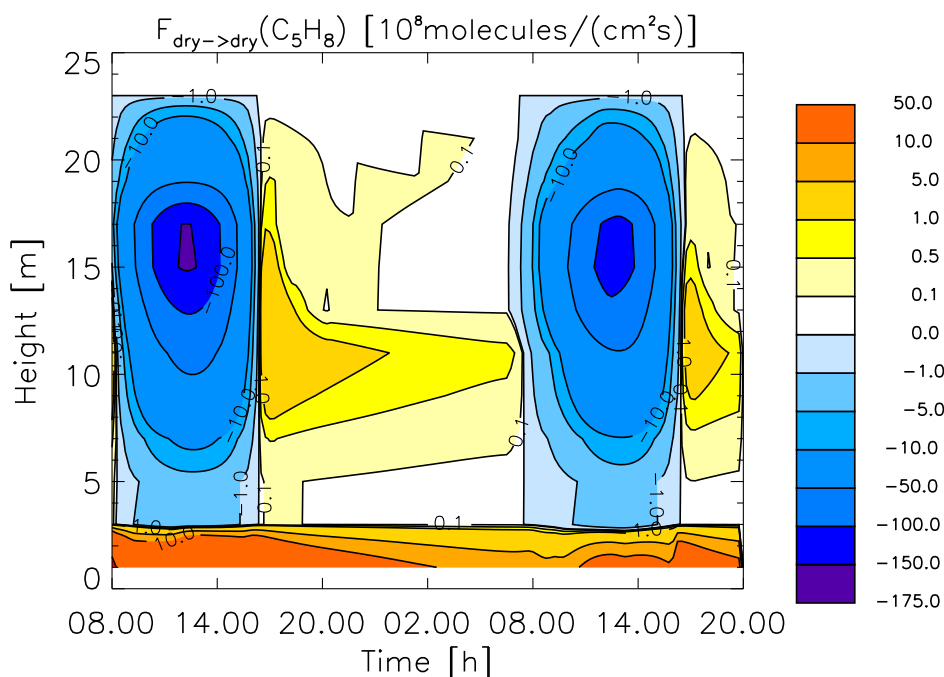
Figure 13.23: Dry deposition flux of isoprene to dry surfaces (REFERENCE).

As a consequence, the loss of $NO_x = NO + NO_2$ and NO_3 via Reactions R 13.5 and R 13.7 is not considered in this model simulation and NO_x and NO_3 concentrations are enhanced. On the other hand, the partitioning of NO_y changes. In the REFERENCE simulation, Reactions R 13.5 and R 13.7 produce ONIT that is not taken up into the aqueous phase nor undergoes fast chemical transformation or dry deposition and therefore accumulates within the canopy. Due to the lack of this pathway in the no_ISO-CHEM simulation, the production of HNO_3 is enhanced. As HNO_3 has a large deposition velocity and is highly soluble, the loss of HNO_3 and, therewith, the loss of NO_y is larger in the no_ISO-CHEM simulation leading to the observed reduction in NO_y.

13.2.3 Isoprene

REFERENCE

Figure 13.23 shows the dry deposition and emission fluxes of isoprene[d]. The emission fluxes are largest, first, within the crown area, where the largest leaf surfaces are located, and second, during daytime, when the photosynthetically active radiation (PAR) is highest. Dry deposition fluxes to the soil and the vegetation surfaces reduce

---

[d]The dry deposition of isoprene to moist surfaces is negligible.
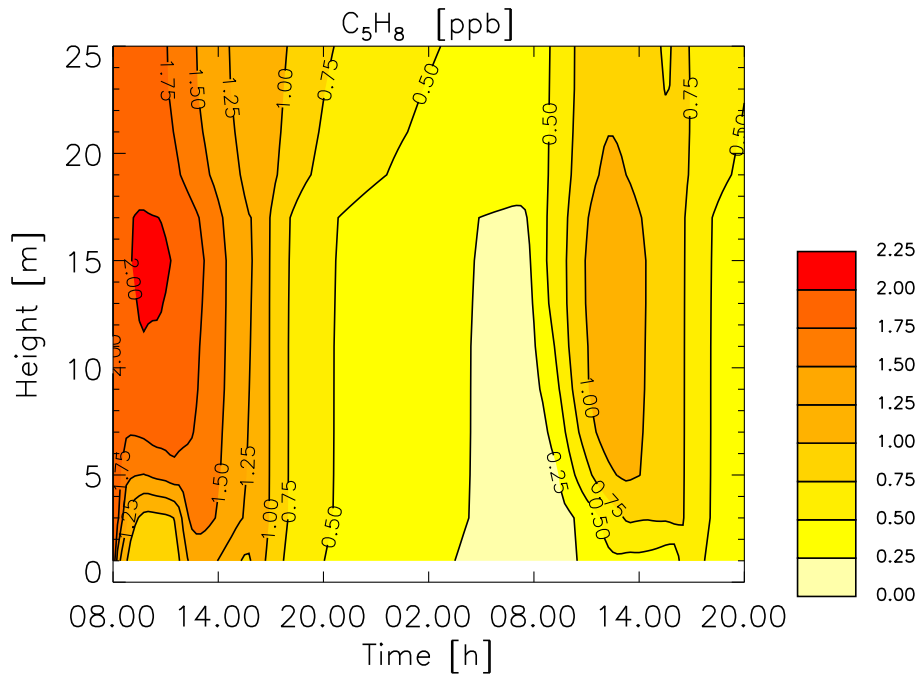
Figure 13.24: VMR of isoprene within the vegetation canopy (REFERENCE).
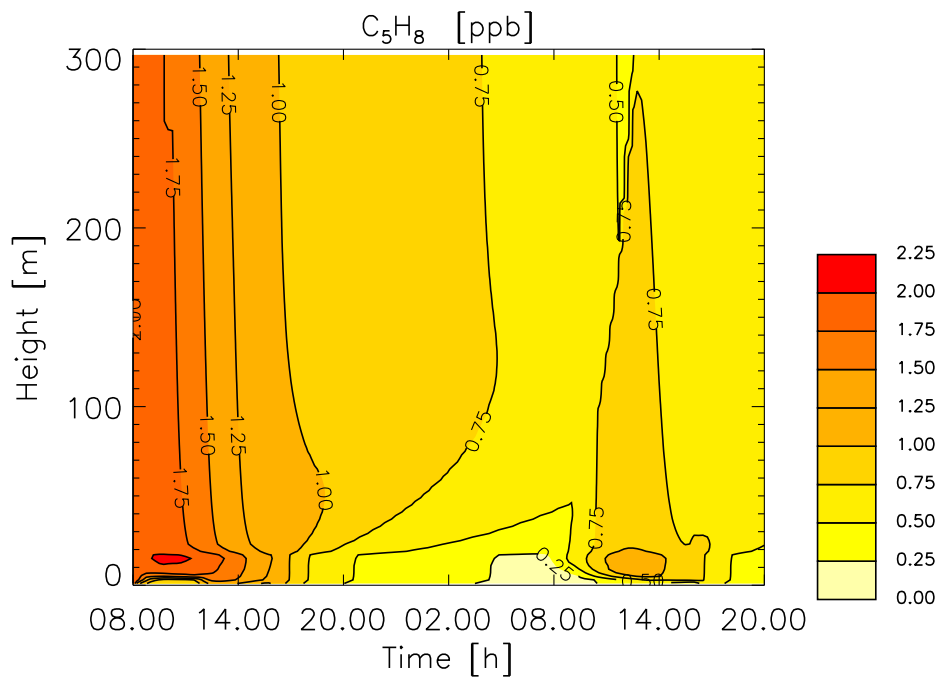
Figure 13.25: VMR of isoprene within the lowest 300 m (REFERENCE).
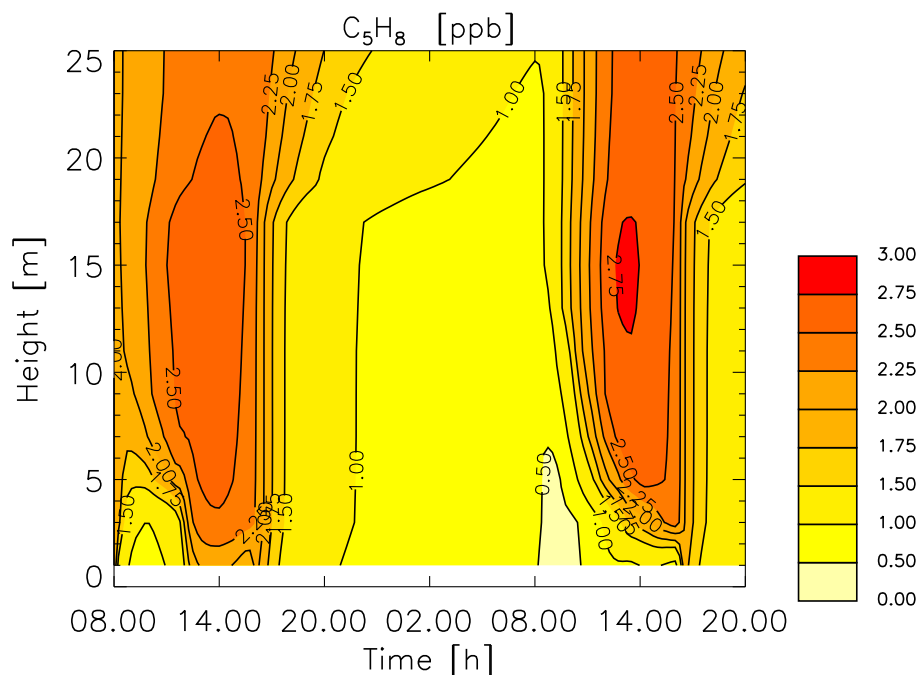
Figure 13.26: VMR of isoprene within the vegetation canopy (no_ISO-CHEM).

the isoprene concentration. The temporal development of isoprene shown in Figures 13.24 and 13.25 mainly depends on the emission flux by the leaves, that represents the only source of isoprene in the atmosphere. Therefore isoprene concentrations maximize during daytime in the crown area of the canopy. During night, chemical reactions and dry deposition to the soil reduce the isoprene concentration within the canopy. In the morning of the second model day, the isoprene emissions are transported throughout the boundary layer more effectively than the NO emissions. This difference is explained by the profile of the turbulent exchange coefficient. As shown in Figure 10.4 diurnal turbulence reaches down to only about the crown area of the canopy. Therefore isoprene, that is emitted in the crown area is transported out of the canopy, whereas NO mainly accumulates in the soil adjacent layers.

no_ISO-CHEM

Figure 13.26 shows the isoprene VMR within the canopy from the no_ISO-CHEM model simulation. The pattern of the spatial and temporal development is similarly influenced by turbulent transport and dry deposition processes like in the REFER-ENCE simulation presented in Figure 13.24. Similar as for NO, also the maximum of the isoprene concentration occurs later due to the missing chemical decomposition by reaction with OH. Overall, the concentration of isoprene is enhanced in the
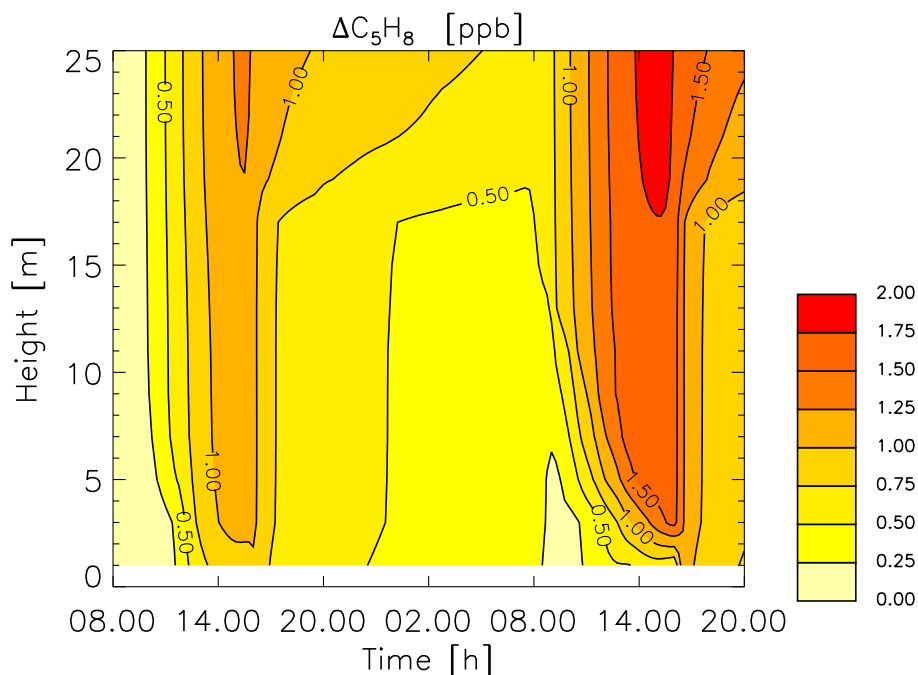
Figure 13.27: Difference between the VMR of isoprene within the vegetation canopy of the no_ISO-CHEM and the REFERENCE simulation.

no_ISO-CHEM model simulation.

Figure 13.27 shows the difference between the isoprene VMR in the no_ISO-CHEM model simulation and the REFERENCE model simulation within the canopy. While during the night the differences are below 1 ppb, during daytime, when turbulent exchange takes place between the canopy and the air above, the differences rise above 1.75 ppb. During nighttime the reduction of isoprene is mainly governed by dry deposition to the soil. During daytime, when isoprene emissions are largest, the chemical reaction with the photochemically produced OH radical is of major importance for the reduction of the isoprene concentration.

Omitting the chemical decomposition, thus, leads to a large outflow of isoprene-rich air masses compared to the results of the REFERENCE simulation, when turbulence sets in in the morning hours of the second model day. Although dry deposition leads to a significant reduction of the isoprene concentration during the night, the daytime production results in a net overall emission of isoprene from the canopy as can be seen in Figure 13.28. Overall, the difference in the isoprene concentration after the turbulent outflow is more than 1.75 ppb in the presented studies. The absolut values, however, depend on the initialization.
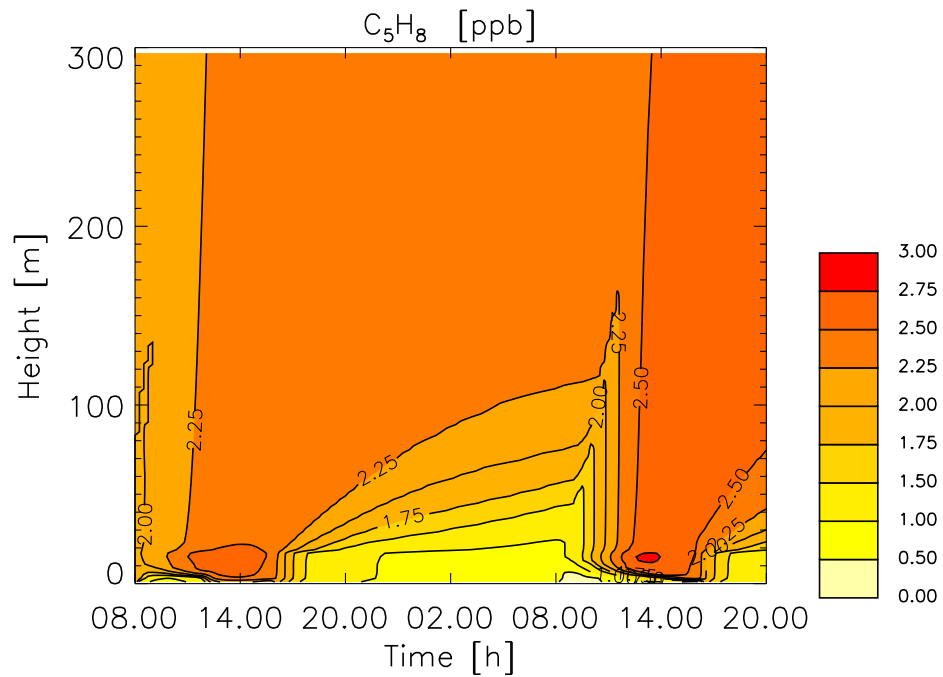
Figure 13.28: VMR of isoprene in the lowest 300 m (no_ISO-CHEM).
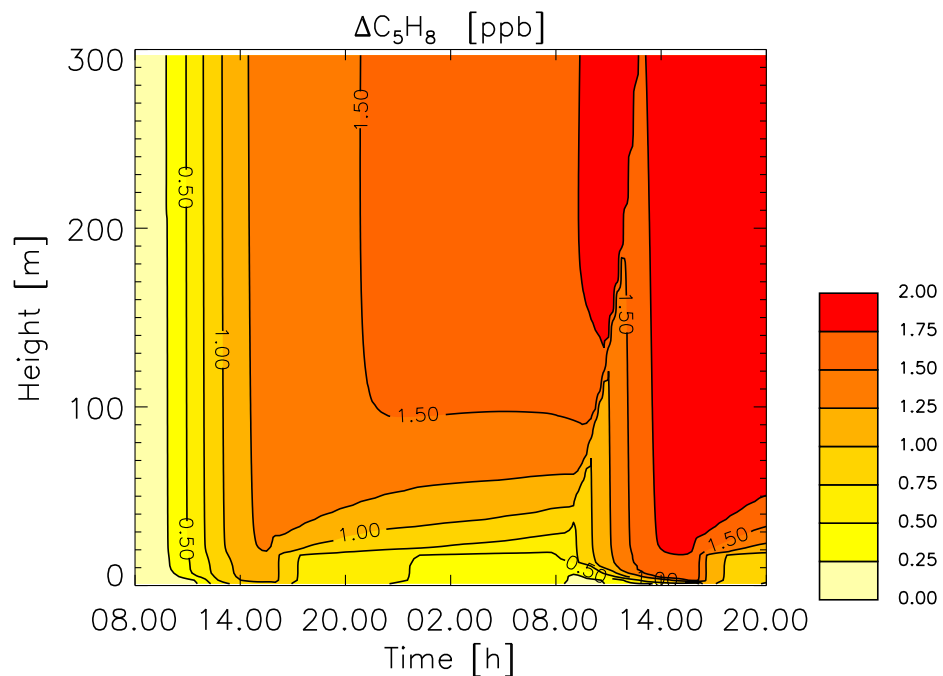
Figure 13.29: Difference between the VMR of isoprene in the lowest 300 m of the no_ISO-CHEM and the REFERENCE simulation.

13.3   Summary and Discussion

Modeling studies on the canopy reduction of NO and isoprene emission have been presented. Simulations have been performed with the one-dimensional chemical-microphysical radiation fog model CHEMIFOG_V. Environmental conditions have been chosen typical for a temperate deciduous forest of 22 m altitude in October. Radiation fog is present during nighttime, while leaf surface water on the vegetation surfaces forms at 16.00 on the first model day and is present during the whole simulation time afterwards (see Figure 10.6).

NO emissions from the soil lead to a significant enhancement of the NO concentration within the lowest model layers during daytime. During nighttime the major fraction of the emitted NO is converted to NO_2 by reaction with O_3. Thus, only few NO accumulates within the canopy during nighttime. As a consequence, the turbulent mixing of canopy air with the air masses above does not lead to a significant enhancement of the NO concentration, also because turbulence does not penetrate down to the lowest model layers. However, the concentration of NO_y is enhanced due to the soil emissions of NO and transported into the boundary layer in the morning. Overall, however, the NO_y concentration is reduced due to deposition to the canopy.

Isoprene emissions are largest during daytime within the crown area of the vegetation canopy, whereas dry deposition is most effective to the soil surface. While during nighttime isoprene is effectively deposited to the soil within the well-mixed canopy, during daytime isoprene is mainly decomposed by reaction with OH.

Besides the REFERENCE simulation, three sensitivity studies have been presented.

In the no_NO-EMIS simulation the NO emissions have been omitted to separate the reactive nitrogen compounds originating from the NO soil emissions. Although NO is effectively decomposed during the night, NO_y concentrations are enhanced throughout the canopy due to NO emissions and transported into the boundary layer after sunrise in the REFERENCE simulation.

In the no_UPTAKE simulation the exchange of trace species between the gas and the aqueous phase has been omitted. Moreover, vegetation surfaces are dry over the whole simulation time. The uptake of NO_y into the liquid phase leads to a reduction of the atmospheric concentration only at the beginning of the mature stage above the canopy, where sedimentation leads to the removal of droplets from this altitude region. Overall, however, NO_y concentrations are enhanced in the REFERENCE simulation, because the dynamical treatment of the deposition to moist surfaces

results in the reemission of previously deposited NO_y species.

In the no_ISO-CHEM simulation the chemical decompostion of isoprene has been omitted in order to, first, investigate the influence of the chemical reactions of isoprene on the overall isoprene canopy reduction and, second, investigate the influence of the isoprene emissions on the NO canopy reduction. Neglecting the chemical decomposition of isoprene significantly enhances the isoprene concentration in the canopy and also in the boundary layer above the canopy. While the chemical reactions of isoprene lead to an enhancement of the NO concentration, on the other hand, the overall NO_y concentration is reduced due to the enhanced production of HNO_3 and subsequent deposition or uptake into the liquid phase.

Consequently, the accurate description of both the strength of the isoprene emissions and the chemical reactions taking place within a vegetation canopy are important for the correct quantification of isoprene as well as NO canopy emissions. Moreover, the accurate description of turbulent transport processes, e.g., the penetration depth into the canopy, combined with a height-resolved determination of emissions are of great importance for the overall canopy reduction of trace gases. The presence of water pools, especially the leaf surface water, has to be considered, when discussing the fate of NO_y within a vegetation canopy.

Part III

Summary

Chapter 14

Conclusions and Outlook

14.1 Conclusions

The primary goal of this study was to improve the understanding of the interactions between the Earth's atmosphere and biosphere in the presence of radiation fog. For this purpose the microphysical fog models MIFOG_V and CHEMIFOG have been coupled and extended by modules focussing on the multiphase chemical processes within a vegetation canopy. These modules comprise the gas and aqueous phase chemical mechanisms, the calculation of activity coefficients for the aqueous phase reactions, the module to calculate photolysis frequencies, the dry deposition and emission of atmospheric trace gases, the sedimentation and moist deposition of fog droplets onto vegetation surfaces, the prognostic determination of leaf surface water, and the inclusion of the leaf surface water into the multiphase chemical module.

It was shown that CHEMIFOG_V is capable of simulating multiphase chemical processes in the presence of radiation fog in a forested environment. Especially the prognostic determination of leaf surface water due to dew formation and fog droplet deposition has turned out to be important. The inclusion of the leaf surface water into the chemistry module has been shown to be highly important for the realistic simulation of chemical processes within a vegetation canopy.

In three studies different aspects of the atmosphere-biosphere exchange have been investigated.

Aqueous phase concentrations in fog droplets are known to be size-dependent. In the presented studies pH values increase with droplet size, while the concentrations of SO_4^{2-} and NH_4^+ increase with decreasing droplet size, however, highest concentrations are found in the leaf surface water. For particles with a radius $r < 11.5\,\mu$m the sulphate concentration is governed by the dissociating aerosol particle that served as

condensation nucleus. The uptake of sulphur dioxide into the fog droplets is largest for medium sized particles. Significant uptake of SO_2 and NH_3 into the fog droplets is found above the canopy. Within the canopy gas phase concentrations are reduced due to the uptake of SO_2 and NH_3 into the leaf surface water. Sulphate concentrations, however, are not necessarily linked to the uptake of SO_2 from the gas phase but influenced by droplet growth. The concentration of the S(IV) reservoir HMS^- indicates the exchange of aqueous phase species between the size classes due to the growing and shrinking of the droplets. Overall, the study points out that temporal and spatial variations in the uptake of SO_2 and the concentration of sulphate are significant. Therefore, the microphysical history of droplets has to be taken into account in the analysis of size-dependent measurements.

The reduction of primary emissions of NO and isoprene within a vegetation canopy depends on several physical and chemical processes. Primary NO emissions from the soil depend on the soil temperature leading to highest emissions during daytime. As turbulent transport is mainly restricted to the upper part of the canopy, however, the exchange with the boundary layer is limited during daytime and NO accumulates in the lowest model layers. During nighttime the canopy is well-mixed, however, the emitted NO is nearly completely chemically decomposed. Therefore no NO accumulates during nighttime and only little NO is emitted on the canopy scale, when the major exchange between the canopy and the boundary layer above takes place after sunrise. NO_y that is formed during night, is released into the boundary layer instead of NO. Overall, however, the vegetation canopy acts as a net sink for NO_y. The chemical reactions of isoprene and its reaction products with nitrogen oxides lead to a reduction of the NO concentration but to an increase of the NO_y concentration. This is due to the chemical decomposition of NO and the change in the NO_y partitioning caused by the production of organic nitrates instead of HNO_3. As a consequence, less NO_y is deposited or taken up into the liquid phase leading to increased NO_y concentrations. The presence of radiation fog and leaf surface water within the vegetation canopy leads to an enhancement of the NO_y canopy emissions. As the uptake of NO_y into the leaf surface water is reversible, the loss of NO_y due to deposition is less in the presence of leaf surface water.

Isoprene emissions from deciduous trees are highest in the crown area during daytime, when stomatal conductance is highest. Consequently, the exchange with the boundary layer is less limited by turbulent transport than for NO. On the other hand, transport to the soil surface is limited for isoprene, so that deposition fluxes do not significantly reduce the isoprene concentration during daytime. During nighttime, however, isoprene is effectively transported to the soil surface and depleted.

Chemical reactions of isoprene are important especially during daytime, when OH concentrations are largest.

The presented studies on dry deposition fluxes to vegetation revealed the importance of the correct description of the uptake of trace gases into the leaf surface water and subsequent reactions. Describing dry deposition fluxes according to the resistance approach is limited to mono-directional fluxes. Calculating the exchange of NH_3 between the leaf surface water and the ambient atmosphere omitting aqueous phase reactions results in a reduction of the deposition flux caused by reemission of NH_3. The consideration of both the exchange between the two phases and aqueous phase chemical reactions leads to an enhanced uptake of NH_3. NH_3 is effectively taken up into the aqueous phase and dissociates. Due to the simultaneous uptake of acidifying compounds the alkalinizing effect of NH_3 is buffered and further uptake made possible. In the presented study the leaf surface water does not evaporate sufficiently to release significant amounts of NH_3 back into the atmosphere during the simulation period.

14.2   Outlook

Based on the results of this thesis, future research activities are expected to further increase our understanding of the interactions between the atmosphere, the biosphere, and multiphase chemistry. Especially the role of the aqueous phase has been shown to be of major importance, but has been neglected in most measurement and modeling studies. Therefore, appropriate field measurements on the atmosphere-biosphere exchange should include measurements of the development and chemical composition of leaf surface water. First approaches of leaf wetness measurements are performed by Klemm et al. (2002).

The variability of SO_2 uptake and subsequent oxidation has been investigated in the presented modeling studies. For a more comprehensive study on the temporal and spatial variations of sulphate concentrations and production the inclusion of a passive tracer into the model is desirable. Reilly et al. (2001) use selenium for the tracing of sulphate production in their measurements. On the other hand, measurements on the temporal and spatial variations are needed to validate the model results.

Isoprene chemical reactions have been shown to enhance the NO_y concentration in the vegetation canopy. The reason for this behaviour is the shift in the NO_y partitioning from HNO_3 to organic nitrates, that are less rapidly removed from the

atmosphere than HNO_3. However, considerable uncertainty exists in the amount of organic nitrate formed in the isoprene oxidation and little is known about their fate in the atmosphere (Chuong and Stevens, 2002, Pöschl et al., 2000, Chen et al., 1998). More laboratory and field measurements are needed.

Turbulent transport is an important process determining the exchange of air masses within and above the canopy and, therefore, the strength of the canopy emissions of isoprene and NO. Turbulent transport in vegetation canopies, however, shows features that cannot be simulated in the one-dimensional K-theory. Possible wave-like intrusions (Kruijt et al., 2000) and counter-gradient transport (Velho et al., 2001) processes are subject to actual research projects .

Aqueous phase chemical processes in CHEMIFOG_V are limited to dissolved species. During the evaporation process, however, crystalization occurs. An inclusion of this processes would be necessary, especially, to describe the evaporation of the leaf surface water and, therefore, reemissions correctly.

The biological processes that determine the emission and uptake of atmospheric trace gases, e.g., the response of plants to depositions and the adaptation of plants to radiative properties, need to be further investigated and parameterized for the use in physico-chemical models.

Overall, it has been shown in this thesis that CHEMIFOG_V is able to simulate the physical and chemical processes within a vegetation canopy. Especially, the coupling of the detailed dynamical and microphysical model with the multiphase chemical model including leaf surface water in a height-resolved vegetation model makes CHEMIFOG_V a unique and powerful tool for further research on the atmosphere-biosphere interactions.

Part IV

Appendices

Appendix A

Constants

Species	δR_b	R_g	R_{mes}	R_{cut}	R_{ws}
O_3	1.2	400	1	$1 \cdot 10^5$	2000
HNO_3	1.4	1	1	1.	1
NO	1.1	$1 \cdot 10^5$	500	$1 \cdot 10^5$	$1 \cdot 10^5$
NO_2	1.2	600	1	$1 \cdot 10^5$	$1 \cdot 10^5$
SO_2	1.6	250	1	$1 \cdot 10^5$	100
H_2O_2	1.2	80	1	$1 \cdot 10^5$	72
HCHO	1.1	1666	1	$1 \cdot 10^5$	254
MeOOH	1.3	3650	1	$1 \cdot 10^5$	293
HCOOH	1.3	$1 \cdot 10^5$	1	2500	$1 \cdot 10^5$
CH_3COOH	1.3	$1 \cdot 10^5$	1	2500	$1 \cdot 10^5$
NH_3	0.9	500	1	$1 \cdot 10^5$	188
PAN	1.7	3994	1	$1 \cdot 10^5$	295
C_5H_8	1.5	500	1	$1 \cdot 10^5$	$1 \cdot 10^5$

Table A.1: Data used for the dry deposition model (Ganzeveld, 1999, *priv. comm.*, see Section 7.2.1). In case of infinite resistance $1 \cdot 10^5$ is applied.

Species	$D_g[\mathrm{cm^2\,s^{-1}}]$	α	k_H^{cp} [M atm^{-1}]	ΔH [K]
ACO$_3$	0.1	$1.9 \cdot 10^{-2}$	669	
Br$_2$	0.1	$3.0 \cdot 10^{-2}$	$7.58 \cdot 10^{-1}$	3800
CH$_3$CHO	0.122	$3.0 \cdot 10^{-2}$	4.8	5600
CH$_3$COOOH	0.102	$1.9 \cdot 10^{-2}$	$6.69 \cdot 10^{2}$	5300
CH$_3$O$_2$	0.135	$3.8 \cdot 10^{-3}$	6	6600
CH$_3$OH	0.116	$1.5 \cdot 10^{-2}$	$2.2 \cdot 10^{2}$	5200
Cl$_2$	0.128	$3.0 \cdot 10^{-2}$	$9.15 \cdot 10^{-2}$	2490
ETHP	0.108	$8.2 \cdot 10^{-3}$	6	6000
ETOH	0.095	$8.2 \cdot 10^{-3}$	$1.9 \cdot 10^{2}$	6600
H$_2$O$_2$	0.146	0.11	$1.05 \cdot 10^{5}$	7400
H$_2$SO$_4$	0.13	$7.0 \cdot 10^{-2}$	$2.1 \cdot 10^{5}$	
HAc	0.124	$1.9 \cdot 10^{-2}$	$5.5 \cdot 10^{3}$	6300
HCHO	0.164	$2.0 \cdot 10^{-2}$	2.5	6800
HCl	0.189	$6.4 \cdot 10^{-2}$	1.10	2021
HCOOH	0.153	$1.2 \cdot 10^{-2}$	$5.53 \cdot 10^{3}$	5700
HNO$_2$	0.13	0.5	49	4883
HNO$_3$	0.132	$5.4 \cdot 10^{-2}$	$2.1 \cdot 10^{5}$	8700
HO$_2$	0.104	$1.0 \cdot 10^{-2}$	$9. \cdot 10^{3}$	5900
HO$_2$NO$_2$	0.13	0.1	$1. \cdot 10^{5}$	6900
MHP	0.131	$3.8 \cdot 10^{-3}$	6	5200
N$_2$O$_5$	0.11	$3.7 \cdot 10^{-3}$	1.4	3400
NH$_3$	0.23	$4.0 \cdot 10^{-2}$	60.7	4200
NO	0.2	$5.0 \cdot 10^{-3}$	$1.9 \cdot 10^{-3}$	1500
NO$_2$	0.192	$1.5 \cdot 10^{-3}$	$1.2 \cdot 10^{-2}$	1263
NO$_3$	0.1	$4.0 \cdot 10^{-3}$	0.6	2000
O$_3$	0.148	$5.0 \cdot 10^{-2}$	$1.14 \cdot 10^{-2}$	2300
OH	0.153	$5.0 \cdot 10^{-2}$	25	4500
PAN	0.063	$1.9 \cdot 10^{-2}$	5	6500
SO$_2$	0.128	$3.5 \cdot 10^{-2}$	1.24	3247

Table A.2: Data used for the exchange between gas and aqueous phase. $k_H^{cc} = RTk_H^{cp}$, data for k_H^{cp} and for the enthalpy, ΔH, are taken from Sander (1999); data for α are taken from Mueller (1998) if available, otherwise set to 0.1 according to Jacob (1986), data for D_g are taken from CHEMIFOG (Bott and Carmichael, 1993) except for CH$_3$OOH (estimated).

Appendix B

Gas Phase Mechanism

Table B.1: List of gas phase species.

Species	Symbol
PROGNOSTIC	
ozone	O_3
oxygen – atomic ground state	$O(^3P)$
oxygen – atomic first singlet state	$O(^1D)$
hydroxyl radical	OH
perhydroxyl radical	HO_2
hydrogen peroxide	H_2O_2
nitric oxide	NO
nitrogen dioxide	NO_2
nitrogen trioxide	NO_3
dinitrogen pentoxide	N_2O_5
nitric acid	HNO_3
peroxynitric acid	HNO_4
methane	CH_4
methylperoxy radical	MeO_2
methyl hydro peroxide	MeOOH
formaldehyde	HCHO
carbon monoxide	CO
methanol	MeOH
ammonia	NH_3
	NH_2
	. . . to be continued.

continued ...	
Species	Symbol
	NH_2O
nitrous oxide	N_2O
ethan	C_2H_6
ethylperoxy radical	EtO_2
ethyl hydro peroxide	EtOOH
acetaldehyde	ALD
peroxyacetylnitrate	PAN
peroxy acetyl radical	PA
peroxy acetylic acid	PAA
acetic acid	CH_3COOH
ethanol	EtOH
formic acid	HCOOH
hydroxy acetone	ACETOL
methyl glyoxal	MGLO
nitrous acid	HONO
nitrate from the methyl peroxy radical	MeO2NO2
isoprene	ISOP
isoprene (hydro) peroxides	ISOOH
methyl vinyl ketone + methacrolein	MVK
MVK (hydro) peroxides	MVKOOH
peroxymethacryloyl nitrate	MPAN
organic C5-nitrates	ONIT
nito-oxy acetaldehyde	NACA
isoprene (hydroxy) peroxy radicals	ISO2
MVK peroxy radicals	MVKO2
sulphur dioxide	SO2
sulphuric acid	H2SO4
FIXED	
water	H_2O
oxygen	O_2

Table B.2: Gas phase mechanism. The units for rate constants k of first-order reactions are s^{-1}; of second order reactions, cm^3 s^{-1}; and for third-order reactions, cm^6 s^{-1}. F(k$_0^{300}$, n, k$_\infty^{300}$, m, F$_c$) describes the Troe expression from DeMore et al. (1997).

No.	Reaction	Rate Constant, k	Reference
RB.1	$O_3 + h\nu \longrightarrow O(^1D)$	$J(O(^1D))$	DeMore et al. (1997)
RB.2	$O_3 + h\nu \longrightarrow O(^3P)$	$J(O(^3P))$	DeMore et al. (1997)
RB.3	$O(^1D) + M \longrightarrow O(^3P)$	$1.8 \cdot 10^{-11} \exp(110./T)\,[N_2] + 3.2 \cdot 10^{-11} \exp(70./T)\,[O_2]$	DeMore et al. (1997)
RB.4	$O(^3P) + O_2 \longrightarrow O_3$	$6.0 \cdot 10^{-34} \cdot (T/300.)^{-2.3}\,[M]$	DeMore et al. (1997)
RB.5	$O(^3P) + O_3 \longrightarrow O_2$	$8.0 \cdot 10^{-12} \exp(-2060./T)$	DeMore et al. (1997)
RB.6	$O(^1D) + H_2O \longrightarrow 2\,OH$	$2.2 \cdot 10^{-10}$	DeMore et al. (1997)
RB.7	$O(^1D) + H_2 \longrightarrow OH + HO_2$	$1.1 \cdot 10^{-10}$	DeMore et al. (1997)
RB.8	$O(^1D) + CH_4 \longrightarrow 0.75\,MeO_2 + 0.75\,OH + 0.25\,HCHO + 0.4\,HO_2$	$1.5 \cdot 10^{-10}$	DeMore et al. (1997)
RB.9	$O_3 + OH \longrightarrow HO_2$	$1.5 \cdot 10^{-12} \exp(-880./T)$	Sander et al. (2000)
RB.10	$O_3 + HO_2 \longrightarrow OH$	$2. \cdot 10^{-14} \exp(-680./T)$	Sander et al. (2000)
RB.11	$HO_2 + OH \longrightarrow H_2O$	$4.8 \cdot 10^{-11} \exp(250./T)$	DeMore et al. (1997)
RB.12	$2\,HO_2 \longrightarrow H_2O_2$	$(k_a + k_b)(1 + k_c)$ $k_a = 2.3 \cdot 10^{-13} \exp(600/T)$ $k_b = 1.7 \cdot 10^{-33} \exp(1000/T)\,[M]$ $k_c = 1.4 \cdot 10^{-21} \exp(2200/T)\,[H_2O]$	DeMore et al. (1997)
RB.13	$H_2O_2 + h\nu \longrightarrow 2\,OH$	$J(H_2O_2)$	DeMore et al. (1997)
RB.14	$OH + H_2O_2 \longrightarrow HO_2$	$2.9 \cdot 10^{-12} \exp(-160./T)$	DeMore et al. (1997)
RB.15	$OH + H_2 \longrightarrow HO_2 + H_2O$	$5.5 \cdot 10^{-12} \exp(-2000./T)$	DeMore et al. (1997)
RB.16	$OH + CO \longrightarrow HO_2 + CO_2$	$1.5 \cdot 10^{-13} \cdot (1. + 0.6 \cdot P_{atm})$	DeMore et al. (1997)
RB.17	$CH_4 + OH \longrightarrow MeO_2 + H_2O$	$2.8 \cdot 10^{-14} \cdot T^{2/3} \cdot \exp(-1575./T)$	DeMore et al. (1997)

. . . to be continued.

No.	Reaction	Rate Constant, k	Reference
R.B.18	$MeO_2 + HO_2 \longrightarrow MeOOH$	$4.15 \cdot 10^{-13} \exp(750./T)$	Tyndall et al. (2001)
R.B.19	$MeO_2 + NO \longrightarrow HCHO + HO_2 + NO_2$	$2.8 \cdot 10^{-12} \exp(300./T)$	Tyndall et al. (2001)
R.B.20	$MeO_2 + MeO_2 \longrightarrow HCHO + MeOH$	$9.5 \cdot 10^{-14} \exp(390./T)/(1.+26.2 \exp(-1130./T))$	Tyndall et al. (2001)
R.B.21	$MeO_2 + MeO_2 \longrightarrow 2\,HCHO + 2\,HO_2$	$9.5 \cdot 10^{-14} \exp(390./T)/(1.+1./26.2 \exp(1130./T))$	Tyndall et al. (2001)
R.B.22	$MeO_2 + NO_3 \longrightarrow HCHO + HO_2 + NO_2$	$1.3 \cdot 10^{-12}$	Atkinson et al. (2001)
R.B.23	$MeO_2 + O_3 \longrightarrow HCHO + HO_2$	$3.0 \cdot 10^{-16} \exp(-1000./T)$	Tyndall et al. (2001)
R.B.24	$MeOH + OH \longrightarrow HCHO + HO_2$	$6.7 \cdot 10^{-12} \exp(-600./T)$	DeMore et al. (1997)
R.B.25	$MeOOH + h\nu \longrightarrow HCHO + HO_2 + OH$	$J(CH_3OOH)$	DeMore et al. (1997)
R.B.26	$MeOOH + OH \longrightarrow 0.7\,MeO_2 + 0.3\,HCHO + 0.3\,OH$	$3.8 \cdot 10^{-12} \exp(200./T)$	DeMore et al. (1997)
R.B.27	$HCHO + h\nu \longrightarrow CO + 2\,HO_2$	$J(CHOH)$	DeMore et al. (1997)
R.B.28	$HCHO + h\nu \longrightarrow CO$	$J(COH_2)$	DeMore et al. (1997)
R.B.29	$HCHO + OH \longrightarrow CO + HO_2$	$1. \cdot 10^{-11}$	DeMore et al. (1997)
R.B.30	$HCHO + O(^3P) \longrightarrow OH + HO_2 + CO$	$3.4 \cdot 10^{-11} \exp(-1600./T)$	DeMore et al. (1997)
R.B.31	$HCHO + NO_3 \longrightarrow HNO_3 + CO + HO_2$	$3.4 \cdot 10^{-13} \exp(-1900./T)$	DeMore et al. (1997), Stockwell et al. (1997)
R.B.32	$NO + O_3 \longrightarrow NO_2 + O_2$	$3. \cdot 10^{-12} \exp(-1500./T)$	Sander et al. (2000)

. . . to be continued.

No.	Reaction	Rate Constant, k	Reference
R.B.33	$NO + HO_2 \longrightarrow NO_2 + OH$	$3.5 \cdot 10^{-12} \exp(250./T)$	DeMore et al. (1997)
R.B.34	$NO + O(^3P) \longrightarrow NO_2$	$F(9.0 \cdot 10^{-32}, 1.5, 3.0 \cdot 10^{-11}, 0.0, 0.6)$	DeMore et al. (1997)
R.B.35	$NO + NO + O_2 \longrightarrow 2NO_2$	$3.3 \cdot 10^{-39} \exp(530./T)$	Atkinson et al. (2001)
R.B.36	$NO_2 + h\nu \longrightarrow NO + O(^3P)$	$J(NO_2)$	DeMore et al. (1997)
R.B.37	$NO_2 + O_3 \longrightarrow NO_3$	$1.2 \cdot 10^{-13} \exp(-2450./T)$	DeMore et al. (1997)
R.B.38	$NO_2 + O(^3P) \longrightarrow NO + O_2$	$5.6 \cdot 10^{-12} \exp(180./T)$	Sander et al. (2000)
R.B.39	$NO_2 + O(^3P) \longrightarrow NO_3$	$F(9.0 \cdot 10^{-32}, 2.0, 2.2 \cdot 10^{-11}, 0.0, 0.6)$	DeMore et al. (1997)
R.B.40	$NO_2 + OH \longrightarrow HNO_3$	k_{NO_2+OH}	Dransfield et al. (1999)
R.B.41	$NO_2 + HO_2 + M \longrightarrow HNO_4$	$F(1.8 \cdot 10^{-31}, 3.2, 4.7 \cdot 10^{-12}, 1.4, 0.6)$	DeMore et al. (1997)
R.B.42	$HNO_3 + h\nu \longrightarrow OH + NO_2$	$J(HNO_3)$	DeMore et al. (1997)
R.B.43	$HNO_3 + OH \longrightarrow NO_3$	$k_d + k_f/(1 + k_f/k_e)$ $k_d = 2.4 \times 10^{-14} \exp(460/T)$ $k_e = 2.7 \times 10^{-17} \exp(2199/T)$ $k_f = 6.5 \times 10^{-34} \exp(1335/T) \, [M]$	Sander et al. (2000)
R.B.44	$NO_3 + h\nu \longrightarrow NO_2 + O(^3P)$	$J(NO_3)_b$	DeMore et al. (1997)
R.B.45	$NO_3 + h\nu \longrightarrow NO + O_2$	$J(NO_3)_b$	DeMore et al. (1997)
R.B.46	$NO_3 + NO \longrightarrow 2NO_2$	$1.5 \cdot 10^{-11} \exp(170./T)$	DeMore et al. (1997)
R.B.47	$NO_3 + NO_2 \longrightarrow N_2O_5$	$F(2.0 \cdot 10^{-30}, 4.4, 1.4 \cdot 10^{-12}, 0.7, 0.6)$	Sander et al. (2000)
R.B.48	$NO_3 + NO_3 \longrightarrow 2NO_2$	$8.5 \cdot 10^{-13} \exp(-2450./T)$	DeMore et al. (1997)
R.B.49	$NO_3 + OH \longrightarrow NO_2 + HO_2$	$2.2 \cdot 10^{-11}$	DeMore et al. (1997)
R.B.50	$NO_3 + HO_2 \longrightarrow .8\,OH + .8\,NO_2 + .2\,HNO_3$	$3.5 \cdot 10^{-12}$	DeMore et al. (1997)

No.	Reaction	Rate Constant, k	Reference
R.B.51	$N_2O_5 + h\nu \longrightarrow NO_3 + NO_2$	$J(N_2O_5)$	DeMore et al. (1997)
R.B.52	$N_2O_5 \overset{M}{\longrightarrow} NO_3 + NO_2$	$k_{NO_3+NO_2}/(3.0\cdot10^{-27}\exp(10991./T))$	Sander et al. (2000)
R.B.53	$N_2O_5 + H_2O \longrightarrow 2HNO_3$	$2.5\cdot10^{-22} + \cdot1.8\cdot10^{-39}[H_2O]$	Wahner et al. (1998)
R.B.54	$HNO_4 + h\nu \longrightarrow 0.39NO_3 + 0.39OH + 0.61NO_2 + 0.61HO_2$	$J(HNO_4)$	DeMore et al. (1997)
R.B.55	$HNO_4 \overset{M}{\longrightarrow} HO_2 + NO_2$	$k_{NO_2+HO_2}/(2.1\cdot10^{-27}\exp(10900./T))$	DeMore et al. (1997)
R.B.56	$HNO_4 + OH \longrightarrow NO_2$	$1.3\cdot10^{-12}\exp(380./T)$	DeMore et al. (1997)
R.B.57	$NH_3 + OH \longrightarrow NH_2 + H_2O$	$1.7\cdot10^{-12}\exp(-710./T)$	DeMore et al. (1997)
R.B.58	$NH_3 + O(^1D) \longrightarrow OH + NH_2$	$2.5\cdot10^{-10}$	DeMore et al. (1997)
R.B.59	$NH_2 + NO_2 \longrightarrow N_2O + H_2O$	$2.1\cdot10^{-12}\exp(650./T)$	DeMore et al. (1997)
R.B.60	$NH_2 + HO_2 \longrightarrow NH_3 + O_2$	$3.4\cdot10^{-11}$	DeMore et al. (1997)
R.B.61	$NH_2 + NO \longrightarrow H_2O$	$4.0\cdot10^{-12}\exp(450./T)$	DeMore et al. (1997)
R.B.62	$NH_2 + O_2 \longrightarrow NO + H_2O$	$6.0\cdot10^{-21}$	DeMore et al. (1997)
R.B.63	$NH_2 + O_3 \longrightarrow NH_2O + O_2$	$4.3\cdot10^{-12}\exp(-930./T)$	DeMore et al. (1997)
R.B.64	$N_2O + O(^1D) \longrightarrow O_2$	$4.9\cdot10^{-11}$	DeMore et al. (1997)
R.B.65	$N_2O + O(^1D) \longrightarrow 2NO$	$6.7\cdot10^{-11}$	DeMore et al. (1997)
R.B.66	$C_2H_6 + OH \longrightarrow EtO_2 + H_2O$	$1.51\cdot10^{-17}\cdot T^2\exp(-492./T)$	Atkinson (1994)
R.B.67	$EtO_2 + HO_2 \longrightarrow EtOOH$	$7.4\cdot10^{-13}\exp(700./T)$	Tyndall et al. (2001)
R.B.68	$EtO_2 + MeO_2 \longrightarrow 0.75HCHO + HO_2 + 0.75ALD + 0.25MeOH + 0.25EtOH$	$1.18\cdot10^{-13}\exp(158./T)$	Stockwell et al. (1997)
R.B.69	$EtO_2+NO \longrightarrow ALD+HO_2+NO_2$	$2.7\cdot10^{-12}\exp(350./T)$	Tyndall et al. (2001)

. . . to be continued.

No.	Reaction	Rate Constant, k	Reference
R.B.70	$EtO_2 + NO_3 \longrightarrow ALD + HO_2 + NO_2$	$2.3 \cdot 10^{-12}$	Atkinson et al. (2001)
R.B.71	$EtOH + OH \longrightarrow ALD + HO_2$	$7.0 \cdot 10^{-12} \exp(-235./T)$	DeMore et al. (1997)
R.B.72	$ALD + OH \longrightarrow PA + H_2O$	$5.6 \cdot 10^{-12} \exp(270./T)$	DeMore et al. (1997)
R.B.73	$ALD + NO_3 \longrightarrow PA + HNO_3$	$1.4 \cdot 10^{-12} \exp(-1900./T)$	DeMore et al. (1997)
R.B.74	$ALD + h\nu \longrightarrow MeO_2 + HO_2 + CO$	$J(CH_3CHO)$	DeMore et al. (1997)
R.B.75	$PA + HO_2 \longrightarrow PAA$	$4.3 \cdot 10^{-13} \exp(1040./T)/(1.+1./37. \exp(660./T))$	Tyndall et al. (2001)
R.B.76	$PA + HO_2 \longrightarrow CH_3COOH + O_3$	$4.3 \cdot 10^{-13} \exp(1040./T)/(1.+37. \exp(-660./T))$	Tyndall et al. (2001)
R.B.77	$PA + NO \longrightarrow MeO_2 + NO_2 + CO_2$	$8.1 \cdot 10^{-12} \exp(270./T)$	Tyndall et al. (2001)
R.B.78	$PA + NO_2 \longrightarrow PAN$	$F(8.5 \cdot 10^{-29}, 6.5, 1.1 \cdot 10^{-11}, 1.0, 0.6)$	Tyndall et al. (2001)
R.B.79	$PA + MeO_2 \longrightarrow HCHO + .9 HO_2 + .9 MeO_2 + .1 CH_3COOH$	$2.0 \cdot 10^{-12} \exp(500./T)$	Tyndall et al. (2001)
R.B.80	$PA + PA \longrightarrow MeO_2 + MeO_2$	$2.5 \cdot 10^{-12} \exp(500./T)$	Tyndall et al. (2001)
R.B.81	$PA + NO_3 \longrightarrow MeO_2 + NO_2$	$4.0 \cdot 10^{-12}$	Stockwell et al. (1997)
R.B.82	$PA + EtO_2 \longrightarrow ALD + .8 MeO_2 + .8 HO_2 + .2 CH_3COOH$	$1.0 \cdot 10^{-11}$	Atkinson et al. (2001), Villenave and Lesclaux (1996)
R.B.83	$PAA + h\nu \longrightarrow MeO_2$	$0.025 \cdot J(HCHO)_a$	von Kuhlmann (2001)
R.B.84	$PAA + OH \longrightarrow PA$	$3.8 \cdot 10^{-12} \exp(200./T)$	DeMore et al. (1997)
R.B.85	$PAN + OH \longrightarrow HCHO + NO_2$	$2. \cdot 10^{-14}$	DeMore et al. (1997)

No.	Reaction	Rate Constant, k	Reference
R.B.86	$PAN + h\nu \longrightarrow .8PA + .8NO_2 + .2MeO_2 + .2NO_3$	$J(PAN)$	DeMore et al. (1997)
R.B.87	$PAN \overset{M}{\longrightarrow} PA + NO_2$	$k_{PA+NO_2}/9.3 \cdot 10^{-29} \exp(-14000./T)$	Tyndall et al. (2001)
R.B.88	$EtOOH + h\nu \longrightarrow ALD + HO_2 + OH$	$J(CH_3OOH)$	DeMore et al. (1997)
R.B.89	$EtOOH + OH \longrightarrow 0.3EtO_2 + 0.7ALD + 0.7OH$	$3.8 \cdot 10^{-12} \exp(200./T)$	DeMore et al. (1997)
R.B.90	$CH_3COOH + OH \longrightarrow MeO_2$	$4.0 \cdot 10^{-13} \exp(200./T)$	DeMore et al. (1997)
R.B.91	$HCOOH + OH \longrightarrow HO_2 + H_2O$	$4.0 \cdot 10^{-13}$	DeMore et al. (1997)
R.B.92	$ISOP + OH \longrightarrow ISO_2$	$2.54 \cdot 10^{-11} \exp(410./T)$	Pöschl et al. (2000)
R.B.93	$ISOP + NO_3 \longrightarrow ONIT$	$3.03 \cdot 10^{-12} \exp(-446./T)$	Pöschl et al. (2000)
R.B.94	$ISOP + O_3 \longrightarrow .28HCOOH + .65MVK + .1MVKO_2 + .1PA + .14CO + .58HCHO + .09H_2O_2 + .08MeO_2 + .256OH + .246HO_2$	$7.86 \cdot 10^{-15} \exp(-1913./T)$	Pöschl et al. (2000)
R.B.95	$ISO_2 + HO_2 \longrightarrow ISOOH$	$2.05446 \cdot 10^{-13} \exp(1300./T)$	Pöschl et al. (2000)
R.B.96	$ISO_2 + NO \longrightarrow NO_2 + MVK + HCHO + HO_2$	$2.428 \cdot 10^{-12} \exp(360./T)$	Pöschl et al. (2000)
R.B.97	$ISO_2 + NO \longrightarrow ONIT$	$0.112 \cdot 10^{-12} \exp(360./T)$	Pöschl et al. (2000)
R.B.98	$ISOOH + h\nu \longrightarrow MVK + .8HCHO + HO_2 + OH$	$J(MeOOH)$	Pöschl et al. (2000)
R.B.99	$ISOOH + OH \longrightarrow MVK + OH$	$1. \cdot 10^{-10}$	Pöschl et al. (2000)

...to be continued.

No.	Reaction	Rate Constant, k	Reference
R.B.100	MVK + OH $\longrightarrow$ MVKO$_2$	$0.5 \cdot (4.1 \cdot 10^{-12}\exp(452./\text{T}) + 1.9 \cdot 10^{-11}\exp(175./\text{T}))$	Pöschl et al. (2000)
R.B.101	MVK + hν $\longrightarrow$ PA + HCHO + CO + HO$_2$	$0.1122243 \cdot J(\text{HCHO})_b$	von Kuhlmann, pers. comm.
R.B.102	MVK + O$_3$ $\longrightarrow$ .45 HCOOH + .9 MGLO + .1 PA + .19 OH + .225 CO + .315 HO$_2$	$0.5 \cdot (1.36 \cdot 10^{-15}\exp(-2112./\text{T}) + 7.51 \cdot 10^{-16}\exp(-1521./\text{T}))$	Pöschl et al. (2000)
R.B.103	MVKO$_2$+NO $\longrightarrow$ NO$_2$+.25 PA+ .25 ACETOL + .75 HCHO + .25 CO +.75 HO$_2$ + .5 MGLO	$2.54 \cdot 10^{-12}\exp(360./\text{T})$	Pöschl et al. (2000)
R.B.104	MVKO$_2$ + HO$_2$ $\longrightarrow$ MVKOOH	$1.82 \cdot 10^{-13}\exp(1300/\text{T})$	Pöschl et al. (2000)
R.B.105	MVKOOH + hν $\longrightarrow$ OH + .5 MGLO + .25 ACETOL + .75 HCHO + .75 HO$_2$ + .25 PA + .25 CO	$J(\text{MeOOH})$	
R.B.106	MVKOOH + OH $\longrightarrow$ MVKO$_2$	$3. \cdot 10^{-11}$	Pöschl et al. (2000)
R.B.107	ONIT + OH $\longrightarrow$ ACETOL + NACA	$1.3 \cdot 10^{-11}$	Pöschl et al. (2000)
R.B.108	ONIT +hν $\longrightarrow$ MVK + HCHO + NO$_2$ + HO$_2$	$3.5 \cdot J(\text{HNO}_3)$	von Kuhlmann, pers. comm.
R.B.109	MVKO$_2$ + NO$_2$ $\longrightarrow$ MPAN	$.25 \cdot k_{\text{PA+NO}_2}$	Pöschl et al. (2000)
R.B.110	MPAN+OH $\longrightarrow$ ACETOL+NO$_2$	$3.6 \cdot 10^{-12}$	Pöschl et al. (2000)
R.B.111	MPAN $\overset{\text{M}}{\longrightarrow}$ MVKO$_2$ + NO$_2$	$k_{PAN \to PA+NO_2}$	

...to be continued.

No.	Reaction	Rate Constant, k	Reference
R.B.112	$ISO_2 + ISO_2 \longrightarrow$ 2 MVK + HCHO + HO$_2$	$2.\cdot 10^{-12}$	Pöschl et al. (2000)
R.B.113	MVKO$_2$ + MVKO$_2$ $\longrightarrow$ ACETOL + MGLO + .5 CO + .5 HCHO + HO$_2$	$2.\cdot 10^{-12}$	Pöschl et al. (2000)
R.B.114	NACA + OH $\longrightarrow$ NO$_2$ + HCHO + CO	$5.6\cdot 10^{-12}\exp(270./T)$	Pöschl et al. (2000)
R.B.115	NACA + hν $\longrightarrow$ NO$_2$ + HCHO + CO	$J(CH_3CHO)$	
R.B.116	ACETOL + OH $\longrightarrow$ MGLO + HO$_2$	$3.0\cdot 10^{-12}$	Atkinson et al. (2001)
R.B.117	ACETOL+hν $\longrightarrow$ PA+HCHO+ HO$_2$	$0.11\cdot J(HCHO)_a$	von Kuhlmann (2001)
R.B.118	MGLO + OH $\longrightarrow$ PA + CO	$8.4\cdot 10^{-13}\exp(830./T)$	Tyndall et al. (1995)
R.B.119	MGLO+hν $\longrightarrow$ PA+CO+HO$_2$	$3.77\cdot J(HCHO)_b$	von Kuhlmann, pers. comm.
R.B.120	MGLO + NO$_3$ $\longrightarrow$ PA + CO + HNO$_3$	k_{ALD+NO_3}	
R.B.121	SO$_2$ + OH $\longrightarrow$ H$_2$SO$_4$ + HO$_2$	$F(3.\cdot 10^{-31}, 3.3, 1.5\cdot 10^{-12}, 0., 0.6)$	DeMore et al. (1997)

Appendix C

Aqueous Phase Mechanism

The aqueous phase chemical mechanism is based on CAPRAM2.3 (Herrmann et al., 2000) and includes updates of kinetic data by Ervens (2001, *priv. comm.*).

No.	Reaction
P C.1	$H_2O_2 + hv \longrightarrow 2OH$
P C.2	$[Fe(OH)]^{2+} + hv \longrightarrow Fe^{2+} + OH$
P C.3	$FeOH_2^+ + hv \longrightarrow Fe^{2+} + OH + OH^-$
P C.4	$FeSO_4^+ + hv \longrightarrow Fe^{2+} + SO_4^-$
P C.5	$NO_2^- + hv \xrightarrow{H^+} NO + OH$
P C.6	$NO_3^- + hv \xrightarrow{H^+} NO_2 + OH$

Table C.1: List of aqueous phase photolysis reactions. Photolysis frequencies are calculated with the model of Landgraf and Crutzen (1998) (see Section 6.3).

Table C.2: List of aqueous phase chemical reactions taken from the CAPRAM2.3 mechanism (Herrmann et al., 2000). k_{298} is the rate constant at a temperature of 298 K; M = mole l^{-1}; n = reaction order $-$ 1; E_a is the activation energy.

No.	Reaction	k_{298} [M^{-n}s^{-1}]	E_a/R [K]
	— HO$_x$ - TMI-chemistry —		
R.C.1	$H_2O_2 + Fe^{3+} \longrightarrow HO_2 + H^+ + Fe^{2+}$	$2.0 \cdot 10^{-3}$	
R.C.2	$H_2O_2 + [Fe(OH)]^{2+} \longrightarrow HO_2 + H_2O + Fe^{2+}$	$2.0 \cdot 10^{-3}$	
R.C.3	$H_2O_2 + [Fe(OH)_2]^+ \longrightarrow HO_2 + OH^- + Fe^{2+} + H_2O$	$2.0 \cdot 10^{-3}$	
R.C.4	$H_2O_2 + Fe^{2+} \longrightarrow OH + OH^- + Fe^{3+}$	76	
R.C.5	$H_2O_2 + Mn^{3+} \longrightarrow HO_2 + H^+ + Mn^{2+}$	$7.3 \cdot 10^4$	
R.C.6	$H_2O_2 + Cu^+ \longrightarrow OH + OH^- + Cu^{2+}$	$7.0 \cdot 10^3$	
R.C.7	$O_2^- + Fe^{3+} \longrightarrow O_2 + Fe^{2+}$	$1.5 \cdot 10^8$	
R.C.8	$HO_2 + [Fe(OH)]^{2+} \longrightarrow Fe^{2+} + O_2 + H_2O$	$1.3 \cdot 10^5$	
R.C.9	$O_2^- + [Fe(OH)]^{2+} \longrightarrow O_2 + Fe^{2+} + OH^-$	$1.5 \cdot 10^8$	
R.C.10	$O_2^- + [Fe(OH)_2]^+ \longrightarrow O_2 + Fe^{2+} + 2OH^-$	$1.5 \cdot 10^8$	
R.C.11	$O_2^- + Fe^{2+} \xrightarrow{2H^+} H_2O_2 + Fe^{3+}$	$1.0 \cdot 10^7$	
R.C.12	$HO_2 + Fe^{2+} \xrightarrow{H^+} H_2O_2 + Fe^{3+}$	$1.2 \cdot 10^6$	5050
R.C.13	$OH + Fe^{2+} \longrightarrow [Fe(OH)]^{2+}$	$4.3 \cdot 10^8$	1100
R.C.14	$O_2^- + Mn^{2+} \xrightarrow{2H^+} H_2O_2 + Mn^{3+}$	$1.1 \cdot 10^8$	
R.C.15	$HO_2 + Mn^{2+} \xrightarrow{H^+} H_2O_2 + Mn^{3+}$	$2.0 \cdot 10^5$	
R.C.16	$OH + Mn^{2+} \longrightarrow OH^- + Mn^{3+}$	$2.6 \cdot 10^7$	
R.C.17	$O_2^- + Cu^+ \xrightarrow{2H^+} H_2O_2 + Cu^{2+}$	$9.4 \cdot 10^9$	
R.C.18	$HO_2 + Cu^+ \xrightarrow{H^+} H_2O_2 + Cu^{2+}$	$2.2 \cdot 10^9$	
R.C.19	$OH + Cu^+ \longrightarrow OH^- + Cu^{2+}$	$3.0 \cdot 10^9$	
R.C.20	$HO_2 + Cu^{2+} \longrightarrow O_2 + Cu^+ + H^+$	$1.2 \cdot 10^9$	
R.C.21	$O_2^- + Cu^{2+} \longrightarrow O_2 + Cu^+$	$1.1 \cdot 10^{10}$	

...to be continued.

... *continued*

No.	Reaction	k_{298} [M^{-n}s^{-1}]	E_a/R [K]
R.C.22	$Fe^{3+} + Cu^+ \longrightarrow Fe^{2+} + Cu^{2+}$	$3.0 \cdot 10^7$	
R.C.23	$[Fe(OH)]^{2+} + Cu^+ \longrightarrow Fe^{2+} + Cu^{2+} + OH^-$	$3.0 \cdot 10^7$	
R.C.24	$FeOH_2^+ + Cu^+ \longrightarrow Fe^{2+} + Cu^{2+} + 2OH^-$	$3.0 \cdot 10^7$	
R.C.25	$Fe^{2+} + Mn^{3+} \longrightarrow Fe^{3+} + Mn^{2+}$	$1.5 \cdot 10^4$	
R.C.26	$O_3 + O_2^- \xrightarrow{H^+} 2O_2 + OH$	$1.5 \cdot 10^9$	
R.C.27	$HO_2 + HO_2 \longrightarrow O_2 + H_2O_2$	$8.3 \cdot 10^5$	2720
R.C.28	$HO_2 + O_2^- \xrightarrow{H^+} H_2O_2 + O_2$	$9.7 \cdot 10^7$	1060
R.C.29	$HO_2 + OH \longrightarrow H_2O + O_2$	$1.0 \cdot 10^{10}$	
R.C.30	$O_2^- + OH \longrightarrow OH^- + O_2$	$1.1 \cdot 10^{10}$	2120
R.C.31	$H_2O_2 + OH \longrightarrow HO_2 + H_2O$	$3.0 \cdot 10^7$	1680
R.C.32	$MHP + OH \longrightarrow CH_3O_2 + H_2O$	$3.0 \cdot 10^7$	1680
R.C.33	$HSO_3^- + OH \longrightarrow H_2O + SO_3^-$	$2.7 \cdot 10^9$	
R.C.34	$SO_3^{2-} + OH \longrightarrow OH^- + SO_3^-$	$4.6 \cdot 10^9$	
— N - chemistry —			
R.C.35	$N2O_5 + H_2O \longrightarrow 2H^+ + 2NO_3^-$	$5.0 \cdot 10^9$	
R.C.36	$NO_3 + OH^- \longrightarrow NO_3^- + OH$	$9.4 \cdot 10^7$	2700
R.C.37	$NO_3 + Fe^{2+} \longrightarrow NO_3^- + Fe^{3+}$	$8.0 \cdot 10^6$	
R.C.38	$NO_3 + Mn^{2+} \longrightarrow NO_3^- + Mn^{3+}$	$1.1 \cdot 10^6$	
R.C.39	$NO_3 + H_2O_2 \longrightarrow NO_3^- + H^+ + HO_2$	$4.9 \cdot 10^6$	2000
R.C.40	$NO_3 + MHP \longrightarrow NO_3^- + H^+ + CH_3O_2$	$4.9 \cdot 10^6$	2000
R.C.41	$NO_3 + HO_2 \longrightarrow NO_3^- + H^+ + O_2$	$3.0 \cdot 10^9$	
R.C.42	$NO_3 + O_2^- \longrightarrow NO_3^- + O_2$	$3.0 \cdot 10^9$	

...to be continued.

...continued

No.	Reaction	k_{298} [M^{-n}s^{-1}]	E_a/R [K]
R C.43	$NO_3 + HSO_3^- \longrightarrow NO_3^- + H^+ + SO_3^-$	$1.3 \cdot 10^9$	2000
R C.44	$NO_3 + SO_3^{2-} \longrightarrow NO_3^- + SO_3^-$	$3.0 \cdot 10^8$	
R C.45	$NO_3 + HSO_4^- \longrightarrow NO_3^- + H^+ + SO_4^-$	$2.6 \cdot 10^5$	
R C.46	$NO_3 + SO_4^{2-} \longrightarrow NO_3^- + SO_4^-$	$1.0 \cdot 10^5$	
R C.47	$NO_2 + OH \longrightarrow NO_3^- + H^+$	$1.2 \cdot 10^{10}$	
R C.48	$NO_2 + O_2^- \longrightarrow NO_2^- + O_2$	$1.0 \cdot 10^8$	
R C.49	$NO_2 + NO_2 \xrightarrow{H_2O} HNO_2 + NO_3^- + H^+$	$8.4 \cdot 10^7$	-2900
R C.50	$O_2NO_2^- \longrightarrow NO_2^- + O_2$	$4.5 \cdot 10^{-2}$	
R C.51	$NO_2^- + OH \longrightarrow NO_2 + OH^-$	$1.1 \cdot 10^{10}$	
R C.52	$NO_2^- + SO_4^- \longrightarrow SO_4^{2-} + NO_2$	$7.2 \cdot 10^8$	
R C.53	$NO_2^- + NO_3 \longrightarrow NO_3^- + NO_2$	$1.4 \cdot 10^9$	0
R C.54	$NO_2^- + Cl_2^- \longrightarrow 2Cl^- + NO_2$	$6.0 \cdot 10^7$	
R C.55	$NO_2^- + Br_2^- \longrightarrow 2Br^- + NO_2$	$1.2 \cdot 10^7$	1720
R C.56	$NO_2^- + CO_3^- \longrightarrow CO_3^{2-} + NO_2$	$6.6 \cdot 10^5$	850
R C.57	$NO_2^- + O_3 \longrightarrow NO_3^- + O_2$	$5.0 \cdot 10^5$	7000
R C.58	$HNO_2 + OH \longrightarrow NO_2 + H_2O$	$1.0 \cdot 10^9$	
R C.59	$HO_2NO_2 + HSO_3^- \longrightarrow HSO_4^- + NO_3$	$3.5 \cdot 10^5$	
	— S - chemistry —		
R C.60	$HMS^- + OH \xrightarrow{O_2/H_2O} H_2O + HO_2 + HCOOH + HSO_3^-$	$3.0 \cdot 10^8$	
R C.61	$HMS^- + SO_4^- \longrightarrow SO_4^{2-} + H^+ + HCHO + SO_3^-$	$2.8 \cdot 10^6$	
R C.62	$HMS^- + NO_3 \longrightarrow NO_3^- + H^+ + HCHO + SO_3^-$	$4.2 \cdot 10^6$	
R C.63	$HMS^- + Cl2^- \longrightarrow 2Cl^- + H^+ + HCHO + SO_3^-$	$5.0 \cdot 10^5$	

...to be continued.

... *continued*

No.	Reaction	k_{298} [$M^{-n}s^{-1}$]	E_a/R [K]
R.C.64	$HMS^- + Br\cdot2^- \longrightarrow 2Br^- + H^+ + HCHO + SO_3^-$	$5.0 \cdot 10^4$	
R.C.65	$HSO_3^- + H_2O_2 + H^+ \longrightarrow SO_4^{2-} + H_2O + 2H^+$	$6.9 \cdot 10^7$	4000
R.C.66	$HSO_3^- + MHP + H^+ \longrightarrow SO_4^{2-} + 2H^+ + CH_3OH$	$1.8 \cdot 10^7$	3800
R.C.67	$HSO_3^- + CH_3COOOH + H^+ \longrightarrow SO_4^{2-} + 2H^+ + P$	$4.8 \cdot 10^7$	3990
R.C.68	$SO_2 + O_3 \xrightarrow{H_2O} HSO_4^- + O_2 + H^+$	$2.4 \cdot 10^4$	
R.C.69	$HSO_3^- + O_3 \longrightarrow HSO_4^- + O_2$	$3.7 \cdot 10^5$	5530
R.C.70	$SO_3^{2-} + O_3 \longrightarrow SO_4^{2-} + O_2$	$1.5 \cdot 10^9$	5280
R.C.71	$[Fe(OH)]^{2+} + HSO_3^- \longrightarrow Fe^{2+} + SO_3^- + H_2O$	39	
R.C.72	$Fe^{2+} + SO_5^- \xrightarrow{H_2O} [Fe(OH)]^{2+} + HSO_5^-$	$4.3 \cdot 10^7$	
R.C.73	$Fe^{2+} + HSO_5^- \longrightarrow [Fe(OH)]^{2+} + SO_4^-$	$3.0 \cdot 10^4$	
R.C.74	$Mn^{2+} + SO_5^- \xrightarrow{H_2O} Mn^{3+} + HSO_5^- + OH^-$	$4.6 \cdot 10^6$	
R.C.75	$Fe^{2+} + SO_4^- \xrightarrow{H_2O} [Fe(OH)]^{2+} + SO_4^{2-} + H^+$	$3.5 \cdot 10^7$	
R.C.76	$Fe^{2+} + S_2O_8^{2-} \xrightarrow{H_2O} [Fe(OH)]^{2+} + SO_4^{2-} + SO_4^- + H^+$	17	
R.C.77	$SO_5^- + SO_5^- \longrightarrow S2O8^{2-} + O_2$	$1.8 \cdot 10^8$	2600
R.C.78	$SO_5^- + SO_5^- \longrightarrow 2SO_4^- + O_2$	$7.2 \cdot 10^6$	2600
R.C.79	$SO_5^- + HO_2 \longrightarrow HSO_5^- + O_2$	$1.7 \cdot 10^9$	
R.C.80	$SO_5^- + O_2^- \xrightarrow{H_2O} HSO_5^- + OH^- + O_2$	$1.7 \cdot 10^9$	
R.C.81	$SO_3^- + O_2 \longrightarrow SO_5^-$	$2.5 \cdot 10^9$	
R.C.82	$SO_5^- + HSO_3^- \longrightarrow HSO_5^- + SO_3^-$	$8.6 \cdot 10^3$	
R.C.83	$SO_5^- + HSO_3^- \longrightarrow SO_4^{2-} + SO_4^- + H^+$	$3.6 \cdot 10^2$	
R.C.84	$SO_5^- + SO_3^{2-} \xrightarrow{H^+} HSO_5^- + SO_3^-$	$2.13 \cdot 10^5$	
R.C.85	$SO_5^- + SO_3^{2-} \longrightarrow SO_4^- + SO_4^{2-}$	$5.5 \cdot 10^5$	

...continued

No.	Reaction	k_{298} [M^{-n}s^{-1}]	E_a/R [K]
R.C.86	OH + HSO$_4^-$ $\longrightarrow$ H$_2$O + SO$_4^-$	$3.5 \cdot 10^5$	
R.C.87	SO$_4^-$ + SO$_4^-$ $\longrightarrow$ S2O8^{2-}	$1.6 \cdot 10^8$	
R.C.88	SO$_4^-$ + HSO$_3^-$ $\longrightarrow$ SO$_4^{2-}$ + SO$_3^-$ + H$^+$	$3.2 \cdot 10^8$	
R.C.89	SO$_4^-$ + SO$_3^{2-}$ $\longrightarrow$ SO$_4^{2-}$ + SO$_3^-$	$3.2 \cdot 10^8$	1200
R.C.90	SO$_4^-$ + Fe^{2+} $\longrightarrow$ FeSO$_4^+$	$3.0 \cdot 10^8$	
R.C.91	SO$_4^-$ + Mn^{2+} $\longrightarrow$ SO$_4^{2-}$ + Mn^{3+}	$2.0 \cdot 10^7$	
R.C.92	SO$_4^-$ + Cu$^+$ $\longrightarrow$ SO$_4^{2-}$ + Cu^{2+}	$3.0 \cdot 10^8$	
R.C.93	SO$_4^-$ + H$_2$O$_2$ $\longrightarrow$ SO$_4^{2-}$ + H$^+$ + HO$_2$	$2.8 \cdot 10^7$	
R.C.94	SO$_4^-$ + MHP $\longrightarrow$ SO$_4^{2-}$ + H$^+$ + CH$_3$O$_2$	$2.8 \cdot 10^7$	
R.C.95	SO$_4^-$ + HO$_2$ $\longrightarrow$ SO$_4^{2-}$ + H$^+$ + O$_2$	$3.5 \cdot 10^9$	
R.C.96	SO$_4^-$ + O$_2^-$ $\longrightarrow$ SO$_4^{2-}$ + O$_2$	$3.5 \cdot 10^9$	
R.C.97	SO$_4^-$ + NO$_3^-$ $\longrightarrow$ SO$_4^{2-}$ + NO$_3$	$5.0 \cdot 10^4$	
R.C.98	SO$_4^-$ + OH$^-$ $\longrightarrow$ SO$_4^{2-}$ + OH	$1.4 \cdot 10^7$	
R.C.99	SO$_4^-$ + H$_2$O $\longrightarrow$ SO$_4^{2-}$ + H$^+$ + OH	11	1110
R.C.100	HSO$_5^-$ + HSO$_3^-$ + H$^+$ $\longrightarrow$ 2SO$_4^{2-}$ + 3H$^+$	$7.14 \cdot 10^6$	
R.C.101	HSO$_5^-$ + SO$_3^{2-}$ + H$^+$ $\longrightarrow$ 2SO$_4^{2-}$ + 2H$^+$	$7.14 \cdot 10^6$	
R.C.102	HSO$_5^-$ + OH $\longrightarrow$ SO$_5^-$ + H$_2$O	$1.7 \cdot 10^7$	
	— ORGANIC CHEMISTRY —		
R.C.103	CH$_3$OH + OH $\xrightarrow{O_2}$ H$_2$O + HO$_2$ + HCHO	$1.0 \cdot 10^9$	580
R.C.104	CH$_3$OH + SO$_4^-$ $\xrightarrow{O_2}$ SO$_4^{2-}$ + H$^+$ + HO$_2$ + HCHO	$9.0 \cdot 10^6$	2190
R.C.105	CH$_3$OH + NO$_3$ $\xrightarrow{O_2}$ NO$_3^-$ + H$^+$ + HO$_2$ + HCHO	$5.4 \cdot 10^5$	4300
R.C.106	CH$_3$OH + Cl2$^-$ $\xrightarrow{O_2}$ 2Cl$^-$ + H$^+$ + HO$_2$ + HCHO	1000	5500

...to be continued.

... *continued*

No.	Reaction	k_{298} [M^{-n}s^{-1}]	E_a/R [K]
RC.107	$CH_3OH + Br2^- \xrightarrow{O_2} 2Br^- + H^+ + HO_2 + HCHO$	$5.4 \cdot 10^5$	
RC.108	$CH_3OH + CO_3^- \xrightarrow{O_2} CO_3^{2-} + H^+ + HO_2 + HCHO$	$2.6 \cdot 10^3$	
RC.109	$ETOH + OH \xrightarrow{O_2} H_2O + HO_2 + CH_3CHO$	$1.9 \cdot 10^9$	
RC.110	$ETOH + SO_4^- \xrightarrow{O_2} SO_4^{2-} + H^+ + HO_2 + CH_3CHO$	$4.1 \cdot 10^7$	1760
RC.111	$ETOH + NO_3 \xrightarrow{O_2} NO_3^- + H^+ + HO_2 + CH_3CHO$	$2.2 \cdot 10^6$	3300
RC.112	$ETOH + Cl2^- \xrightarrow{O_2} 2Cl^- + H^+ + HO_2 + CH_3CHO$	$1.2 \cdot 10^5$	
RC.113	$ETOH + Br2^- \xrightarrow{O_2} 2Br^- + H^+ + HO_2 + CH_3CHO$	$3.8 \cdot 10^3$	
RC.114	$ETOH + CO_3^- \xrightarrow{O_2} CO_3^{2-} + H^+ + HO_2 + CH_3CHO$	$1.5 \cdot 10^4$	
RC.115	$CH_2(OH)_2 + OH \xrightarrow{O_2} H_2O + HO_2 + HCOOH$	$1.0 \cdot 10^9$	1020.
RC.116	$CH_2(OH)_2 + SO_4^- \xrightarrow{O_2} SO_4^{2-} + H^+ + HO_2 + HCOOH$	$1.4 \cdot 10^7$	1300
RC.117	$CH_2(OH)_2 + NO_3 \xrightarrow{O_2} NO_3^- + H^+ + HO_2 + HCOOH$	$1.0 \cdot 10^6$	4500
RC.118	$CH_2(OH)_2 + Cl2^- \xrightarrow{O_2} 2Cl^- + H^+ + HO_2 + HCOOH$	$3.1 \cdot 10^4$	4400
RC.119	$CH_2(OH)_2 + Br2^- \xrightarrow{O_2} 2Br^- + H^+ + HO_2 + HCOOH$	$3.0 \cdot 10^3$	
RC.120	$CH_2(OH)_2 + CO_3^- \xrightarrow{O_2} CO_3^{2-} + H^+ + HO_2 + HCOOH$	$1.3 \cdot 10^4$	
RC.121	$CH_3CH(OH)_2 + OH \xrightarrow{O_2} H_2O + HO_2 + HAc$	$1.2 \cdot 10^9$	
RC.122	$CH_3CHO + OH \xrightarrow{O_2} HO_2 + HAc$	$3.6 \cdot 10^9$	
RC.123	$CH_3CH(OH)_2 + SO_4^- \xrightarrow{O_2} SO_4^{2-} + H^+ + HO_2 + HAc$	$1.0 \cdot 10^7$	
RC.124	$CH_3CH(OH)_2 + NO_3 \xrightarrow{O_2} NO_3^- + H^+ + HO_2 + HAc$	$1.9 \cdot 10^6$	
RC.125	$CH_3CH(OH)_2 + Cl2^- \xrightarrow{O_2} 2Cl^- + H^+ + HO_2 + HAc$	$4.0 \cdot 10^4$	
RC.126	$CH_3CH(OH)_2 + Br2^- \xrightarrow{O_2} 2Br^- + H^+ + HO_2 + HAc$	$4.0 \cdot 10^4$	
RC.127	$CH_3CH(OH)_2 + CO_3^- \xrightarrow{O_2} CO_3^{2-} + H^+ + HO_2 + HAc$	$1.0 \cdot 10^4$	
RC.128	$HCOOH + OH \xrightarrow{O_2} H_2O + HO_2 + CO_2$	$1.3 \cdot 10^8$	1000

... continued

No.	Reaction	k_{298} $[M^{-n}s^{-1}]$	E_a/R [K]
R C.129	$HCOO^- + OH \xrightarrow{O_2} OH^- + HO_2 + CO_2$	$4.0 \cdot 10^9$	1000
R C.130	$HCOOH + SO_4^- \xrightarrow{O_2} SO_4^{2-} + H^+ + HO_2 + CO_2$	$2.5 \cdot 10^6$	
R C.131	$HCOO^- + SO_4^- \xrightarrow{O_2} SO_4^{2-} + HO_2 + CO_2$	$2.1 \cdot 10^7$	
R C.132	$HCOOH + NO_3 \xrightarrow{O_2} NO_3^- + H^+ + HO_2 + CO_2$	$3.8 \cdot 10^5$	3400
R C.133	$HCOO^- + NO_3 \xrightarrow{O_2} NO_3^- + HO_2 + CO_2$	$5.1 \cdot 10^7$	2200
R C.134	$HCOOH + Cl2^- \xrightarrow{O_2} 2Cl^- + H^+ + HO_2 + CO_2$	5500	4500
R C.135	$HCOO^- + Cl2^- \xrightarrow{O_2} 2Cl^- + HO_2 + CO_2$	$1.3 \cdot 10^6$	
R C.136	$HCOOH + Br2^- \xrightarrow{O_2} 2Br^- + H^+ + HO_2 + CO_2$	$4.0 \cdot 10^3$	
R C.137	$HCOO^- + Br2^- \xrightarrow{O_2} 2Br^- + HO_2 + CO_2$	$4.9 \cdot 10^3$	
R C.138	$HCOO^- + CO_3^- \xrightarrow{O_2} CO_3^{2-} + HO_2 + CO_2$	$1.4 \cdot 10^5$	3300
R C.139	$HAc + OH \xrightarrow{O_2} H_2O + ACO_3 + CO_2$	$1.5 \cdot 10^7$	1330
R C.140	$Ac^- + OH \xrightarrow{O_2} OH^- + ACO_3 + CO_2$	$1.0 \cdot 10^9$	1800
R C.141	$HAc + SO_4^- \xrightarrow{O_2} SO_4^{2-} + H^+ + ACO_3 + CO_2$	$2.0 \cdot 10^5$	
R C.142	$Ac^- + SO_4^- \xrightarrow{O_2} SO_4^{2-} + CH_3O_2 + CO_2$	$2.8 \cdot 10^7$	1210
R C.143	$HAc + NO_3 \xrightarrow{O_2} NO_3^- + H^+ + ACO_3 + CO_2$	$1.4 \cdot 10^4$	3800
R C.144	$Ac^- + NO_3 \xrightarrow{O_2} NO_3^- + CH_3O_2 + CO_2$	$2.9 \cdot 10^6$	3800
R C.145	$HAc + Cl2^- \xrightarrow{O_2} 2Cl^- + H^+ + ACO_3 + CO_2$	1950	4800
R C.146	$Ac^- + Cl2^- \xrightarrow{O_2} 2Cl^- + CH_3O_2 + CO_2$	$2.6 \cdot 10^5$	4800
R C.147	$HAc + Br2^- \xrightarrow{O_2} 2Br^- + H^+ + ACO_3 + CO_2$	10	
R C.148	$Ac^- + Br2^- \xrightarrow{O_2} 2Br^- + CH_3O_2 + CO_2$	100	
R C.149	$Ac^- + CO_3^- \xrightarrow{O_2} CO_3^{2-} + CH_3O_2 + CO_2$	580	
R C.150	$CH_3O_2 + CH_3O_2 \longrightarrow CH_3OH + HCHO + O_2$	$1.7 \cdot 10^8$	2200

... to be continued.

...continued

No.	Reaction	k_{298} $[\mathrm{M^{-n}s^{-1}}]$	E_a/R [K]
R.C.151	$CH_3O_2 + HSO_3^- \longrightarrow MHP + SO_3^-$	$5.0 \cdot 10^5$	
R.C.152	$ETHP + ETHP \longrightarrow Prod$	$1.5 \cdot 10^8$	-1500
R.C.153	$ACO_3 + ACO_3 \longrightarrow 2CH_3O_2 + 2CO_2 + O_2$	$1.5 \cdot 10^8$	
	— CHLORINE CHEMISTRY —		
R.C.154	$SO_4^- + Cl^- \longrightarrow SO_4^{2-} + Cl$	$3.3 \cdot 10^8$	0
R.C.155	$NO_3 + Cl^- \longrightarrow NO_3^- + Cl$	$1.0 \cdot 10^7$	4300
R.C.156	$Cl2^- + Cl2^- \longrightarrow Cl2 + 2Cl^-$	$8.7 \cdot 10^8$	
R.C.157	$Cl2^- + Fe^{2+} \longrightarrow 2Cl^- + Fe^{3+}$	$1.0 \cdot 10^7$	3030
R.C.158	$Cl2^- + Mn^{2+} \longrightarrow 2Cl^- + Mn^{3+}$	$8.5 \cdot 10^6$	4090
R.C.159	$Cl2^- + Cu^+ \longrightarrow 2Cl^- + Cu^{2+}$	$1.0 \cdot 10^7$	
R.C.160	$Cl2^- + H_2O_2 \longrightarrow 2Cl^- + H^+ + HO_2$	$7.0 \cdot 10^5$	3340
R.C.161	$Cl2^- + MHP \longrightarrow 2Cl^- + H^+ + CH_3O_2$	$7.0 \cdot 10^5$	3340
R.C.162	$Cl2^- + OH^- \longrightarrow 2Cl^- + OH$	$4.0 \cdot 10^6$	
R.C.163	$Cl2^- + HO_2 \longrightarrow 2Cl^- + H^+ + O_2$	$1.3 \cdot 10^{10}$	
R.C.164	$Cl2^- + O_2^- \longrightarrow 2Cl^- + O_2$	$6.0 \cdot 10^9$	
R.C.165	$Cl2^- + HSO_3^- \longrightarrow 2Cl^- + H^+ + SO_3^-$	$1.7 \cdot 10^8$	400
R.C.166	$Cl2^- + SO_3^{2-} \longrightarrow 2Cl^- + SO_3^-$	$6.2 \cdot 10^7$	
R.C.167	$Cl2 + H_2O \longrightarrow H^+ + Cl^- + HOCl$	0.401	7900
	— BROMINE CHEMISTRY —		
R.C.168	$SO_4^- + Br^- \longrightarrow SO_4^{2-} + Br$	$2.1 \cdot 10^9$	
R.C.169	$NO_3 + Br^- \longrightarrow NO_3^- + Br$	$3.8 \cdot 10^9$	
R.C.170	$Br2^- + Br2^- \longrightarrow Br2 + 2Br^-$	$1.7 \cdot 10^9$	

...to be continued.

. . . continued

No.	Reaction	k_{298} [$M^{-n}s^{-1}$]	E_a/R [K]
R.C.171	$Br2^- + Fe^{2+} \longrightarrow 2Br^- + Fe^{3+}$	$3.6 \cdot 10^6$	3330
R.C.172	$Br2^- + Mn^{2+} \longrightarrow 2Br^- + Mn^{3+}$	$6.3 \cdot 10^6$	4330
R.C.173	$Br2^- + Cu^+ \longrightarrow 2Br^- + Cu^{2+}$	$3.6 \cdot 10^6$	
R.C.174	$Br2^- + H_2O_2 \longrightarrow 2Br^- + H^+ + HO_2$	$1.0 \cdot 10^5$	
R.C.175	$Br2^- + MHP \longrightarrow 2Br^- + H^+ + CH_3O_2$	$1.0 \cdot 10^5$	
R.C.176	$Br2^- + OH^- \longrightarrow 2Br^- + OH$	$1.1 \cdot 10^4$	
R.C.177	$Br2^- + HO_2 \longrightarrow 2Br^- + H^+ + O_2$	$6.5 \cdot 10^9$	
R.C.178	$Br2^- + O_2^- \longrightarrow 2Br^- + O_2$	$1.7 \cdot 10^8$	
R.C.179	$Br2^- + HSO_3^- \longrightarrow 2Br^- + H^+ + SO_3^-$	$5.0 \cdot 10^7$	780
R.C.180	$Br2^- + SO_3^{2-} \longrightarrow 2Br^- + SO_3^-$	$3.3 \cdot 10^7$	650
R.C.181	$Br2 + H_2O \longrightarrow H^+ + Br^- + HOBr$	1.7	7500
	— CARBONATE CHEMISTRY —		
R.C.182	$HCO_3^- + OH \longrightarrow H_2O + CO_3^-$	$1.7 \cdot 10^7$	1900
R.C.183	$CO_3^{2-} + OH \longrightarrow OH^- + CO_3^-$	$3.9 \cdot 10^8$	2840
R.C.184	$CO_3^{2-} + SO_4^- \longrightarrow SO_4^{2-} + CO_3^-$	$4.1 \cdot 10^7$	
R.C.185	$HCO_3^- + SO_4^- \longrightarrow SO_4^{2-} + CO_3^- + H^+$	$2.8 \cdot 10^6$	2090
R.C.186	$CO_3^{2-} + NO_3 \longrightarrow NO_3^- + CO_3^-$	$4.1 \cdot 10^7$	
R.C.187	$CO_3^{2-} + Cl2^- \longrightarrow 2Cl^- + CO_3^-$	$2.7 \cdot 10^6$	
R.C.188	$CO_3^{2-} + Br2^- \longrightarrow 2Br^- + CO_3^-$	$1.1 \cdot 10^5$	
R.C.189	$CO_3^- + CO_3^- \overset{O_2}{\longrightarrow} 2O_2^- + 2CO_2$	$2.2 \cdot 10^6$	
R.C.190	$CO_3^- + Fe^{2+} \longrightarrow CO_3^{2-} + Fe^{3+}$	$2.0 \cdot 10^7$	
R.C.191	$CO_3^- + Mn^{2+} \longrightarrow CO_3^{2-} + Mn^{3+}$	$1.5 \cdot 10^7$	

. . . to be continued.

. . . continued

No.	Reaction	k_{298} [M^{-n}s^{-1}]	E$_a$/R [K]
R.C.192	CO$_3^-$ + Cu$^+$ $\longrightarrow$ CO$_3^{2-}$ + Cu^{2+}	$2.0 \cdot 10^7$	
R.C.193	CO$_3^-$ + H$_2$O$_2$ $\longrightarrow$ HCO$_3^-$ + HO$_2$	$4.3 \cdot 10^5$	
R.C.194	CO$_3^-$ + MHP $\longrightarrow$ HCO$_3^-$ + CH$_3$O$_2$	$4.3 \cdot 10^5$	
R.C.195	CO$_3^-$ + HO$_2$ $\longrightarrow$ HCO$_3^-$ + O$_2$	$6.5 \cdot 10^8$	
R.C.196	CO$_3^-$ + O$_2^-$ $\longrightarrow$ CO$_3^{2-}$ + O$_2$	$6.5 \cdot 10^8$	
R.C.197	CO$_3^-$ + HSO$_3^-$ $\longrightarrow$ HCO$_3^-$ + SO$_3^-$	$1.0 \cdot 10^7$	
R.C.198	CO$_3^-$ + SO$_3^{2-}$ $\longrightarrow$ CO$_3^{2-}$ + SO$_3^-$	$5.0 \cdot 10^6$	470
R.C.199	CO$_3^{2-}$ + SO$_4^-$ $\longrightarrow$ SO$_4^{2-}$ + CO$_3^-$	$4.1 \cdot 10^7$	
R.C.200	HCO$_3^-$ + SO$_4^-$ $\longrightarrow$ SO$_4^{2-}$ + CO$_3^-$ + H$^+$	$2.8 \cdot 10^6$	2090
R.C.201	CO$_3^{2-}$ + NO$_3$ $\longrightarrow$ NO$_3^-$ + CO$_3^-$	$4.1 \cdot 10^7$	
R.C.202	CO$_3^{2-}$ + Cl2$^-$ $\longrightarrow$ 2Cl$^-$ + CO$_3^-$	$2.7 \cdot 10^6$	
R.C.203	CO$_3^{2-}$ + Br2$^-$ $\longrightarrow$ 2Br$^-$ + CO$_3^-$	$1.1 \cdot 10^5$	
R.C.204	CO$_3^-$ + CO$_3^-$ $\xrightarrow{\text{O}_2}$ 2O$_2^-$ + 2CO$_2$	$2.2 \cdot 10^6$	
R.C.205	CO$_3^-$ + Fe^{2+} $\longrightarrow$ CO$_3^{2-}$ + Fe^{3+}	$2.0 \cdot 10^7$	
R.C.206	CO$_3^-$ + Mn^{2+} $\longrightarrow$ CO$_3^{2-}$ + Mn^{3+}	$1.5 \cdot 10^7$	
R.C.207	CO$_3^-$ + Cu$^+$ $\longrightarrow$ CO$_3^{2-}$ + Cu^{2+}	$2.0 \cdot 10^7$	
R.C.208	CO$_3^-$ + H$_2$O$_2$ $\longrightarrow$ HCO$_3^-$ + HO$_2$	$4.3 \cdot 10^5$	
R.C.209	CO$_3^-$ + MHP $\longrightarrow$ HCO$_3^-$ + CH$_3$O$_2$	$4.3 \cdot 10^5$	
R.C.210	CO$_3^-$ + HO$_2$ $\longrightarrow$ HCO$_3^-$ + O$_2$	$6.5 \cdot 10^8$	
R.C.211	CO$_3^-$ + O$_2^-$ $\longrightarrow$ CO$_3^{2-}$ + O$_2$	$6.5 \cdot 10^8$	
R.C.212	CO$_3^-$ + HSO$_3^-$ $\longrightarrow$ HCO$_3^-$ + SO$_3^-$	$1.0 \cdot 10^7$	
R.C.213	CO$_3^-$ + SO$_3^{2-}$ $\longrightarrow$ CO$_3^{2-}$ + SO$_3^-$	$5.0 \cdot 10^6$	470

Table C.3: List of aqueous phase equilibria. Indices f and b mark forward and backward reactions, respectively.

No.	Reaction	$k_{f,298}$ [M^{-n}s^{-1}]	E_a/R [K]	$k_{b,298}$ [M^{-n}s^{-1}]	E_a/R [K]
EC.1	$H_2O \rightleftharpoons H^+ + OH^-$	$2.34 \cdot 10^{-5}$	6800	$1.3 \cdot 10^{11}$	
EC.2	$CO_2 + H_2O \rightleftharpoons H_2CO_3$	$4.3 \cdot 10^{-2}$	9250	$5.6 \cdot 10^4$	8500
EC.3	$H_2CO_3 \rightleftharpoons H^+ + HCO_3^-$	$1.0 \cdot 10^7$		$5.0 \cdot 10^{10}$	
EC.4	$HCO_3^- \rightleftharpoons H^+ + CO_3^{2-}$	2.35	1820	$5.0 \cdot 10^{10}$	
EC.5	$HCL \rightleftharpoons H^+ + CL^-$	$2.95 \cdot 10^{17}$	-6890	$5.9 \cdot 10^5$	
EC.6	$NH_3 + H_2O \rightleftharpoons NH_4^+ + OH^-$	$1.1 \cdot 10^4$	560	$3.4 \cdot 10^{10}$	
EC.7	$HO_2 \rightleftharpoons H^+ + O_2^-$	$8.0 \cdot 10^5$	0	$5.0 \cdot 10^{10}$	0
EC.8	$HNO_3 \rightleftharpoons H^+ + NO_3^-$	$1.1 \cdot 10^{12}$	-1800	$5.0 \cdot 10^{10}$	
EC.9	$HNO_2 \rightleftharpoons H^+ + NO_2^-$	$2.65 \cdot 10^7$	1760	$5.0 \cdot 10^{10}$	
EC.10	$HO_2NO_2 \rightleftharpoons H^+ + O_2NO_2^-$	$5.0 \cdot 10^5$		$5.0 \cdot 10^{10}$	
EC.11	$NO_2 + HO_2 \rightleftharpoons HO_2NO_2$	$1.0 \cdot 10^7$		$4.6 \cdot 10^{-3}$	
EC.12	$SO_2 + H_2O \rightleftharpoons HSO_3^- + H^+$	$6.27 \cdot 10^4$	-1940	$2.0 \cdot 10^8$	
EC.13	$HSO_3^- \rightleftharpoons SO_3^{2-} + H^+$	3110	-1960	$5.0 \cdot 10^{10}$	
EC.14	$HSO_4^- \rightleftharpoons SO_4^{2-} + H^+$	$1.02 \cdot 10^9$	-2700	$1.0 \cdot 10^{11}$	
EC.15	$H_2SO_4 \rightleftharpoons HSO_4^- + H^+$	$5.0 \cdot 10^{13}$		$5.0 \cdot 10^{10}$	
EC.16	$HCOOH \rightleftharpoons HCOO^- + H^+$	$8.85 \cdot 10^6$	12	$5.0 \cdot 10^{10}$	
EC.17	$HAc \rightleftharpoons Ac^- + H^+$	$8.75 \cdot 10^5$	-46	$5.0 \cdot 10^{10}$	
EC.18	$Fe^{3+} + H_2O \rightleftharpoons [Fe(OH)]^{2+} + H^+$	$4.7 \cdot 10^4$		$4.3 \cdot 10^8$	
EC.19	$[Fe(OH)]^{2+} + H_2O \rightleftharpoons FeOH_2^+ + H^+$	$1.1 \cdot 10^3$		$8.0 \cdot 10^9$	
EC.20	$Fe^{3+} + SO_4^{2-} \rightleftharpoons FeSO_4^+$	$3.2 \cdot 10^3$		$1.8 \cdot 10^5$	
EC.21	$HCHO + H_2O \rightleftharpoons CH_2(OH)_2$	0.18	-4030	$5.1 \cdot 10^{-3}$	
EC.22	$CH_3CHO + H_2O \rightleftharpoons CH_3CH(OH)_2$	$1.4 \cdot 10^{-4}$	-2500	$5.69 \cdot 10^{-3}$	

. . . to be continued.

. . . continued

No.	Reaction	$k_{f,298}$ [M^{-n}s^{-1}]	E_a/R [K]	$k_{b,298}$ [M^{-n}s^{-1}]	E_a/R [K]
EC.23	$CH_2(OH)_2 + HSO_3^- \rightleftharpoons HMS^- + H_2O$	0.436	2990	$2.2 \cdot 10^{-9}$	2990
EC.24	$CH_2(OH)_2 + SO_3^{2-} \rightleftharpoons HMS^- + OH^-$	$1.36 \cdot 10^5$	2450	$4.15 \cdot 10^3$	5530
EC.25	$Cl + Cl^- \rightleftharpoons Cl2^-$	$2.7 \cdot 10^{10}$		$1.4 \cdot 10^5$	
EC.26	$Br + Br^- \rightleftharpoons Br2^-$	$1.2 \cdot 10^{10}$		$1.9 \cdot 10^4$	
EC.27	$Cl^- + OH \rightleftharpoons ClOH^-$	$4.3 \cdot 10^9$		$6.1 \cdot 10^9$	
EC.28	$ClOH^- + H^+ \rightleftharpoons Cl + H_2O$	$2.1 \cdot 10^{10}$		$1.3 \cdot 10^3$	
EC.29	$ClOH^- + Cl^- \rightleftharpoons Cl2^- + OH^-$	$1.0 \cdot 10^4$		$4.5 \cdot 10^7$	
EC.30	$Br^- + OH \rightleftharpoons BrOH^-$	$1.1 \cdot 10^{10}$		$3.3 \cdot 10^7$	
EC.31	$BrOH^- + H^+ \rightleftharpoons Br + H_2O$	$4.4 \cdot 10^{10}$		$2.45 \cdot 10^{-2}$	
EC.32	$BrOH^- + Br^- \rightleftharpoons Br2^- + OH^-$	$1.9 \cdot 10^8$		$2.7 \cdot 10^6$	

References

Asman, W. A. H.: 2001, 'Modelling the atmospheric transport and deposition of ammonia and ammonium: an overview with special reference to Denmark'. *Atmos. Environ.* **35**, 1969–1983.

Atkinson, R.: 1994, 'Gas-phase Tropospheric Chemistry of Organic Compounds'. Monograph No. 2 of the J. Phys. Chem. Ref. Data.

Atkinson, R., D. L. Baulch, R. A. Cox, J. N. Crowley, R. F. Hampson, Jr., J. A. Kerr, M. J. Rossi, and J. Troe: 2001, 'Summary of Evaluated Kinetic and Photochemical Data for Atmospheric Chemistry, December 2001'. http://www.iupac-kinetic.ch.cam.ac.uk/.

Baker, K.: 2001, 'Evaluation of PAR estimation methods - DRAFT - 6/15/01'. http://www.ladco.org/biogenics/par/par.htm.

Bator, A. and J. L. Collett, Jr.: 1997, 'Cloud chemistry varies with drop size'. *J. Geophys. Res.* **102**(D23), 28,071–28,078.

Bergin, M. H., S. N. Pandis, C. I. Davidson, J. L. Jaffrezo, J. E. Dibb, A. G. Russell, and H. D. Kuhns: 1996, 'Modeling of the processing and removal of trace gas and aerosol species by Arctic radiation fogs and comparison with measurements'. *J. Geophys. Res.* **101**(D9), 14,465–14,478.

Bergot, T. and D. Guedalia: 1994, 'Numerical forecasting of radiation fog. 1. Numerical-model and sensitivity tests'. *Mon. Wea. Rev.* **122**(6), 1218–1230.

Bott, A.: 1989, 'A positive definite advection scheme obtained by nonlinear renormalization of the advective fluxes'. *Mon. Wea. Rev.* **117**, 1006–1015.

Bott, A.: 1992, *Theoretical and numerical investigations on the physico-chemical microstructure of radiation fogs.* Institute of Atmospheric Physics. Habilitation thesis.

Bott, A.: 1999, 'A numerical model of the cloud-topped planetary boundary-layer: chemistry in marine stratus and the effects on aerosol particles'. *Atmos. Environ.* **33**(12), 1921–1936.

Bott, A. and G. R. Carmichael: 1993, 'Multiphase chemistry in a microphysical radiation fog model — a numerical study'. *Atmos. Environ.* **27A**, 503–522.

Bott, A., U. Sievers, and W. Zdunkowski: 1990, 'A radiation fog model with a detailed treatment of the interaction between radiative transfer and fog microphysics'. *J. Atmos. Sci.* **90**, 2153–2166.

Bott, A. and T. Trautmann: 2002, 'PAFOG – A new efficient forecast model of radiation fog and low level stratiform clouds'. *Atmos. Res.* in press.

Box, E. O.: 1981, 'Foliar biomass: Data base of the international biological program and other sources'. In: J. Bufalini and R. Arnts (eds.): *Atmospheric Biogenic Hydrocarbons.* Butterworth, Stoneham, Mass.

Chameides, W. L. et al.: 1992, 'Ozone precursor relationships in the ambient atmosphere'. *J. Geophys. Res.* **97**, 6037–6055.

Chameides, W. L. and A. W. Stelson: 1992, 'Aqueous-phase chemical processes in deliquescent sea-salt aerosols: A mechanism that couples the atmospheric cycles of S and sea salt'. *J. Geophys. Res.* **97**(D18), 20,565–20,580.

Chen, X., D. Hulbert, and P. B. Shepson: 1998, 'Measurements of the organic nitrate yield from OH reaction with isoprene'. *J. Geophys. Res.* **103**(D19), 25,563–25,568.

Chuang, C. C. and J. E. Penner: 1995, 'Effects of anthropogenic sulfate on cloud drop nucleation and optical-properties'. *Tellus* **47**(B5), 566–577.

Chuong, B. and P. S. Stevens: 2002, 'Measurements of the kinetics of the OH-initiated oxidation of isoprene'. *J. Geophys. Res.* **107**(D13), 10.1029/2001JD000865.

Clark, P. A. and W. P. Hopwood: 2001, 'One-dimensional site-specific forecasting of radiation fog. Part 1: Model formulation and idealised sensitivity studies'. *Meteorol. Appl.* **8**(3), 279–286.

Clegg, S. L. and P. Brimblecombe: 1995, 'Application of a multicomponent thermodynamic model to activities and thermal properties of $0 - 40$ mol kg^{-1} aqueous sulphuric acid from less than 200 K to 328 K'. *J. Chem. Eng. Data* **40**(1), 43–64.

Collett, Jr., J. L., A. Bator, X. Rao, and B. B. Demoz: 1994, 'Acidity variations across the cloud drop size spectrum and their influence on rates of atmospheric sulfate production'. *Geophys. Res. Lett.* **21**(22), 2393–2396.

Cox, P. M., R. A. Betts, C. B. Bunton, R. L. H. Essery, P. R. Rowntree, and J. Smith: 1999, 'The impact of new land surface physics on the GCM simulation of climate and climate sensitivity'. *Climate Dyn.* **15**(3), 183–203.

Crutzen, P. J., M. G. Lawrence, and U. Pöschl: 1999, 'On the background photochemistry of tropospheric ozone'. *Tellus* **51 A-B**(1), 123–146.

Damian-Iordache, V.: 1996, 'KPP — Chemistry simulation development environment'. Master's thesis, University of Iowa.

Deardorff, J. W.: 1978, 'Efficient prediction of ground surface temperature and moisture, with inclusion of a layer of vegetation'. *J. Geophys. Res.* **83**(C4), 1889–1903.

DeMore, W. B., S. P. Sander, D. M. Golden, R. F. Hampson, M. J. Kurylo, C. J. Howard, A. R. Ravishankara, C. E. Kolb, and M. J. Molina: 1997, *Chemical Kinetics and Photochemical Data for Use in Stratospheric Modeling, Evaluation 12*. NASA JPL Pub. 97-4.

Dransfield, T. J., K. K. Perkins, N. M. Donahue, J. G. Anderson, M. M. Sprengnether, and K. L. Demerjian: 1999, 'Temperature and pressure dependent kinetics of the gas-phase reaction of the hydroxyl radical with nitrogen dioxide'. *Geophys. Res. Lett.* **26**(6), 687–690.

Emmons, L. K. et al.: 1997, 'Climatologies of NO_x and NO_y: A comparison of data and models'. *Atmos. Environ.* **31**(12), 1851–1904.

Erisman, J. W., T. Brydges, K. Bull, E. Cowling, P. Grennfelt, L. Nordberg, K. Satake, T. Schneider, S. Smeulders, K. W. Van der Hoek, J. R. Wisniewski, and J. Wisniewski: 1998, 'Nitrogen, the confer-N-s – First International Nitrogen Conference 1998 – Summary statement'. *Environ. Poll.* **102**(Suppl. 1), 3–12.

Erisman, J. W., A. van Pul, and P. Wyers: 1994, 'Parametrization of surface resistance for the quantification of atmospheric deposition of acidifying compounds and ozone'. *Atmos. Environ.* **28**(16), 2595–2607.

Ervens, B.: 2001, 'Troposphärische Multiphasenchemie: Modellrechnungen und kinetische Untersuchungen von Reaktionen des OH-Radikals in wäßriger Lösung'. Ph.D. thesis, University of Leipzig (in german).

Fehsenfeld, F. et al.: 1992, 'Emission of volatile organic compounds from vegetation and the implications for atmospheric chemistry'. *Global Biogeochem. Cycles* **6**, 389–430.

Feingold, G. and S. Kreidenweis: 2000, 'Does cloud processing of aerosol enhance droplet concentrations?'. *J. Geophys. Res.* **105**(D19), 24351–24361.

Flechard, C. R., D. Fowler, M. A. Sutton, and J. N. Cape: 1999, 'A dynamic chemical model of bi-directional ammonia exchange between semi-natural vegetation and the atmosphere'. *Quart. J. Royal Met. Soc.* **125**, 2611–2641.

Flender, M., T. Trautmann, C. Wanner, and W. Zdunkowski: 2001, 'Explicit microphysical simulations of boundary layer clouds over the sea and over vegetated land surfaces'. In: R. Jaenicke (ed.): *Dynamics and Chemistry of Hydrometeors.* Wiley - VCH, pp. 81–105. Deutsche Forschungsgesellschaft: Final Report of the Collaborative Reasearch Centre 233 "Dynamik und Chemie der Hydrometeore".

Früh, B.: 2000, 'Entwicklung und Evaluierung einer Modellhierarchie zur Simulation der aktinischen Strahlung in aerosolbelasteter und bewölkter Atmospäre'. Ph.D. thesis, University of Mainz (in german).

Fuzzi, S.: 1998, 'Overview of the Po Valley fog experiment 1994 (CHEMDROP)'. *Contr. Atmos. Phys.* **71**(1), 3–19.

Ganzeveld, L. N. and J. Lelieveld: 1995, 'Dry deposition parameterization in a chemistry general circulation model and its influence on the distribution of reactive trace gases'. *J. Geophys. Res.* **100**(D10), 20,999–21,012.

Ganzeveld, L. N., J. Lelieveld, F. J. Dentener, M. C. Krol, and G.-J. Roelofs: 2002, 'Atmosphere-biosphere trace gas exchanges simulated with a single-column model'. *J. Geophys. Res.* accepted.

Geron, C. D., A. Günther, and T. Pierce: 1994, 'An improved model for estimating emissions of volatile organic compounds from forests in the eastern United States'. *J. Geophys. Res.* **99**(D6), 12,773–12,791.

Graedel, T. E. and P. J. Crutzen: 1993, *Atmospheric Change: An Earth System Perspective.* W. H. Freeman and Company, New York.

Grantz, D. A., X. J. Zhang, W. J. Massman, A. Delany, and J. R. Pederson: 1997, 'Ozone deposition to a cotton (Gossypium hirsutum L) field: stomatal and surface wetness effects during the California Ozone Deposition Experiment'. *Agricul. Forest Meteorol.* **85**(1-2), 19–31.

Günther, A. et al.: 1995, 'A global model of natural volatile organic compound emissions'. *J. Geophys. Res.* **100**(D5), 8873–8892.

Günther, A., P. Zimmerman, and M. Wildermuth: 1994, 'Natural volatile organic-compound emission rate estimates for United-States woodland landscapes'. *Atmos. Environ.* **28**(6), 1197–1210.

Halldin, S.: 1985, 'Leaf and bark area distribution in a pine forest'. In: B. A. Hutchinson and B. B. Hicks (eds.): *The Forest-Atmosphere Interaction*. Reidel, Dordrecht/Boston/Lancaster.

Herrmann, H., B. Ervens, H.-W. Jacobi, R. Wolke, P. Nowacki, and R. Zellner: 2000, 'CAPRAM2.3: A chemical aqueous phase radical mechanism for tropospheric chemistry'. *J. Atmos. Chem.* **36**, 231–284.

Hoffmann, P. et al.: 2001, 'Iron in the atmosphere'. In: R. Jaenicke (ed.): *Dynamics and Chemistry of Hydrometeors*. Wiley - VCH, pp. 440–467. Deutsche Forschungsgesellschaft: Final Report of the Collaborative Reasearch Centre 233 "Dynamik und Chemie der Hydrometeore".

Inclán, M. G., J. Schween, and R. Dlugi: 1999, 'Estimation of volatile organic compound fluxes using the forest-land-atmosphere model (FLAME)'. *J. Appl. Meteorol.* **38**(7), 913–921.

Jacob, D.: 1986, 'Chemistry of OH in remote clouds and its role in the production of formic acid and peroxymonosulfate'. *J. Geophys. Res.* **91**(D9), 9807–9826.

Jacob, D. J. and P. S. Bakwin: 1991, 'Cycling of NO_x in tropical forest canopies and its implications for the global source of biogenic NO_x to the atmosphere'. In: W. B. Whitman (ed.): *Microbial Production and Consumption of Greenheouse Gases*. American Society of Microbiology, Washington, D. C.

Jacob, D. J. and S. C. Wofsy: 1990, 'Budgets of reactive nitrogen, hydrocarbons, and ozone over the Amazon forest during the wet season'. *J. Geophys. Res.* **95**, 16,737–16,754.

Jacobs, A. F. G., J. H. Van Boxel, and R. M. M. El-Kilani: 1994, 'Nighttime free convection characteristics within a plant canopy'. *Bound. Lay. Meteorol.* **71**, 375–391.

Jaenicke, R.: 1988, 'Aerosol physics and chemistry'. In: Landolt-Boernstein (ed.): *Zahlenwerte und Funktionen aus Naturwissenschaften und Technik*. Springer, Chapt. V 4b, pp. 391–457.

Kavouras, I. G., N. Mihalopoulos, and E. G. Stephanou: 1998, 'Formation of atmospheric particles from organic acids produced by forests'. *Nature* **395**, 683–686.

Kirkman, G. A., W. X. Yang, and F. X. Meixner: 2001, 'Biogenic nitric oxide emissions upscaling: An approach for Zimbabwe'. *Global Biogeochem. Cycles* **15**(4), 1005–1020.

Klemm, O., C. Milford, M. A. Sutton, G. Spindler, and E. van Putten: 2002, 'A climatology of leaf surface wetness'. *Theoret. Appl. Climatology* **71**(1-2), 107–117.

Kondo, J. and T. Watanabe: 1992, 'Studies on the bulk transfer coefficients over a vegetated surface with a multilayer energy budget model'. *J. Atmos. Sci.* **49**(23), 2183–2199.

Krämer, M., N. Beltz, D. Schell, L. Schütz, C. Sprengard-Eichel, and S. Wurzler: 2000, 'Cloud processing of continental aerosol particles: Experimental investigations for different drop sizes'. *J. Geophys. Res.* **105**(D9), 11,739–11,752.

Kruijt, B., Y. Malhi, J. Lloyd, A. D. Nobre, A. C. Miranda, M. G. P. Pereira, A. Culf, and J. Grace: 2000, 'Turbulence statistics above and within two Amazon rain forest canopies'. *Bound. Lay. Meteorol.* **94**, 297–331.

Lamb, B., D. Gay, and H. Westberg: 1993, 'A biogenic hydrocarbon emission inventory for the U.S.A. using a simple forest canopy model'. *Atmos. Environ.* **27A**(11), 1673–1690.

Lamb, B., A. Günther, D. Gay, and H. Westberg: 1987, 'A national inventory of biogenic hydrocarbon emissions'. *Atmos. Environ.* **21**(8), 1695–1705.

Landgraf, J. and P. Crutzen: 1998, 'An efficient method for online calculations of photolysis and heating rates'. *J. Atmos. Sci.* **55**(5), 863–878.

Larcher, W.: 1994, *Ökophysiologie der Pflanze*. Ulmer, Stuttgart. 394 pp. (in german).

Lawrence, M. G., P. J. Crutzen, P. J. Rasch, B. E. Eaton, and N. M. Mahowald: 1999, 'A model for studies of tropospheric photochemistry: Description, global distributions, and evaluation'. *J. Geophys. Res.* **104**(D21), 26,245–26,277.

Lerdau, M. T., J. W. Munger, and D. J. Jacob: 2000, 'The NO_2 flux conundrum'. *Science* **289**, 2291–2293.

Liang, J. and M. Z. Jacobsen: 1999, 'A study of sulfur dioxide oxidation pathways over a range of liquid water contents, pH values, and temperatures'. *J. Geophys. Res.* **104**(D11), 13,749–13,769.

Lillis, D., C. N. Cruz, J. Collett, Jr., L. W. Richards, and S. N. Pandis: 1999, 'Production and removal of aerosol in a polluted fog layer: model evaluation and fog effect on PM'. *Atmos. Environ.* **33**, 4797–4816.

Loughlin, P. E., T. Trautmann, A. Bott, W.-G. Panhans, and W. Zdunkowski: 1997, 'The effects of different radiation parametrizations on cloud evolution'. *Quart. J. Royal Met. Soc.* **123**(543), 1985–2007. Part A.

Ludwig, J., F. X. Meixner, B. Vogel, and J. Forstner: 2001, 'Soil-air exchange of nitric oxide: An overview of processes, environmental factors, and modeling studies'. *Biogeochemistry* **52**(3), 225–257.

Luo, B., K. S. Carslaw, T. Peter, and S. L. Clegg: 1995, 'Vapour pressures of $H_2SO_4/HNO_3/HCl/HBr/H_2O$ solutions to low stratospheric temperatures'. *Geophys. Res. Lett.* **22**, 247–250.

MacDonald, R. C. and R. Fall: 1993, 'Detection of substantial emissions of methanol from plants to the atmosphere'. *Atmos. Environ.* **27A**(11), 1709–1713.

Matthias-Maser, S. and R. Jaenicke: 1995, 'The size distribution of primary biological aerosol particles with radii $> 0.2\,\mu$m in an urban rural influenced region'. *Atmos. Res.* **39**(4), 279–286.

Mellor, G. L. and T. Yamada: 1982, 'Development of a turbulence closure model for geophysical fluid problems'. *Rev. Geoph. Space Phys.* **20**(4), 851–875.

Meyers, T. P.: 1987, 'The sensitivity of modeled SO_2 fluxes and profiles to stomatal and boundary layer resistances'. *Water, Air, and Soil Pollut.* **35**, 261–278.

Millet, M., A. Sanusi, and H. Wortham: 1997, 'Chemical composition of fogwater in an urban area: Strasbourg (France)'. *Environ. Pollut.* **94**(3), 345–354.

Mueller, F.: 1998, 'Mass Accommodation Coefficients'. http://www.mi.uni-hamburg.de/technische_meteorologie/Meso/homepages/fmueller/mass_acc.html.

Munger, J. W., S. M. Fan, P. S. Bakwin, M. L. Goulden, A. H. Goldstein, A. S. Colman, and S. C. Wofsy: 1998, 'Regional budgets for nitrogen oxides from continental sources: Variations of rates for oxidation and deposition with season and distance from source regions'. *J. Geophys. Res.* **103**(D7), 8355–8368.

Nemitz, E., C. Milford, and M. A. Sutton: 2001, 'A two-layer canopy compensation point model for describing bi-directional biosphere-atmosphere exchange of ammonia'. *Quart. J. Royal Met. Soc.* **127**, 815–833.

Noone, K. J., R. J. Charlson, D. S. Covert, J. A. Ogren, and J. Heintzenberg: 1988, 'Cloud droplets: Solute concentration is size dependent'. *J. Geophys. Res.* **93**, 9477–9482.

O'Dowd, C. D., P. Aalto, K. Hameri, M. Kulmala, and T. Hoffmann: 2002, 'Aerosol formation - Atmospheric particles from organic vapours'. *Nature* **416**(6880), 497–498.

Pandis, S. N. and J. H. Seinfeld: 1989, 'Mathematical modeling of acid deposition due to radiation fog'. *J. Geophys. Res.* **94**, 12,911–12,923.

Pandis, S. N., J. H. Seinfeld, and C. Pilinis: 1990, 'Chemical composition differences in fog and cloud droplets of different sizes'. *Atmos. Environ.* **24**(A), 1957–1969.

Panhans, W.-G.: 1997, 'PIFM bei partieller Vegetation'. Institute for Physics of the Atmosphere, University of Mainz, Internal Report.

Penner, J. E., C. S. Atherton, J. Dignon, S. J. Ghan, and J. J. Walton: 1991, 'Tropospheric nitrogen: A three-dimensional study of sources, distributions and deposition'. *J. Geophys. Res.* **96**, 959–990.

Pielke, R. A.: 1984, *Mesoscale meteorological modeling*. Academic Press, Orlando.

Pitzer, K. S.: 1991, *Activity coefficients in electrolyte solutions, 2nd edition*. CRC Press, INc., Boca Raton, FL.

Pöschl, U., R. von Kuhlmann, N. Poisson, and P. J. Crutzen: 2000, 'Development and intercomparison of condensed isoprene oxidation mechanisms for global atmospheric modeling'. *J. Atmos. Chem.* **37**(1), 29–52.

Potter, C. S., S. E. Alexander, J. C. Coughlan, and S. A. Klooster: 2001, 'Modeling biogenic emissions of isoprene: exploration of model drivers, climate control algorithms, and use of global satellite observations'. *Atmos. Environ.* **35**(35), 6151–6165.

Pruppacher, H. R. and J. D. Klett: 1997, *Microphysics of clouds and precipitation.* Dordrecht: Kluwer Academic Publisher, 2 edition.

Rao, X. and J. L. Collett, Jr.: 1998, 'The drop size-dependence of iron and manganese concentrations in clouds and fogs: Implications for sulfate production'. *J. Atmos. Chem.* **30**, 273–289.

Rattigan, O. V., J. Reilly, C. Judd, K. F. Moore, M. Das, D. E. Sherman, V. A. Dutkiewicz, J. L. Collett, Jr., and L. Husain: 2001, 'Sulfur dioxide oxidation in clouds at Whiteface Mountain as a function of drop size'. *J. Geophys. Res.* **106**, 17,347–17,358.

Raupach, M. R. and A. S. Thom: 1981, 'Turbulence in and above plant canopies'. *Ann. Rev. Fluid Mech.* **13**, 97–129.

Reilly, J. E., O. V. Rattigan, K. F. Moore, C. Judd, D. E. Sherman, V. A. Dutkiewicz, S. M. Kreidenweis, L. Husain, and J. L. Collett, Jr.: 2001, 'Drop size-dependent S(IV) oxidation in chemically heterogeneuos radiation fogs'. *Atmos. Environ.* **35**, 5717–5728.

RGAR: 1997, 'Acid Deposition in the United Kingdom 1992–94'. Fourth report of the review group on acid rain, Department of the Environment, Transport and the Regions, London, UK.

Roach, W. T.: 1976, 'On the effect of radiative exchange on the growth by condensation of a cloud or fog droplet'. *Quart. J. Royal Met. Soc.* **102**, 361–372.

Roache, P. J.: 1982, *Computational Fluid Dynamics.* Hermosa Publishers, Albuquerque, N. M.

Rummel, U., C. Ammann, A. Gut, F. Meixner, and M. Andreae: 2002, 'Eddy covariance measurements of nitric oxide flux within an Amazonian rain forest'. *J. Geophys. Res.* submitted.

Sander, R.: 1999, 'Henry's law constants'. http://www.mpch-mainz.mpg.de/~sander/res/henry.html.

Sander, S. P., R. R. Friedl, W. B. DeMore, A. R. Ravishankara, D. M. Golden, C. E. Kolb, M. J. Kurylo, R. F. Hampson, R. E. Huie, M. J. Molina, and G. K. Moortgat: 2000, *Chemical Kinetics and Photochemical Data for Use in Stratospheric Modeling, Evaluation 13, Supplement to Evaluation 12: Update of Key Reactions*. NASA JPL Pub. 00-3, http://jpldataeval.jpl.nasa.gov/.

Schemenauer, R. S. and P. Cereceda: 1994, 'A proposed standard fog collector for use in high-elevations regions'. *J. Appl. Meteorol.* **33**(11), 1313–1322.

Schwartz, S. E.: 1986, 'Mass-transport considerations pertinent to aqueous-phase reactions of gases in liquid-water clouds'. In: W. Jaeschke (ed.): *Chemistry of Multiphase Atmospheric Systems*. Springer Verlag, New York, pp. 415–471.

Schween, J. H., R. Dlugi, C. N. Hewitt, and P. Foster: 1997, 'Determination and accuracy of VOC-fluxes above pine/oak forest at Castelporziano'. *Atmos. Environ.* **31**(S1), 199–215.

Seinfeld, J. H. and S. N. Pandis: 1998, *Atmospheric Chemistry and Physics: From Air Pollution to Climate Change*. John Wilsey & Sons, Inc.

Shuttleworth, W. J.: 1977, 'The exchange of wind-driven-fog and mist between vegetation and the atmosphere'. *Bound. Lay. Met.* **12**, 463–489.

Siebert, J., A. Bott, and W. Zdunkowski: 1992, 'Influence of a vegetation-soil model on the simulation of radiation fog'. *Contr. Atmos. Phys.* **65**, 93–106.

Spindler, G., U. Teichmann, and M. A. Sutton: 2001, 'Ammonia dry deposition over grassland – micrometeorological flux-gradient measurements and bidirectional flux calculations using an inferential model'. *Quart. J. Royal Met. Soc.* **127**, 795–814.

Stevens, R. K., T. G. Dzubay, C. W. Lewis, and R. W. Shaw: 1984, 'Source apportionment methods applied to the determination of the origin of ambient aerosols that affect visibility in forested areas'. *Atmos. Environ.* **18**, 261–272.

Stockwell, W., F. Kirchner, M. Kuhn, and S. Seefeld: 1997, 'A new mechanism for regional atmospheric chemistry modeling'. *J. Geophys. Res.* **102**(D22), 25847–25879.

Sutton, M. A., J. K. Schjørring, and G. P. Wyers: 1995, 'Plant-atmosphere exchange of ammonia'. *Phil. Trans. Roy. Soc. Land.* **A351**, 261–278.

Teixeira, J. and P. M. A. Miranda: 2001, 'Fog prediction at Lisbon Airport using a one-dimensional boundary layer model'. *Meteorol. Appl.* **8**(4), 497–505.

Thom, A. S.: 1975, 'Momentum, mass and heat exchange of plant communities'. In: J. L. Monteith (ed.): *Vegetation and the Atmosphere.* Academic Press, London/New York/San Francisco, pp. 57–110.

Tyndall, G. S., R. A. Cox, C. Granier, R. Lesclaux, G. K. Moortgat, M. J. Pilling, A. R. Ravishankara, and T. J. Wallington: 2001, 'Atmospheric chemistry of small organic peroxy radicals'. *J. Geophys. Res.* **106**(D11), 12157–12182.

Tyndall, G. S., T. A. Staffelbach, J. J. Orlando, and J. G. Calvert: 1995, 'Rate coefficients for the reactions of OH radicals with methylglyoxal and acetaldehyde'. *Int. J. Chem. Kinet.* **27**, 1009–1020.

Velho, H. F. C., R. R. Rosa, F. M. Ramos, R. A. Pielke, G. A. Degrazia, C. R. Neto, and A. Zanandrea: 2001, 'Multifractal model for eddy diffusivity and countergradient term in atmospheric turbulence'. *Physica A* **295**(1–2), 219–223.

Verstraete, M. M.: 1987, 'Radiation transfer in plant canopies: Transmission of direct solar radiation and the role of leaf orientation'. *J. Geophys. Res.* **92**(D9), 10,985–10,995.

Verwer, J. G., E. J. Spee, J. G. Blom, and W. H. Hundsdorfer: 1997, 'A second order Rosenbrock method applied to photochemical dispersion problems'. Technical report, Report MAS-R9717, CWI, Amsterdam. http://www.cwi.nl/static/publications/reports/reports.html.

Verwer, J. G., E. J. Spee, J. G. Blom, and W. H. Hundsdorfer: 1999, 'A second order Rosenbrock method applied to photochemical dispersion problems'. *SIAM J. Sci. Comp.* **20**, 1456–1480.

Villenave, E. and R. Lesclaux: 1996, 'Kinetics of the Cross Reactions of CH_3O_2 and $C_2H_5O_2$ Radicals with Selected Peroxy Radicals'. *J. Phys. Chem. A* **100**, 14372–14382.

von Glasow, R. and A. Bott: 1999, 'Interaction of radiation fog with tall vegetation'. *Atmos. Environ.* **33**, 1333–1346.

von Kuhlmann, R.: 2001, 'Tropospheric photochemistry of ozone, its precursors and the hydroxyl radical: A 3D-modeling study considering non-methane hydrocarbons'. Ph.D. thesis, University of Mainz.

Wahner, A., T. F. Mentel, and M. Sohn: 1998, 'Gas-phase reaction of N_2O_5 with water vapor: Importance of heterogeneous hydrolysis of N_2O_5 and surface desorption of HNO_3 in a large teflon chamber'. *Geophys. Res. Lett.* **25**(12), 2169–2172.

Wang, Y., D. J. Jacob, and J. A. Logan: 1998, 'Global simulation of tropospheric O_3-NO_x-hydrocarbon chemistry 1. Model formulation'. *J. Geophys. Res.* **103**(D9), 10,713–10,725.

Watanabe, T. and J. Kondo: 1990, 'The influence of canopy structure and density upon the mixing length within and above vegetation'. *J. Met. Soc. Japan* **68**(2), 227–235.

Wiedinmyer, C., S. Friedfeld, W. Baugh, J. Greenberg, A. Günther, M. Fraser, and D. Allen: 2001, 'Measurement and analysis of atmospheric concentrations of isoprene and its reaction products in central Texas'. *Atmos. Environ.* **35**, 1001–1013.

Wilson, N. R. and R. H. Shaw: 1977, 'A higher order closure model for canopy flow'. *J. Appl. Meteorol.* **16**, 1197–1205.

Winkler, P.: 1974, 'Die relative Zusammensetzung des atmosphärischen Aerosols in Stoffgruppen'. *Meteorol. Rdsch.* **27**, 129–136. (in german).

Winterrath, T. and A. Bott: 2001, 'CHEMIFOG_V — A model to simulate radiation fogs and their interaction with vegetation and chemistry'. *Water, Air, and Soil Pollut.: Focus* **1**, 373–380.

Wrzesinsky, T. and O. Klemm: 2000, 'Summertime fog chemistry at a mountainous site in central Europe'. *Atmos. Environ.* **34**(9), 1487–1496.

Wurzler, S., T. G. Reisin, and Z. Levin: 2000, 'Modification of mineral dust particles by cloud processing and subsequent effects on drop size distributions'. *J. Geophys. Res.* **105**(D4), 4501–4512.

Yamada, T.: 1982, 'A numerical model study of turbulent airflow in and above a forest canopy'. *J. Met. Soc. Jap.* **60**(1), 439–454.

Yienger, J. J. and H. Levy II: 1995, 'Empirical model of global soil-biogenic NO_x emissions'. *J. Geophys. Res.* **100**(D6), 11,447–11,464.

Zdunkowski, W., W.-G. Panhans, R. Welch, and G. Korb: 1982, 'A radiation scheme for circulation and climate models'. *Contr. Atmos. Phys.* **55**, 215–238.

Zeng, N., J. D. Nelin, K.-M. Lau, and C. J. Tucker: 1999, 'Enhancement of inter-decadal climate variability in the Sahel by vegetation interaction'. *Science* **286**, 1537–1540.

Zimmerling, R. and U. Dammgen: 2002, 'Concentrations of air-borne acidifying and eutrophying species in the Schorfheide nature reserve in Brandenburg, Germany'. *J. Appl. Botany* **76**(1–2), 52–61.

Zimmerman, P. R., J. P. Greenberg, and C. E. Westberg: 1988, 'Measurements of atmospheric hydrocarbons and biogenic emission fluxes in the Amazon boundary layer'. *J. Geophys. Res.* **93**(D2), 1407–1416.

Zimmermann, L. and F. Zimmermann: 2002, 'Fog deposition to Norway Spruce stands at high-elevation sites in the Eastern Erzgebirge (Germany)'. *J. Hydrol.* **256**(3–4), 166–175.

Danksagung

Bei den Menschen, die zum Gelingen dieser Arbeit beigetragen haben, möchte ich mich herzlich bedanken. Aus datenschutzrechtlichen Gründen ist es leider nicht möglich, Namen zu nennen.

CURRICULUM VITAE

Tanja Winterrath

Email: winterra@mail.uni-mainz.de

Date and Place of Birth	January 2, 1971, Osnabrück, Germany
Citizenship	German

Ph.D:

September 2002	Ph.D. (mark "magna cum laude")
1998–2002	Doctorate studies at the Institute for Physics of the Atmosphere, Physics Department of the Johannes Gutenberg University Mainz.

Higher Education:

December 1997	Final exam (Diplom, mark 1.6) in physics. Title of exam thesis: The influence of clouds on DOAS zenith sky measurements — Analysis and interpretation(in german).
1993–1997:	Studies of physics at the University of Bremen, with focus on atmospheric physics and chemistry.
December 1992	B.Sc (Vordiplom) in physics.
1990–1993:	Studies of physics at the University of Osnabrück.

School Education:

1983–1990	Graf–Stauffenberg–Gymnasium, Osnabrück, with final examination A-level (Abitur, mark 1.5).
1981–1983	Orientierungsstufe Kalkhügel, Osnabrück
1977–1981	Piusschule, Osnabrück

Professional Experience:

1998	Graduate scientific research assistant at the Institute of Environmental Physics, Bremen.
1994–1997	Scientific research assistant at the Institute of Environmental Physics, Bremen
1996	Scientific research assistant at the Alfred Wegener Institute of polar and marine research, Bremerhaven, on the research vessel Polarstern during a cruise to Antartica (chemical oceanography).
1994	Internship at the oceanography department of the Alfred Wegener Institute of polar and marine research, Bremerhaven.